APPLIED COMPUTATIONAL ELECTROMAGNETICS SOCIETY JOURNAL

May 2016
Vol. 31 No. 5
ISSN 1054-4887

The ACES Journal is abstracted in INSPEC, in Engineering Index, DTIC, Science Citation Index Expanded, the Research Alert, and to Current Contents/Engineering, Computing & Technology.

The illustrations on the front cover have been obtained from the research groups at the Department of Electrical Engineering, The University of Mississippi.

EMERITUS EDITORIAL ASSISTANTS

MAY 2016 REVIEWERS

THE APPLIED COMPUTATIONAL ELECTROMAGNETICS SOCIETY

JOURNAL

Vol. 31 No. 5 May 2016

TABLE OF CONTENTS

Integration of an Equivalent Aperture Method into Full-wave Electromagnetic Simulation of Airborne Radomes

Benjamin L. Cannon [1] and Jared Williams Jordan [2]

[1] Nuvotronics Inc., Durham, NC 27703, USA
bcannon@nuvotronics.com

[2] Raytheon Missile Systems, Tucson, AZ 85756 USA
jaredwilliamsjordan@gmail.com

Abstract ─ A method is provided for performing efficient, accurate, full-wave electromagnetic simulations of airborne radomes by representing the enclosed antenna with an equivalent aperture field distribution. In this case, the antenna and radome problems are essentially decoupled, and fine meshing details in the antenna region of the problem are eliminated. The equivalent aperture governing equations are discussed, and an algorithm for forming a representative aperture field distribution from far-field radiation patterns is provided. The success of the equivalent aperture method is demonstrated via an example problem. Equivalent aperture results are compared to full-wave simulations of a corresponding fully-detailed slot array antenna. For both the equivalent aperture and corresponding slot array antennas, a 2:1 fineness ratio tangent ogive radome with dielectric constant of 7 and metallic tip is simulated to determine the effects on radiation patterns, loss, and boresight error. Radome insertion loss agreement is achieved to within 0.3 dB or better and boresight error agreement is achieved to within 0.05 deg or better in both elevation and azimuth scan planes for a significantly detuned radome wall. Both transmit-mode and receive-mode formulations of the full-wave radome analysis and their appropriate uses are described.

Index Terms ─ Airborne radomes, aperture antennas, boresight error (BSE), Fourier transform, Lorentz reciprocity, monopulse radar.

I. INTRODUCTION

The simulation of radome effects on an enclosed radar antenna has been a topic of investigation for more than half of a century. The analysis of sharp-nosed, airborne radomes is particularly challenging. These airborne radomes are often electrically large structures—with respect to the operating frequency of the enclosed radar—which can require large amounts of computational resources to solve. Additionally, this class of radomes can often be considered electrically complex, particularly in the sharp-nosed tip region of the radome where the geometry does not appear locally flat and diffractive effects can dominate the electromagnetic interactions. For these two reasons, airborne radome modeling still remains an ongoing topic of investigation, and a universally accepted modeling technique has yet to exist.

Computational resources have improved drastically over the years, allowing for larger and more complicated antenna and radome simulations to be performed. As a result, the techniques used to model large, complicated radomes have evolved, with the fidelity of simulations being primarily limited by the computational resources available to the design engineer.

The first methods that were developed for radome analysis were based off of geometric optics (GO) [1-4], or ray-tracing, which is a high-frequency approximation method for analyzing the distortion of electromagnetic energy propagating through the radome. Bundles of rays are tracked as they propagate through and bounce off of the inner radome surface. This ray-optical approximation is typically based off of analytic Fresnel transmission and reflection coefficients [5] for planar slabs of infinite extent and therefore yields relatively quick results. Radome effects over entire scan spaces for both electrically and mechanically scanned arrays can be solved for in only a few minutes. This approach is particularly advantageous for modeling multi-layer structures because radome transmission and reflection coefficients can be determined by cascading 2x2 ABCD transmission line matrices for each of the layers [6]. However, the GO approximation does not fully capture the distortion of electromagnetic waves due to the radome, especially in the sharp-nosed tip region of the airborne radome where the geometry of the radome does not appear locally flat.

Over the years, advances have been made to

Submitted On: August 19, 2014
Accepted On: March 24, 2016

increase the fidelity of high-frequency approximation methods. Physical Optics (PO) methods and Aperture Integration Surface Integration (AiSi) methods [7-12] were developed to treat monolithic and layered radomes as scattering objects. In both the PO and AiSi approximations, equivalent electric and magnetic "currents" induced on the radome surfaces are integrated to determine radome effects. In both cases, the currents can be approximated by the same Fresnel transmission and reflection coefficients that are used in GO approximations. Additional advancements have been made in comprehending diffractive tip effects by hybridizing high frequency approximation methods with full-wave method [13, 14].

While radome simulation accuracy has indeed been increased as simulation fidelity is improved, all of the aforementioned approaches are at a fundamental level an approximation to the true electromagnetic wave interactions that take place in an antenna/radome system. Present-day computing capabilities have now permitted full-wave field solutions of certain radome geometries that are not too large or too complex. Commercially available software packages contain fast, accurate solvers which generate numerical solutions to Maxwell's equations for arbitrary, complex geometries [15-17].

Presented in this paper are the results of full-wave simulations in CST's commercially available time-domain solver, modeling the effects of a sharp-nosed airborne radome on a mechanically gimbaled seeker antenna. A case study is presented where a slotted array antenna sits in close proximity to a high fineness ratio radome with a sharp metallic tip. The seeker antenna is then replaced by an equivalent aperture field distribution that was derived from the far-field radiation patterns of the slotted array antenna. The use of an equivalent aperture to represent the seeker antenna eliminates the fine meshing details that are often required for complicated radiating elements and feeding structures (resonant cavities, power dividers/combiners, layer-to-layer transitions, etc.). The approximations that exist when using an equivalent aperture representation of the seeker antenna will be described.

By comparing results from a full-wave radome simulation that includes a physical antenna model to another full-wave radome simulation with a representative equivalent aperture, one can isolate and study the impact of decoupling the antenna and the radome. Additionally, there are benefits towards using full-wave simulation results as the basis for quantifying the accuracy of another proposed modeling technique instead of measured data. Firstly, expensive manufacturing of antenna and radome test articles and test facilities are avoided. Secondly, measurement errors associated with antenna and radome ranges are removed. Finally, accounting for discrepancies between the manufactured benchmark test articles and nominal simulation models is unnecessary.

II. RADOME/ANTENNA PROBLEM UNDER INVESTIGATION AND THEORETICAL BACKGROUND

The radome and antenna system under evaluation is shown in Fig. 1. The antenna diameter is 10 in and consists of 4 quadrants, each containing 17 half-wavelength resonant slots [18] designed for operation at 7 GHz. Each slot is individually fed by a WR-137 waveguide located behind the ground plane. The radome is a tangent ogive with an approximate fineness ratio of 2:1, inside base radius of 11 in, and an inner length of 22 in. The radome gimbal center is positioned 4 in into the radome from its base. The plane that the slots reside in is located 1 in from the gimbal center. The edge of the antenna is less than 0.25 in (15% of a freespace wavelength at 7 GHz) from the inside of the radome. The top 1 in of the radome is a sharp metal tip, modeled as a perfect electric conductor (PEC). The radome shell is 0.3 in thick and is constructed from a lossless dielectric with a relative permittivity of 7. The thickness of the radome wall was intentionally chosen to provide a detuned response at the operating frequency of 7 GHz to demonstrate the presented modeling methodology in a circumstance where significant bounce energy exists.

The normal of the antenna faceplate is directed along the positive z-axis and the radiating slots are y-polarized. The elevation plane is defined as the YZ plane, and the azimuth plane is defined as the XZ plane. The radome is gimbaled about the gimbal center while the antenna is fixed and results will be presented as such.

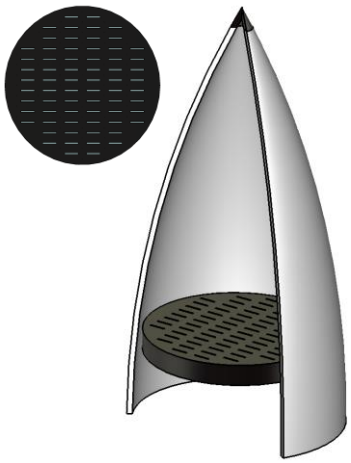

Fig. 1. Radome and antenna geometry under evaluation with a portion of the radome cut away for visual access to the antenna. An array of 68 half-wavelength resonant radiating slots is in close proximity to the radome.

Far-field radiation patterns, antenna boresight transmission loss and boresight errors are modeled using two different simulation methodologies. In both cases, simulations are performed in CST's time-domain solver based on the Finite Integration Technique (FIT). Firstly, the entire radome and antenna are simulated together using the previously provided parameters. By modeling the radome and antenna together the mutual coupling between these two entities is fully captured. The results from these simulations will be considered "truth" for the purpose of this paper, and henceforth be the standard by which we compare the proposed modeling method. As stated previously, it is convenient to allow a simulation to represent "truth" rather than a measured result as it eliminates any uncertainties in both the measurement system and the device under test. The second design methodology replaces the antenna with an equivalent aperture defined by representative fields or currents with no physical scattering object present. As a result, this method does not capture mutual coupling between the seeker antenna and radome. For this approximation to be valid, little energy propagating from the seeker antenna should bounce off the radome and couple back into the antenna and re-scatter off the antenna. Such interactions are fully captured in the first simulation methodology. Moneum et al. [13] believed this mutual coupling to be small for well-tuned radomes of this shape. The presented antenna/radome system under investigation aims to demonstrate the validity of this approach for a radome of this size/shape, even when the radome wall is significantly detuned.

The notion of using an equivalent aperture to represent an antenna is not new, but rather an old and well-understood concept [19]. The significance of what is presented here is the use of this method in conjunction with a full-wave radome solution that can accurately quantify the validity of this approach for radome design and analysis. Furthermore, the equivalent aperture method is applied to an intentionally detuned radome, which is a scenario that often yields unsatisfactory results in high-frequency approximation methods for radome analysis.

It is well-known that for large (many wavelengths in diameter), well-collimated antennas, one can perform a 2D Fourier Transform of the antenna's far-field radiation pattern to generate a well-representative equivalent aperture plane field distribution, which if inverse transformed, would reconstruct the original far-field pattern [20]. This method requires both the magnitude and phase of the far-field data for uniqueness. It is clear to see from (1) and (2) that the equivalent aperture field, $F(x,y)$ is related to the far-field response $U_p(k_x,k_y)$ by a two-dimensional Fourier transform, where k_x (3) and k_y (4) are the x and y components of the free space propagation vector **k** (5). The far-field response is normalized by the freespace scalar Green's function, removing the amplitude and phase dependence associated with absolute far-field data;

$$F(x,y) \approx \iint_{k_y k_x} f(k_x,k_y) e^{-j(x\cdot k_x + y\cdot k_y)} dk_x dk_y \,, \tag{1}$$

$$f(k_x,k_y) = \frac{-j\lambda U_p(k_x,k_y)}{\frac{e^{-jkR}}{R}\cdot(1+\cos(\theta))} \,, \tag{2}$$

$$k_x = k\sin(\theta)\cos(\phi) \,, \tag{3}$$

$$k_y = k\sin(\theta)\sin(\phi) \,, \tag{4}$$

$$|\mathbf{k}| = \frac{2\pi}{\lambda} \,. \tag{5}$$

The equivalent aperture approach is a high-frequency approximation, and for the size of the antenna under consideration it is applicable. The method starts with the acquisition of measured or simulated far-field radiation patterns for the antenna under evaluation in the absence of a radome. In this specific case study, simulated far-field patterns were computed utilizing the full-wave antenna-only model where the four quadrants are individually and simultaneously excited. The far-field radiation patterns are then Fourier transformed to form equivalent aperture field distributions. Because only propagating-mode information from the far-field is initially provided to the Fourier transform, this is an inversion problem.

Since the far-field data does not contain evanescent mode information, the equivalent aperture derived from the propagating mode far-field data is initially not a good representation of the antenna and is lacking in its ability to accurately model the antenna's near-fields. Correctly modeling the aperture near-field is imperative when the antenna is in close proximity to the radome. In an effort to reconstruct the lost evanescent mode energy, an extrapolation algorithm was implemented [19]. The method requires as an input a user-defined diameter of the resulting equivalent aperture. Future research could focus on non-circular apertures, and determining the optimal outer-aperture contour to be used in the extrapolation algorithm. The diameter used for this study was chosen to be equal to the ground plane diameter of the radiating slot antenna. The equivalent aperture should be as large as the physical extent of the antenna it is representing. Consequently, the original farfield pattern data must be sampled in fine enough increments to create an equivalent aperture with maximum extents larger than that of the physical antenna. The extrapolation algorithm is summarized as follows:

1) *Far-field data is Fourier transformed to create an equivalent aperture.*
2) *Aperture fields outside of a user-defined aperture diameter are removed.*
3) *The truncated aperture is inverse Fourier transformed to obtain its corresponding far-field data.*
4) *The newly created evanescent mode information from this far-field data is appended to the original far-field data.*
5) *Steps 1-4 are repeated until fields in the aperture plane have converged to a steady value.*

The aperture is flat and exists in a 2D plane. In general, because the Fourier transform operates on a scalar, this process must be repeated separately for the two orthogonal far-field polarizations to form the two orthogonal polarizations that fully define the tangential aperture fields.

The magnitude and phase for the initial antenna far-field simulation can be seen in Fig. 2 (a) and Fig. 2 (b), respectively. Ludwig's 3rd definition of co- and cross-polarization is utilized, and the co-polarized far-field radiation pattern is what is shown [21]. According to Ludwig's 3rd definition, the y-polarized radiating slot array in the absence of the radome produces a primarily co-polarized far-field response and very little cross-polarized energy exists. Full-wave solutions of the equivalent aperture behind the radome will fully comprehend the polarization distortion that the radome causes. By applying the two-dimensional Fourier transform to the co-polarized far-field response, the y-directed electric field distribution in the aperture plane is approximated as shown in Fig. 2 (c) and Fig. 2 (d). As stated previously, if the antenna under investigation had produced significant cross-polarized energy in the far-field, an additional transform would have been necessary to approximate the x-component of the electric fields in the aperture plane. The corresponding equivalent aperture magnetic fields are determined by applying the same relationship that exists between electric and magnetic fields under far-field conditions [22].

The implementation of (1)-(5) in conjunction with the extrapolation algorithm was successful in producing a 10 in diameter equivalent aperture surrounded by energy approximately -30 dB or lower from the peak aperture field value outside of the user-specified diameter. These fields outside the 10 in diameter aperture are removed prior to performing analysis with the radome. Containing the aperture energy into a diameter no greater than the original antenna is desirable for its use in applications where the radome is in close proximity to the employed antenna.

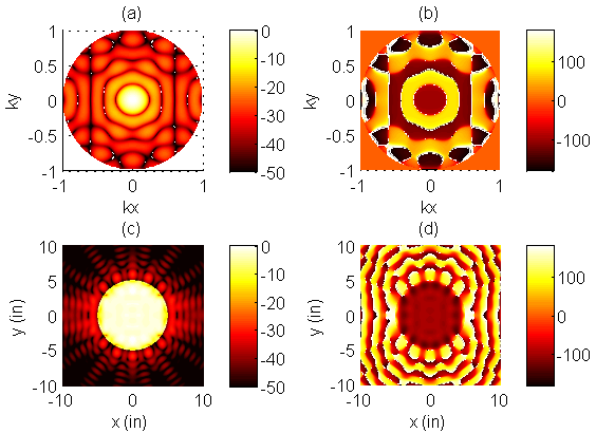

Fig. 2. Transformation of antenna far-field patterns to an equivalent aperture. (a) Normalized magnitude (dB) of antenna far-field in k-space. (b) Phase (deg) of antenna far-field in k-space. (c) Normalized magnitude (dB) of equivalent aperture. (d) Phase (deg) of equivalent aperture.

The resulting aperture field distribution can be utilized in two ways. Firstly, as a source to the radome problem where the radome scatters electromagnetic energy propagating from the aperture plane to the far-field, herein referred to as "transmit-mode." Alternatively, the fields can be utilized to receive energy from a plane wave passing through the radome by exploiting the Lorentz reciprocity integral provided in (6) [22] herein referred to as "receive-mode." $\mathbf{E_R}$ and $\mathbf{H_R}$ are the fields in the aperture plane due to the incident plane wave passing through the radome, while $\mathbf{E_T}$ and $\mathbf{H_T}$ are the equivalent aperture source fields. Because mutual coupling to the radome is neglected, these transmit and receive fields in the Lorentz reaction integral are approximate;

$$VR_{APER} = C\iint_{yx} (\mathbf{E_T} \times \mathbf{H_R} - \mathbf{E_R} \times \mathbf{H_T}) \cdot \hat{\mathbf{n}}\, dxdy. \quad (6)$$

The complex scale factor C in (6), is required for determining an absolute received voltage; however, this term is not necessary when only a relative or normalized voltage is needed, as is the case when determining radome boresight errors or relative transmission losses.

The antenna and associated equivalent aperture are divided into four equal quadrants as is done in a conventional monopulse tracking system. Sum and difference channels are formed by adding or subtracting the received or transmitted voltages for each of these quadrants from one another, as is provided in (7)-(9) where VR_{SUM}, $VR_{\Delta EL}$, and $VR_{\Delta AZ}$ are the received voltages for the formed sum, delta elevation, and delta azimuth channels, respectively;

$$VR_{SUM} = VR_{Q1} + VR_{Q2} + VR_{Q3} + VR_{Q4}\,, \quad (7)$$

$$VR_{\Delta EL} = VR_{Q1} + VR_{Q2} - VR_{Q3} - VR_{Q4}\,, \tag{8}$$

$$VR_{\Delta AZ} = VR_{Q1} - VR_{Q2} - VR_{Q3} + VR_{Q4}\,. \tag{9}$$

The loss due to the radome is calculated in (10) by comparing the formed sum channel transmission through the radome (7) to the case when the radome is not present, referred to as "Air Radome". Additionally, the elevation boresight error and azimuth boresight error are calculated in (11), (12), where S_{EL} and S_{AZ} are the monopulse slopes for the formed delta elevation and formed delta azimuth channels, respectively [23];

$$\text{RadomeLoss}_{dB} = 20\log_{10}\left(\frac{VR_{SUM}(\text{Radome})}{VR_{SUM}(\text{Air Radome})}\right), \tag{10}$$

$$BSE_{EL} = \frac{1}{S_{EL}}\,imag\left(\frac{VR_{\Delta EL}}{VR_{SUM}}\right), \tag{11}$$

$$BSE_{AZ} = \frac{1}{S_{AZ}}\,imag\left(\frac{VR_{\Delta AZ}}{VR_{SUM}}\right). \tag{12}$$

In the section to follow, far-field radiation pattern results make use of the transmit-mode application of the aperture fields, while boresight radome loss and boresight error calculations utilize the receive-mode application of the aperture fields. Boresight radome loss and boresight error can also be calculated via transmit mode, but this requires the individual simulation of each of the aperture channels within the radome. By calculating these results using a receive-mode formulation, the radome simulation only needs to be run once per look direction with an incident plane wave source, and the Lorentz reaction integral can be utilized in post-processing to calculate the different aperture received voltages. It is important to note that in this method a full Lorentz reciprocity is not achieved as scattered fields from the radome back into the aperture plane are ignored. A transmit-mode simulation would be required to acquire such information. Furthermore, since the radome problem is only run once for each gimbal direction, numerous apertures can be analyzed independently and seamlessly integrated with the radome simulation results to quantify boresight radome loss and boresight error for various antennas.

III. RADOME MODELING RESULTS AND DISCUSSION

The equivalent aperture method is demonstrated by comparing far-field radiation pattern cuts along the elevation and azimuth planes at three radome gimbal directions of interest, using either the full antenna or the equivalent aperture as the radiation source within the radome under investigation. Each of the four curves within each far-field pattern figure are created by one of the four radiation scenarios: the full slot antenna by itself, the equivalent aperture by itself, the full slot antenna enclosed by the radome, and the equivalent aperture enclosed by the radome. As stated previously simulation results including the full antenna (designated by solid lines) are considered to be "truth" and serve as the baseline to quantify the accuracy of the equivalent aperture method simulation results (designated by dashed lines).

Radiation patterns with the antenna looking out the radome nose are of particular interest since the tip is directly illuminated by the main beam of the antenna/aperture and diffractive effects are significant. The pattern comparisons along the elevation and azimuth planes are presented in Figs. 3 (a) and (b), respectively. One feature of primary significance is how much the detuned radome influences the main beam of the antenna. In this case study, there is approximately 2 dB of attenuation due to the radome; meaning almost forty percent of the original energy transmitted towards antenna/aperture boresight is now scattered in different directions. The energy lost from the main beam results in an overall increase in sidelobe levels.

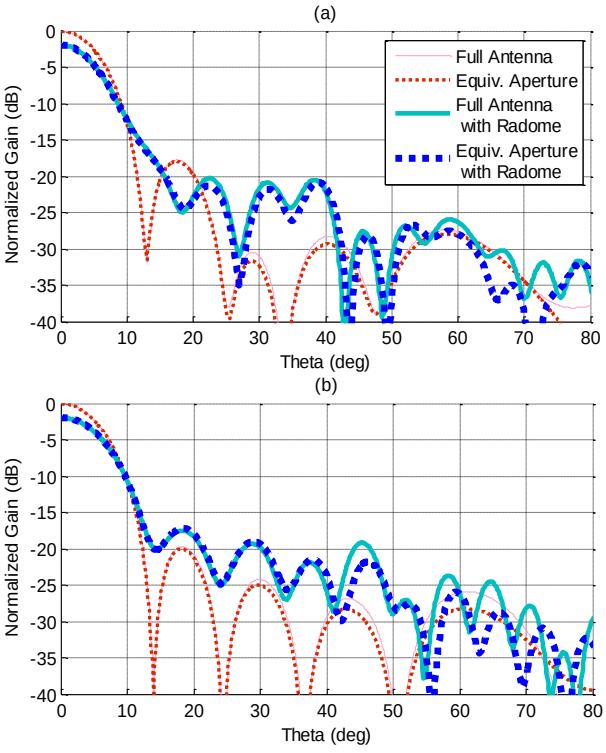

Fig. 3. Effect of radome on antenna/aperture far-field patterns where the radome is gimbaled 0 degrees in Azimuth and 0 degrees in elevation. (a) Far-field patterns in EL-plane. (b) Far-field patterns in AZ-plane. Patterns are normalized to peak antenna/aperture far-field value.

Even though the radome has such a dramatic effect on the radiation pattern of the antenna, it is clearly

shown that the equivalent aperture method is indeed applicable in predicting these RF radiation pattern perturbations. Peak gain is predicted to within small fractions of a dB for the main beam and first three sidelobes, and to within a few dB for a majority of the remaining low-energy sidelobes. This agreement is an indication that the coupling of energy back into the antenna is likely low for this radome shape, for this look-direction, even with its detuned thickness. Similar agreement between the two methods is witnessed in the azimuth plane.

Another radome gimbal angle of interest is 0 deg in azimuth and 20 deg in elevation. Excellent agreement between far-field patterns in the elevation plane can be seen in Fig. 4. The sidelobes are relatively unaffected by the presence of the radome at this gimbal angle, but significant deflection of the main beam is present, which is successfully predicted by the equivalent aperture simulations.

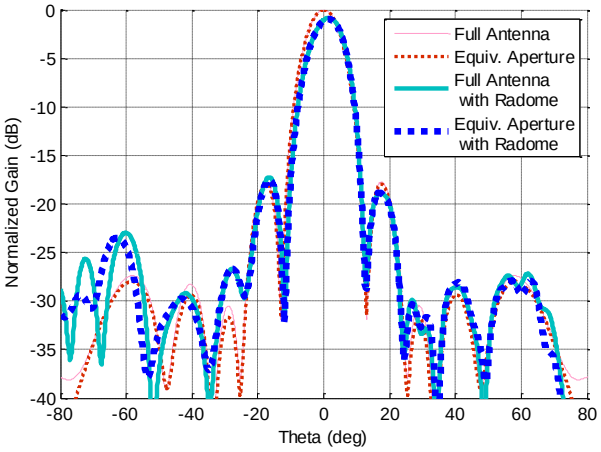

Fig. 4. Effect of radome on antenna/aperture EL-plane far-field patterns where the radome is gimbaled 0 degrees in Azimuth and 20 degrees in Elevation. Patterns are normalized to peak antenna/aperture far-field value.

The remaining radome gimbal angle of interest is 14 deg in azimuth and 0 deg in elevation. Here, a noteworthy phenomenon is successfully predicted and can be seen in Fig. 5. A bounce lobe—sometimes referred to as a flash lobe—has formed in the azimuth plane far-field pattern cut and is centered about 60 deg theta. Bounce lobes are a result of strong main beam reflections off the radome wall which coherently add to form a sidelobe of significant amplitude. This is a common occurrence for poorly tuned radomes which possess high fineness ratios.

Loss at antenna boresight is an important radome performance parameter and is difficult to appreciate in Figs. 3 – Fig. 5 due to their large vertical scale ranges. With such a large scale it is very difficult to quantify how well the radome-induced loss is being predicted. That being the case, the radome loss at boresight for both the elevation and azimuth planes is presented in Fig. 6, where zero to half-power transmission is used as the plot's y-axis. It can be seen that using the aperture fields in receive mode, the deviation from our "truth" baseline is at most 0.2–0.3 dB which is approximately 2–4 % error in the far-field intensity prediction.

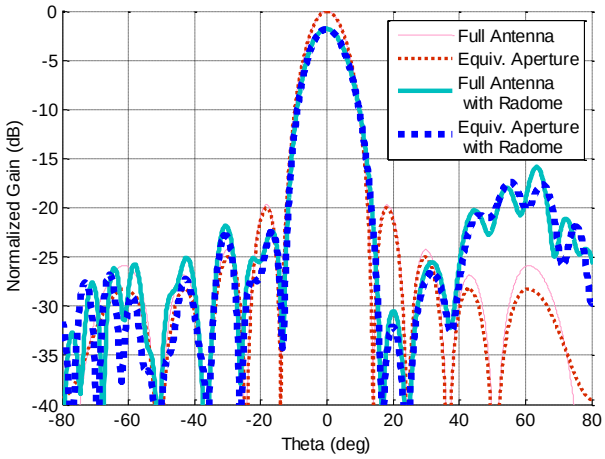

Fig. 5. Effect of radome on antenna/aperture AZ-plane far-field patterns where the radome is gimbaled 14 degrees in azimuth and 0 degrees in elevation. Patterns are normalized to peak antenna/aperture far-field value.

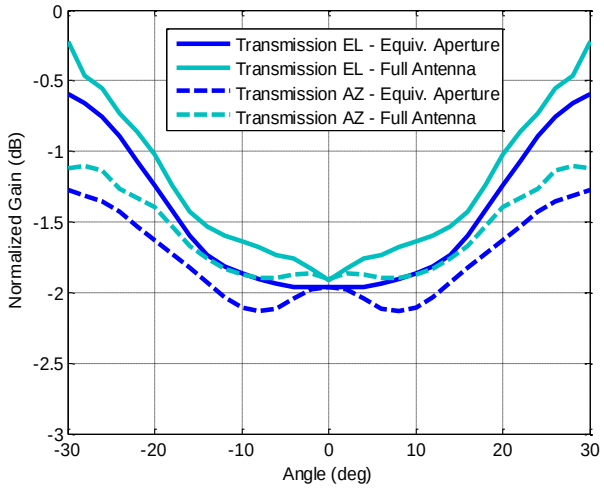

Fig. 6. Effect of radome on antenna/aperture bore-sight transmission as radome is gimbaled in the elevation/ azimuth plane. Transmission values are normalized to antenna/aperture bore-sight transmission.

Another radome performance characteristic often considered is the induced boresight error as a result of

the radome perturbing the magnitude and phase of energy as it propagates through the radome at varying incident angles and thicknesses. The results for both the elevation and azimuth plane boresight error can be found in Fig. 7. Excellent agreement is achieved between the two methods for both BSE AZ and BSE EL, indicating that the equivalent aperture has sufficiently represented the full seeker antenna in the radome simulation without including higher order effects that may exist due to mutual antenna and radome interactions.

With the presented modeling approach, an antenna/radome engineer can utilize the receive mode formulation to quickly compare several different antennas under the same radome. First, several different antennas can be simulated independently. Next, the effects of the radome on each different antenna's transmission and induced angle errors can be quickly quantified by performing an approximate Lorentz reaction integral. Conversely, if the radome engineer has the time and computation resources and requires more accurate results, radome loss and boresight error can be calculated in transmit mode; however, this will require up to N (i.e., number of aperture channels) simulations per antenna per radome gimbal direction and is no longer independent of the antenna(s) under consideration.

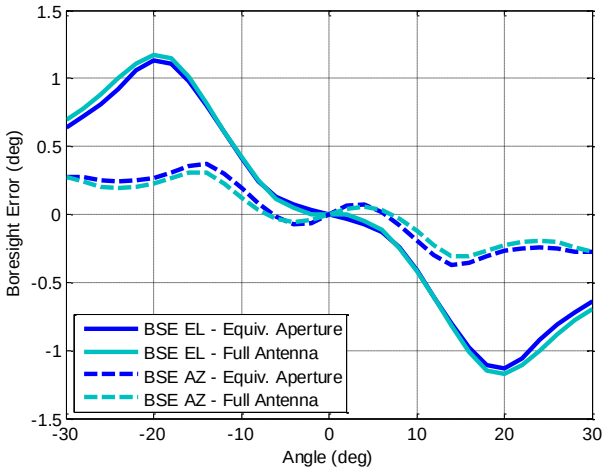

Fig. 7. Antenna/aperture bore-sight error as radome is gimbaled in the elevation/azimuth plane.

IV. CONCLUSIONS

There is a growing demand for accurate, full-wave modeling of radome induced angle errors, insertion loss, and effects on antenna patterns, while being mindful of computational resources and run time. The presented equivalent aperture method helps to bridge the gap between the speed of high frequency approximation solvers and the accuracy of full-wave modeling.

It is important to re-iterate that the equivalent aperture that is formed via the presented transformation/ extrapolation method is in no way specific to the radome. The aperture is formed from *antenna-only* radiation patterns and does not depend on the radome or its properties. As a result, the antenna and radome problems can be decoupled, simulated separately and combined seamlessly using the equivalent aperture receive mode to obtain accurate and efficient predictions of radome loss and boresight error. Furthermore, radiation pattern predictions using the equivalent aperture transmit mode are obtained without the additional cost of meshing the complex antenna structure behind the antenna, which results in significant cost savings in computer memory and runtime. This approach is valid for the sharp-nosed airborne geometry that was presented because little energy that scatters off the radome reflects back into the aperture plane.

REFERENCES

[1] G. K. Huddleston, H. L. Bassett, and J. M. Newton, "Parametric Investigation of Radome Analysis Methods," *Georgia Institute of Technology, School of Electrical Engineering*, 1980.

[2] G. Tricoles, "Application of ray tracing to predicting the properties of a small, axially symmetric, missile radome," *Antennas and Propagation, IEEE Transactions on*, vol. 14, no. 2, pp. 244-246, 1966.

[3] K. Siwiak, T. B. Dowling, and L. Lewis, "Boresight errors induced by missile radomes," *Antennas and Propagation, IEEE Transactions on*, vol. 27, no. 6, pp. 832-841, 1977.

[4] D. Burks, E. Graf, and M. Fahey, "A high-frequency analysis of radome-induced radar pointing error," *Antennas and Propagation, IEEE Transactions on*, vol. 30, no. 5, pp. 947-955, 1982.

[5] C. A. Balanis, *Advanced Engineering Electromagnetics*. New York, NY: John Wiley & Sons, 1989.

[6] D. M. Pozar, *Microwave Engineering*. John Wiley & Sons, 2009.

[7] C. D. Finlay, S. Gregson, R. W. Lyon, and J. McCormick, "SPIKE a physical optics based code for the analysis of antenna radome interactions," *In Radar Systems, 2007 IET International Conference on*, IET, pp. 1-5, 2007.

[8] H. F. Meng, W. Dou, and K. Yin, "Analysis of antenna-radome system at millimeter wave band," *In Millimeter Waves, 2008, GSMM 2008, Global Symposium on, IEEE*, pp. 380-383, 2008.

[9] T. Schuster and M. Sabielny, "REACH/ PREACH—A physical optics based tool for simulation of radome effects on antenna patterns," *In Antennas and Propagation (EUCAP), 2012 6th European Conference on, IEEE*, pp. 3225-3229,

2012.
[10] D. Paris, "Computer-aided radome analysis," *Antennas and Propagation, IEEE Transactions on*, vol. 18, no. 1, pp. 7-15, 1970.
[11] D. C. Wu and R. Rudduck, "Plane wave spectrum-surface integration technique for radome analysis," *Antennas and Propagation, IEEE Transactions on*, vol. 22, no. 3, pp. 497-500, 1974.
[12] J. A. Shifflett, "CADDRAD: A physical optics radar/radome analysis code for arbitrary 3D geometries," *Antennas and Propagation Magazine, IEEE*, vol. 39, no. 6, pp. 73-79, 1997.
[13] M. A. Abdel Moneum, Z. Shen, J. L. Volakis, and O. Graham, "Hybrid PO-MoM analysis of large axi-symmetric radomes," *Antennas and Propagation, IEEE Transactions on*, vol. 49, no. 12, pp. 1657-1666, 2001.
[14] H. Meng and W. Dou, *Analysis and Design of Radome in Millimeter Wave Band*, Microwave and Millimeter Wave Technologies from Photonic Bandgap Devices to Antenna and Applications, Igor Minin (Ed.), ISBN: 978-953-7619-66-4, InTech, DOI: 10.5772/9054, 2010.
[15] CST Microwave Studio, Computer Simulation Technology, Darmstadt, Germany, www.cst.com
[16] HFSS ANSYS, High Frequency Structural Simulator, www.ansys.com
[17] Comsol Multiphysics, Comsol, Inc., Burlington, MA, www.comsol.com
[18] R. S. Elliott, *Antenna Theory and Design*. John Wiley & Sons, 2003.
[19] G. K. Huddleston, "Aperture synthesis of monopulse antenna for radome analysis using limited measured pattern data," *In SOUTHEASTCON'81; Proceedings of the Region 3 Conference and Exhibit*, vol. 1, pp. 350-354, 1981.
[20] S. Silver, *Microwave Antenna Theory and Design*. vol. 19, Iet, 1949.
[21] A. Ludwig, "The definition of cross polarization," *Antennas and Propagation, IEEE Transactions on*, vol. 21, no. 1, pp. 116-119, 1973.
[22] R. F. Harrington, *Time Harmonic Electromagnetic Fields*. McGraw-Hill Book Co., New York, 1961.
[23] D. J. Kozakoff, *Analysis of Radome-Enclosed Antennas*. Artech House Publishers, 2009.

Benjamin L. Cannon was born in McKeesport, PA in 1986. He received the B.S. degree in Electrical and Computer Engineering from Carnegie Mellon University, Pittsburgh, PA, in 2008 and the S.M. degree in Electrical Engineering from the Massachusetts Institute of Technology, Cambridge, MA in 2010. He worked as a Senior Electrical Engineer at Raytheon Missile Systems, Tucson, AZ (2010-2013), and is currently a Member of the Technical Staff at Nuvotronics, Inc., Durham, NC. He is interested in electromagnetic field and wave interactions with materials.

Jared Williams Jordan was born in Farmington, Maine on February 6, 1983. He received the B.S. degree in Electrical and Computer Engineering from University of Maine, Orono, ME, in 2005 and the M.S. degree in Electrical and Computer Engineering from University of Arizona, Tucson, AZ, in 2008. He has worked at Newpage Corporation as a Reliability Engineer (2005–2006) and at the University of Arizona as a Senior Research Engineer (2008–2010). He previously worked as a Senior Electrical Engineer at Raytheon Missile Systems, Tucson, AZ (2010-2014), and is currently an Associate Technical Staff at MIT Lincoln Laboratory, Lexington, MA in the Advanced Technology Division: RF Technology (group 86). is current research interests include antenna and radome analysis and design, computational electromagnetics and material characterization.

Calculating Radiation from Arbitrarily Shaped Aperture Antennas Using the Free Space Radiation Integrals

Adriaan J. Booysen

Antenna Systems Group
Saab Grintek Defence (Pty) Ltd.
Pretoria, South Africa
riaan.booysen@za.saabgroup.com

Abstract ─ A technique is derived by means of which the calculation of radiation from arbitrarily shaped aperture antennas can be greatly simplified compared to the conventional approach. In the conventional approach the null field region of an equivalence problem is typically filled with a conductor, effectively short-circuiting the aperture and the electric surface current density everywhere. The remaining aperture magnetic surface current density, which is known, then radiates in the presence of the conductor and the Green's function associated with each particular antenna configuration has to be derived, usually a very cumbersome process. In the proposed technique a conductor is again placed within *S*, but with an infinitesimal small distance between the conductor and *S*. The image of the electric current density on *S* is shown to be induced on the conductor and the free space radiation integrals can now be used to solve the radiation problem. Examples are presented to prove the new technique and to demonstrate the mechanics of the equivalence principle when applied to aperture antenna problems.

Index Terms ─ Aperture antennas, aperture theory, equivalence principle, horn antennas, image theory, reflector antennas, slot antennas.

I. INTRODUCTION

This paper is intended to augment a technique published by the author in 2003 [1] through which radiation from arbitrarily shaped aperture antennas can be calculated by means of the free space radiation integrals, circumventing the need to derive problem-specific Green's functions as stated in most textbooks on the topic. The technique is based on the placement of a conductor in the null field region of a surface equivalence problem to "short-circuit" the aperture, and in [1] the author merely conjectured how the process should be interpreted from a mathematical point of view. In this paper it is demonstrated through an example that the author's initial assumptions were valid, and the implementation and limitations of the technique are discussed through additional examples. Whereas only radiated fields were presented for the examples discussed in [1], this paper focusses specifically on the induced current densities in the aperture region of the free space equivalence problem. Through the examples it is shown that the short-circuited aperture indeed reproduces the original aperture fields as would be required.

Figure 1 (a) depicts a physical aperture antenna radiating in free space (two-dimensional, for the sake of simplicity). The surface equivalence principle [2,3] can be applied to replace the physical antenna with equivalent electric and magnetic surface current densities radiating in free space, as shown in Fig. 1 (b). The equivalent electric and magnetic surface current densities are defined by (1) and (2), respectively, with $\hat{\mathbf{n}}$ a unit vector normal to *S*, pointing towards Region 1. The magnetic current density is zero everywhere except in the aperture region.

The electromagnetic fields external to *S* are equal to the electromagnetic fields in the original problem, but the fields internal to *S* are selected to be zero (Love's equivalence [4]). The sources $\mathbf{J_s}$ and $\mathbf{M_s}$ in Fig. 1 (b) radiate in an unbounded medium (same μ,ε everywhere) and can be used in conjunction with the free space radiation integrals (two-dimensional) in (3) and (4) to calculate the fields both regions of Fig. 1 (b). In Equations (3) and (4) f is the frequency, λ the wavelength, $\omega=2\pi f$ the angular frequency, $k=2\pi/\lambda$ the wavenumber, μ and ε the constituent parameters for the medium of propagation and r the distance from the integration point to the field evaluation point.

For many aperture antenna problems the distribution of the electric field in the aperture is known to good approximation, but not necessarily so the distribution and relative magnitude and phase of the magnetic field in the aperture, with slot antennas being a good example. *One would, therefore, try to redefine the problem such that only the magnetic current density needs to be taken into account as a source*;

$$\mathbf{J_s} = \hat{\mathbf{n}} \times \mathbf{H}_1, \tag{1}$$

Submitted On: February 14, 2016
Accepted On: March 27, 2016

$$\mathbf{M_s} = -\,\hat{\mathbf{n}} \times \mathbf{E}_1, \tag{2}$$

$$\mathbf{E}(\mathbf{J_s}, \mathbf{M_s}) = -\frac{\omega\mu}{4}\int_S \mathbf{J_s}\, H_0^{(2)}(kr)\,dS + \frac{k}{4\omega\varepsilon}\int_S (\nabla_S \bullet \mathbf{J_s})\,\hat{\mathbf{r}}\, H_1^{(2)}(kr)\,dS + \frac{jk}{4}\int_S \mathbf{M_s}\times\hat{\mathbf{r}}\, H_1^{(2)}(kr)\,dS, \tag{3}$$

$$\mathbf{H}(\mathbf{J_s}, \mathbf{M_s}) = -\frac{\omega\varepsilon}{4}\int_S \mathbf{M_s}\, H_0^{(2)}(kr)\,dS + \frac{k}{4\omega\mu}\int_S (\nabla_S \bullet \mathbf{M_s})\,\hat{\mathbf{r}}\, H_1^{(2)}(kr)\,dS - \frac{jk}{4}\int_S \mathbf{J_s}\times\hat{\mathbf{r}}\, H_1^{(2)}(kr)\,dS. \tag{4}$$

Since the electromagnetic fields inside *S* are zero, the medium inside *S* can be replaced by a different medium without affecting the fields external to *S* [5]. If we fill the area inside *S* with an electric conductor as shown in Fig. 1 (c), the reciprocity theorem can be invoked to show that the electric current density $\mathbf{J_s}$ (including $\mathbf{J_s}$=$\mathbf{J_{ap}}$) will no longer produce any fields ("We can think of the conductor as shorting out the current" [6]), and we are left with a magnetic current density $\mathbf{M_s}$=$\mathbf{M_{ap}}$ impressed upon an electric conductor. However, since $\mathbf{M_s}$ no longer radiates in an unbounded medium, the free space radiation integrals of (3) and (4) can no longer be used to calculate the fields external to *S*. Consequently, as stated in two prominent antenna theory textbooks:

> "The introduction of the perfect conductor will have an effect on the equivalent source $\mathbf{J_s}$, and it will prohibit the use of [the free space radiation integrals] because the current densities no longer radiate into an unbounded medium. … *The problem of a magnetic current density radiating in the presence of an electric conducting surface must be solved. So it seems that the equivalent problem is just as difficult as the original problem itself*." [7],

and

> "If a perfect conductor is placed along S, Js will vanish. The explanation is often given the electric current is 'shorted out' by the conductor. This leaves a magnetic current density Ms radiating in the presence of the electric conductor … these problems are difficult to solve as long as S is a general surface." [8].

What this implies is that the Green's function associated with the specific radiating geometry needs to be derived, typically a very cumbersome process that is limited to elementary geometries (see for example [9,10]). Furthermore, it is clear that some uncertainty exists about just how the conductor "shorts out" the electric current density.

We will next endeavour to show that it is possible to derive a new technique for solving the above problem which "shorts out" $\mathbf{J_s}$, while still allowing the free space radiation integrals to be used (see also [1, Section 2]).

II. DERIVATION OF THE NEW TECHNIQUE

Since the electromagnetic fields within *S* (Region II) are zero, we can as before place an electric conductor within *S*, with the difference that the conductor does not fill Region II completely as shown in Fig. 1 (d). We can treat this as simply another equivalence problem in which the physical conductor, which is illuminated by external sources $\mathbf{J_s}$, $\mathbf{J_{ap}}$ and $\mathbf{M_{ap}}$, is replaced by an equivalent electrical surface current density $\mathbf{J_c}$ on *C*, with all current densities now radiating in free space. The induced electrical surface current density $\mathbf{J_c}$ in Fig. 1 (d) is equal to zero as all the electromagnetic fields within *S* are zero, but can still be expressed as:

$$\mathbf{J_c} = \mathbf{J_c}(\mathbf{J_s}) + \mathbf{J_c}(\mathbf{J_{ap}}) + \mathbf{J_c}(\mathbf{M_{ap}}) \equiv 0. \tag{5}$$

We next bring *C* infinitely close to *S* ($C=S^-$), with *d* small but not zero (i.e., $d \ll \lambda$). As proven by the reciprocity theorem, an electric current density radiating in the immediate presence of an electric conductor will produce no field. In terms of the configuration shown in Fig. 1 (d), and keeping in mind that all the current densities radiate in free space, this is mathematically speaking only possible if $\mathbf{J_c}(\mathbf{J_s}) \approx -\mathbf{J_s}$ at any point on the conducting part of *S* and likewise $\mathbf{J_c}(\mathbf{J_{ap}}) \approx -\mathbf{J_{ap}}$ in the aperture region. The fields radiated by $\mathbf{J_s} + \mathbf{J_c}$, external to *S* are calculated from (3) and (4) and can only be zero if $\mathbf{J_c} = -\mathbf{J_s}$. The "image" of $\mathbf{J_s}$ is therefore induced on the conductor that backs $\mathbf{J_s}$, irrespective of the shape of *S*.

With the electric source current densities having accordingly been cancelled everywhere on *S*, the problem in Fig. 1 (d) is reduced to the one shown in Fig. 1 (e), where $\mathbf{M_{ap}}$ induces $\mathbf{J_c}(\mathbf{M_{ap}})$ on S^-, which now is a closed electrical conductor. In other words, the aperture has been short-circuited with $\mathbf{M_{ap}}$ placed infinitely close to it in the aperture region as shown in Fig. 1 (e), and $\mathbf{J_c}(\mathbf{M_{ap}})$ is merely the electric current density it induces on *C*.

The magnetic surface current density $\mathbf{M_{ap}}$ is usually known for many aperture antennas and $\mathbf{J_c}$ can then be solved for by techniques such as the Electric Field Integral Equations (EFIE) and the Method of Moments (MoM) [11]. *Significantly, it is no longer necessary to derive the Green's function of the specific radiating structure*. Note that it does not matter whether the conductor is placed inside *S* on S^-, or on *S* with $\mathbf{M_{ap}}$ moved an infinitesimal distance outside *S* to S^+. The latter approach is often easier to implement as the radiating structure may be quite complex while the aperture field distribution typically is simple by comparison (see the horn antenna examples at the end). *This forms the premise of the new technique.*

One may ask whether the new technique will reproduce the original surface current densities $\mathbf{J_s}$ and $\mathbf{J_{ap}}$ on S^- and this is indeed what we can expect. From (5) we have:

$$\mathbf{J_c}(\mathbf{M_{ap}}) = -\mathbf{J_c}(\mathbf{J_s}) - \mathbf{J_c}(\mathbf{J_{ap}}), \quad (6)$$

and as we have argued above, for d approximating zero, $\mathbf{J_c}(\mathbf{J_s}) = -\mathbf{J_s}$ and $\mathbf{J_c}(\mathbf{J_{ap}}) = -\mathbf{J_{ap}}$ on C, which yields:

$$\mathbf{J_c}(\mathbf{M_{ap}}) = \mathbf{J}_s + \mathbf{J_{ap}}, \quad (7)$$

or to be more precise, $\mathbf{J_c}(\mathbf{M_{ap}}) = \mathbf{J_{ap}}$ in the aperture region of S and zero elsewhere, and $\mathbf{J_c}(\mathbf{M_{ap}}) = \mathbf{J_s}$ in the conducting region of S and zero elsewhere.

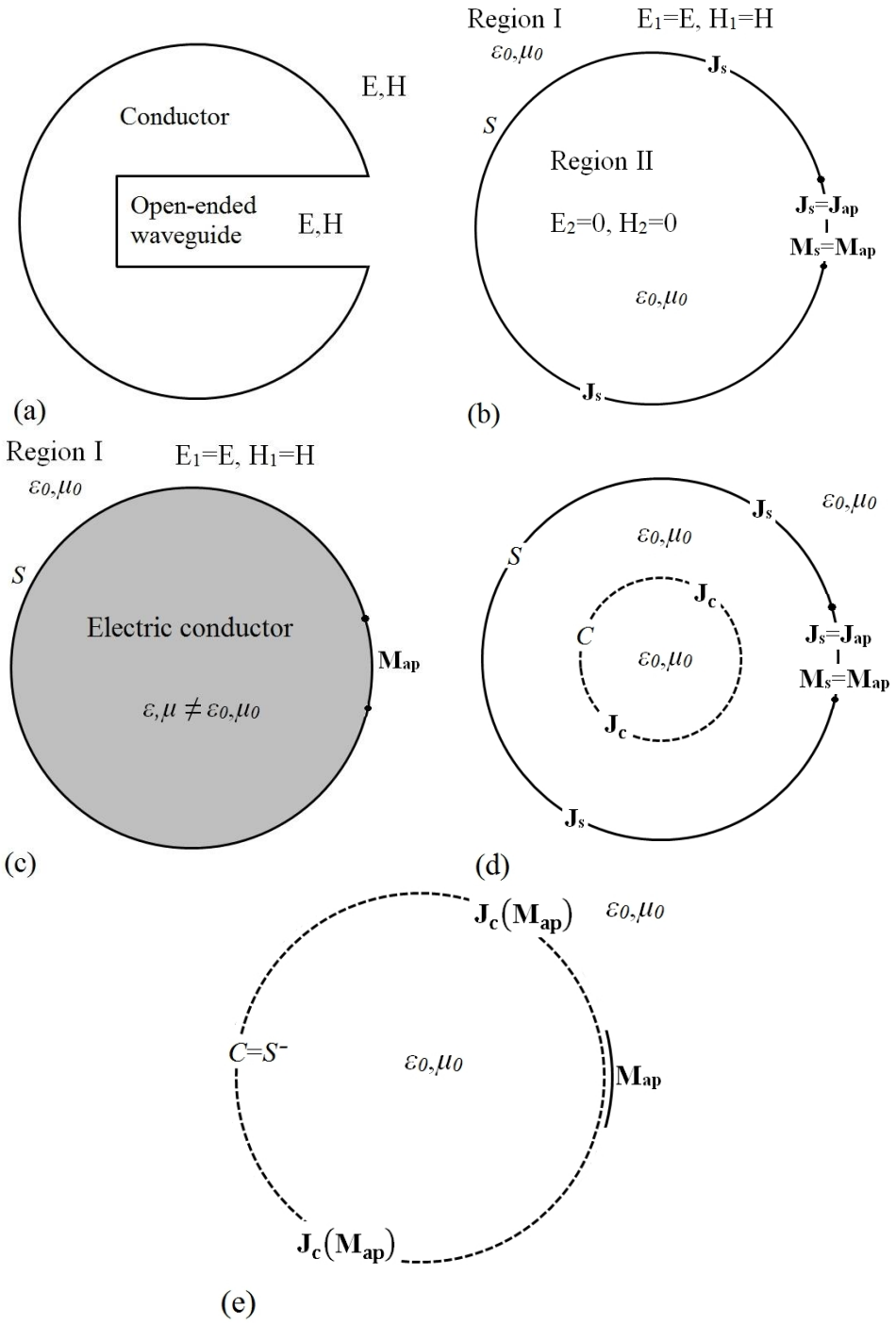

Fig. 1. Application of the equivalence principle to an aperture antenna problem.

III. SHORT-CIRCUITING AN ELECTRIC SURFACE CURRENT DENSITY RADIATING IN FREE SPACE

In order to prove the validity of the new technique, we will first demonstrate through an example that when an electrical conductor is brought infinitely close to an electric surface current density $\mathbf{J_s}$ defined on an arbitrarily shaped surface *S*, radiating in free space, the oppositely directed current density will be induced on the conductor ($\mathbf{J_c} = -\mathbf{J_s}$) and $\mathbf{J_s}$ will effectively be short-circuited. No electromagnetic fields will be radiated by the combination of $\mathbf{J_s}$ and the current density $\mathbf{J_c}$ on the conductor. Although this sounds logical, it is important to note that the conductor can be replaced by the negative image of $\mathbf{J_s}$ everywhere on *S*, although classical image theory [12] does not apply to the problem in any sense.

As an example, Fig. 2 depicts a surface current density $\mathbf{J_s}$ superimposed onto a circular surface *S* of radius R=λ, with an electrical conductor of radius *r* having been placed at the centre of *S*. The gap between *S* and the conductor is given by *d*=R-*r*. The surface current density $\mathbf{J_s}$ is defined by (8) to (10) and does *not* produce a zero field inside *S*. Note that the phase function α is calculated first for $0 \le \varphi \le \pi$, from which the magnitude function *J* is calculated over the same sector. As indicated by (10), the current in the sector $-\pi \le \varphi \le 0$ is numerically duplicated from the $0 \le \varphi \le \pi$ sector. Placing a conductor inside *S* will therefore affect the total radiated field.

The induced surface current density $\mathbf{J_c}$ and the total radiated field were calculated by means of the EFIE and MoM for *r*=0 (i.e., no reflector, denoted 'Source' in the plots), *r*=0.5λ, *r*=0.95λ and *r*=0.999λ, respectively. Figure 3 shows the magnitude and phase of the calculated electric current density $\mathbf{J_c}$ for the abovementioned reflector radii, and Fig. 4 the radiated far field (calculated at 100 m at *f*=2 GHz). It is clear that as $d \to 0$ (i.e., $r \to$ R), $\mathbf{J_c} \to -\mathbf{J_s}$ and the total radiated field given by $\mathbf{J_s} + \mathbf{J_c}$ tends to zero (already being 45 dB down from the case where *r*=0). In Fig. 3 (b) a value of +180° was added to the phase of $\mathbf{J_c}$ in order to facilitate a direct overlay of the curves.

$$\alpha(\varphi) = \varphi + \pi \cos 2\varphi, \quad 0 \le \varphi \le \pi, \tag{8}$$

$$J(\varphi) = \left|\cos\left(\frac{\alpha(\varphi)}{3}\right)\right|, \quad 0 \le \varphi \le \pi, \tag{9}$$

$$\mathbf{J_s}(\varphi) = J(\varphi)e^{j\alpha(\varphi)}, \quad \mathbf{J_s}(-\varphi) = \mathbf{J_s}(\varphi). \tag{10}$$

We will next discuss the application of the new technique through several examples.

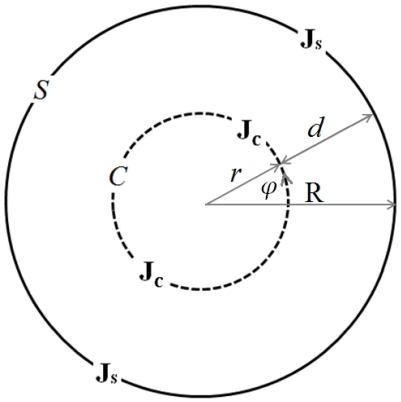

Fig. 2. $\mathbf{J_s}$ superimposed onto a circular surface *S* with conductor *C* placed inside *S*, $r \to$ R.

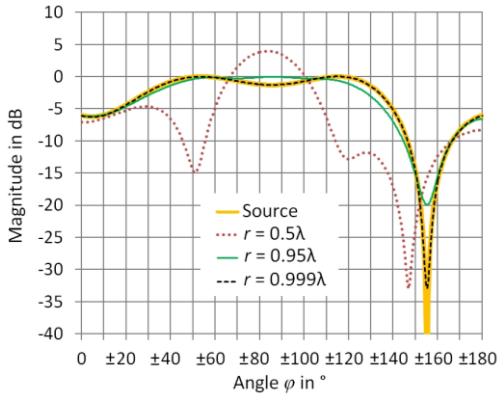

(a) Magnitude

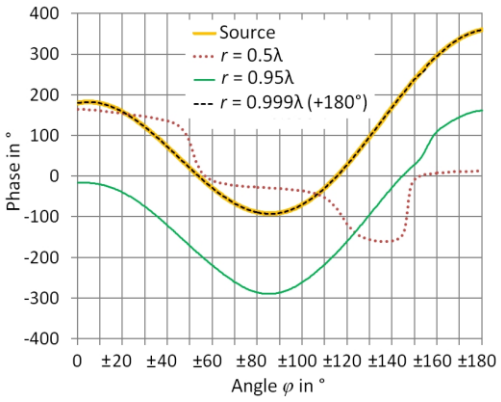

(b) Phase

Fig. 3. Magnitude and phase of $\mathbf{J_c}$ for *r*=0, *r*=0.5λ, *r*=0.95λ and *r*=0.999λ.

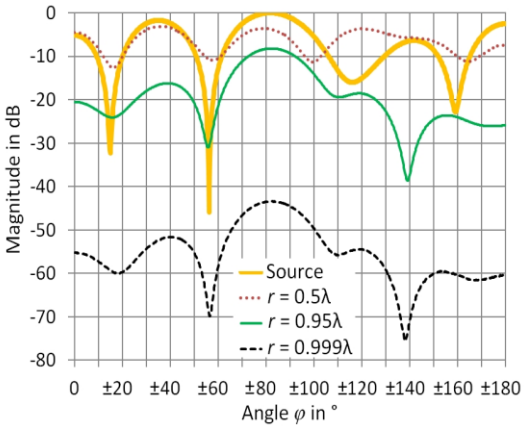

Fig. 4. Radiated patterns for r=0, r=0.5λ, r=0.95λ and r=0.999λ.

IV. EXAMPLE 1 – A LINE SOURCE RADIATING IN FREE SPACE

Perhaps the simplest example for demonstrating how the new technique can be used is the case of a line source radiating in two-dimensional free space, as shown in Fig. 5. The electric and magnetic source fields at distance r from the source are expressed by Equations (11) and (12), respectively:

$$\mathbf{E}_i(r) = \frac{1}{\sqrt{r}} e^{-jkr}\,\hat{\mathbf{z}} = E_i(r)\,\hat{\mathbf{z}}, \qquad (11)$$

$$\mathbf{H}_i(r) = -\frac{1}{\eta} E_i(r)\,\hat{\boldsymbol{\varphi}}. \qquad (12)$$

In (12) η represents the free space wave impedance.

An equivalent surface S can now be placed around the line source and together with the surface current densities $\mathbf{J}_{s1}$ and $\mathbf{M}_{s1}$, it will produce the true fields with S and a null field external to S. For external equivalence, the surface current densities $\mathbf{J}_{s2}=-\mathbf{J}_{s1}$ and $\mathbf{M}_{s2}=-\mathbf{M}_{s1}$ will produce null fields internal to S and the original (true) fields external to S. For the sake of simplicity, we define surface current densities $\mathbf{J}_1=-\mathbf{J}_{s1}$ and $\mathbf{M}_1=-\mathbf{M}_{s1}$ to produce the external fields (Region 1 as defined in Fig. 1). Two examples were considered, one in which S is a circle and the other in which S is a square with the line source at its centre. Note that since $\mathbf{J}_s$ is z-directed, the surface divergence term in (3) is zero. The surface divergence integral in (4) can also be neglected for slowly varying $\mathbf{M}_s$ as the coefficients of the two integrals involving $\mathbf{M}_s$ differ by a factor of $k=2\pi/\lambda$ and for evaluation points directly below $\mathbf{M}_s$, we have $\hat{\mathbf{n}}=-\hat{\mathbf{r}}$, so that from (1) and (4) the cross product will be zero. As before, an electric conductor C is next placed inside S and brought infinitely close to S.

The free-space fields can be viewed as aperture fields and, in accordance with the new technique, S can be viewed as a conductor ($\hat{\mathbf{n}} \times \mathbf{E} = \mathbf{0}$ on its surface) with $\mathbf{J}_c$ on S and $\mathbf{M}_{s2}$ having been placed an infinitesimally small distance outside S.

We first consider the case where S is circular, f = 3 GHz and $r = R_o = 3\lambda$. From Equations (1), (2), (11) and (12) we have:

$$\mathbf{J}_1 = -\frac{1}{\eta} E_i(R_o)\,\hat{\mathbf{z}} = -46.29\text{ dB} \angle 180°\,\hat{\mathbf{z}}, \qquad (13)$$

$$\mathbf{M}_1 = +E_i(R_o)\,\hat{\boldsymbol{\varphi}} = +5.23\text{ dB} \angle 0°\,\hat{\boldsymbol{\varphi}}, \qquad (14)$$

everywhere on S, due to the symmetry of the problem. With d=0.03 λ, the value for $\mathbf{J}_c$ calculated by means of the MoM (the author used a rather elementary pulse basis function with point matching scheme) was $\mathbf{J}_c$ = -46.19 dB ∠ 168° $\hat{\mathbf{z}}$. Note that since $\mathbf{M}_1$ was used as the source and it was placed a distance d away from the equivalent surface S (see Fig. 6), one should expect a phase difference between $\mathbf{J}_1$ and $\mathbf{J}_c$ of about $-kd$ = -10.8°, which is indeed the case (180°-10.8°=169.2°). Since the source surface current density $\mathbf{M}_s$ will typically be approximated by segments, a general rule of thumb for the ratio between d and $\Delta\mathbf{M}$, the length of the segments, is $\Delta\mathbf{M} \le d$. Conversely, the distance between integration or sampling points on $\mathbf{M}_s$ should be smaller than d.

We next consider the case where S takes the form of a square that replaces the circle with radius R_o, as shown in Fig. 6. In this case (13) and (14) still hold where $r = R_o$, but the equivalent surface current densities $\mathbf{J}_1$ and $\mathbf{M}_1$ are no longer uniform on S. With r(x,y) and $\hat{\boldsymbol{\varphi}}$ as defined in Fig. 5, we can derive the following equations for the right hand side of the square, and similar equations for the other three sides of the square:

$$r = r(x,y) = \sqrt{x^2+y^2}, \qquad (15)$$

$$\hat{\mathbf{n}} = \hat{\mathbf{x}}, \qquad (16)$$

$$\hat{\boldsymbol{\varphi}} = -\sin(\varphi)\,\hat{\mathbf{x}} + \cos(\varphi)\,\hat{\mathbf{y}}, \qquad (17)$$

$$\mathbf{J}_1 = \hat{\mathbf{n}} \times \mathbf{H}_i(r) = -\frac{1}{\eta} E_i(r)\cos(\varphi)\,\hat{\mathbf{z}}, \qquad (18)$$

$$\mathbf{M}_1 = -\hat{\mathbf{n}} \times \mathbf{E}_i(r) = E_i(r)\,\hat{\mathbf{y}}. \qquad (19)$$

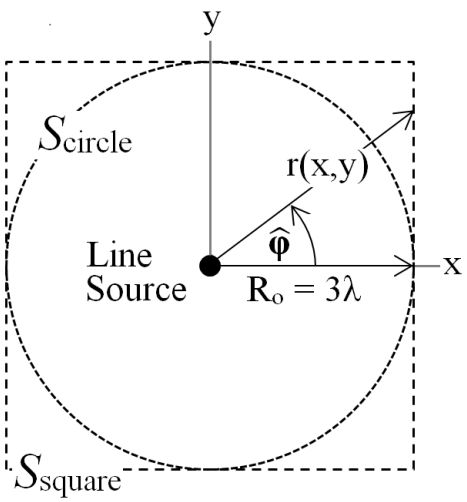

Fig. 5. Line source in two-dimensional space with S circular and square.

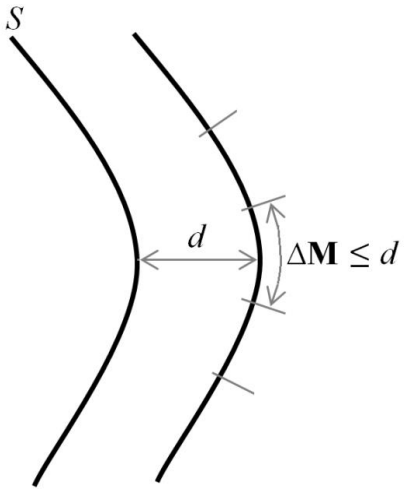

Fig. 6. Rule of thumb for ratio of d to $\Delta\mathbf{M}$.

Figure 7 shows the geometrical optics current density from (18) as well as the MoM current density calculated from $\mathbf{M_1}$ in (19) as backed by a conductor a distance d inside S. The erratic behaviour of the current density amplitude at the corners is most likely due to the field distribution at the 90° corners, which would generate a diffraction term for d not equal to zero. The phase difference of about 10° is like before due to the distance d between $\mathbf{M_1}$ and the conductor on which $\mathbf{J_1}$ is induced.

From these graphs it is clear that $\mathbf{M_1}$ backed by a perfect electrical conductor does indeed reproduce the original free space electrical surface current density $\mathbf{J_1}$ on S.

It is instructive look at the total fields radiated by $\mathbf{J_1}$ and $\mathbf{M_1}$ as well (integration is performed along the entire length of S). For this example a cross section of the equivalent surface was taken as shown in Fig. 8.

Inside S we expect the fields radiated by $\mathbf{J_1}$ and $\mathbf{M_1}$ to add up to zero, and to the true (geometrical optics) fields outside S. This is indeed the case, as shown in Figs. 9 (a) to 9 (c). In these figures 'Original' designates the electric field as calculated from (11), 'J&M' the results obtained from the geometrical optics expressions for $\mathbf{J_1}$ and $\mathbf{M_1}$, 'Circle + SC' the MoM $\mathbf{J_1}$ obtained by placing $\mathbf{M_1}$ on a concentric circle around the line source and backing (short-circuiting) it with a conductor, and 'Square + SC' the same for the square surface. As expected, the fields in the null region are not identically equal to zero, most likely due to the limitations of the pulse basis function with point matching scheme used by the author, and phase differences between $\mathbf{J_1}$ and $\mathbf{M_1}$.

Inside (left) of S, $\mathbf{J_1}$ and $\mathbf{M_1}$ will more or less add correctly in phase as $\mathbf{J_1}$ already lags $\mathbf{M_1}$ in phase by $-kd$, but when $\mathbf{M_1}$ radiates inward, it will also have undergone a phase change of $-kd$ (see Fig. 10). However, for external radiation $\mathbf{J_1}$, which already lags by $-kd$, will undergo another phase shift of $-kd$ before reaching $\mathbf{M_1}$. The new technique will, therefore, introduce a local phase difference of $-2kd$ between $\mathbf{J_1}$ and $\mathbf{M_1}$, which will have some effect on the total radiated fields. Nevertheless, the effect will still be almost negligible when the closed surface integration is performed as is evident from Fig. 9 (c), which shows the magnitude and phase differences between MoM calculated results and the original field calculated form (11).

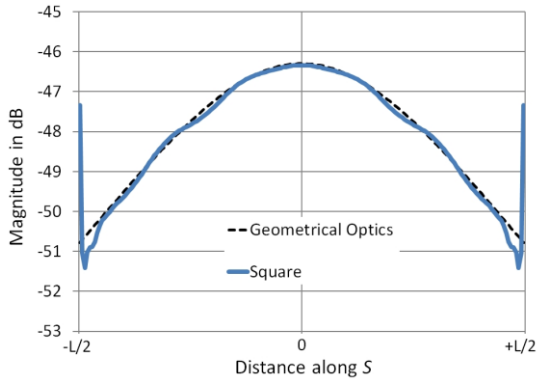

(a) Magnitude

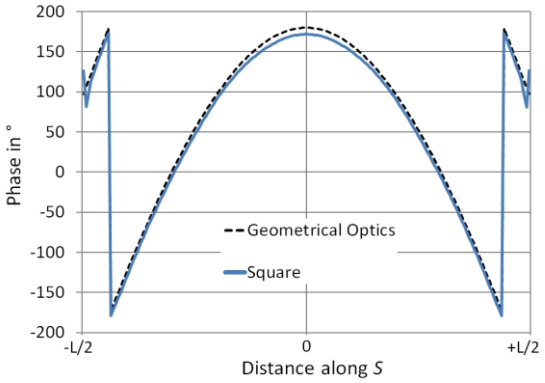

(b) Phase

Fig. 7. Magnitude and phase distribution of $\mathbf{J_1}$ along one side of the square.

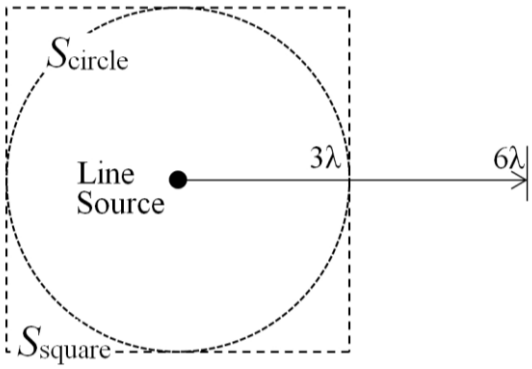

Fig. 8. Cross section through S for electric field strength calculation.

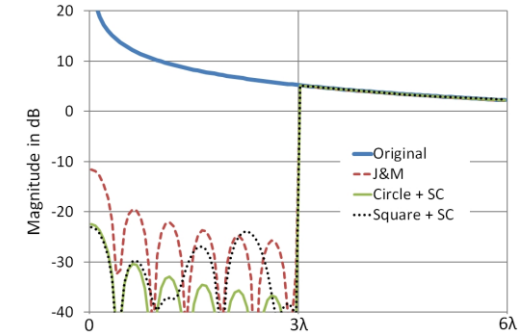

(a) Magnitude

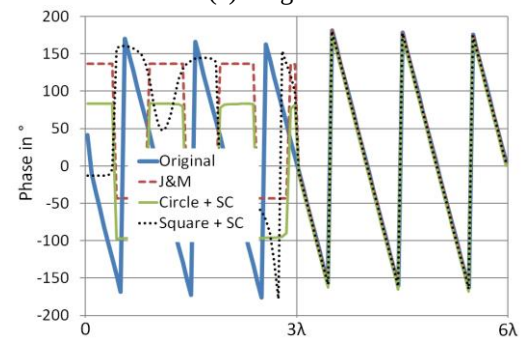

(b) Phase

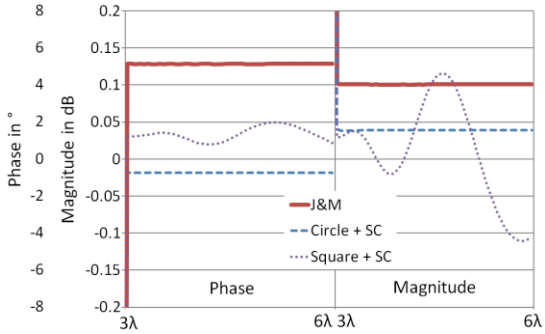

(c) Relative magnitude and phase errors

Fig. 9. Magnitude, phase and errors between GO field and MoM calculated electric field along cross section through *S*.

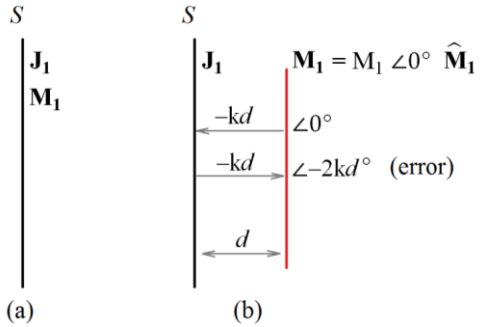

Original problem

M₁ moved a distance *d* to the right of *S*

Fig. 10. Phase error in field component radiated by **J₁** in new technique.

V. EXAMPLE 2 – REFLECTOR WITH LINE SOURCE FEED

The next example demonstrates how the new technique can be used with arbitrarily shaped aperture fields and radiating structures. The basic problem is depicted in Fig. 11 (a), where a line source illuminates a parabolic reflector with dimensions D=10λ, F=1λ, which is evaluated at *f*=10 GHz. The problem was initially solved by means of the MoM, following which an artificial circular equivalent surface *S* was introduced as shown in Fig. 11 (b), with r=3.02λ. The electric field along this surface was calculated by means of the MoM and was then converted to the magnetic source current density **M₁**. *S* was then "short-circuited" (i.e., treated as a continuation of the reflector surface), and **M₁** was moved a distance *d*=0.05λ away from *S*, in accordance with Fig. 1 (e), and the equivalent electric current density **J**$_c$ on *S* was calculated by means of the MoM.

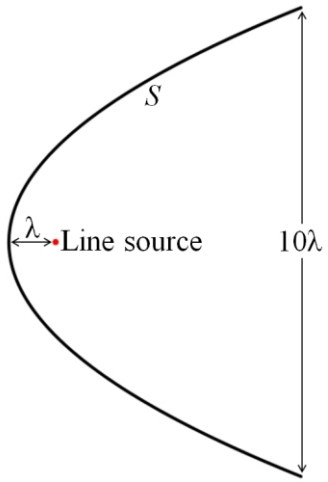

(a) Original problem

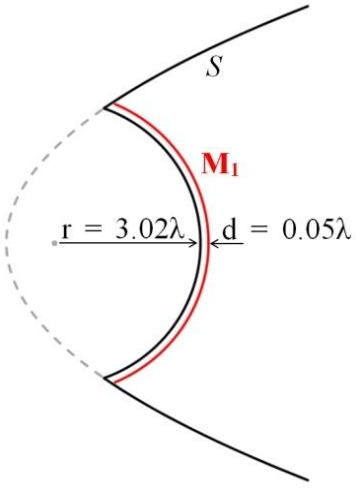

(b) With circular equivalent surface

Fig. 11. Parabolic reflector with artificial equivalent aperture surface.

It is relatively straightforward to calculate the geometrical optics reflected electric and magnetic fields on *S* as depicted in Fig. 12, from which the geometrical optics magnetic and electric equivalent current densities $\mathbf{M_{GO}}$ and $\mathbf{J_{GO}}$ at point (x,y) can be calculated as:

$$\mathbf{M_{GO}} = \left(\frac{e^{-jkl_a}}{\sqrt{l_a}} - \frac{e^{-jk(l_b+l_c)}}{\sqrt{l_b}} \right) \hat{\boldsymbol{\varphi}}, \tag{14}$$

and

$$\mathbf{J_{GO}} = \left(-\frac{e^{-jkl_a}}{\eta\sqrt{l_a}} + \frac{e^{-jk(l_b+l_c)}}{\eta\sqrt{l_b}} \cos\varphi \right) \hat{\mathbf{z}}. \tag{15}$$

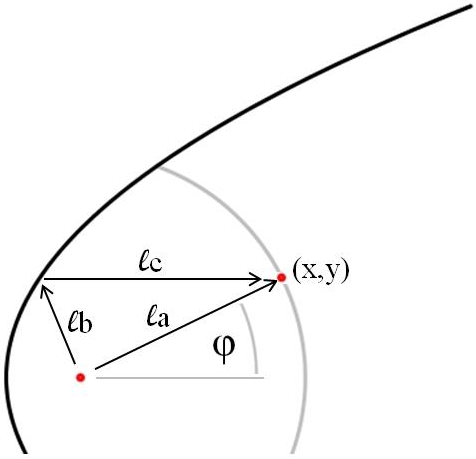

Fig. 12. Geometrical optics ray paths for direct and reflected fields.

Figures 13 and 14 show the magnitude and phase plots of the MoM calculated magnetic and electric current densities $\mathbf{M_1}$ and $\mathbf{J_c}$, respectively, compared to the geometrical optics calculated current densities $\mathbf{M_{GO}}$ and $\mathbf{J_{GO}}$. The difference between the MoM and GO current densities in the centre region can most likely be attributed to the fact that diffracted fields from the edges of the reflector had been ignored in the GO calculations (these would add in phase along the axis of the reflector). At the magnitude peaks in Fig. 14 (a) the difference between the MoM and GO results is, however, very small and the phase difference in Fig. 14 (b) at these points is about -18.6°, as can be expected for d=0.05λ (-k*d*=-18.0°). The abrupt discontinuity in the electric surface current density of (1) at the transition from the reflector to the circular region is due to the abrupt change in the direction of $\hat{\mathbf{n}}$ at this point. It will become less as the segmentation (the distance between sampling points) is made smaller.

Note that the x-axis in these graphs reflects only *the number of sampling points*, of which the density is greater in the centre of the parabola, and not the true distance along *S*. The Physical Optics current density [13] (PO), which is given by the approximation $\mathbf{J_{PO}}=2\,\hat{\mathbf{n}}\times\mathbf{H_i}$, is also shown in Fig. 14, overlaid with the MoM current density as calculated outside the aperture area. The magnitude difference between the PO and MoM results is typically less than 0.5 dB and in fact reduces even further as the electrical size of the parabola is increased.

It is of interest that the stationary phase solution of the radiation integrals associated with $\mathbf{J_{PO}}$ can be shown to yield the geometrical optics reflected fields [14] as used to derive (14) and (15).

This example again confirms that a short-circuited magnetic current density radiating in free space induces the corresponding free space electric current density on the conducting surface, which also radiates in free space. It would be near impossible to derive a Green's function for the geometry shown in Fig. 11 (b).

Figure 15 shows the far field radiation patterns for the original configuration of Fig. 11 (a) and the configuration with the circular equivalent surface shown in Fig. 11 (b), respectively. Despite the two approaches being fundamentally different, the agreement is excellent.

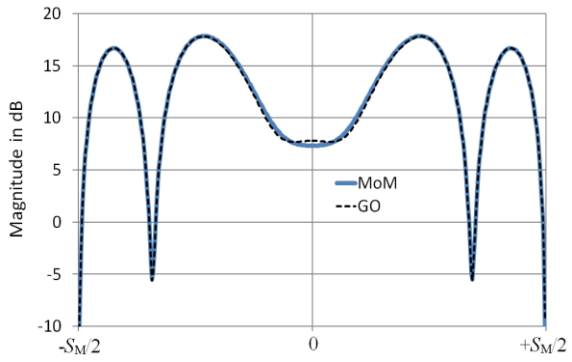

(a) Magnitude

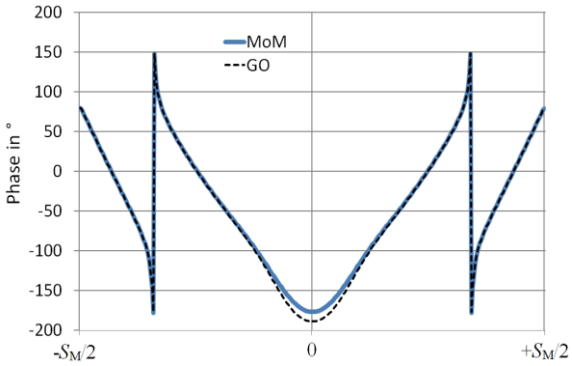

(b) Phase

Fig. 13. Magnitude and phase of calculated $\mathbf{M_1}$ in circular aperture region.

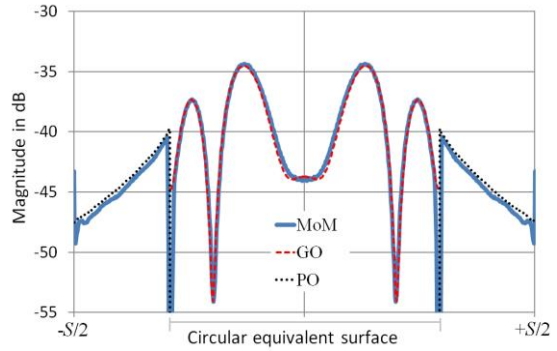

(a) Magnitude

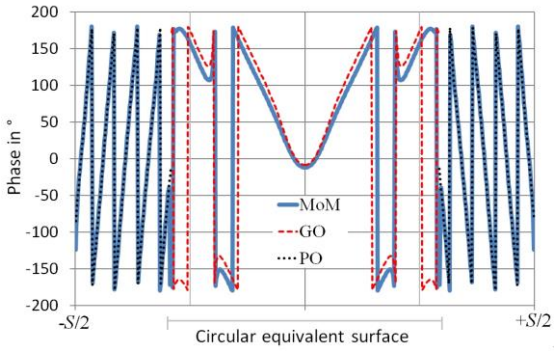

(b) Phase

Fig. 14. Magnitude and phase distribution of $\mathbf{J_c}$ along S for parabolic reflector example.

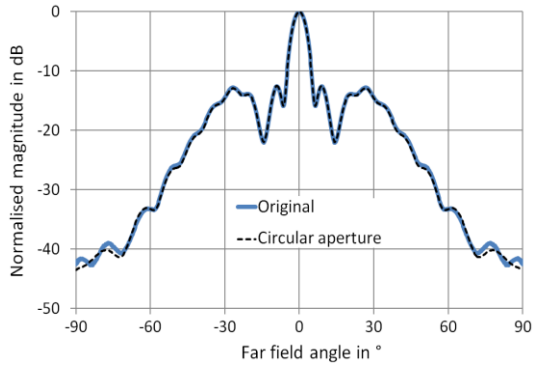

Fig. 15. Far field radiation patterns for parabolic reflector example.

VI. HORN ANTENNA EXAMPLES

It is important to note some of the practical applications of the new technique. As an example, radiation from an X-band flared horn antenna with waveguide dimensions W_W=22.86 mm and W_H=10.16 mm, aperture dimensions A_W=22.86 + 2x20 = 62.86 mm and A_H=10.16 + 2x20 =50.16 mm, and length L=20 mm (Fig. 16) was calculated by means of 2D and 3D (FEKO [15]) simulation software. In the 2D case, the waveguide aperture was short-circuited and the equivalent magnetic current densities $\mathbf{M_W}=\cos(y/W_W*\pi)\hat{\mathbf{y}}$ for $-W_W/2 \le y \le +W_W/2$ and $\mathbf{M_H}=\hat{\mathbf{z}}$ for $-W_H/2 \le y \le +W_H/2$, were placed a distance d=0.02λ to the right of the short-circuited waveguide aperture, respectively.

Note that for the 2D calculations the E-plane and H-plane problems were solved independently of each other. The 3D horn antenna was fed by a waveguide which was excited with the FEKO rectangular waveguide source model. As shown in Fig. 17, the correlation between the 2D patterns and the 3D principal plane patterns is very good despite the simplifications made from the 3D to the 2D models. This example also serves to demonstrate the usefulness of 2D simulation to obtain first-order design results for problems that can be reduced to 2D analysis.

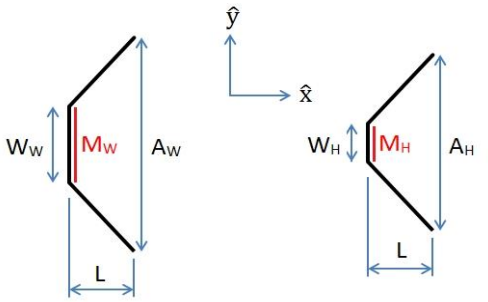

(a) 2D H-plane (b) 2D E-plane

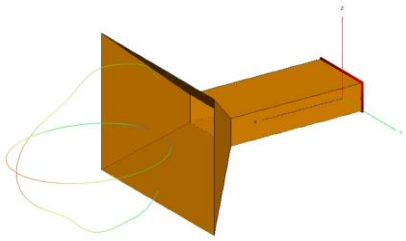

(c) 3D FEKO

Fig. 16. 2D and 3D models of X-band flared horn antenna.

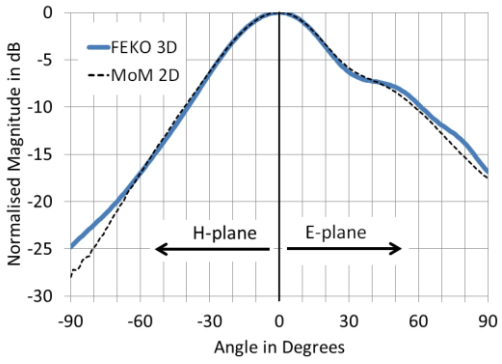

Fig. 17. E- and H-plane radiation patterns of an X-band flared horn antenna.

VII. CONCLUSION

The aim of this paper is to augment an equivalence principle-based technique earlier published by the author, for simplifying the calculation of radiation from arbitrarily shaped aperture antennas when the electric field distribution in the aperture is known. Traditionally the Green's function specific to the problem had to be derived, but with the new technique the aperture can be short-circuited and the free space Green's functions (i.e., the free space radiation integrals) can be used to calculate the fields radiated from the aperture in the presence of the arbitrarily shaped surrounding antenna structure. The validity of this technique is demonstrated and the examples presented provide valuable insight into the mechanics of the equivalence principle and the concept of placing a conductor in the null field region of surface equivalence problems.

The author would also, in conclusion, like to present a brief overview of the arduous route the development of the new technique had taken. During the mid-1990s he had developed an elementary Electric Field Integral Equation free space MoM code for the design of certain types of antennas. As an afterthought he decided to add aperture antennas as well, because of its apparent simplicity. The problem was that although the electric field in the aperture is usually known, the magnetic field is not, and he soon found that for certain examples completely inaccurate results were obtained. Through trial and error he discovered that when the aperture is short-circuited and $\mathbf{M}_s$ is placed a small distance away from it, the free space calculated results agreed perfectly with measured and theoretical results. This was in direct contrast to all the textbooks he could find at the time, in which it was stated that the free space radiation integrals could not be applied to such problems, as discussed above.

The author submitted a paper to a prominent antenna journal in August of 1996, but it was eventually rejected in March 1998, in hindsight for perfectly valid reasons. An opportunity then came along to present a paper on the topic at a local symposium in South Africa in September 1998 [16], but there were no experts in the field who could venture an opinion either for or against it. The author then presented the same topic at the international AP Symposium in Orlando, Florida, in 1999 [17], to which he invited several recognised experts in the field of electromagnetic theory. At both of these presentations the author proceeded to show through examples that it is possible to use the free space radiation integrals to calculate radiation from arbitrarily shaped aperture antennas, and presented an admittedly somewhat heuristic mathematical approach in an attempt to prove the validity of the new technique. More importantly, however, the author *mistakenly* argued that the placement of a conductor in the null field of an equivalence problem was incorrect, as no current would be induced on the conductor and no 'image' could therefore ever be generated. At that stage he had not realised that although the total induced current would be zero in the null region, it is comprised of the sum of more than one source, as expressed by (5), and that the electric current density would indeed be short-circuited as discussed by Harrington and others. It was in fact this realisation that had eventually led to the technique presented in this paper ([1, Section 2], Section II above). Needless to say, no support for or interest in the proposed technique was expressed during these presentations.

The author then derived a new theoretical 'proof' of the new technique *based purely on a mathematical manipulation of the free space radiation integrals* [1, Section 3], that did not rely on the placement of a conductor in the null field of the equivalence problem. He next contacted Prof. Sembiam Rengarajan, whom he had met before and who generously agreed to work through the paper the author intended to submit to the *IEEE Antennas and Propagation Society Magazine*. After a couple of months of back-and-forth correspondence, it was agreed that the paper was probably suitable for submission to the *Magazine*, which the author proceeded to do. The author was soon afterwards contacted by Prof. Joseph Mautz, who had been appointed as Reviewer of the paper, but was concerned that he might not be able to completely follow the author's arguments. He graciously suggested that the author and he correspond about the contents of the paper, which resulted in a series of friendly battle-of-wits exchanges until he was finally prepared to accept the paper for publication (see [1]).

Due to an apparent lack of recognition of his proposed technique, the author decided to take another look at it during the latter half of 2015, with the emphasis on the calculation of the actual induced electrical current density in the short-circuited aperture, as demonstrated by the examples presented above. It was during this process that he managed to demonstrate the validity of the "short-circuiting" concept (Section II), which is now reconciled with the conductor-in-the-null-field approach presented in practically all antenna textbooks that deal with aperture theory. In his opinion the value of this paper is not only to present confirmation of the new technique he had discovered earlier, but also to provide students with additional insight into the application of the equivalence principle to a specific class of antenna radiation problems.

REFERENCES

[1] A. J. Booysen, "Aperture theory and the equivalence principle," *IEEE Antennas and Propagation Magazine*, vol. 45, no. 3, pp. 29-40, June 2003.

[2] R. F. Harrington, *Time-Harmonic Electromagnetic Fields*. New York: McGraw-Hill, pp. 106-113,

1961.
[3] K.-M. Chen, "A mathematical formulation of the equivalence principle," *IEEE Trans. Microw. Theory Techn*., vol. 37, no. 10, pp. 1576-1581, Oct. 1989.
[4] A. E. H. Love, "The integration of equations of propagation of electric waves," *Phil. Trans. Roy. Soc. London, Ser. A*, 197, pp. 1-45, 1901.
[5] *Time-Harmonic Electromagnetic Fields*, pp. 108-109.
[6] *Ibid.*, p. 109.
[7] C. A. Balanis, *Antenna Theory: Analysis and Design*. 4th ed., Hoboken, New Jersey: John Wiley & Sons, Inc., pp. 642-643, 2016.
[8] W. L. Stutzman and G. A. Thiele, *Antenna Theory and Design*. 3rd ed., Hoboken, New Jersey: John Wiley & Sons, Inc., p. 346, 2013.
[9] C. A. Balanis, *Advanced Engineering Electromagnetics*. New York: John Wiley & Sons, ch. 14, 1989.
[10] Y. Svezhentsev, "Mixed-potential reen's function of an axially symmetric sheet magnetic current on a circular metal surface," *Progress In Electromagnetics Research, PIER*, 60, pp. 245-264, 2006.
[11] R. F. Harrington, *Field Computation by Moment Methods*. Wiley-IEEE Press, 1993 reprint of the 1968 ed.
[12] *Advanced Engineering Electromagnetics*, Section 7.4.
[13] *Time-Harmonic Electromagnetic Fields*, pp. 127-128.
[14] A. J. Booysen, "On the equivalence of the geometrical-optics reflected fields and the stationary-phase solution of the associated radiation integrals," *IEEE Antennas and Propagation Magazine*, vol. 44, no. 5, pp. 120-123, Oct. 2002.
[15] FEKO (Altair Hyperworks), ver. 14, www.feko.info, 2016.
[16] A.J . Booysen, "Aperture theory and the equivalence theorem," *Proceedings of the 1998 South African Communications and Signal Processing Conference*, Rondebosch, Cape Town, pp. 353-358, Sept. 1998.
[17] A. J. Booysen, "Aperture theory and the equivalence theorem," *IEEE Antennas and Propagation Society International Symposium*, Orlanda, Florida, vol. 2, pp. 1258-1261, July 1999.

Adriaan J. Booysen received his Ph.D. in Electronic Engineering (Electromagnetics) from the University of Pretoria in 1990. He has since worked at the Antenna Systems Group of Saab Grintek Defence, initially as a Development Engineer and currently as Head of the group. Although his main interest is the design and manufacture of microwave antennas for a variety of EW platforms, he has throughout his career maintained a keen interest in antenna theory and design. Booysen is a Senior Member of the *Institute of Electrical and Electronics Engineers* and has published a number of papers on antenna and electromagnetic theory.

Field-Simulation Based Engineering of RF Antenna Probes with Non-Uniform Substrates for High-Field Magnetic Resonance Imaging Systems

Navid P. Gandji, Akshay V. Palle, George B. Semouchkin, and Elena Semouchkina

Department of Electrical and Computer Engineering
Michigan Technological University, Houghton, Michigan 49931, USA
npourram@mtu.edu, apalle@mtu.edu, gbsemouc@mtu.edu, esemouch@mtu.edu

Abstract ─ It is proposed to replace RF volume coils in high-field Magnetic Resonance Imaging (MRI) scanners by a microstrip patch antenna system. The performed computational studies have demonstrated an opportunity to form extended 3D volumes of homogenous RF magnetic fields by using a system of placed *vis-à-vis* two patch antennas. In order to control antenna dimensions and homogeneity of antenna near fields, the substrates of antennas have been engineered by appropriate patterning of high permittivity dielectric inserts. A variety of antennas with engineered substrates responding at 600 MHz for application in 14T MRI scanners have been designed, and the homogeneity of magnetic fields achieved inside the antenna system has been demonstrated.

Index Terms ─ High-field MRI systems, magnetic field uniformity, patch antenna, RF probe.

I. INTRODUCTION

Magnetic resonance imaging (MRI) is a major tool for investigating a comprehensive range of biological systems from single cells to humans. The advantage of high-field MRI scanners is their potential to provide higher signal-to-noise ratio and, consequently, improved anatomic and temporal resolution [1]. Major advancements are anticipated, in particular, for animal and plant imaging carried out in MRI scanners with the strength of the applied static magnetic field B_0 exceeding 7T. Employing higher magnetic fields leads to increased Larmor frequency, which characterizes the precession of nuclear magnetic moments around the direction of B_0. In particular, in 14T systems this frequency is equal to 600 MHz. RF coils, serving for both transmitting and receiving functions in MRI, generate an oscillating magnetic field B_1, which is normal to B_0. If oscillations of the B_1 field match the Larmor frequency, the energy of the B_1 field can be effectively transmitted to the nuclear spin system. The performance of conventional volume coils, such as birdcage coils [2], degrades at high frequencies in the high field MRI, since dimensions of coils become large compared to wavelengths, so that wave phenomena take place. As a result, obtaining a spatially homogeneous magnetic field covering a larger field of view (FOV) that is required for high image quality becomes a principal challenge [3].

Recently, it was proposed to apply a microstrip patch antenna for excitation of circularly polarized travelling wave in the scanner's bore that acted as a waveguide, with expectations to provide a more homogeneous fields over larger FOV compared to that achieved by using conventional volume coils. However, this approach demonstrated relatively poor transmit efficiency and receive sensitivity, therefore, it was proposed to add multi-channel receive-only arrays to increase the sensitivity [4, 5]. In order to decrease patch antenna size for fitting it inside a 16.4T magnet bore, a substrate of high relative permittivity ($\varepsilon_r = 9.6$) was used that decreased radiation efficiency. In addition, high cutoff frequency for the dominant mode of the magnet bore in 16.4T scanner did not allow for supporting wave propagation at 698 MHz, so only an evanescent wave was generated [4].

In this work we propose to substitute volume coils in 14T MRI scanner operating at 600 MHz by a system of two microstrip patch antennas. The system is, in particular, applicable for small animal imaging. The target of the design is to produce extended 3D volumes of highly homogeneous and strong magnetic fields inside the system of miniaturized antennas with engineered multi-dielectric substrates. The transient solver of the commercial software package CST Microwave studio was used for conducting full-wave electromagnetic simulations to control antenna near fields, characterize antenna performance, and guide antenna substrate engineering. The field post-processing option of the CST solver was employed to plot the curves of spatial field distribution.

II. DESIGNING PATCH ANTENNA SYSTEM

Figure 1 presents the schematic of the projected placement of two patch antennas in 14T magnet bore

Submitted On: September 6, 2015
Accepted On: March 16, 2016

with the diameter of 5.4 cm. The dimensions of the antenna system were chosen to accommodate an object between two patches with the size of about 2 cm × 2 cm (representing the head of a mouse), so that the antenna substrate had a square shape and the area of 3 cm × 3 cm while the separation between two patches was 2 cm. The patch electrodes had rectangular shape with the length L along Z axis and the width W along X-axis, so that B_1 field produced by the antenna at the half-wavelength resonance along the patch length was directed along X-axis, i.e., normal to B_0 oriented along Z-axis (Fig. 1).

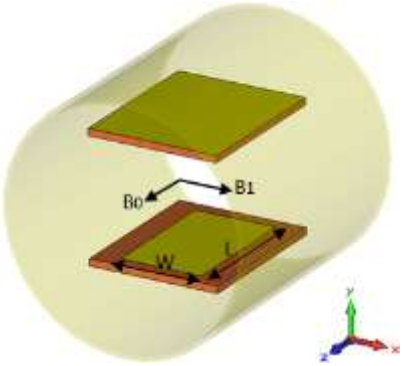

Fig. 1. Schematic of patch antenna placement in the magnet bore.

A. Conventional patch antenna with uniform substrate

It is known that the length of rectangular patch electrode of a microstrip patch antenna is related to its operation frequency *f* at the half-wavelength resonance by the expression:

$$L = \frac{\lambda}{2} = \frac{c_0}{2f\sqrt{\varepsilon_r^{eff}}}, \quad (1)$$

where c_0 is the speed of light in free space and ε_r^{eff} is the effective permittivity of the substrate defined by the relative permittivity of the substrate (ε_r), height (H) of the substrate and width (W) of the patch electrode [6].

As the first step in developing patch antenna for 14T MRI system operating at 600 MHz, an antenna with uniform substrate made of a typical material Arlon (ε_r = 3, tan $\delta \approx 0.028$) [7] was designed. Figure 2 (a) presents the schematic of the antenna fed by a 50-ohms coaxial probe, where the feed point location was optimized to provide impedance matching The S_{11} and the fringing field spectra shown in Fig. 2 (b) demonstrate that the antenna does radiate at 600 MHz. The dimensions of this antenna, however, were L′ × W′=17 cm × 13 cm at the substrate height (H) of 1.6 mm, while the patch electrode dimensions were L × W=13 cm × 10 cm. It is obvious that such conventional patch antenna cannot fit in the magnet bore with the diameter of 5.4 cm. Although, according to (1), the antenna size could be decreased by using a substrate of high permittivity material, this would lead to pulling fields inside the substrate at the expense of fields outside antenna.

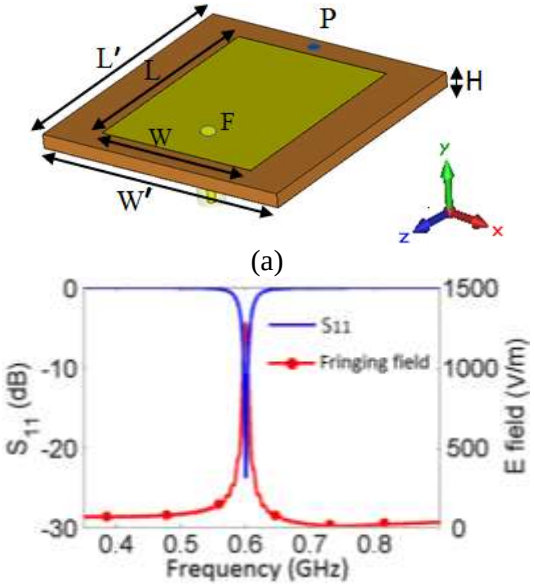

Fig. 2. (a) Antenna schematic and (b) S_{11} of the antenna and the spectrum of the fringing E-field magnitude sampled at point P located at 1.5 mm distance from the patch edge. The point F denotes the optimised feed location.

In our earlier work [8, 9] we proposed to use a substrate composed of a combination of low and high permittivity materials for both shrinking the antenna size and manipulating its characteristics. In the following sections we show how, based on the analysis of simulated field distributions, non-uniform substrates could be designed to provide uniform and strong magnetic near fields and desired antenna size for its application in the MRI system.

B. Patch antenna with one high permittivity insert inside the low permittivity substrate

For the first design of a miniaturized antenna we followed our approach proposed in [8] to insert a rectangular plug of a material with high permittivity such as Calcium Titanate (ε_r = 170, tan $\delta \approx 0.004$) into Arlon substrate with the thickness of 1.6 mm, so that dimensions of the plug were smaller than the patch dimensions in order to minimize fringing field distortion. Targeting the operation frequency of 600 MHz and the area of the substrate of L′ × W′= 3 cm × 3 cm, the chosen combination of materials allowed for designing the antenna with the patch electrode dimensions L × W =2.4 cm × 1.9 cm, while the dimensions of high permittivity plug after optimization were 2.1 cm × 1.6 cm. The dimension of inserts were chosen to make the effective permittivity

under the patch being close to 110 so that the antenna would resonate at 600 MHz.

The simulated electric field pattern inside the substrate and magnetic field pattern sampled at 10 mm above the patch of the miniaturized antenna are presented in Fig. 3 at the frequency of 600 MHz and at optimized feed location providing matched input impedance of the antenna at this frequency.

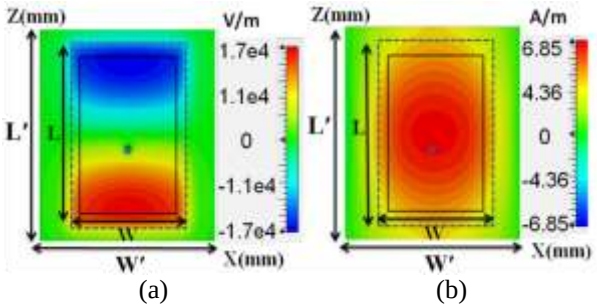

Fig. 3. Distributions of: (a) E_y field component in XZ plane inside the substrate at its half height, and (b) H_x field component in XZ plane located 10 mm above the patch at 600 MHz for the antenna with one high permittivity insert in the substrate. Dashed lines mark the patch electrode and solid lines mark the insert.

The designed antenna has appropriate dimensions to fit in the magnet bore and its magnetic near field, as seen from Fig. 3, covers the major portion of the area above the patch, except for the regions along the boundaries. In the next section we investigate opportunities to further increase the uniformity of near magnetic fields by using multiple high permittivity inserts instead of one in the antenna substrate.

C. Patch antennas with multiple high permittivity inserts in low permittivity substrates

As illustrated by Fig. 3 (a), electric field inside the antenna substrate at the half-wavelength resonance is concentrated in the substrate under the patch edges. Since high permittivity material provides for wave compression by directly influencing electric field, high permittivity inserts located under patch edges should be more efficient for antenna miniaturization, than similar inserts placed under the central part of the patch. Consequently, in order to increase miniaturization efficiency of a non-uniform substrate and to make its fabrication easier, the next step in advancing the antenna design was to use instead of one big high permittivity insert two smaller inserts near substrate edges, where electric field was concentrated (Fig. 4 (a)).

In order to maintain the level of miniaturization with smaller inserts, a higher permittivity insert material was required, which was chosen to be Strontium Titanate ($\varepsilon_r = 300$, $\tan\delta \approx 0.002$).

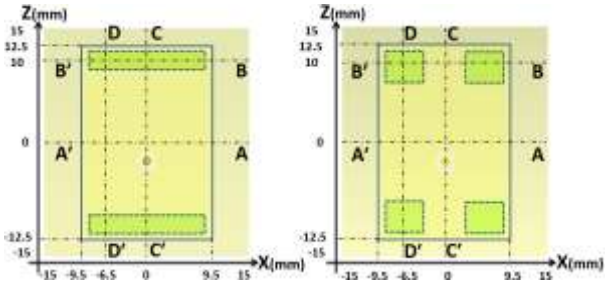

Fig. 4. Schematics of high permittivity insert placement under the patch in antenna substrates: (a) two inserts and (b) four inserts.

Figure 4 (a) shows the schematic of the substrate with two high permittivity inserts having the dimensions of 2 mm × 18 mm and the thickness of 1.6 mm (equal to the substrate thickness). The inserts with the above parameters were found to provide antenna operation at 600 MHz with the same dimensions of the patch electrode (2.4 cm × 1.9 cm) as those of the antenna with one big insert. Figure 5 compares magnetic field distributions for antennas with one and two inserts sampled at 10 mm above the patch at 600 MHz and at feed locations in antennas providing for matched input impedance.

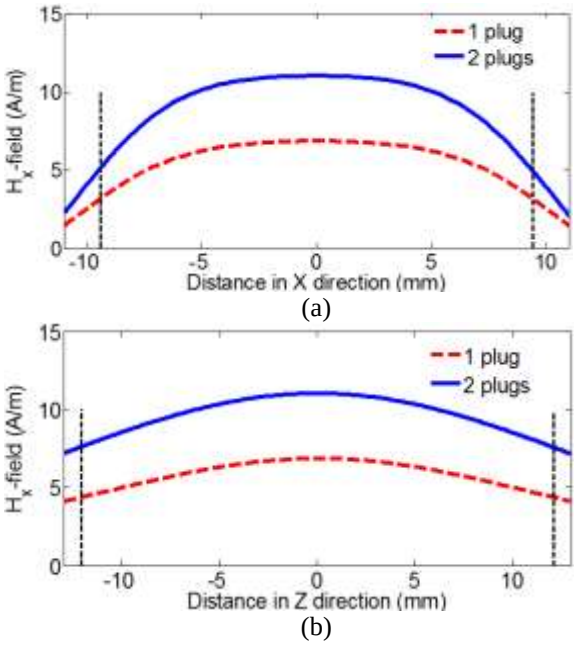

Fig. 5. Distributions of H_x field in XZ plane located 10 mm above patch antennas with one and two inserts: (a) along antenna width (X-direction), i.e., along A-A′ in Fig. 4 (a), and (b) along antenna length (Z-direction), i.e., along C-C′ in Fig. 4 (a). Vertical dashed lines mark the edges of the patch.

As seen in the Fig. 5, smaller high permittivity inserts, which are easier to fabricate, provide, in addition to similar antenna miniaturization, similar magnetic field uniformity, as one big insert does, and even about twice higher magnitude of magnetic field above the patch. The latter could be related to additional secondary field originating from displacement currents in high permittivity material [10]. Based on the results presented in Fig. 5, it is reasonable to suggest that placing various permittivity materials under patch locally would increase or decrease local magnetic field in a controlled manner. This consideration guided the placement of four high permittivity inserts in the next design of the antenna depicted in Fig. 4 (b).

In order to keep the same dimensions of the antenna for operation at the same frequency of 600 MHz, the dimensions of each of four inserts made of the same material ($\varepsilon_r = 300$) as that of the design with two inserts, were found to be: 4 mm × 4 mm × 1.6 mm. Figure 6 compares magnetic field distributions for antennas with two and four high permittivity inserts sampled at 10 mm above the patch electrodes at 600 MHz and at feed locations in antennas providing for matched input impedance. Although field distributions were not significantly different, the uniformity of magnetic field along antenna shorter edge was improved, as expected, for antenna with four high permittivity inserts (Fig. 6 (b)).

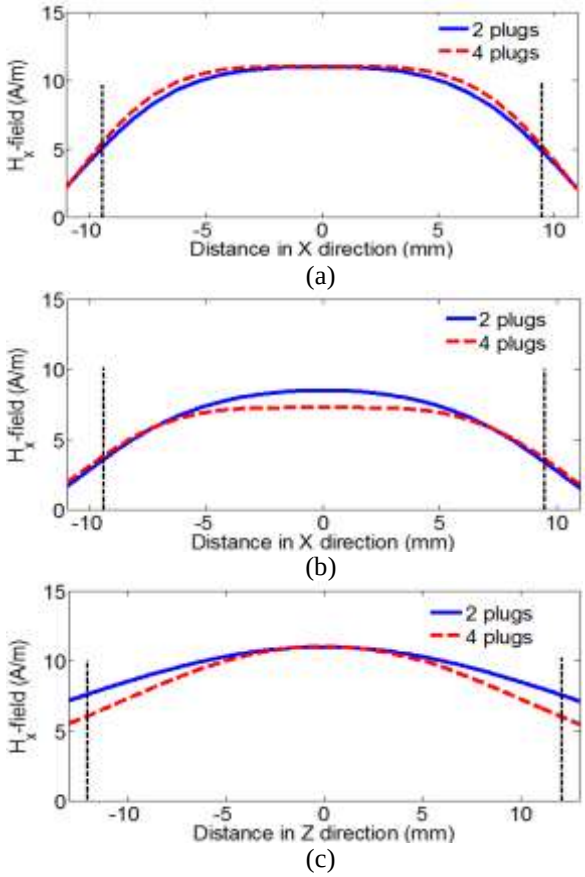

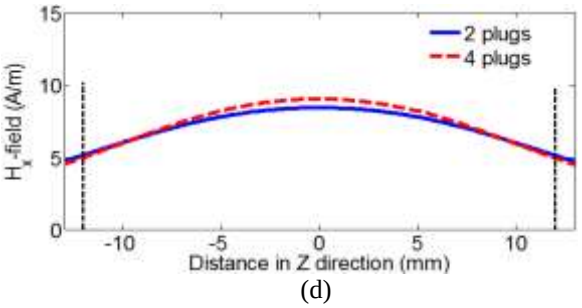

Fig. 6. Distribution of H_x field in XZ plane located 10 mm above patch antennas with two and four inserts along antenna width (X-direction), i.e., along (a) A-A′ in Fig. 4 and (b) B-B′ in Fig. 4, and along antenna length (Z-direction), i.e., along (c) C-C′ in Fig. 4 and (d) D-D′ in Fig. 4.

D. Combining miniaturized antennas in an antenna system

As illustrated in Fig. 1, two identical miniaturized patch antennas should be placed *vis-à-vis* in the magnet bore 20 mm apart. Antennas should be excited with 180° phase difference, therefore, their magnetic near fields H_x will add in the space between antennas. Figure 7 (a) presents the distributions of magnetic fields of each antenna and of the field resulting from summation, along the axis normal to the patches within the separation distance between antennas.

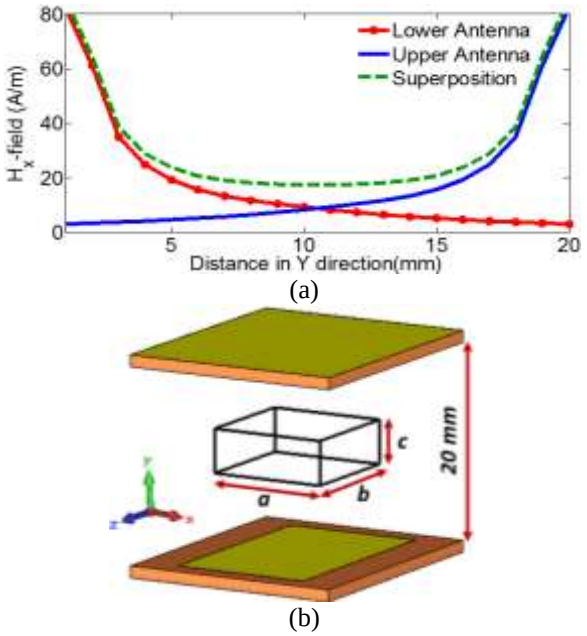

Fig. 7. (a) Distribution of H_x field for each antenna and for the antenna system along the axis normal to patches (Y-axis) within the separation distance of 20 mm between antennas, and (b) schematic of placement of the MRI object with dimensions ($a \times b \times c$) between two antennas.

As seen in Fig. 7 (a), the distribution of the magnetic field in the antenna system along the axis normal to patches demonstrates high uniformity. To illustrate the level of field uniformity in all three directions, Fig. 7 (b) shows the schematic of placement of an MRI object with dimensions ($a \times b \times c$) in the space between two antennas. The uniformity of field can be defined by the ratio of minimal and maximal field strengths along the dimensions of the phantom [11, 12]. Then it can be calculated that the field uniformity in Y-direction, i.e., along the object height c in Fig. 7 (b), when c = 6 mm, is almost 97%, while for the object with the height c = 10 mm it is 90%. From the results presented in the previous section, it could be obtained that in Z-direction along the object length of 10 mm (a = 10 mm) the achieved uniformity is 91%, while in X-direction along the object width of 10 mm (b = 10 mm) the uniformity is around 90%. Overall, for a sample with dimensions ($a \times b \times c$) = (10 mm × 10 mm × 10 mm) placed between two antennas, the magnetic field uniformity in the volume covered by the object is not less than 90% and is even higher for smaller objects, respectively.

III. CONCLUSION

A system of two microstrip patch antennas has been designed to substitute RF volume coils in 14T MRI system operating at 600 MHz. In order to miniaturize antennas for fitting in the magnet bore with the diameter of 5.4 cm it is proposed to use a combination of two dielectric materials with low and high permittivity in the antenna substrates. Based on the analysis of simulated near fields produced by antenna, several designs of miniaturized antennas have been developed. It is demonstrated that uniformity of the magnetic field within the volume of an object with the dimensions (10 mm × 10 mm × 10 mm) placed between two antennas exceeds 90%.

ACKNOWLEDGMENT

This work was supported by the National Science Foundation under Award IDBR-1353664.

The authors also wish to thank Dr. Michael Lanagan and Dr. Thomas Neuberger (The Pennsylvania State University) for helpful discussions.

REFERENCES

[1] Y. Hyoungsuk, G. Anand, and J. T. Vaughan, "A method to control non-uniformity RF B_1 field for high field magnetic resonance imaging," *IEEE MTT-S Int. Microwave Symp. Dig*., Anaheim, CA, pp. 752-755, May 2010.

[2] J. T. Vaughan, G. Adriany, C. J. Snyder, J. Tian, T. Thiel, L. Bolinger, H. Liu, L. DelaBarre, and K. Ugurbil, "Efficient high-frequency body coil for high-field MRI," *Magnetic Resonance in Medicine*, 52, pp. 851-859, Sep. 2004.

[3] J. Hoffmann, J. Budde, G. Shajan, and R. Pohmann, "Slice-selective B_1 phase shimming at 9.4 T," *Proc. Int. Soc. Mag. Reson. Med.*, 18, Stockholm, Sweden, pp. 1470, 2010.

[4] G. Shajan, J. Hoffmann, D. Z. Balla, D. K. Deelchand, K. Scheffler, and R. Pohmann, "Rat brain MRI at 16.4T using a capacitively tunable patch antenna in combination with a receive array," *NMR in Biomedicine*, vol. 25, no. 10, pp. 1170-1176, 2012.

[5] J. Hoffmann, G. Shajan, J. Budde, K. Scheffler, and R. Pohmann, "Human brain imaging at 9.4 T using a tunable patch antenna for transmission," *Magnetic Resonance in Medicine*, 69, pp. 1494-1500, 2013.

[6] H. A. Wheeler, "Transmission-line properties of a strip on a dielectric sheet on a plane," *IEEE Tran. Microwave Theory Tech*., vol. MTT-25, pp. 631-647, Aug. 1977.

[7] T. Reynalda, A. Munir, and E. Bharata, "Characterization of 4x4 high gain microstrip array antenna for 3.3GHz WiMAX application," *IEEE TSSA, 6th Int. Conference*, Bali, Indonesia, pp. 215-218, Oct. 2011.

[8] E. Semouchkina, A. Baker, G. Semouchkin, T. Kerr, and M. Lanagan, "Wearable patch antenna for voice communications with substrate composed of high contrast dielectrics," *IEEE APS Int. Symp.*, Honolulu, HI, pp. 4188-4191, June 2007.

[9] E. Semouchkina, J. Scholz, S. Perini, G. B. Semouchkin, M. Lanagan, R. Haupt, and H. Simonds, "Metamaterials inspired miniaturization of UHF patch antennas with circular polarization," *Microwave and Optical Technology Letters*, vol. 53, no. 8, pp. 1938-1943, Aug. 2011.

[10] W. M. Brink, R. F. Remis, and A. G. Webb, "A theoretical approach based on electromagnetic scattering for analyzing dielectric shimming in high-field MRI," *Magnetic Resonance in Medicine*, June 2015.

[11] X. Chen, "Analytical path to improved RF field homogeneity for high field MRI," *Ph.D. Thesis*, Department of Physics, CASE Western Reserve University, 2009.

[12] J. T. Vaughan, M. Garwood, C. M. Collins, W. Liu, L. DelaBarre, G. Adriany, P. Andersen, H. Merkle, R. Goebel, M. B. Smith, and K. Ugurbil, "7T vs. 4T: RF power, homogeneity, and signal-to-noise comparison in head images," *Magnetic Resonance in Medicine*, vol. 46, no. 1, pp. 24-30, Jan. 2001.

Navid P. Gandji received the M.S. degree in Microwave Communication Engineering from Iran University of Science and Technology, Tehran, Iran, in 2009.

He is currently a Ph.D. degree candidate in Electrical Engineering with Michigan Technological University. His research interests include designing antennas and filters, and metamaterials.

Akshay V. Palle received the Bachelor of Technology degree in Electronics and Communication Engineering from Jawaharlal Nehru Technological University, Hyderabad, India, in 2014.

He is currently a M.S. degree candidate in Electrical Engineering with Michigan Technological University. His research interests include designing antennas and microwave structures.

George Semouchkin received the M.S. degree in Electrical Engineering, Ph.D. degree in Materials, and Doctor of Science degree in Physics and Mathematics from Leningrad Polytechnic Institute (now St. Petersburg State Technical University), St. Petersburg, Russia, in 1962, 1970, and 1990, respectively.

He is currently Research Professor of Electrical Engineering with Michigan Technological University. Prior to joining Michigan Technological University in 2010, he was a Visiting Professor of Materials with the Materials Research Institute, the Pennsylvania State University, University Park, from 1999, and, earlier he was with the St. Petersburg State Technical University, Russia, as a Professor, a Leading Scientist, a Head of the Laboratory, and a Senior Scientist, where he studied ionic crystals, ceramic materials, inorganic dielectrics and developed microelectronic devices. He has authored over 150 technical publications. His current research interests include microwave devices and all-dielectric metamaterials.

Elena Semouchkina received the M.S. degree in Electrical Engineering and the Ph.D. degree in Physics and Mathematics from Tomsk State University, Tomsk, Russia, in 1978 and 1986, respectively, and the Ph.D. degree in Materials from The Pennsylvania State University, University Park, in 2001.

She is currently Associate Professor of Electrical Engineering and Adjunct Professor of Physics with Michigan Technological University, as well as Adjunct Professor with the Pennsylvania State University. Prior to working at the Materials Research Institute, the Pennsylvania State University, from 1997 to 2009, initially as a Graduate Research Assistant, then as a Postdoctoral Scholar, later as a Research Associate, and, then as a Senior Research Associate and Associate Professor, she was a Scientist with Russian academic centers, such as the Siberian Physics-Technical Institute, St. Petersburg State Technical University, and Ioffe Physics-Technical Institute, where she was involved with the investigation of metal-oxide-semiconductor devices and the development of infrared photodetectors. She has authored and co-authored over 80 publications in scientific journals. Her current research interests are focused on electromagnetic analysis of microwave materials, metamaterials and devices.

Semouchkina was a recipient of the best Ph.D. Thesis Award of the Materials Research Institute at The Pennsylvania State University in 2001 and the National Science Foundation 2004 Advance Fellows Award.

Analysis, Design and Demonstration of a Dual-Reflectarray Antenna in Ku-band for European Coverage

Carolina Tienda [1], Jose A. Encinar [2], Mariano Barba [2], and Manuel Arrebola [3]

[1] Department of Radar Concepts, Microwave and Radar Institute, DLR
Oberpfaffenhofen, 82234, Germany
Carolina.Tienda@dlr.de

[2] Department of Electromagnetism and Circuit Theory Universidad Politécnica de Madrid, ETSIT
Ciudad Universitaria s/n, Madrid, E-28040, Spain
encinar@etc.upm.es, mbarba@etc.upm.es

[3] Department of Electrical Engineering (Group of Signal Theory and Communications)
Universidad de Oviedo, Gijón (Asturias), E-33203, Spain
arrebola@tsc.uniovi.es

Abstract ─ An accurate technique has been proposed for the analysis of dual-reflectarray antennas, which takes into account the angle of incidence of the field impinging on main reflectarray cells. The technique has been applied to the analysis and design of a contoured beam antenna in Ku-band that provides a European coverage. The reflected field on the sub-reflectarray is computed using Spectral-Domain Method of Moments assuming local periodicity, as customary. The sub-reflectarray is divided in groups of elements and the radiation from each group is used to compute the incident and reflected fields on the main reflectarray cells. Different degrees of accuracy can be achieved depending on the number of groups considered. A 50-cm antenna demonstrator has been manufactured and measured in a compact range. The measured radiation patterns are in good concordance with the simulations and practically fulfill the coverage requirements with a cross-polar discrimination better than 25 dB in the frequency band 12.975 GHZ - 14.25 GHz.

Index Terms ─ Antenna, countered beam, dual-reflectarray.

I. INTRODUCTION

Reflectarray antennas present a competitive performance for applications like long distance communications [1], spaceborne antennas for contoured beams [2,3] and Synthetic Aperture Radar (SAR) [4], when compared with phased arrays and reflector antennas. Reflectarrays are manufactured by photo-etching and bonding processes which are a well-established technology in multi-layer printed circuit boards (PCB). The reduced bandwidth of the printed elements used on the reflectarrays and the differential spatial phase delay limit the total bandwidth in reflectarrays [5,6]. To overcome this problem, different techniques have been applied, such as the use of several layers of patches [7,8], multi-resonant elements [9], aperture-coupled patches with delay lines [10], or faceted configurations [11].

Although, single reflectarray antennas have been deeply studied in the last years, dual reflector configurations present some advantages with respect to single reflectarrays [12,13]. Two of these advantages are the reduction of the volume of the antenna for a large focal distance and the possibility of using a small reflectarray subreflector with a main large parabolic reflector. The last configuration combines the broadband and high gain capabilities of parabolic reflectors with the advantage of using a small reflectarray that can be used to improve the behavior of the antenna. In this kind of antennas, the sub-reflectarray can be used to correct the errors in the surface of the very large deployable reflectarrays [14] or to provide beam scanning in a limited angular range [13,15]. The beam can be reconfigured or scanned when the phase-shift on the reflectarray subreflector is electronically controlled by using MEMS [16-18], pin diodes [19], varactor diodes [20,21], or liquid crystals (LC) [22-24] for frequencies around 100 GHz and beyond.

The main, the sub-or both reflectors in a dual-reflector configuration can be replaced by reflectarrays [14,15,25]. Antennas implemented with two reflectarrays [25] as shown in Fig. 1 (a), one as sub-reflector and the other as main-reflector, provide phase control in both surfaces which gives additional degrees of freedom that can be used to improve the performance of the antenna

Submitted On: November 16, 2015
Accepted On: February 26, 2016

for certain applications. The bifocal antenna principle applied to dual reflectarray antennas can be used for designing multi-beam antennas providing a stable performance for all beams as shown in [26]. Dual reflectarray antennas implemented with two flat reflectarrays have a high degree of compactness. In dual reflectarray antennas, the beam can be scanned or reconfigured by controlling the phases at the elements of the sub-reflectarray while using the main reflectarray for additional functionalities or improvements in the antenna performance. The sub reflectarray can be also used to change the linear polarization of the feed horn to circular. Applications of this kind of antenna configuration can be Synthetic Aperture Radar (SAR) [27] and radiometric remote-sensing [15].

The accurate analysis of a dual-reflectarray antenna is difficult and requires a high computational effort, since for every single element of the main reflectarray all the field contributions radiated by the cells of the sub-reflectarray must be considered. An analysis technique has been recently reported for the analysis of dual-reflectarray antennas [25], in which the reflection coefficients on the elements of both reflectarrays are computed by Spectral-Domain Method of Moments (SD-MoM) [28] assuming local periodicity. A reflection matrix, which relates the incident and reflected fields, should be computed for every pair of cells in the main and sub-reflectarray. Since the computation of the reflection coefficients NMR×NSR times was computationally unaffordable, being NMR and NSR the number of cells in the main and sub-reflectarrays respectively, the impinging electric field on every cell of the main reflectarray was approximated by a single plane wave. In this approximation, the incident plane wave is computed as the superposition of the fields coming from every sub-reflectarray cell. The field reflected on every cell of the main reflectarray was computed approximating the incidence angle by that coming from the center of the sub-reflectarray (fix angle of incidence). The approximation reduces significantly the computation time, since each reflection coefficient matrix is computed NMR, instead of NMR×NSR times. When the phase response of the cells in the main reflectarray is practically no affected by the incidence angles from different sub-reflectarray cells, this approximated approach will provide an accurate analysis on the main reflectarray. In many practical configurations, incidence angles up to 30 degree produce a negligible effect on the response of the main reflectarray cells. The approximate technique was successfully used in [29] to design a compact dual-reflectarray antenna in Ku-band that produces a pencil beam with gain better than 32 dBi and a cross-polar discrimination (XPD) better than 30 dB in a 20% bandwidth (12.2 GHz - 15 GHz), covering Tx and Rx frequency bands. To ensure the validity of the approximation, the reflectarray elements on the main reflectarray were chosen to be almost insensitive to the angle of incidence. They were made of a single layer of varying-sized patches in a small period (0.4λ x 0.4λ at 15 GHz, which is the highest frequency). The experimental results showed a good concordance with the simulations, even though the incidence angles on the main reflectarray were up to 50º in some extreme elements.

The approximation of the fix angle of incidence used in the main reflectarray may not be accurate in many cases, when other reflectarray elements more sensitive to the angle of incidence are used, or when large angles of incidence exist in the antenna configuration. Furthermore, when the antenna is used to produce a contoured beam as in Direct Broadcast Satellite (DBS) applications [2,3,30], the phase errors produce a more drastic distortion in the contoured radiation patterns than in the simple case of a pencil beam, as demonstrated in [3].

The high performance in broadband and cross-polarization achieved by dual-reflectarray configurations shown in [29] for a pencil beam can be also extended to contoured beams for Tx-Rx DBS antennas with high requirements in coverage and cross-polarization [31]. Up to the knowledge of the authors, the only dual-reflectarray prototype designed to produce a shaped beam (sectored in azimuth) was reported in [33], for the particular case of a centered configuration with the reflectarray subreflector placed on a polarizing grid, which limits the operation to single polarization.

In this paper, an analysis technique is presented to provide an accurate and flexible model for dual-reflectarray antennas, which improves the simulation accuracy by taking into account the angles of incidence in each element of the main reflectarray. A dual-reflectarray antenna demonstrator has been completely designed and analyzed using the proposed technique to produce a contoured beam for DBS European coverage. To simplify manufacturing, a limited size demonstrator of 50 cm is implemented, although a larger aperture of approximately one meter should be necessary for a real coverage. The antenna optics has been chosen to limit the total phase variation on the two reflectarrays to a range of 360º to eliminate any need for phase-delay elements. The idea that motivated this paper is to demonstrate that the coverage can be achieved in both transmit and receive frequency bands by using a dual-reflectarray configuration that emulates a large F/D (F/D=4)). An appropriate analysis technique for dual reflectarray configurations has been applied and validated in the present paper to produce a contoured beam. The antenna was manufactured and measured at Universidad Politécnica de Madrid and the results show good performance in coverage and cross-polarization in the entire working band (12.975-14.250 GHz).

II. GENERAL ANALYSIS TECHNIQUE FOR DUAL-REFLECTARRAY ANTENNAS

The proposed dual-reflectarray configuration comprises a feed-horn and two flat reflectarrays with the phasing elements arrange in a rectangular lattice. The analysis method described here can be used for a flat sub-reflectarray (SRA) and a flat main reflectarray (MRA) with any type of reflectarray elements, including single or multiple layers of patches. The analysis technique consists of four main steps as explained in [25]. The sub-reflectarray is analyzed as a single reflectarray through SD-MoM considering local periodicity. For the analysis of the main reflectarray cells, the sub-reflectarray is divided in groups of elements, and the field radiated by each group with its incident angle is used to compute the reflection response on every main reflectarray cell by SD-MoM. Finally, the radiation pattern is computed from the field on the main reflectarray by applying FFT. This is a very general analysis technique since it provides the chance of making the analysis with different degrees of accuracy and efficiency, by dividing the sub-reflectarray in higher or lower number of groups. The demanded analysis accuracy will depend on the antenna geometry, which defines the maximum angles of incidence on the main reflectarray, on the period and type of cells used in the main reflectarray. $\mathbf{R}_{(p,q)}(m,n)$ matrix represents the reflection coefficients of every cell of the main reflectarray (m,n) for a plane wave coming from each cell of the sub-reflectarray (p,q), this matrix depends on the positions of the cells (m,n) and (p,q) in the main and sub-reflectarrays, and therefore on the angle of incidence. Note that, if the $\mathbf{R}_{(p,q)}(m,n)$ matrix is computed for all combinations of cells (m,n) – (p,q) an extremely long CPU time will be required.

In a dual-reflectarray antenna when the reflectarray subreflector is small and far from the main reflectarray, every field contribution coming from the different cells of the sub-reflectarray are very similar. Thus, there is practically no difference in the computation of the reflection coefficient if the origin of the incident field is considered to be the center of the sub-reflectarray, in this case the effect of the angle of incidence can be neglected ($\mathbf{R}_{(p,q)}(m,n) \approx \mathbf{R}(m,n)$) as in [25]. However, if the main reflectarray cells are located in the near field zone of the sub-reflectarray, the incidence angle can vary strongly for some sub-reflectarray cells. This effect can be neglected if the two sub-reflectarray cells are neighbors but it is strong if they are far away one from each other. To consider this effect, the sub-reflectarray is divided in groups of elements. The incident field on every element of the main reflectarray is decomposed in waves radiated by each group. Each group of cells of the sub-reflectarray produces an electric field contribution in every single cell of the main reflectarray. Each of these contributions has a different incidence angle, which is taken into account in the computation of the reflected coefficients for each cell in the main reflector. Therefore, for every cell of the main reflectarray, a number of NG reflected coefficients are calculated, being NG the number of groups. The size of the groups is calculated such that the main reflectarray cells fulfill the far field conditions with respect to each group in the sub-reflectarray. For simplicity the size of the groups is maintained constant, although near the reflectarray edge the groups may have some elements left, particularly when the reflectarray subreflector is not rectangular, see Fig. 1 (b).

The field contributions of the cells integrating a group are added before computing the corresponding $\mathbf{R}(m,n)$ matrix on the main reflectarray. All these field contributions are considered to leave from the center of their group. The incident and reflected field on every (m,n) cell of the main reflectarray due to one group of cells is shown in Eq. (1) and Eq. (2) respectively:

$$\mathbf{E}^{X/Y}_{\mathrm{inc}(g)}\left(m,n\right) = \sum_{r=1}^{Size\_x}\sum_{s=1}^{Size\_y} \mathbf{E}^{X/Y}_{\mathrm{inc}(r,s)}\left(m,n\right), \quad (1)$$

Size_x and Size_y are the number of elements for each group "g" in the x- and y-axis respectively. $\mathbf{E}^{X/Y}_{inc(g)}(m,n)$ is the electric field impinging on the cell (m,n) of the main reflectarray from the group of cells (g) of the sub-reflectarray, according to Fig. 1 (b), for X or Y polarization. The field reflected at each cell (m,n) of the MRA is:

$$\mathbf{E}^{X/Y}_{\mathrm{ref}}\left(m,n\right) = \sum_{g=1}^{NG} \mathbf{R}_{(g)}\left(m,n\right)\cdot \mathbf{E}^{X/Y}_{\mathrm{inc}(g)}\left(m,n\right), \quad (2)$$

where

$$\mathbf{R}_{(g)}(m,n) = \begin{pmatrix} \rho^{(m,n)}_{(g)\ xx} & \rho^{(m,n)}_{(g)\ yx} \\ \rho^{(m,n)}_{(g)\ xy} & \rho^{(m,n)}_{(g)\ yy} \end{pmatrix}, \quad (3)$$

$\mathbf{R}_{(g)}(m,n)$ is the reflection matrix for the cell (m,n) of the main reflectarray due to the group g. The components $\rho^{(m,n)}_{(g)\ xx}$ and $\rho^{(m,n)}_{(g)\ yx}$ are the direct and cross polarization reflection coefficients for an incident wave polarized with the electric field on X_{SR} direction (without component in Y_{SR}). On the other hand, $\rho^{(m,n)}_{(g)\ yy}$ and $\rho^{(m,n)}_{(g)\ xy}$ are the reflection coefficients for an incident electric field on Y_{SR} direction.

For this general analysis method, there are two possible limit cases: the full-wave case, in which each group of sub-reflectarray elements has only one cell, and the case based on the approximation of fix angle of incidence, in which there is only one group of elements in the sub-reflectarray. In the first case, the electric field coming from each cell of the sub-reflector impinges on each cell of the main reflectarray with different angle, which is taken into account in the computation of the

field reflected by each cell in the main reflectarray. In the opposite case, a unique angle of incidence is assumed for all the field contributions arriving from sub-reflectarray elements, as described in [25].

Finally, the co-polar and cross-polar radiations patterns are computed from the field on the main reflectarray by applying an Inverse Discrete Transform.

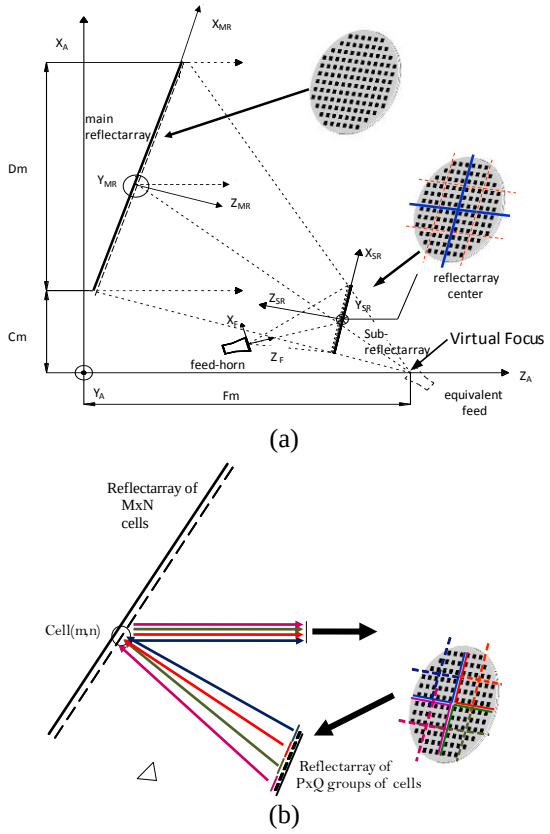

Fig. 1. Scheme of a dual reflectarray structure (a). Scheme of a dual reflectarray structure with the sub-reflectarray divided in groups of elements (b).

III. DESIGN OF A CONTOURED BEAM DUAL-REFLECTARRAY ANTENNA

A dual-reflectarray demonstrator of limited size is designed to provide a European coverage. The antenna optics parameters are given in Table 1 and they are similar to the dual-offset configuration presented previously in [29], considering the same feed-horn, sub-reflectarray, and relative positions respect to the main reflectarray. The phase-shift distribution on the SRA is defined to emulate a hyperbolic subreflector in order to provide an equivalent parabolic system with a large F/D (F/D=4), which reduces the range of phase-shift required in the subreflector to eliminate the steps of 360º. However, in this work the phase-shift distribution on the MRA is synthesized to produce a contoured beam that provides European coverage.

Table 1: Geometrical parameters of the dual-reflectarray antenna

Main Reflectarray (MRA)	
Main reflectarray dimensions	41 × 37 elements
Rows x columns	492 mm × 444 mm
Period	12 mm × 12 mm
Sub-Reflectarray (SRA) (Data in main reflectarray coordinate system)	
Center coordinates	(-217, 0, 370) mm
Direction cosines matrix (Relates MRA and SRA coordinate systems)	$\begin{bmatrix} 0.715 & 0 & 0.698 \\ 0 & -1 & 0 \\ 0.698 & 0 & -0.715 \end{bmatrix}$
Sub-reflectarray dimensions	380 mm × 380 mm
Rows x columns	38 × 38 elements
Period	10 mm × 10 mm
Feed-Horn (Data in sub-reflectarray coordinate system)	
Coordinates of phase-center	(193.73, 0, 635.54) mm
Intersection of feed axis and SRA	(15, 0, 0) mm

The sub-reflectarray is illuminated by a corrugated horn operating in dual-linear polarization, vertical (V) and horizontal (H), with the electric field polarized towards the Y_F and X_F axes, respectively. The antenna position on the satellite is assumed with the Y_{MR} axis perpendicular to the Equator and pointing the North, so that V-polarized field is parallel to Y_{MR}. Since the same coverage is considered for both linear polarizations, the antenna can operate in dual circular polarization by simply using a dual-circular feed. For this antenna configuration the reflectarray subreflector is placed on the Fresnel-zone of the corrugated horn, and therefore a near-field model of the feed-horn [35,36] should be used for an accurate analysis. The incident field on the sub-reflectarray is computed from the field radiated by the feed represented by a spherical wave expansion [37]. The feed-horn produces an illumination taper of -13.48 dB at the sub-reflectarray edges and -16.24 dB at the main reflectarray edges.

The phase shift required on the sub-reflectarray surface is calculated through ray tracing. The phase-shift at each cell is proportional to the difference of the distances from the cell to the feed and to the virtual focus as shown in [29], see Fig. 1 (a).

A. Phase synthesis for European coverage

The European coverage to be synthesized is referred to a geostationary satellite located at 10ºE longitude and 0º latitude. For the limited sized demonstrator, a minimum gain of 25 dBi is required in the enlarged European region defined in [32], which accounts for the satellite pointing errors. This enlarged coverage is plotted in solid blue line in Fig. 2. The main reflectarray is designed with a phase distribution

synthesized to produce a contoured beam that provides this coverage. Note that a simple coverage has been chosen because of the limited size of the main reflectarray (45 cm x 50 cm). More stringent requirements as shown in [31], or higher levels of gain can be achieved using a more realistic size of the main reflectarray, at least 1 meter for Ku-band antennas.

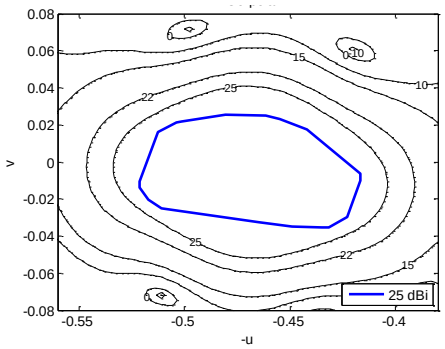

Fig. 2. Synthesized radiation pattern for vertical polarization at 13.75 GHz superimposed to the coverage mask.

A phase-only synthesis technique based on the intersection approach [38] is used to obtain the phase distribution on the main reflectarray surface to produce the required contoured beam. The intersection approach [38] has been successfully used in the design of contoured-beam reflectarrays for DBS antennas [30,31]. The phase-shift to be implemented on the reflectarray is obtained as the difference between the phase of the field obtained from the pattern synthesis and the phase corresponding to the distance from the virtual focus to each cell of the main reflectarray, since the sub-reflectarray is emulating a field radiated by the virtual focus. Considering this phase distribution, the calculated radiation pattern is superimposed to the required mask for the European coverage in Fig. 2. The radiation pattern fulfills the coverage requirements but the gain contours are not able to accurately match the coverage contour because of the limited size of the antenna demonstrator.

B. Design of main and sub-reflectarrays

Once the illumination and the phase distribution are determined, the design is carried out for both reflectarrays, considering dual-linear polarizations at 13.75 GHz. The patch dimensions are obtained by the iterative process described in [7] that calls an analysis routine based on SD-MoM [28] assuming local periodicity. The sub-reflectarray has been designed as described in [29]. The same sandwich configuration is used for both the main and sub reflectarrays. The sandwich stack-up, including the thickness and electrical properties of each layer are provided in Table 2. In the two-layer main reflectarray, the patches are distributed in a rectangular lattice within an ellipse of 492 mm × 444 mm. The selected period is 12 mm in x- and y-axes, thus the main reflectarray is arranged in 41 × 37 elements. The period of the elements in the sub reflectarray is 10 mm in x- and y-axis and they are arranged in a grid of 38 × 38 elements.

Table 2: Lay-up of the sandwich and radio-electric characteristics of the materials

Dielectric/Metallization	εr	tag δ	Thickness (mm)
Copper (printed patch layer 2)	-	-	0.05
(SRA) Cuclad 217LX/ (MRA)Diclad880B	2.17	0.0009	1.524
(SRA/MRA)Cuclad6250 (thermoplastic bonding film)	2.32	0.0013	0.038
Copper (printed patch layer 1)	-	-	0.05
(SRA) Cuclad 217LX/ (MRA)Diclad880B	2.17	0.0009	1.524
Copper (ground plane)	-	-	0.05

For both reflectarrays, the phase-shift as a function of the patch size for the design frequency (13.75 GHz) present a practically linear variation covering a phase range of around 400º when the patch side on the first layer vary from 4-mm to 9-mm, for incidence angles up to 50º as can be seen in Figs. 3 (c and d) for both linear polarizations. The losses in the reflectarray cells are very low, with an average value less than 0.1 dB, see Figs. 3 (a and b). For an incidence of 50º, the phase can vary up to 80° in the main and 30º in the sub-reflectarray, respect to normal incidence. For the angle of incidence θ=50° and φ=0° in the main reflectarray, the losses drastically increases when the patch length is 9 mm due to a resonance. Note that the elements with an incident angle of 50º are near the edge with an illumination 10 dB below than in the center and their effect is less significant in the radiation pattern.

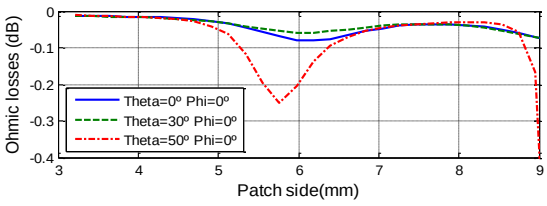

(a)

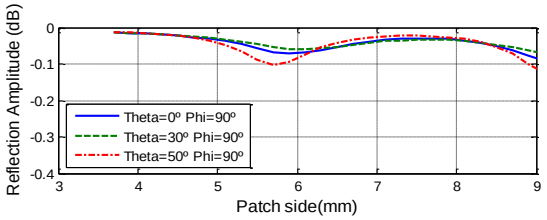

(b)

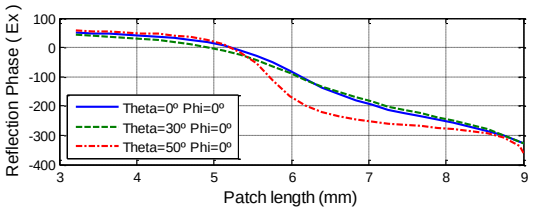

(c)

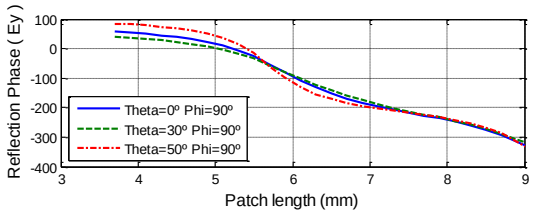

(d)

Fig. 3. Reflection coefficient vs. the patch length in the first layer for the cell used in the main reflectarray for (a) amplitude and (c) phase of E_X field component at $\varphi = 0^o$ (horizontal polarization), and (b) amplitude and (d) phase of E_Y field component, $\varphi = 90^o$ (vertical polarization) at 13.75 GHz.

IV. SIMULATIONS AND EXPERIMENTAL RESULTS

The previously designed dual-reflectarray antenna has been analyzed by the technique described in section II under different degrees of accuracy. First, a full wave analysis is considered, when the elements in the sub-reflectarray are considered individually, without grouping (Size_x=1, Size_y=1). As a second case, the main reflectarray is analyzed using the approximation of the fix incidence angle. Then, the division of the sub-reflectarray aperture is used to analyze the antenna, when dividing the sub-reflectarray in a high number of groups, the radiation pattern are getting closer to those obtained with the full wave analysis:

The number of groups in the sub reflectarray to fulfill the far field conditions with every cell of the main reflectarray is computed, considering the minimum distance between the sub and the main reflectarrays, 23.6 cm. The diameter of one group in the sub should be at least 5 cm to fulfill far-field conditions and between 5 cm and 14 cm to be in the Fresnel zone. If the period in the sub reflectarray is 10 mm, every group of elements has at least 5 elements in each direction, groups of 5x5 elements will fulfill the far field and groups with more than 5x5 elements and less than 14x14 elements will be in Fresnel zone. Taking into account that the sub reflectarray has 38x38 elements, when grouping 13x13 elements, 9 groups are considered in the analysis and when grouping 8x8 elements, 25 groups are considered in the analysis. In both cases, the elements of the main reflectarray closer to the sub reflectarray are in the Fresnel Zone, nevertheless most of the elements in the main reflectarray with 25 groups in the sub reflectarray fulfil the far field conditions.

The contoured co-polar patterns for the full wave approach (black line) are superimposed in Fig. 4 with those obtained when the sub-reflectarray is divided in 1 (red line), 9 (blue line) and 25 (green line) groups, for both linear polarizations. As expected, the green line converges to the black one. Also when the reflectarray is divided in 3x3 groups (blue line) a good agreement is observed in the main beam. Note that for V-polarization the agreement in the main beam is reasonable under the assumption of fix angle of incidence (one group), because the sensitivity with the angle of incidence of the reflectarray elements is lower for patch dimensions smaller than 9 mm, as shown in Fig 3.

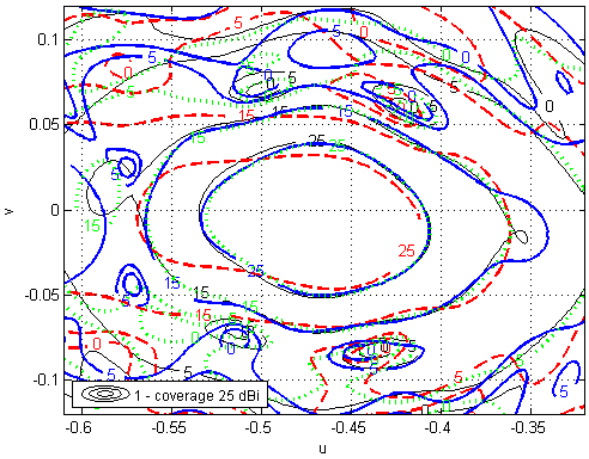

(a)

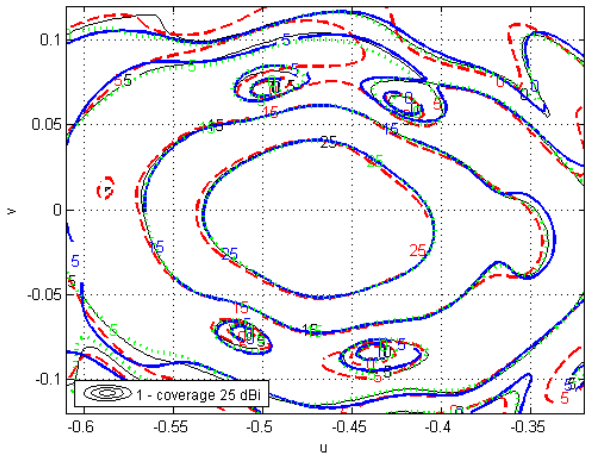

(b)

Fig. 4. Contour plots of the copolar components of the radiation pattern for vertical polarization (a) and horizontal polarization (b) simulated for the full wave analysis (solid black line (-)), approximate case (dashed red line (--)) and the more general approach dividing the sub-reflectarray in 9 (dashed dot blue line(.-)) and in 25 (dashed green line(:)) groups.

Figure 5 shows the antenna demonstrator in the Compact Test Range of Universidad Politécnica de Madrid. The antenna has been measured at the center and at the edges of the frequency band (12.975 GHz, 13.75 GHz and 14.25 GHz). The measured radiation pattern practically fulfils the mask to provide the European coverage with more than 25 dBi gain at the three measured frequencies. The measured and simulated (considering 25 groups) co-polar radiation patterns are superimposed for both linear polarizations at 13.75 GHz in Figs. 6 (a)-(b). A good agreement is observed between simulated and measured patterns, although there are small discrepancies as consequence of a small misalignment between the two layers of printed patches on the main reflectarray. The mentioned misalignment produces phase errors of up to 30° in certain areas of the reflectarray, where the angles of incidence are higher. These errors have been considered in the simulations and compared again with measurements in Figs. 6 (c)-(d), showing a better agreement. The behavior of the antenna is very stable in the required frequency band (12.975 GHz - 14.250 GHz) as shown in Fig. 7. Figure 8 shows the levels of the cross-polarization measured for both linear polarizations at 13.75 GHz. The level of the cross-polar discrimination in the entire frequency band is greater than 25 dB.

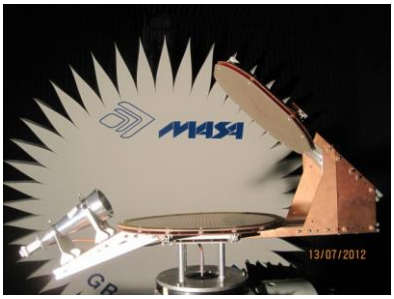

Fig. 5. Dual reflectarray antenna for contoured beam in the compact range anechoic chamber.

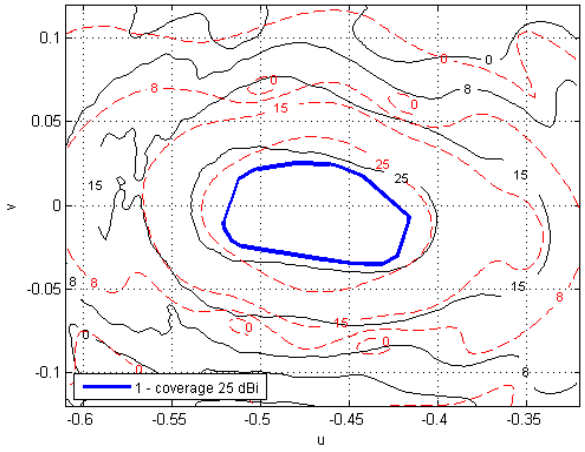

(a)

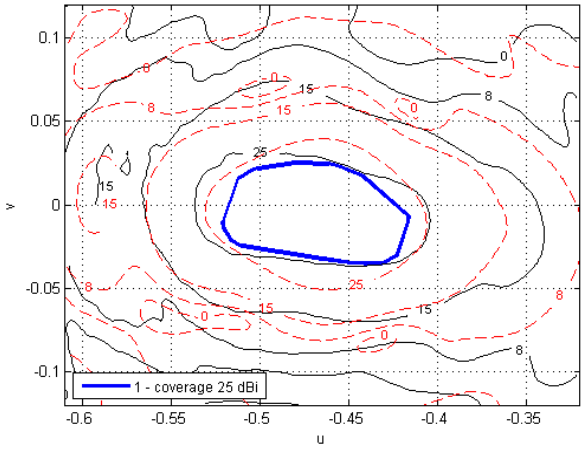

(b)

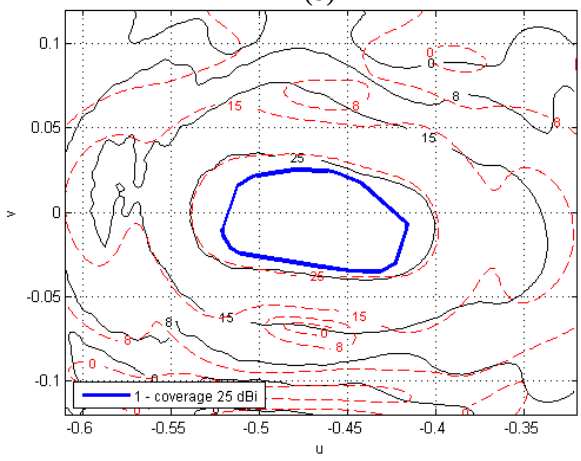

(c)

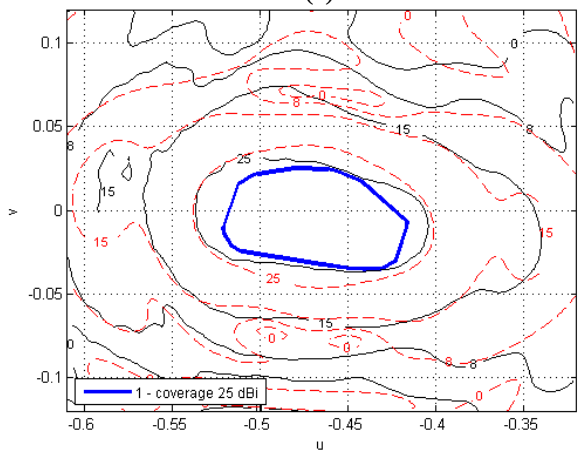

(d)

Fig. 6. Contour plots of the simulated copolar components of the radiation pattern (dashed red line (--)), measurements (solid black line (-)) and the mask (thicker solid blue line) for vertical (a) and horizontal (b) polarizations at 13.75 GHz. The simulations are repeated accounting for the phase errors (red line) and compared with measurements for vertical (c) and horizontal (d) polarizations.

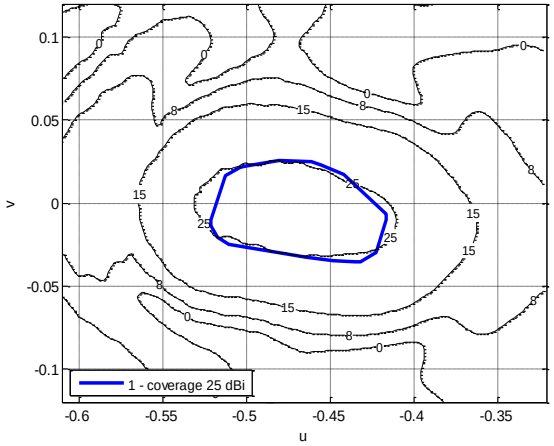

(a)

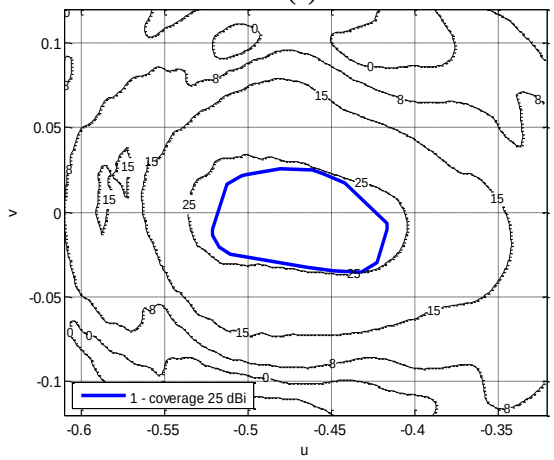

(b)

Fig. 7. Measured contoured patterns in dBi (solid black line) superimposed to the coverage mask (thicker solid blue line) for vertical polarizations at 12.975 GHz (a) and 14.25 GHz (b).

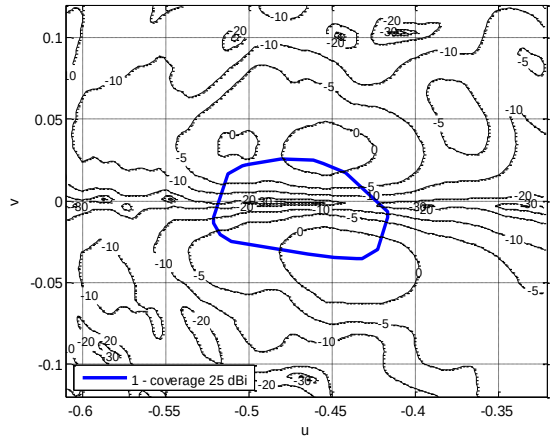

(a)

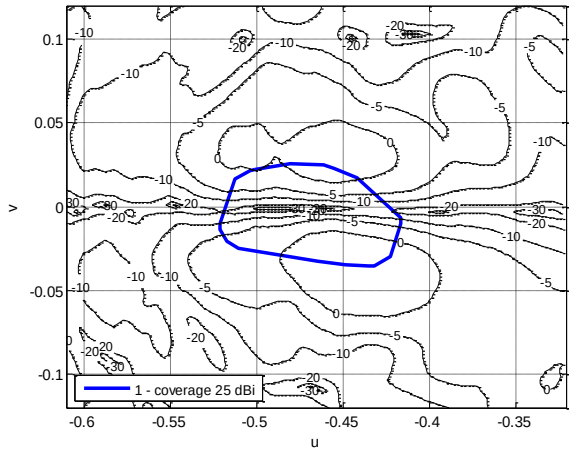

(b)

Fig. 8. Measured contoured plots of the cross-polar components of the radiation pattern (solid black line) superimposed to the coverage mask (thicker solid blue line) for vertical (a) and horizontal (b) polarizations at 13.75 GHz.

V. CONCLUSION

An accurate analysis technique has been proposed and demonstrated for dual-reflectarray antennas. In the analysis, the sub-reflectarray is divided in groups of elements and the radiation of each group is used to compute the incident and reflected field on each cell of the main reflectarray. The number of groups can be increased to improve the accuracy at the cost of higher computation time. The method of analysis has been validated by designing, manufacturing and testing a limited-size antenna demonstrator with a main reflectarray of 45 cm x 50 cm that provides a contoured beam in dual linear polarization for a DBS European coverage. The measured radiation patterns show a good concordance with the simulations. However, some slight differences in the shape of the beam are observed as consequence of the tolerance errors in the manufacturing process. The antenna provides a cross-polar discrimination higher than 25 dB and a stable performance in the working frequency bandwidth, from 12.975 GHz to 14.25 GHz.

The results obtained with the limited-sized antenna demonstrator shows the capability of the proposed dual-reflectarray configuration to design contoured beam space borne antennas in Ku-band with low levels of cross-polarization. This dual-reflectarray configuration can also be used for multi-spot antennas in Ka-band, since the capability of adjusting the phase distribution simultaneously in both surfaces can be used to design multifocal antennas.

REFERENCES

[1] J. Huang and J. A. Encinar, *Reflectarray Antennas*. IEEE Press, John Wiley, 2008.

[2] D. M Pozar, S. D. Targonski, and R. Pokuls, "A shaped–beam microstrip patch reflectarray," *IEEE Trans. Antennas Propagat.*, vol. 47, no. 7, pp. 1167-1173, 1999.

[3] J. A. Encinar and J. A. Zornoza, "Three-layer printed reflectarrays for contoured beam space applications," *IEEE Trans. Antennas Propagat.*, vol. 52, no. 5, pp. 1138-1148, 2004.

[4] H. Legay, B. Salome, E. Girard, S. Ramongassie, J. A. Encinar, and G. Toso, "Reflectarrays antennas for SAR missions," *Proc. Int. Symp. on Antenna Technology and Applied Electromagnetics*, Saint–Malo, France, June 2005.

[5] J. Huang, "Bandwidth study of microstrip reflectarray and a novel phased reflectarray concept," *IEEE Antennas and Propagation Society Intl. Symp.*, pp. 582-585, June 1995.

[6] D. M. Pozar, "Bandwidth of reflectarrays," *Electr. Lett.*, vol. 39, no. 21, pp. 1490-1491, 2003.

[7] J. A. Encinar, "Design of two-layer printed reflectarrays using patches of variable size," *IEEE Trans. Antennas Propagat.*, vol. 49, no. 10, pp. 1403-1410, 2001.

[8] J. A. Encinar and J. A. Zornoza, "Broadband design of three-layer printed reflectarrays," *IEEE Trans. Antennas Propagat.*, vol. 51, no. 7, pp. 1662-1664, 2003.

[9] M. R. Chaharmir, J. Shaker, M. Cuhaci, and A. Ittipiboon, "A broadband reflectarray antenna with double square rings," *Microw. Opt. Technol. Lett.*, vol. 48, no. 7, pp. 1317-1320, 2006.

[10] E. Carrasco, J. A. Encinar, and M. Barba, "Bandwidth improvement in large reflectarrays by using true–time delay," *IEEE Trans. Antennas Propagat.*, vol. 56, no. 8, pp. 2496-2503, 2008.

[11] H. Legay, D. Bresciani, E. Labiole, R. Chiniard, E. Girard, G. Caille, D. Calas, R. Gillard, and R. Toso, "A 1.3 m facetted reflectarray in Ku band," *15th International Symposium on Antenna Technology and Applied Electromagnetics (ANTEM)*, pp. 1-4, June 2012.

[12] B. Khayatian, Y. Rahmat–Samii, and J. Huang, "Radiation characteristics of reflectarray antennas: methodology and applications to dual configurations," *Proceeding of First European Conference on Antennas and Propagation*, Nice, France, Nov. 2006.

[13] M. Arrebola, L. Haro, and J. A. Encinar, "Analysis of dual–reflector antennas," *IEEE Antennas and Propagation Magazine*, vol. 50, no. 6, pp. 39-51, 2008.

[14] S. Xu, Y. Rahmat–Sami, and W. A. Imbriale, "Subreflectarrays for reflector surface distortion compensation," *IEEE Trans. Antennas Propagat.*, vol. 57, no. 2, pp. 364-372, 2009.

[15] H. Wenfei, M. Arrebola, R. Cahill, J. A. Encinar, V. Fusco, H. S. Gamble, H. Y. Alvarez, and F. Las-Heras, "94 GHz dual-reflector antenna with reflectarray sub-reflector," *IEEE Trans. Antennas Propag.*, vol. 57, no. 10, pp. 3043-3050, 2009.

[16] R. Sorrentino, "MEMS-based reconfigurable reflectarrays," *The Second European Conference on Antennas and Propagation*, Edinburgh, UK, Nov. 2007.

[17] J. Perruisseau-Carrier and A. K. Skriverviky, "Monolithic MEMS-based reflectarray cell digitally reconfigurable over a 360-phase range," *IEEE Antennas and Wireless Propagation Letters*, vol. 7, pp. 138-141, 2008.

[18] E. Carrasco, M. Barba, B. Reig, C. Dieppedale, and J. A. Encinar, "Characterization of a reflectarray gathered element with electronic control using ohmic RF MEMS and patches aperture-coupled to a delay line," *IEEE Trans. Antennas Propagat.*, vol. 60, no. 9, pp. 4190-4201, 2012.

[19] E. Carrasco, M. Barba, and J. A. Encinar, "X-Band reflectarray antenna with switching-beam using PIN diodes and gathered elements," *IEEE Trans. Antennas Propagat.*, vol. 60, no. 12, pp. 5700-5708, 2012.

[20] M. Riel and J. J. Laurin, "Design of an electronically beam scanning reflectarray using aperture–coupled elements," *IEEE Trans. Antennas Propagat.*, vol. 55, no. 5, pp. 1260-1266, 2007.

[21] S. V. Hum, M. Okoniewski, and R. J. Davies, "Realizing an electronically tunable reflectarray using varactor diode–tuned elements," *IEEE Microwave and Wireless Components Letters*, vol. 15, no. 6, pp. 422-424, 2005.

[22] A. Mössinger, R. Marin, S. Mueller, J. Freese, and R. Jakoby, "Electronically reconfigurable reflectarrays with nematic liquid crystals," *IEE Electronics Letters*, vol. 42, pp. 899-900, 2006.

[23] W. Hu, R. Cahill, J. A. Encinar, R. Dickie, H. Gamble, V. Fusco, and N. Grant, "Design and measurement of reconfigurable millimeter wave reflectarray cells with nematic liquid crystal," *IEEE Trans. Antennas Propagat.*, vol. 56, no. 10, pp. 3112-3117, 2008.

[24] G. Perez-Palomino, P. Baine, R. Dickie, M. Bain, J. A. Encinar, R. Cahill, M. Barba, and G. Toso, "Design and experimental validation of liquid crystal-based reconfigurable reflectarray elements with improved bandwidth in F-Band," *IEEE Trans. Antennas Propagat.*, vol. 61, no. 4, pp. 1704-1713, 2013.

[25] C. Tienda, M. Arrebola, J. A. Encinar, and G. Toso, "Analysis of a dual-reflectarray antenna,"

IET Microwave Antennas & Propagation, vol. 5, no. 13, pp. 1636-1645, 2011.

[26] W. Menzel, M. Al-Tikriti, and R. Leberer, "A 76 GHz multiple-beam planar reflector antenna," *European Microw. Conf.*, Milano, Italy, pp. 977-980, Sept. 2002.

[27] H. M. Braun and P. E. Knobloch, "SAR on small satellites-shown on the SAR-Lupe example," *Proceedings of the International Radar Symposium*, Cologne, Germany, Sept. 5-7, 2007.

[28] C. Wan and J. A. Encinar, "Efficient computation of generalized scattering matrix for analyzing multilayered periodic structures," *IEEE Trans. Antennas Propagat.*, vol. 43, no. 10, pp. 233-1242, 1995.

[29] C. Tienda, J. A. Encinar, M. Arrebola, M. Barba, and E. Carrasco, "Design, manufacturing and test of a dual-reflectarray antenna with improved bandwidth and reduced cross-polarization," *IEEE Trans. Antennas Propagat.*, vol. 61, no. 3, pp. 1180-1190, 2012.

[30] J. A. Encinar, L. She Datashvili, J. A. Zornoza, M. Arrebola, M. Sierra-Castaner, J. L. Besada-Sanmartin, H. Baier, and H. Legay, "Dual-polarization dual-coverage reflectarray for space applications," *IEEE Trans. Antennas Propagat.*, vol. 54, no. 10, pp. 2827-2837, 2006.

[31] J. A. Encinar, M. Arrebola, L. F. de la Fuente, and G. Toso, "A transmit–receive reflectarray antenna for direct broadcast satellite applications," *IEEE Trans. Antennas Propagation*, vol. 59, no. 9, pp. 3255-3264, 2011.

[32] J. A. Encinar, M. Arrebola, M. Dejus, and C. Jouve, "Design of a 1-metre reflectarray for DBS application with 15% bandwidth," *First European Conference on Antennas and Propagation, Davos*, Switzerland, pp. 1-5, Nov. 6-10, 2006.

[33] R. Leberer and W. Menzel, "A dual planar reflectarray with sinthesized phase and amplitude distribution," *IEEE Trans. Antennas Propagat.*, vol. 53, no. 11, 2005.

[34] J. A. Zornoza, R. Lebber, J. A. Encinar, and W. Menzel, "Folded multi-layer microstrip reflectarray with shaped pattern," *IEEE Trans. Antennas Propagat.*, vol. 54, pp. 510-518, 2006.

[35] J. E. Hansen, "Spherical near-field antenna measurements," *IEE Electromagnetic Waves Series 26*.

[36] M. Arrebola, Y. Alvarez, J. A. Encinar, and F. Las-Heras, "Accurate analysis of printed reflectarrays considering the near field of the primary feed," *IET Microw., Antennas Propag*., vol. 3, no. 2, pp. 187-194, 2009.

[37] K. Pontoppidan, Technical Description of GRASP8 (TICRA).

[38] O. Bucci, "Intersection approach to array pattern synthesis," *IEE Proceedings*, vol. 137, no. 6, pp. 349-57, 1990.

Carolina Tienda was born in Málaga and she currently resides in Munich, Germany. She received the Telecommunication Engineer degree from the Universidad de Málaga (UMA), Málaga, Spain, in October 2005, and the Tele-communication Ph.D. degree from the Universidad Politecnica de Madrid (UPM), Spain, in March 2012.

From October 2005 to April 2006, she was with the Communications Department, UMA as a Project Assistant. From April 2006 to April 2008, she was working as an RF & Antenna Engineer for INDRA ESPACIO, Madrid, Spain. In May 2008, she joined the Antenna and Sub-Millimeter Wave Section, Electromagnetic Division, European Space Agency ESTEC, The Netherlands, where she worked as Spanish Trainee. From May 2010 to June 2012, Tienda was with the Electromagnetism and Circuits Theory Department at Universidad Politecnica de Madrid (UPM), Spain, as Antenna Researcher. Tienda participated in different research projects supported by the Spanish Government and the European Space Agency (ESA). Since October 2012, she is with the Radar Concepts Department at the German Aerospace Center (DLR). Her current research interests include the analysis and design of space antennas, particularly Digital Beam Forming parabolic reflector antennas and printed reflectarray antennas in single and dual reflectarray configurations.

José A. Encinar (S'81-M'86-SM'09-FM'10) was born in Madrid, Spain. He received the Electrical Engineer and Ph.D. degrees, both from Universidad Politécnica de Madrid (UPM), in 1979 and 1985, respectively. Since January 1980 has been with the Applied Electro-magnetism and Microwaves Group at UPM, as a Teaching and Research Assistant from 1980 to 1982, as an Assistant Professor from 1983 to 1986, and as Associate Professor from 1986 to 1991. From February to October of 1987 he stayed at Polytechnic University, Brooklyn, NY, as a Post-doctoral Fellow of the NATO Science Program. Since 1991 he is a Professor of the Electromagnetism and Circuit Theory Department at UPM. He was with the Laboratory of Electromagnetics and Acoustics at Ecole Polytechnique Fédérale de

Lausanne (EPFL), Switzerland in 1996, and with the Institute of Electronics, Communication and Information Technology (ECIT), Queen's University Belfast, U.K. in 2006 and 2011, as a Visiting Professor. His research interests include numerical techniques for the analysis of multi-layer periodic structures, design of frequency selective surfaces, printed arrays and reflectarrays. Encinar has published more than one hundred and fifty journal and conference papers, and he is holder of five patents on array and reflectarray antennas. He was a co-recipient of the 2005 H. A. Wheeler Applications Prize Paper Award and the 2007 S. A. Schelkunoff Transactions Prize Paper Award, given by IEEE Antennas and Propagation Society. He has been a Member of the Technical Programme Comity of several International Conferences (European Conference on Antennas and Propagation, ESA Antenna Workshops, Loughborough Antennas & Propagation Conference). He is an IEEE Fellow Member.

Mariano Barba was born in Murcia, Spain. He received the Ingeniero de Telecomunicación and Ph.D. degrees from the Universidad Politécnica de Madrid, Madrid (UPM), Spain, in 1990 and 1996, respectively. From 1991 to 1994 he was with the Depto. de Electromagnetismo y Teoría de Circuitos (UPM) as postgraduate researcher. During this time, he developed numerical methods and algorithms to characterize and design microwave passive devices. From 1994 to 2002, he has been involved in the R&D departments of several companies and institutions developing antennas and microwave circuits for space and terrestrial communication applications. In 2002, he joined to the "Depto. de Electromagnetismo y Teoría de Circuitos", (UPM) as Associate Professor. His research interests include the analysis, characterization and design of antenna and microwave circuits. He is currently involved in the development and design of multibeam and reconfigurable antennas.

Manuel Arrebola (S'99-M'07) was born in Lucena (Córdoba), Spain. He received the Ingeniero de Telecomunicación degree from the Universidad de Málaga (UMA), Málaga, Spain, in 2002, and the Ph.D. degree from the Universidad Politécnica de Madrid (UPM), Madrid, Spain, in 2008. From 2003 to 2007 he was with the Electromagnetism and Circuit Theory Department at UPM as a Research Assistant. From August to December 2005, he was with the Microwave Techniques Department at the Universität Ulm, Ulm, Germany, as a Visiting Scholar. In December 2007, he joined the Electrical Engineering Department at the Universidad de Oviedo, Gijón, Spain, where he is an Associate Professor. In 2009, he enjoyed a two-month stay at the European Space Research and Technology Centre, European Space Agency (ESTE-ESA), Noordwijk, The Netherlands. His current research interests include analysis and design techniques of contoured-beam and reconfigurable printed reflectarrays both in single and dual-reflector configurations and planar antennas. Arrebola was co-recipient of the 2007 S. A. Schelkunoff Transactions Prize Paper Award, given by IEEE Antennas and Propagation Society.

Out-of-Core Solver Based DDM for Solving Large Airborne Array

Yan Yan Li, Xun Wang Zhao, and Huan Huan Zhang

School of Electronic Engineering
Xidian University, Xi'an, Shaanxi 710071, China
liyanyan0418@126.com, xdzxw@126.com, zhanghuanajkd@outlook.com

Abstract ─ In this paper, we present a new methodology for an overlapping domain decomposition by using higher-order MoM and out-of-core solver (HO-OC-DDM) for analyzing large electromagnetic (EM) problems. This paper proposes two main novelties. First, the required number of meshes is decreased with the application of new higher-order basis function in the discretization of integral equation (IE). As a consequence, the number of unknowns for large EM problems can be reduced. Second, a parallel out-of-core solver is presented in this paper, which can accelerate the matrix filling and solving process without loss of accuracy. The out-of-core solver breaks the limitation of computer RAM and can be efficiently implemented in domain decomposition method (DDM).

Index Terms ─ Domain decomposition method, higher-order MoM, integral equation, out-of-core.

I. INTRODUCTION

The computer simulation has emerged as a powerful and indispensable tool in engineering design and analysis. Integral equations (IE) method, only the discretization of the surface of the object and with high accuracy, has been widely used for analyzing EM problems [1]. However, it will result in a large and dense matrix for the analysis of electrically large problems. Considering that we are interested in studying airborne antenna radiation on a large platform, such as an aircraft. The electromagnetic radiation and scattering from both the antennas and the platform need to be simulated accurately. Such an EMC problem is extremely challenging and is possibly beyond the capabilities of any conventional numerical methods. Domain decomposition method (DDM) could be an effective way to solve the EM properties from electrically large problem [2]. Combining the method of integral equations with DDM should enable some problems that we faced to be solved.

The DDM have been commonly applied in finite elements, finite difference and integral equations methods [3-6]. Among them, the domain decomposition method based on integral equations for the solution of electromagnetic radiation and scattering problems has proved its ability in solving complex EM problems, but the scale of the problem is small, which cannot satisfy the demand for solving electrically large problem, such as airborne array. In addition, the introduction of fast algorithm would further bring into error, reducing the accuracy and iterative convergence speed. Reference [7] discussed the multiple existing CEM solvers DDM, which employ diffident techniques for each of the subdomains, such as MoM and FEM. This method has been successfully used to model multiple antennas on a large air platform. However, the CPU time and storage for each subdomain are very large when simulating an even large problem or the frequency is enhanced.

A new solution scheme based on overlapping domain decomposition method, higher-order MoM and parallel out-of-core solver, called as HO-OC-DDM, is proposed in this paper. The greatest advantage of the out-of-core solver [8] is that during the evaluation of the matrix elements and its solution through the LU decomposition, the original matrix is decomposed into a set of smaller matrices fitted in-core. This technique extends the capability of MoM to solve problems, which can be as large as the amount of storage on the hard disk. For HO-OC-DDM, the simulation model is divided into several parts and out-of-core MoM is employed for each part. Moreover, higher-order basis functions are used to approximate the current distribution [8-9], which produce fewer unknowns than lower-order basis functions and further increase the scale of the problem to be solved. This method provides unprecedented flexibility and convenience for the object with changeable parts, since it just needs to re-compute the changed portion of the model during the design process, such as the analysis of antenna distribution on airborne system.

The rest of this paper is organized as follows. In Section II, the algorithm of DDM, higher-order basis function and out-of-core scheme is presented. Section III provides numerical examples to demonstrate the correctness and robustness of the proposed method.

Submitted On: March 22, 2016
Accepted On: May 3, 2016

Finally, some conclusions are given in Section IV.

II. FORMULATION

A. Domain decomposition method

The 3D EM scattering or radiation problem of an arbitrarily shaped object can be modeled with surface integral equations (SIE) [10]. The surface of the object is discretized into many quadrangle patches, and then the integral equation can be represented by a matrix equation using high order basis functions, which will be discussed in the next section. The matrix equation is as follows:

$$\mathbf{ZI} = \mathbf{V}, \tag{1}$$

where the coefficient matrix Z is an $M \times M$ square matrix, I is the unknown current coefficient vector and V is the vector of excitation.

As shown in Fig. 1, the entire problem is divided into n subdomains Ω_i (i=1,2…n), each subdomain is extended with its buffer regions as $\tilde{\Omega}_i = \Omega_i + \Omega_{Fi} + \Omega_{Bi}$, the dot line in Fig. 1, Ω_{Fi} and Ω_{Bi} are the forward and backward buffer regions. Ω_i denotes as the ith subdomain. The matrix Equation (1) can be expressed as:

$$\begin{bmatrix} \mathbf{Z}_{11} & \mathbf{Z}_{12} & \cdots & \mathbf{Z}_{1n} \\ \mathbf{Z}_{21} & \mathbf{Z}_{22} & \cdots & \mathbf{Z}_{2n} \\ \vdots & \vdots & & \vdots \\ \mathbf{Z}_{n1} & \mathbf{Z}_{n2} & \cdots & \mathbf{Z}_{nn} \end{bmatrix} \begin{bmatrix} \mathbf{I}_1 \\ \mathbf{I}_2 \\ \vdots \\ \mathbf{I}_n \end{bmatrix} = \begin{bmatrix} \mathbf{V}_1 \\ \mathbf{V}_2 \\ \vdots \\ \mathbf{V}_n \end{bmatrix}, \tag{2}$$

where Z_{ij} (i=j) is the self-impedance matrix in Ω_i, Z_{ij} (i≠j) is the mutual impedance matrix between Ω_j and Ω_i, I_i is the current coefficient vector in Ω_i and V_i is the excitation vector in Ω_i.

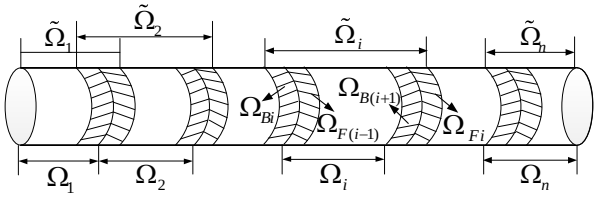

Fig. 1. Notations for domain decomposition.

The excitation in the computational subdomain includes both the information of incident plane wave and the coupling from the other subdomains, which can be calculated using the newly restricted currents after discarding the currents in bilateral buffer regions. Thus, the current edge effects in both sides are depressed and then the convergence is accelerated [11].

As all of the subdomains are extended with the buffer regions, the Gauss-Seidel iterative procedure should be modified here. Initialize the number of iteration k=0, the currents in all subdomains $I_i^{(0)}$=0 (i=1, 2,…,n) and the error limitation δ. Set k=1, 2 …, the iterative scheme inform of matrix equation can be expressed as:

$$\tilde{\mathbf{I}}_i^{(k)} = -\tilde{\mathbf{Z}}_{ii}^{-1} \sum_{j<i} \tilde{\mathbf{Z}}_{ij} \mathbf{I}_j^{(k)} - \tilde{\mathbf{Z}}_{ii}^{-1} \sum_{j>i} \tilde{\mathbf{Z}}_{ij} \mathbf{I}_j^{(k-1)} + \tilde{\mathbf{Z}}_{ii}^{-1} \tilde{\mathbf{V}}_i, \tag{3}$$

where $\tilde{\mathbf{Z}}_{ii}$ is the self-impedance matrix in $\tilde{\Omega}_i$, $\tilde{\mathbf{Z}}_{ij}$ is the mutual impedance matrix between Ω_j (discard the overlap region) and $\tilde{\Omega}_i$, $\tilde{\mathbf{I}}_i^{(k)}$ is the vector of current coefficients in $\tilde{\Omega}_i$ to be solved during the kth iteration, $\mathbf{I}_j^{(k)}$ is the vector of current coefficients in Ω_j (discard the overlap region) at the kth iteration, $\tilde{\mathbf{V}}_i$ is the excitation vector in $\tilde{\Omega}_i$.

The relative residual error at kth iteration is used for expressing the convergence behaviour of the iterative method, which is defined as:

$$error(k) = \max\left\{ \left\| \mathbf{I}_i^{(k)} - \mathbf{I}_i^{(k-1)} \right\| \Big/ \left\| \mathbf{I}_i^{(k)} \right\| \right\} \ (i = 1, 2, \ldots, n). \tag{4}$$

The iteration will not stop until the error (k) ≤ δ.

Noting that the mutual impedance in Equation (3) is actually unnecessary to be stored during the procedure, the coupling voltage can be obtained using the near field produced by the current. The inverse of self-impendence for each subdomain is computed using the parallel and out-of-core LU decomposition algorithm and will be reused. In this way, the computing procedure can be largely accelerated.

B. High-order MoM and out-of-core solver

The object under consideration is firstly decomposed into several subdomains. Because antennas usually contain metallic and dielectric materials, the integral equation employed is the PMCHW formulation [10]. Both electric and magnetic currents are used for electromagnetic modeling of dielectric components. The geometric modeling is achieved by using bilinear quadrilateral patches to characterize, as shown in Fig. 2. Efficient approximation for the unknown currents is obtained by using higher-order basis functions (5):

$$\mathbf{F}_{ij}(p,s) = \frac{\boldsymbol{\alpha}_s}{\left| \boldsymbol{\alpha}_p \times \boldsymbol{\alpha}_s \right|} \, p^i s^j, -1 \le p \le 1, -1 \le s \le 1, \tag{5}$$

where p and s are the local coordinates, i and j are the orders of basis functions, and $\boldsymbol{\alpha}_p$ and $\boldsymbol{\alpha}_s$ are covariant unitary vectors. The polynomials can also be used as the basis functions for wire structures. In this case, truncated cones are used for geometric modeling [9].

The capacity of the RAM available for our high performance cluster is 8700 GB, which can support a double-precision complex matrix of order at most 764098, which is too small for electrically large problems. However, it is noticed that the total hard disk storages available are about 200TB. If the disk storage can be used instead of RAM, the scale of problem that can be solved will largely increase. The main feature of out-of-core algorithm is the original full matrix is decomposed into a set of smaller matrices that can be

fitted in-core. The (double-precision complex) matrix with M rows and columns requires $N_{\text{storage}} = M \times M \times 16$ bytes of hard-disk storage. The computer system has M_{RAM} bytes of in-core buffer available to each process. To complete the decomposition of the matrix, each process will handle a specific number of portions I_{slab}:

$$I_{\text{slab}} = ceiling\left\{\frac{N_{\text{storage}}}{pM_{\text{RAM}}}\right\}, \tag{6}$$

where p is the total number of processes, and the *ceiling* function returns the smallest integer greater than or equal to the number.

milestone

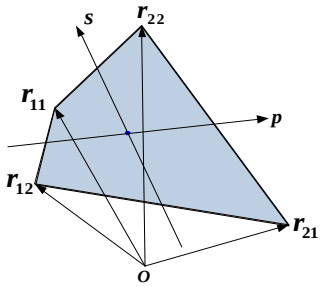

Fig. 2. Bilinear quadrilateral patch defined by four vertices with $\boldsymbol{r}_{11}$, $\boldsymbol{r}_{12}$, $\boldsymbol{r}_{21}$ and $\boldsymbol{r}_{22}$.

Setting the decomposition is oriented along the column, as shown in Fig. 3, one slab consisting of M rows of the matrix by the number of columns that will fit in the total amount of the in-core buffer available.

The width of ith out-of-core slab is K_i, thus:

$$M = \sum_{i=1}^{I_{\text{slab}}} K_i. \tag{7}$$

The width of last slab (i=I_{slab}) K_{last} is:

$$K_{last} = M - \sum_{i=1}^{I_{\text{slab}}-1} K_i. \tag{8}$$

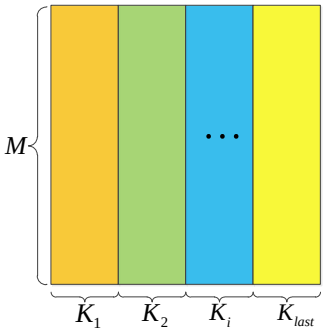

Fig. 3. Data decomposition for storing an out-of-core matrix.

The assignment to fill each slab is distributed over p processes by using the block distribution scheme of ScaLAPACK or PLAPACK [8]. It is important that the matrix filling schemes should be designed to avoid redundant calculation for better parallel efficiency. For the out-of-core LU factorization, the one-slab left-looking out-of-core algorithm is applied and the right-looking in-core algorithm is used when factoring each slab. Thus, the advantages of both the left-looking and the right-looking algorithms are retained. The detail of parallel out-of-core algorithm for MoM can be found in [9].

The flowchart of the HO-OC-DDM is shown in Fig. 4.

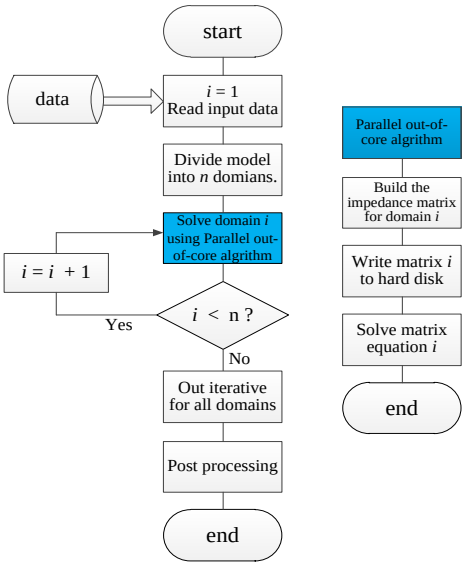

Fig. 4. Flowchart of HO-OC-DDM.

III. NUMERICAL RESULTS

Three EM examples are presented to demonstrate the efficiency and accuracy of the proposed method. The residual error for outer iterative convergence is set to 3.0e–3 without any specification. Two computational platforms are used in this paper.

Platform I: A workstation with two six-core 64 bit Intel Xeon E5-2620 2.0 GHz CPUs, 64 GB RAM and 6TB disk.

Platform II: High-Performance Computing (HPC) cluster with 136 computing nodes. Each computing node has two 12-core bit Intel Xeon E5-2692 2.2 GHz CPUs, 64 GB RAM and 1.8TB disk.

A. An umbrella microstrip array with 30×1 elements

To validate the accuracy and efficiency of the proposed HO-OC-DDM for discontinuous problems, an umbrella microstrip array with 30×1 elements of umbrella microstrip patch is simulated. As shown in Fig. 5, the dielectric substrate of the antenna is 0.8 mm in thickness and ε_r=10.2. The array is divided into two equal sized sub-domains and the overlap part is unnecessary for the subdomains are discontinuous in geometry.

The simulation is performed on Platform I, and the operating frequency is 2.5 GHz. The two-dimensional

(2D) radiation patterns obtained by the proposed HO-OC-DDM are shown in Fig. 6. The patterns of overall solution using high-order MoM and the MoM from FEKO software are also given for comparison. The number of unknowns of the microstrip array is 24330 for higher-order MoM and 60115 for MoM (FEKO). To compare out-of-core performance of the proposed method with MoM (FEKO) in the same number of unknowns, an umbrella microstrip array with 25×3 elements is simulated using MoM (HO-OC). It can be seen that the results agree with each other very well. For the HO-OC-DDM, the computer memory is reduced by a half (see Table 1), the CPU time is not sharply reduced when simulating a small problem. For the overall solution of microstrip array with 30×1 elements, MoM (HO-OC) costs 625s and MoM (FEKO) costs 16571s. For the microstrip array with 25×3 elements, which has the same number of unknowns with MoM (FEKO), the CPU time of MoM (HO-OC) is 11554s.

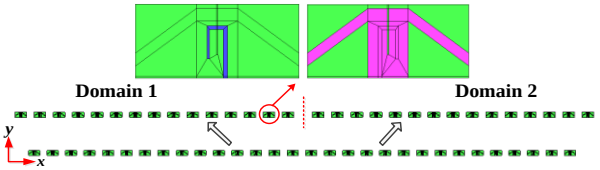

Fig. 5. Model of umbrella microstrip array with 30×1 elements.

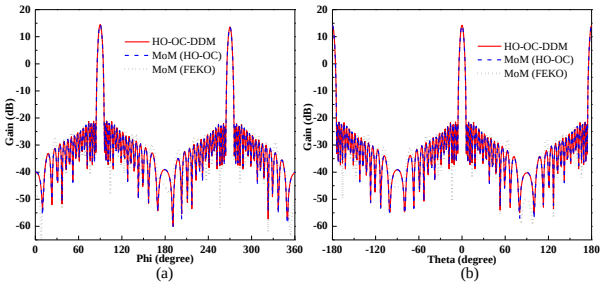

Fig. 6. 2D radiation patterns of the umbrella microstrip array: (a) x-y and (b) x-z.

Table 1: Computational statistics of umbrella microstrip array

Method	Unknowns	Storage (GB)	CPU Time(s)
DDM	12165(domain 1)	4.41	720
	12165(domain 2)		
MoM (HO-OC)	24330(30×1)	8.82	967
	60825(25×3)	55.13	11554
MoM (FEKO)	60115(30×1)	53.85	16571

B. A rectangle microstrip array with 20×4 elements

Consider a rectangle patch microstrip array with 20×4 elements as shown in Fig. 7. The units are connected with each other. The thickness of dielectric substrate is 0.018 m and ε_r=4.5, the operating frequency is 440 MHz, the dimension of antenna is 5.27 m × 0.95 m. The model is divided into two overlapping subdomains (extending two units into each other) in this example.

The simulation is performed on Platform I. The radiation patterns of the antenna array obtained by HO-OC-DDM and the overall solution by higher-order MoM are shown in Fig. 8. They are in good agreement with each other. The computational statistics for solving each subdomain and entire problem are recorded in Table 2. It can be observed that the HO-OC-DDM leads to over 25% memory reduction compared with the overall solution for this example.

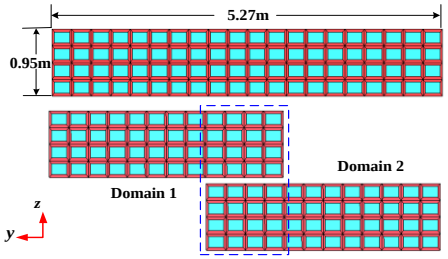

Fig. 7. Model of rectangle microstrip array with 20×4 elements.

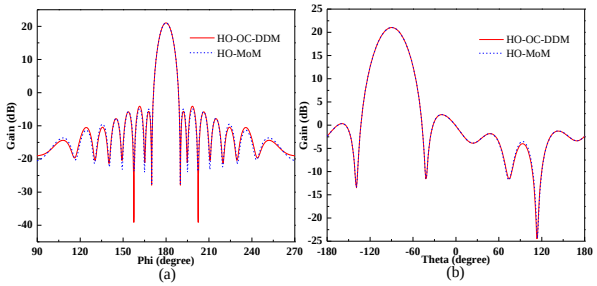

Fig. 8. 2D radiation patterns of the rectangle microstrip array: (a) x-y and (b) x-z.

Table 2: Computational statistics of rectangle microstrip array

Method	Unknowns	Storage (GB)	CPU Time(s)
DDM	12000(domain 1)	4.28	951
	12000(domain2)		
MoM	19840	5.86	1080

C. Radiation of a dipole array above a PEC cylinder

The radiation of a dipole array above a PEC cylinder is simulated in this example to discuss the effect of the size of buffer region. As shown in Fig. 9, the radius and length of cylinder is 1.5 m and 18 m. The working frequency is 1.0 GHz. The dipole antenna is located

above the cylinder and the direction of feeder is +x. As shown in Fig. 9, the model is divided into four subdomains. The antenna represents domain 1, and each color of the cylinder represents the rest three subdomains. Three different sizes of buffer region, 0.5λ, 1λ and 1.5λ, is considered during the simulation.

The simulation is performed on Platform I. The 2D radiation pattern of the object obtained by HO-OC-DDM is shown in Fig. 10 and the overall solution by MoM is also given for comparing. Compared with 0.5λ buffer region, the results of 1λ and 1.5λ buffer region are in good agreement with that of the overall solution. The computational statistics for solving each subdomain are accorded in Table 3. As shown in Fig. 10, the accuracy is good enough in engineer application when the size of the buffer region increase to 1λ.

The memory and CPU time are increasing while the size of buffer region is enlarging. The root mean square error (RMSE) of radiation for different size of buffer region is defined as $RMSE = \sqrt{\frac{\left\| Gain^{DDM} - Gain^{MoM} \right\|_2^2}{n}}$, where $Gain^{DDM}$ is the gain vector obtained by the proposed method and $Gain^{MoM}$ is the overall solution vector obtained by high-order MoM. When size of buffer regions are 0.5λ, 1λ and 1.5λ, the RMSE of the proposed method is 0.1193, 0.0871 and 0.0892 respectively. Considering the simulation accuracy and computation resources, the buffer region with 1λ size is acceptable in this method.

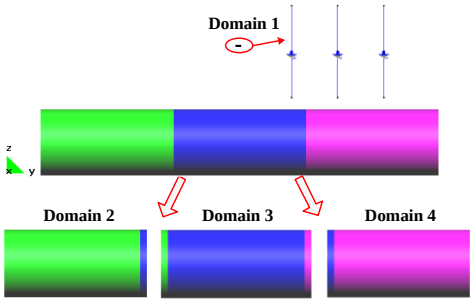

Fig. 9. Model of a dipole array above a PEC cylinder.

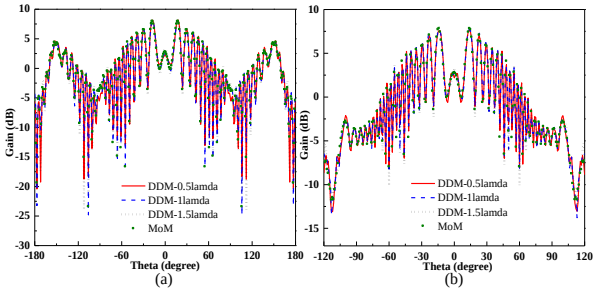

Fig. 10. 2D radiation patterns of the dipole antenna above a cylinder: (a) x-z and (b) y-z.

Table 3: Computational statistics of rectangle microstrip array

Method	Buffer Region	Unknowns	Storage (GB)	CPU Time(s)
DDM	0.5λ	9	16.41	1680
		18704		
		19824		
		18928		
	1λ	9	17.73	1750
		19152		
		20944		
		19600		
	1.5λ	9	19.67	2100
		20048		
		22512		
		20272		
MoM	19840	53657	42.9	5674

D. Radiation of phased airborne array with 55×15 elements

The accuracy of the proposed method has been proved in the above two examples. An electrically large problem for engineering application will be solved in this example. Consider a 55×15 microstrip patch array mounted on an airplane, as illustrated in Fig. 11. The antenna array is arranged on x-z plane. The dimensions of patch are 0.144 m × 0.072 m × 0.00072 m, and the distance between two neighboring elements is 0.1225 m along both the length and width directions. The working frequency of the array is 2.0 GHz. The array is installed 5.0 m above an airplane that is 36 m long, 40.0 m wide and 10.5 m high, and the distance between the center of the array and the nose of the airplane is 17.8 m.

A −40 dB Taylor distribution is utilized in the array feed along the *x*-direction and −25 dB along the *z*-direction, the mainlobe is directed towards the tail and sweeps 5° and 10° toward the wing. The number of unknowns of the airborne array is 1,569,836, which is too large for the computing resource available. However, the problem can be solved by the HO-OC-DDM. In this example, we divide the model into eight sub-domains as shown in Fig. 12. Each color represents a subdomain respectively. The simulation is performed on Platform II and 720 CPU cores are used.

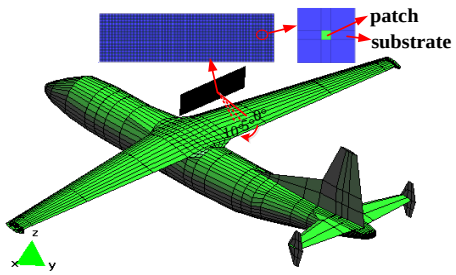

Fig. 11. Model of airborne antenna array.

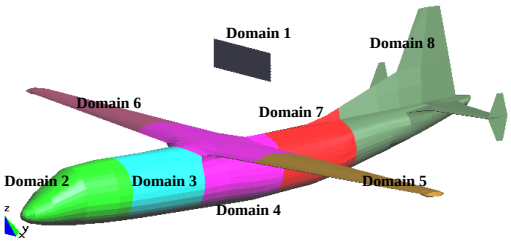

Fig. 12. Domain decomposition model (each color represents a sub-domain).

The phased shift patterns of antenna array before and after it is mounted on the airplane are computed by the proposed HO-OC-DDM as shown in Fig. 13 and Fig. 14. The sidelobe level of the airborne array increases in the azimuth plane. Furthermore, there is a decrease in the maximum gain compared with that of the array, as shown in Fig. 13. The deterioration of the patterns is most serious when the mainlobe is directed towards the tail. In Table 4, a comparison of the computational statistics between the HO-OC-DDM and MoM is shown. It is worth noting that the overall CPU time include two parts, subdomains solution time and iteration time. In the solution time, the computing time for platform is 3.52h and the iteration time is only 0.66h. For the phased airborne array, the platform subdomains (domain 2-8) are unchanged and can be reused during the solution. Thus, the memory requirement and CPU time are greatly reduced. The proposed method is of great significance especially for the solution of very large problems in engineering application

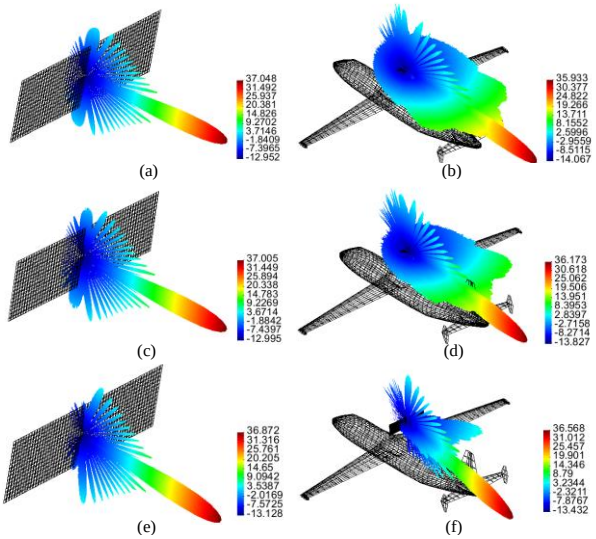

Fig. 13. 3D radiation patterns of phased airborne array: (a) the array with scan 0°, (b) the array over the airplane with scan 0°, (c) the array with scan 5°, (d) the array over the airplane with scan 5°, (e) the array with scan 10°, and (f) yhe array over the airplane with scan 10°.

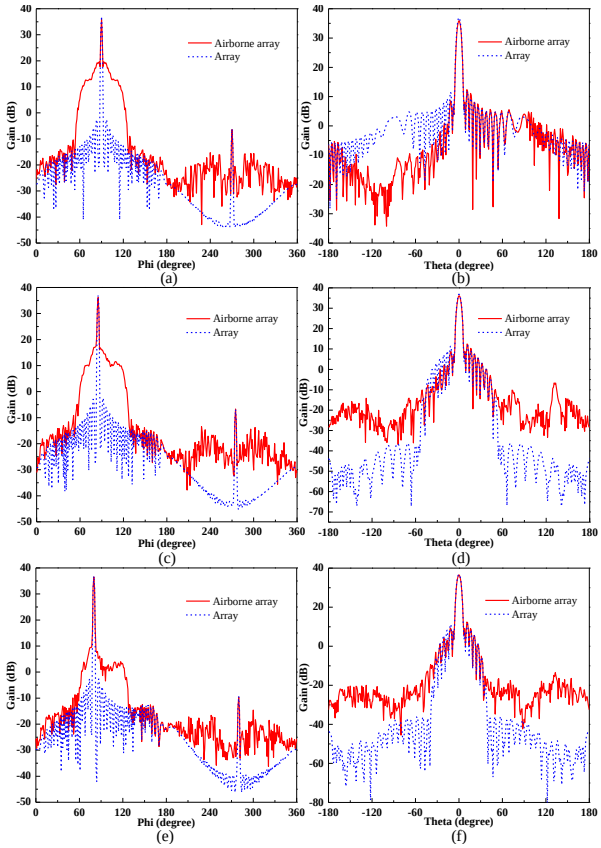

Fig. 14. 2D radiation patterns of phased airborne array: (a) azimuth plane pattern with scan 0°, (b) elevation plane pattern with scan 0°, (c) azimuth plane pattern with scan 5°, (d) elevation plane pattern with scan 5°, (e) azimuth plane pattern with scan 10°, and (f) elevation plane pattern with scan 10°.

Table 4: Computational statistics of airborne array

Method	Unknowns	Storage (TB)	CPU Time (h)
DDM	305408(1)	1.36	3.05 (1)
	96524(2)	0.14	
	95073(3)	0.13	
	212711(4)	0.66	3.52 (2-8)
	102207(5)	0.16	
	102753(6)	0.16	
	97261(7)	0.14	
	247282(8)	0.89	17.23 (total)
MoM	1569836	35.86	— —

IV. CONCLUSION

An efficient HO-OC-DDM algorithm is developed to solve large complex problem such as airborne array. Particularly, our emphasis herein is the combination of out-of-core technology, higher order MoM and domain decomposition method, which allows the matrices for each domain to be written in the hard disk, extending the capacity of MoM based domain decomposition methods.

Moreover, the proposed method is also suitable for solving the problems with changeable parts.

ACKNOWLEDGMENT

This work is supported by the National High Technology Research and Development Program of China (863 Program) (2012AA01A308), the program for New Century Excellent Talents in University of China (NCET-13-0949), the NSFC (61301069), the Fundamental Research Funds for the Central Universities (JB160218).

REFERENCES

[1] R. F. Harrington, *Field Computations by Moment Methods*. Macmillan, New York, 1968.

[2] L. Yin, J. Wang, and W. Hong, "A novel algorithm based on the domain-decomposition method for the full-wave analysis of 3D electromagnetic problems," *IEEE Trans. Microw. Theory Tech.*, vol. 50, no. 8, pp. 2011-2017, 2002.

[3] Z. Lou and J. M. Jin, "A novel dual-field time-domain finite-element domain-decomposition method for computational electromagnetics," *IEEE Trans. Antennas Propagat.*, vol. 54, no. 6, pp. 1850-1862, 2006.

[4] Z. H. Lai, J. F. Kiang, and R. Mittra, "A domain decomposition finite difference time domain (FDTD) method for scattering problem from very large rough surfaces," *IEEE Trans. Antennas Propagat.*, vol. 63, no. 10, pp. 4468-4476, 2015.

[5] W. D. Li, W. Hong, and H. X. Zhou, "Integral equation-based overlapped domain decomposition method for the analysis of electromagnetic scattering of 3D conducting objects," *Microwave and Optical Technology Letters*, vol. 49, no. 2, pp. 265-274, 2007.

[6] S. M. Rao, "A true domain decomposition procedure based on method of moments to handle electrically large bodies," *IEEE Trans. Antennas Propagat*., vol. 60, no. 9, pp. 4233-4238, 2012.

[7] X. C. Wang, Z. Peng, and J. F. Lee, "Multisolver domain decomposition method for modeling EMC effects of multiple antennas on a large air platform," *IEEE Trans. Electromagn. Compat*., vol. 54, no. 2, pp. 375-388, 2012.

[8] Y. Zhang, R. A. van ce Geijn, M. C. Taylor, and T. K. Sarkar, "Parallel MoM using higher order basis function and PLAPACK in-core and out-of-core solvers for challenging EM simulations," *IEEE Antennas Propagat. Magazine*, vol. 51, no. 5, pp. 42-60, 2009.

[9] Y. Zhang and T. K. Sarkar, *Parallel Solution of Integral Equation Based EM Problems in the Frequency Domain. Hoboken*, Hoboken NJ, USA: Wiley, 2009.

[10] G. Mumcu, K. Sertel, and J. Volakis, "Surface integral equation solution for modeling 3-D uniaxial media using closed-Form dyadic Green's functions," *IEEE Trans. Antennas Propagat.*, vol. 56, no.8, pp. 2381-2388, 2008.

[11] W. D. Li, W. Hong, and H. X. Zhou, "An IE-ODDM-MLFMA scheme with DILU preconditioner for analysis of electromagnetic scattering from large complex objects," *IEEE Trans. Antennas Propagat.*, vol. 56, no. 5, pp. 1368-1380, 2008.

Li Yanyan received the B.S. degree from Xinzhou Teacher's University, Shanxi, China, in 2012, and is currently working toward the Ph.D. degree at Xidian University. Her current research interests is computational electromagnetic.

Xunwang Zhao received the B.S., and Ph.D. degrees from Xidian University, Xi'an, China, in 2004, and 2008, respectively. He joined Xidian University as a Faculty Member in 2008. As Principal Investigator, he is doing or has completed some projects including project of NSFC.

Huan Huan Zhang received the Bachelor degree in Electronic Information Engineering from Henan Polytechnic University in 2009, the Ph.D. degree in Electromagnetic Fields and Microwave Technology from Nanjing University of Science and Technology in 2015. He was a Post-doctoral Fellow with the Center of Electromagnetics and Optics, the University of Hong Kong, Hong Kong, from 2015 to 2016. He is currently a Lecturer with the School of Electronic Engineering, Xidian University, Xi'an, China.

Zhang serves as the Reviewer of the IEEE Trans-actions on Antenna and Propagation, Communications in Computational Physics, IET Radar, Sonar & Navigation, etc. His current research interests include computational electromagnetics, IC signal and power integrity, EMC/ EMI and radar signal processing.

Comparison Between Genetic and Particle Swarm Optimization Algorithms in Optimizing Ships' Degaussing Coil Currents

S. Mahmoudnezhad Makouie and A. Ghorbani

Department of Electrical Engineering
Amirkabir University of Technology, Tehran, Iran
sina.mm@aut.ac.ir, a.ghorbani@aut.ac.ir

Abstract ─ This paper presents a comparison between two well-known evolutionary algorithms in optimization of the degaussing coils currents of a ship which are used to reduce the magnetic anomalies of the ferromagnetic hull of the ships induced by the Earth's magnetic field. To achieve this, first the magnetic anomalies of a simple model of a ship and the effect of each degaussing coil are simulated by using 3D finite element analysis (FEA) software. Then, both genetic algorithm and particle swarm optimization are used to find the best fitting coil currents which can reduce the anomalies of the ship. Using these algorithms is much simpler than optimizing this problem in FEA software in which a huge amount of numerical analyses are needed. This comparison will show which of these algorithms works better in this specific problem.

Index Terms ─ Degaussing system, ferromagnetic material, genetic algorithm, magnetic anomaly, magnetization, particle swarm optimization.

I. INTRODUCTION

When iron ships are exposed to the Earth's magnetic field, magnetic regions of the ferromagnetic iron are aligned in the direction of the external field. This process, which is called Magnetization, produces some magnetic anomalies in their environment, which are named as induced component. Besides, due to the magnetic history of the iron, another component of magnetization is generated which is called remnant magnetization. For ships, it is vital to reduce these anomalies as least as possible for safety against magnetic mines and torpedoes.

Determination of the remnant component needs some measurement data and is discussed in some references like [1]. It is almost impossible to calculate this component with software because the magnetic history of the ferromagnetic material is unknown and all works are done based on measurements. On the other hand, induced component can be simulated by software and there is no need for measurements. The common point of these two magnetization components is that the countermeasure methods against them are somehow similar. Degaussing and deperming both use some coils in order to produce the same anomalies of the ship but exactly in the reverse direction in order to reduce the total magnetic anomalies.

This paper will focus on the induced magnetization and optimization of the degaussing coil currents. First, the magnetic signature of a ship is analyzed with FEA software and then the effects of each degaussing coil are simulated considering the hull effect of the ship. The hull effect is some kind of shielding effect that causes some changes in the generated filed of each coil which comes from additional magnetization of the hull induced by the coil currents [2, 3].

Because the optimization of the degaussing currents with software is a three dimensional inverse problem, it will need a huge amount of numerical analyses which will be very time consuming. In [2-4] it is proposed to do these optimizations separately with taking the linearity of the system into account. In this case, instead of solving problem for a large volume, a measurement line in a specific depth beneath the ship is considered as a region of the solution and the aim of the optimization is the reduction of the total field on this line as least as possible. This method is so effective which can reduce the time of the optimizations in a considerable way.

Although this method is very effective, it can be improved by some changes in the optimization process. Each of references has optimized this problem with a different algorithm and it seems that a comparison among optimization algorithms is necessary. In this paper, this comparison will be done between two well-known genetic algorithm and particle swarm optimization methods. These algorithms are stochastic search methods and their results could be somehow fortuitous. In order to omit this effect, ten tests for each algorithm are done and the results are presented in average form. Finally, the best results of each algorithm are compared to identify which algorithm could be more effective in degaussing problem.

Submitted On: January 8, 2015
Accepted On: November 7, 2015

II. MAGNETIC SIGNATURE OF THE SHIP

Based on the directions of the ship and the Earth's magnetic field, three general magnetic signatures are introduced; induced longitudinal magnetization (ILM), induced vertical magnetization (IVM) and induced athwartship magnetization (IAM) [5, 6]. Any other arbitrary field can be expressed in the form of these three modes which are shown in Fig. 1. The dimensions of the ship are about 130×20×17 m with 3-4 cm thickness. The magnitude of the Earth's magnetic field is supposed to be 55000 nT and the relative permeability of the hull is assumed to be 80. Simulations of the magnetic signatures were done through FEA software by a computer with an Intel Core i7-2640M @ 2.8 GHz and the results are shown in Fig. 2. The fields are measured over a hypothetical line in the depth of 10 m exactly under the keel of the ship and with the length of 400 m. The results of the whole simulations have been obtained in the range of 0-400 m, but for increasing the resolution of the figures and clarifying the differences of their curves only the 200 m middle part of the measurement line is represented in the figures. The values in hidden parts (0-100 m and 300-400 m) in all figures are close to zero.

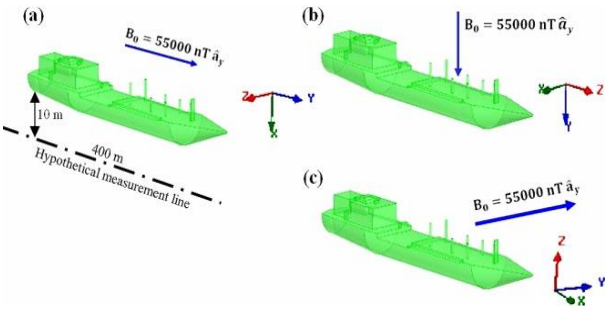

Fig. 1. Three general signatures: (a) ILM, (b) IVM, and (c) IAM.

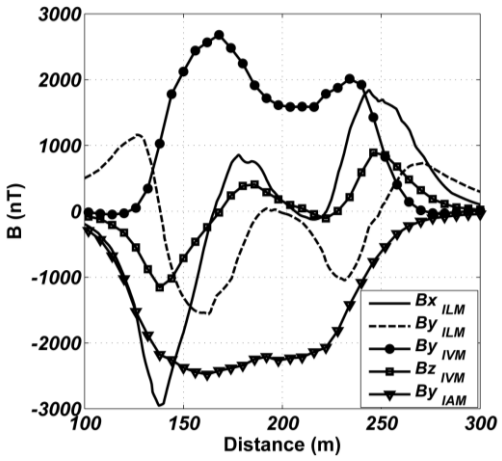

Fig. 2. Magnetic signature of the ship in three modes.

III. DEGAUSSING SYSTEM

For cancelation of magnetic signature, ships are equipped with three types of coils which are named as L-coils, V-coils and A-coils. These coils are designed to cancel longitudinal, vertical and athwartship signatures of the ships, respectively [7]. The degaussing system which is used in this paper is shown in Fig. 3. In this system 20 L-coils with approximate dimension of 11×6 m, 20 V-coils with approximate dimension of 11×6 m and 10 A-coils with approximate dimension of 12×5 m are designed. In Fig. 3, it is obvious that some coils are smaller and the above-mentioned dimensions are related to the big ones.

For achieving the effects of each coil, simulations are done by exciting single coil with a reference current of 1 KA while other coils having no current. It took approximately 35 minute to obtain FEA solution for only one coil. In Fig. 4 the fields of A-coils are shown. The magnetic fields of these coils have no x or z component on the measurement line and it is due to the symmetry of these fields according to the assumed measurement line.

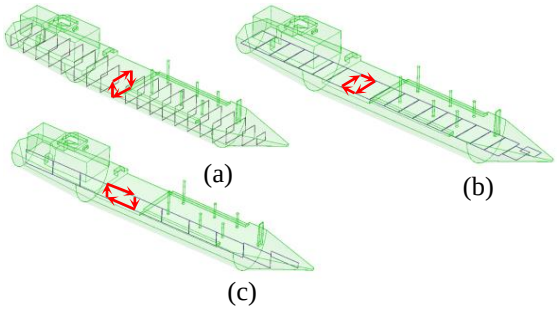

Fig. 3. Degaussing coils: (a) L-coils, (b) V-coils, and (c) A-coils.

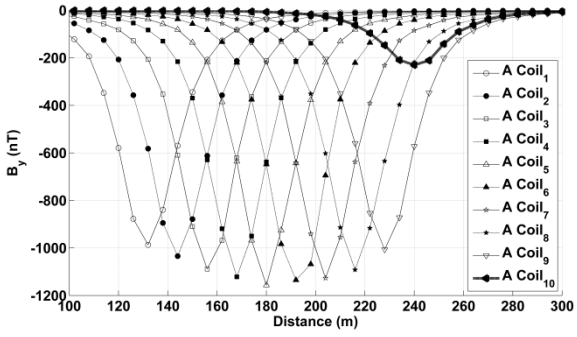

Fig. 4. Magnetic fields produced by A-coils.

The generated magnetic fields of L-coils and V-coils have two components (for L-coils: B_x and B_y; and for V-coils: B_y and B_z) which results in a total number of eighty curves for these forty coils. The results of these coils are somehow similar to Fig. 4, and to avoid repetition are not shown here.

IV. OPTIMIZATION ALGORITHMS

A. Particle swarm optimization

The PSO is inspired by the social behaviour of a flock of migrating birds trying to reach an unknown destination. In PSO, each solution is a 'bird' in the flock and is referred to as a 'particle' [8]. The strategy and exact formulation of this algorithm is explained in details in [9, 10]. Here a brief review on its process is presented. In this algorithm first a random population of particles is generated and the cost value for each particle is calculated. Then the best cost value is saved as global best answer and the cost value of each particle is saved as personal best answer. After that, particles start to move in search space and the position and the velocity of each particle is determined based on the global and personal best values in every iteration. The algorithm continues until the global cost value reaches to the desired limit or until last iteration. The general formulation of PSO is represented as follow [8]:

$$\begin{cases} X_i = (x_{i1}, x_{i2}, \dots, x_{is}) & current\ position\ of particle\ i \\ P_i = (p_{i1}, p_{i2}, \dots, p_{is}) & best\ pervious\ position \\ V_i = (v_{i1}, v_{i2}, \dots, v_{is}) & flying\ velocity \end{cases}$$

$$New\ V_i = w \times current\ V_i + c_1 \times rand(.) \times (P_i - X_i) + c_2 \times rand(.) \times (P_g - X_i), \quad (1)$$

$$New\ X_i = X_i + New\ V_i, \quad (2)$$

$$-V_{max} \le V_i \le V_{max}. \quad (3)$$

In these equations S is the number of variables, w is an inertia weight, c_1 and c_2 are two positive constants named learning factors and V_{max} is an upper limit on the maximum change of the velocity of a particle.

In Table 1 the parameters of PSO which are used in this paper are shown. In compensation of ILM and IVM signatures, each signature has two components (as shown in Fig. 2; for ILM: B_x and B_y and for IVM: B_y and B_z) and the optimizations are done on both components simultaneously, therefore, in these modes bigger iteration number is chosen.

Table 1: Parameters of the particle swarm optimization

Name	Value
Population size	200
Iteration	500 for ILM and IVM 200 for IAM
c_1, c_2	2
V_{max}	2
Initial range	[−2,0] for IAM and IVM [0,2] for ILM

B. Genetic algorithm

Genetic algorithm is inspired by biological systems' improved fitness through evolution. A solution to a given problem is represented in the form of a string, called 'chromosome', consisting of a set of elements, called 'genes', that hold a set of values for the optimization variables [8]. This algorithm works based on a random population of solutions (chromosomes) and then the fitness value (cost) of each chromosome is evaluated in cost function. In the next iterations chromosomes exchange information with each other in the form of crossover and mutation and offspring chromosomes are generated. After that, the best chromosomes are saved for the next iterations and the weak members of the population are omitted. More explanation about GA could be found in [11, 12]. The specified parameters of GA which are used in optimization of the degaussing coil currents are shown in Table 2.

Table 2: Parameters of the genetic algorithm

Name	Value
Population size	200
Iteration	500 for ILM and IVM 200 for IAM
Crossover rate	75%
Mutation rate	5%
Initial range	[−2,0] for IAM and IVM [0,2] for ILM

V. IMPLEMENTATION OF THE OPTIMIZATIONS

The magnetic signatures of the ship and the generated fields of the degaussing coils are achieved in section two and section three, respectively. Now the optimizations could be done by determining cost function as follow:

$$F = \min\left(\max\left(\sum_{i=1}^{n}\sum_{j=1}^{p}\left|B_j^{xship} - c_i B_j^{x,Li}\right|, \sum_{i=1}^{n}\sum_{j=1}^{p}\left|B_j^{yship} - c_i B_j^{y,Li}\right|, \sum_{i=1}^{n}\sum_{j=1}^{p}\left|B_j^{zship} - c_i B_j^{z,Li}\right|\right)\right), \quad (4)$$

where $i = 1,2,\dots,n$ are the number of coil, $j = 1,2,\dots,p$ are the number of measurement points (sensors), B_j^{xship} is the x component of the signature of the ship and $B_j^{x,Li}$ is the x component of the generated filed of the i-th coil in the j-th sensor. It should be noted that the $c_i = c_1, c_2, \dots, c_n$ are the coefficients which are the answers of the optimization. Finally these coefficients will be multiplied by the reference current (or mmf) to find the value of the coils currents.

Due to the fortuitous natures of the GA and PSO, comparing these algorithms in a specific problem through only one test could not be correct and it is necessary to

compare the performance of theses algorithms during multiple tests. The only parameter that varies in these tests is the starting point of the algorithms. Both algorithms use a random function to choose the starting point (initial answer of the problem) but in some cases one of the algorithms starts with an answer very close to the optimum answer. In situations like this, the algorithm which has started with a worse point may have a better performance than the other algorithm but this better performance is not clear when comparing the final answers. Therefore, ten tests for each algorithm have been done for each type of signature which leads to the total number of sixty tests. In the next parts, the best result of each algorithm for ILM, IVM and IAM will be compared and after that a final comparison between average performances will be done.

A. Induced longitudinal magnetization

As mentioned before, the ILM signature of the model ship (according to the coordinate system and the position of the measurement line) has two components of x and y which are shown in Fig. 2. Just like the signature of the ship, L-coils generate magnetic field in these two directions and they could compensate the signature of the ship in this case. The calculated current value of each L-coil is depicted in Fig. 5 and the best results from ten tests are shown in Fig. 6. It should be noted that the signature of the ship in Fig. 6 is reversed. The exact value of remnant field after degaussing, its percentage and the optimization time are shown in Table 3.

Although the running time of GA is 3.5% more than PSO's, the best result of GA is 3.75% and 7.16% more accurate in x and y directions respectively in comparison with the best result of PSO. Finally, the cost value in each iteration is shown in Fig. 7. It is obvious that after first iterations, GA has lower cost in comparison with PSO for the same number of iterations.

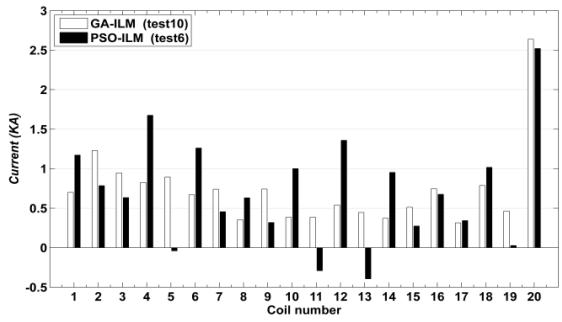

Fig. 5. Current values of the L-coils.

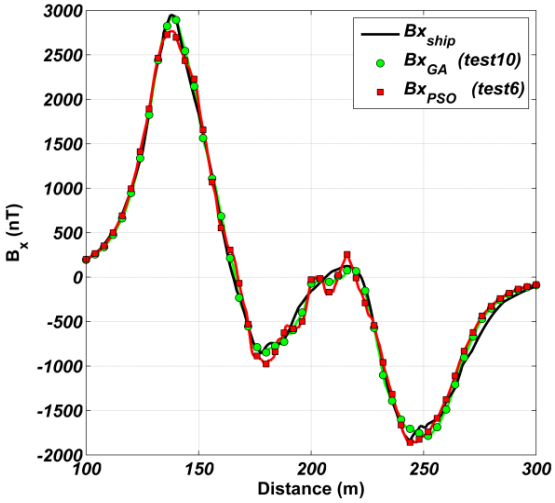

(a)

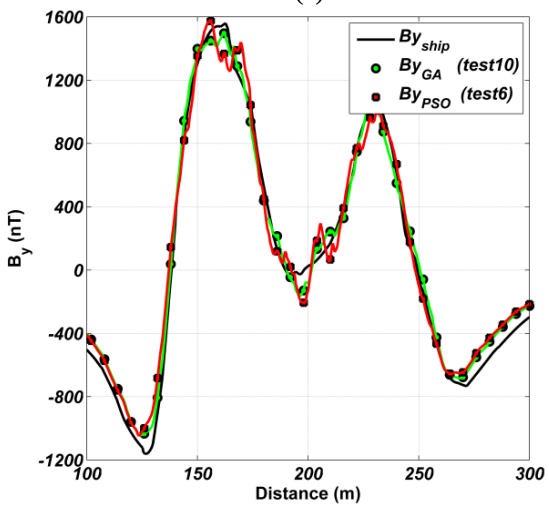

(b)

Fig. 6. Degaussing result for L-coils in comparison with the ILM signature of the ship (reversed): (a) Bx and (b) By.

Table 3: Optimization result of the ILM signature

Name (Best Results)	ILM-GA (Test 10)	ILM-PSO (Test 6)
Best cost -x direction (nT)	140.30	250.79
Best cost -y direction (nT)	139.39	251.07
Remnant field after degaussing -x direction (%)	4.75	8.50
Remnant field after degaussing -y direction (%)	8.94	16.10
Run time(s)	144.9	140.0

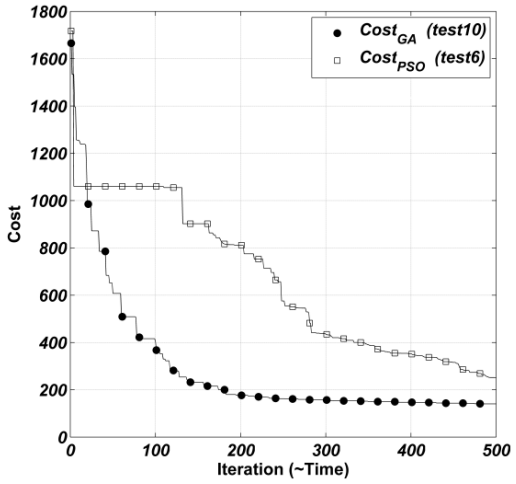

Fig. 7. Comparison of the convergence speed in ILM.

B. Induced vertical magnetization

The IVM signature of the model ship has two components of y and z which are shown in Fig. 2. Just like the signature of the ship, V-coils generate magnetic field in these two directions and they could compensate the signature of the ship in IVM mode. The best results from ten tests are shown in Fig. 8 and the current value of each V-coil is depicted in Fig. 9.

Remnant field after degaussing, its percentage and the optimization time are presented in Table 4. Just like the ILM mode, although the running time of GA is 7.76% more than PSO's, the best result of GA is 2.56% and 5.83% more accurate in y and z directions respectively in comparison with the best result of PSO. Finally, the cost value in each iteration is shown in Fig. 10. It is obvious that after first iterations, the GA has lower cost in compared with PSO for the same number of iterations.

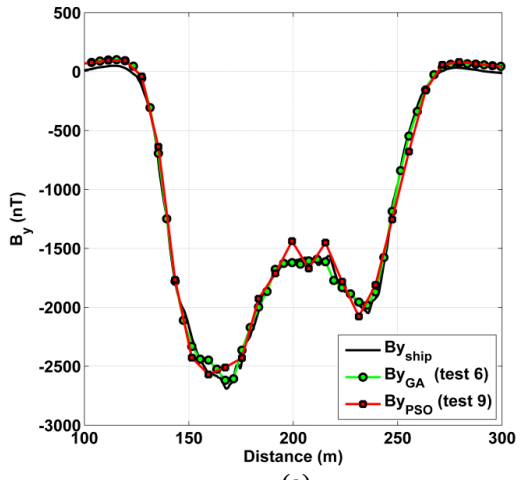

(a)

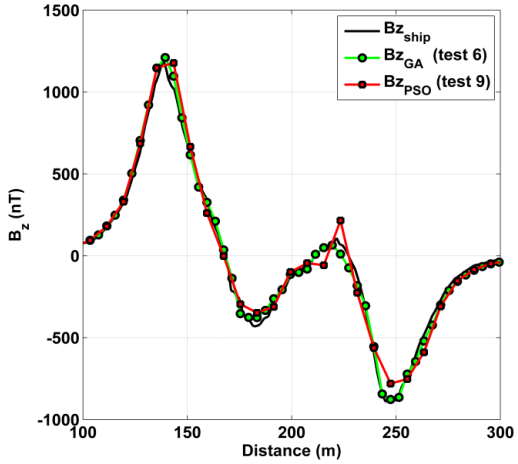

(b)

Fig. 8. Degaussing result for V-coils in comparison with the IVM signature of the ship (reversed): (a) By and (b) Bz.

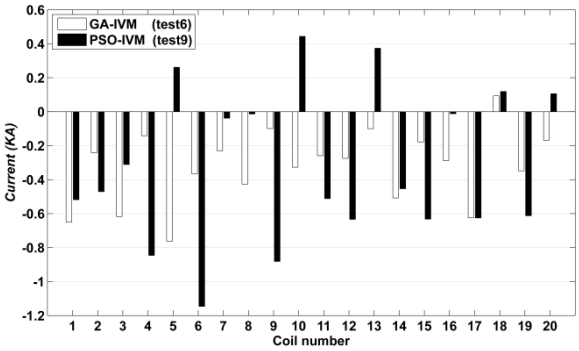

Fig. 9. Current values of the V-coils.

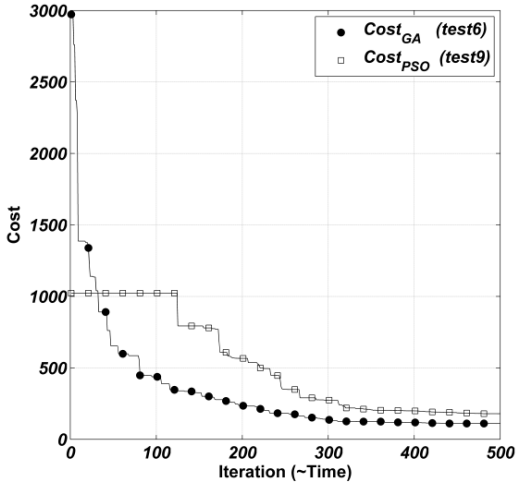

Fig. 10. Comparison of the convergence speed in IVM.

Table 4: Optimization result of the IVM signature

Name (Best Results)	IVM-GA (Test 6)	IVM-PSO (Test 9)
Best cost -y direction (nT)	110.06	178.90
Best cost -z direction (nT)	109.43	178.95
Remnant field after degaussing -y direction (%)	4.08	6.64
Remnant field after degaussing -z direction (%)	9.18	15.01
Run time(s)	145.8	135.3

C. Induced athwartical magnetization

The IAM signature has only one component, y, which is shown in Fig. 2. Just like the signature of the ship, A-coils generate magnetic field in this direction and they could compensate the signature of the ship. The best results from ten tests are shown in Fig. 11 and the current value of each A-coil is depicted in Fig. 12. The exact value of remnant field after degaussing, its percentage and the optimization time are shown in Table 5. Finally, for investigating the convergence speed of algorithms, the cost value in each iteration is shown in Fig. 13. The running time of GA is 8.47% more than the PSO's but the result of PSO is 0.05% more accurate in comparison with the best result of GA.

It is obvious that after first iterations, GA has lower cost in comparison with PSO for the same number of iterations. Although the final result of PSO in IAM mode is more accurate in comparison with GA (only 0.05%), Fig. 13 shows the better performance of GA. The better result of PSO in this specific case is a good sample of the fortuitous natures of these algorithms and reveals that comparing the performance of these algorithms through only one simple test is not logical.

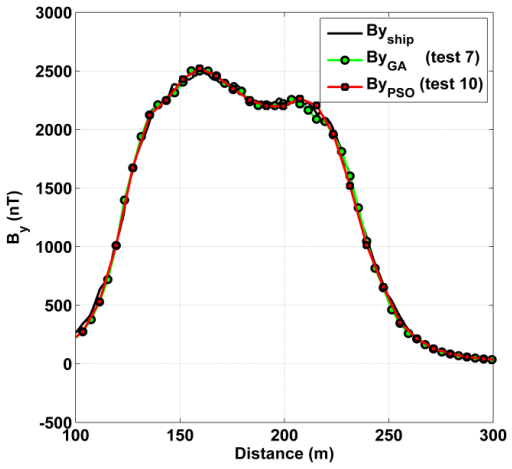

Fig. 11. Degaussing result for A-coils in comparison with the IAM signature of the ship (reversed).

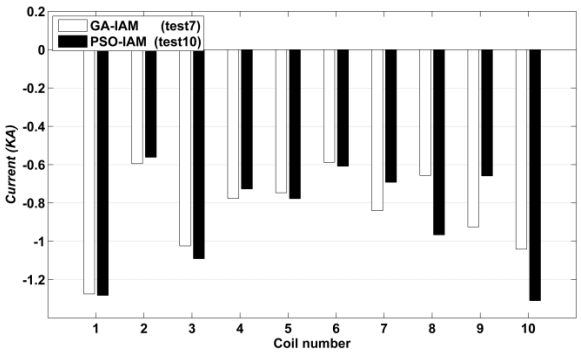

Fig. 12. Current values of the A-coils.

Table 5: Optimization result of the IAM signature

Name (Best Results)	IAM-GA (Test 7)	IAM-PSO (Test 10)
Best cost -y direction (nT)	97.93	96.66
Remnant field after degaussing -y direction (%)	3.87	3.82
Run time(s)	25.6	23.6

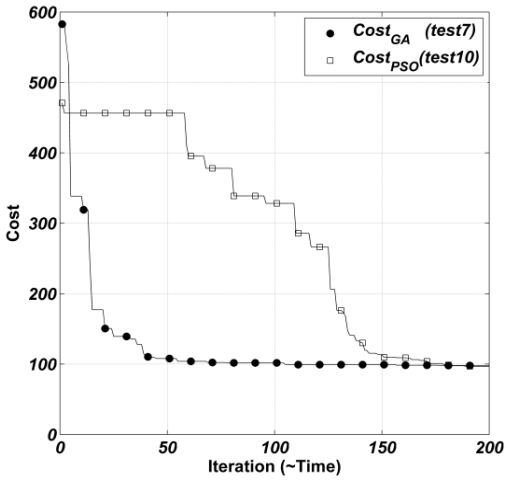

Fig. 13. Comparison of the convergence speed in IAM.

In Fig. 14 the results of the simulation of the degaussed ship are depicted. In this figure, the signature of the ship before and after degaussing process is compared for both PSO and GA optimizations. All coils are excited with the values of the electric currents represented in Fig. 9. To avoid the repetition of the figures only the results of IVM mode is represented. The maximum remnant fields after degaussing in PSO for y and z components are 252.3 and 174.4 nT respectively. By comparing these values with the ones reported in Table 4 (178.9 for y and 178.95 for z), it is revealed that the final results have 2.73% and 0.38% error for y and z components respectively (the difference between results

are normalized based on the maximum values of the signatures that are 2688 nT and 1189 nT for y and z components respectively). These errors for GA optimizations are about 0.27% and 1.87%. The errors are small and tolerable, but the important point here is that these errors have two main sources. The mutual inductances between coils and the approximations which are used in any numerical simulations are the important factors that could easily affect the final results. Typically the distance between two adjacent coils is long enough to decrease their mutual inductance, and as a result in almost all references the mutual inductance is assumed as a negligible parameter.

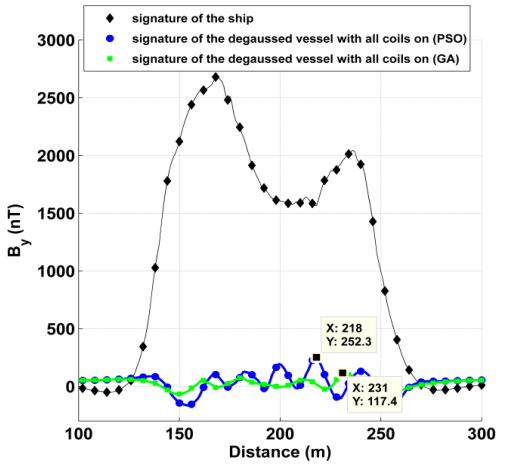

(a)

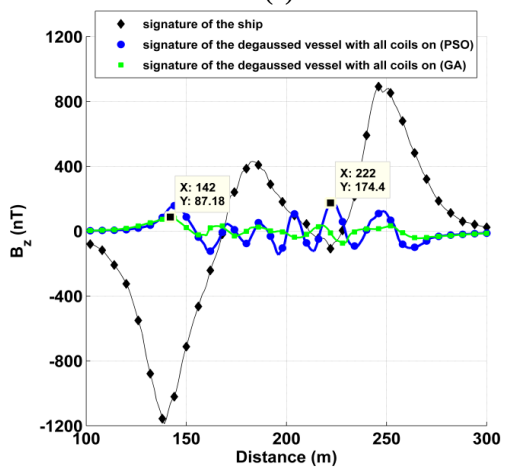

(b)

Fig. 14. Simulation of the degaussed ship in the IVM mode (V-coils are excited with the values of the electric currents represented in Fig. 9): (a) By and (b) Bz.

D. Average results

Table 6 shows the average results of ten tests for all optimizations which are done for three ILM, IVM and IAM signatures. The average results reveal that the GA has better performance in comparison with PSO. However, it has more running time. This means that by tolerating a little bit increase in running time (in order of few seconds) the final result could be improved. Since the running time of the optimizations is not so long, it seems rational to use GA instead of PSO. It should be noted that both of these algorithms have been improved since their first development and the algorithms which are used in this paper are the base form of the optimization techniques.

Table 6: Average results of the optimizations

Average Results	Cost in 1st Direction (nT)	Cost in 2nd Direction (nT)	Remnant Field in 1st Direction (%)	Remnant Field in 2nd Direction (%)	Run Time (s)
ILM-GA	184.33	183.82	6.24	11.79	144.33
ILM-PSO	268.88	268.48	9.72	18.37	139.44
IVM-GA	175.65	175.79	14.73	6.52	147.61
IVM-PSO	252.73	253.02	21.19	9.39	136.5
IAM-GA	103.76	-	4.10	-	25.6
IAM-PSO	126.67	-	5.00	-	23.4

VI. CONCLUSION

In this paper a comparison between genetic algorithm and particle swarm optimization in optimization of the degaussing currents is done. PSO has a reputation of being fast and easy to apply, but it is important to study the performance of these algorithms in this specific problem. In the case of the degaussing system, it seems that using GA is more beneficial in comparison with PSO. The main reason for this difference is that PSO could be easily trapped in local minimums. In PSO, the movement of the particles is strongly related to their local and global best positions. As a result if the algorithm finds a local minimum in the search space, the particles will move toward this point which will result a trap condition. This condition for GA is less possible. In GA due to the nature of crossover and mutation, it is always possible for the algorithm to find a solution away from the local answers. On the other hand, GA takes more time to run but considering the running time, this difference will be in the order of few seconds.

REFERENCES

[1] K. J. Lee, G. Jeung, C.-S. Yang, H.-J. Chung, J. G. Park, H.-G. Kim, et al., "Implementation of material sensitivity analysis for determining unknown remanent magnetization of a ferromagnetic thin shell," *IEEE Trans. Magnetics*, vol. 45, pp. 1478-1481, 2009.

[2] N.-S. Choi, G. Jeung, C.-S. Yang, H.-J. Chung, and D.-H. Kim, "Optimization of degaussing coil

currents for magnetic silencing of a ship taking the ferromagnetic hull effect into account," *IEEE Trans. Applied Superconductivity*, vol. 22, 2012.
[3] N.-S. Choi, G. Jeung, S. S. Jung, C.-S. Yang, H.-J. Chung, and D.-H. Kim, "Efficient methodology for optimizing degaussing coil currents in ships utilizing magnetomotive force sensitivity information," *IEEE Trans. Magnetics*, vol. 48, pp. 419-422, 2012.
[4] H. Liu and Z. Ma, "Optimization of vessel degaussing system based on poly-population particle swarm algorithm," *ICMA. Int. Mechatronics and Automation Conf.*, Harbin, HL, pp. 3133-3137, August 2007.
[5] J. J. Holmes, *Exploitation of a Ship's Magnetic Field Signatures*, *Synthesis Lectures on Computational Electromagnetics*, Morgan & Claypool Publishers, San Rafael, Calif., 2006.
[6] J. J. Holmes, *Modeling a Ship's Ferromagnetic Signatures*, *Synthesis Lectures on Computational Electromagnetics*, Morgan & Claypool Publishers, San Rafael, Calif., 2007.
[7] J. J. Holmes, *Reduction of a Ship's Magnetic Field Signatures*, *Synthesis Lectures on Computational Electromagnetics*, Morgan & Claypool Publishers, San Rafael, Calif., 2008.
[8] E. Elbeltagi, T. Hegazy, and D. Grierson, "Comparison among five evolutionary-based optimization algorithms," *Advanced Engineering Informatics*, vol. 19, pp. 43-53, 2005.
[9] M. Clerc, *Particle Swarm Optimization*, John Wiley & Sons, 2010.
[10] A. Lazinica, *Particle Swarm Optimization*, InTech, Kirchengasse, 2009.
[11] S. Sivanandam and S. Deepa, *Genetic Algorithm Optimization Problems*, Springer, Berlin Heidelberg, 2008.
[12] R. L. Haupt and D. H. Werner, *Genetic Algorithms in Electromagnetics*, John Wiley & Sons, 2007.

Sina Mahmoudnezhad Makouie was born in 1989 in Tabriz, Iran. He received his B.Sc. and M.Sc. degrees in Electrical Engineering (Communication Engineering) from University of Tabriz, East Azerbaijan and AmirKabir University of Technology, Tehran, Iran, in 2011 and 2015 respectively. He is currently a Ph.D. candidate at AmirKabir University of Technology, Tehran, Iran. His research interests include Electromagnetic anomalies, Degaussing systems and evolutionary optimization algorithms.

Ayaz Ghorbani received Post-graduate Diploma, M.Phil. and Ph.D. degrees in Electrical and Communication Engineering as well as Postdoctoral degree from the University of Bradford, UK, in 1984, 1985, 1987 and 2004, respectively. Since 1987 up to now, he has been teaching various courses in the Department of Electrical Engineering, AmirKabir University of Technology (Tehran Polytechnic), Tehran, Iran. Also from 2004 to 2005, he was with Bradford University for sabbatical leave. He has authored or co-authored more than 160 papers in various national and international conferences as well as refereed journals. In 1987 Ghorbani received the John Robertshaw Travel Award to visit the USA. In 1990, he received the URSI Young Scientists Award at the General Assembly of URSI, Prague, Czech Republic. He also received the Seventh and Tenth Kharazmi International Festival Prize in 1993 and 1995 for designing and implementation of anti-echo chamber and microwave subsystems, respectively. His research areas include Radio wave propagation, antennas bandwidth, nonlinear modeling of HPA, anti-echo chambers modeling and design, electromagnetic shielding as well as EMI/EMC analysis and modeling. He has authored two books in Microwave Circuit and Devices and Radar Systems, respectively.

A Split-Step Pade Solution of 3D-PE Method for EM Scattering from PEC Targets

Z. He and R. S. Chen

Department of Communication Engineering
Nanjing University of Science and Technology, Nanjing, 210094, China
eerschen@njust.edu.cn

Abstract ─ In this paper, the split-step Pade scheme is introduced to solve the three dimensional parabolic equation for EM scattering problems. By implementing the finite differential method, the calculation can be taken from plane to plane along the paraxial direction and a sparse-matrix equation needs to be solved in each transverse plane. In this way, the computational resources can be saved significantly when compared with the rigorous numerical methods. Numerical results demonstrate that the proposed method can obtain accurate results at wider angles up to 45°.

Index Terms ─ Electromagnetic scattering, parabolic equation method, split-step Pade.

I. INTRODUCTION

The parabolic equation (PE) method has been used as an efficient tool to analyze the EM scattering problems for a few decades [1-5]. The parabolic equation is an approximation of the wave equation and it is traditionally computed with first order Taylor expansion. By using the finite differential method (FD), the parabolic equation can be solved plane by plane along the paraxial direction. In other words, a three dimensional problem can be converted into a series of two dimensional problems to be solved by the standard parabolic equation (SPE) method. Therefore, less computational resources are needed for the SPE method than the rigorous numerical methods [6-8], such as the method of moments (MoM), the finite-difference time-domain (FDTD), and the finite element method (FEM). However, the standard PE method is a narrow-angle approximation which can only get accurate bistatic RCS results at angles within 15° of the paraxial direction.

Several kinds of high-order approximations have been introduced to the parabolic equation for wider angle bistatic computation [9-15]. These high-order approximations are based on higher order Pade approximations of a composition of the exponential or square-root functions. Both the Pade(1,1) and the Claerbout approximations were applied to the parabolic equation, which can obtain accurate results at angles within 25° of the paraxial direction for the analysis of three dimensional EM wave propagation [9]. In [10-11], the Pade(2,1) and Pade(2,2) approximations are accurate at angles even more than 40° of the paraxial direction. However, both the difference accuracy and the computation efficiency will become low with the order of Pade approximation increasing. Therefore, more efficient approximations should be developed. By using the split-step Pade scheme, a high order Pade approximation can be split as a summation of several lower order Pade approximations [12-15]. As a result, both the computational accuracy and efficiency can be guaranteed. The split-step Pade scheme was firstly introduced to solve the Helmholtz equation for propagation within optical fibers by Feit and Fleck [15]. Then more work about the split-step Pade based parabolic equation has been done by Collins and Thomson [12-14]. However, all of these works are focus on two-dimension scalar parabolic equation for EM propagating problems.

In this paper, the split-step Pade scheme is introduced to the three dimensional vector parabolic equations for the analysis of EM scattering problems. Accurate bistatic RCS results can be obtained at wider angles up to 45° of the paraxial direction. The inhomogeneous boundary conditions are added on the surface of the scattering target in each transverse plane. Moreover, the perfect matching layers (PML) are used to truncate the computational region. The rotating PE method is also used to obtain the full bistatic RCS curves.

The remainder of this paper is organized as follows. In Section 2, the theory and the formulations are given. Three numerical experiments are presented in Section 3 to show the accuracy and efficiency of the proposed

Submitted On: October 17, 2015
Accepted On: May 1, 2016

method. Section 4 concludes this paper.

II. THEORY AND FORMULATIONS

A. Standard parabolic equation method

Suppose that a PEC object in free space is illuminated by a plane wave. The scattered field components E_x^s, E_y^s, E_z^s can be solved with the scalar wave equation:

$$\begin{aligned}
&\frac{\partial^2 E_x^s}{\partial x^2}+\frac{\partial^2 E_x^s}{\partial y^2}+\frac{\partial^2 E_x^s}{\partial z^2}+k^2 E_x^s=0\\
&\frac{\partial^2 E_y^s}{\partial x^2}+\frac{\partial^2 E_y^s}{\partial y^2}+\frac{\partial^2 E_y^s}{\partial z^2}+k^2 E_y^s=0\\
&\frac{\partial^2 E_z^s}{\partial x^2}+\frac{\partial^2 E_z^s}{\partial y^2}+\frac{\partial^2 E_z^s}{\partial z^2}+k^2 E_z^s=0
\end{aligned} \tag{1}$$

where k is the wave number.

When the paraxial direction of the parabolic equation is chosen as the x axis, the reduced scattered fields u_x^s, u_y^s, u_z^s can be defined as:

$$\begin{aligned}
u_x^s(x,y,z)&=e^{-ikx}E_x^s(x,y,z)\\
u_y^s(x,y,z)&=e^{-ikx}E_y^s(x,y,z)\\
u_z^s(x,y,z)&=e^{-ikx}E_z^s(x,y,z)
\end{aligned} \tag{2}$$

Substitute Equation (2) into Equation (1), the following equations are obtained:

$$\begin{aligned}
&\frac{\partial^2 u_x^s}{\partial x^2}+2ik\frac{\partial u_x^s}{\partial x}+\frac{\partial^2 u_x^s}{\partial y^2}+\frac{\partial^2 u_x^s}{\partial z^2}=0\\
&\frac{\partial^2 u_y^s}{\partial x^2}+2ik\frac{\partial u_y^s}{\partial x}+\frac{\partial^2 u_y^s}{\partial y^2}+\frac{\partial^2 u_y^s}{\partial z^2}=0\\
&\frac{\partial^2 u_z^s}{\partial x^2}+2ik\frac{\partial u_z^s}{\partial x}+\frac{\partial^2 u_z^s}{\partial y^2}+\frac{\partial^2 u_z^s}{\partial z^2}=0
\end{aligned} \tag{3}$$

After the factorization, we can get the forward parabolic equations:

$$\begin{aligned}
\frac{\partial u_x^s}{\partial x}&=-ik(1-\sqrt{Q})u_x^s\\
\frac{\partial u_y^s}{\partial x}&=-ik(1-\sqrt{Q})u_y^s\\
\frac{\partial u_z^s}{\partial x}&=-ik(1-\sqrt{Q})u_z^s
\end{aligned} \tag{4}$$

where the pseudo-differential operator Q is defined as

$$Q=\frac{1}{k^2}\left(\frac{\partial^2}{\partial y^2}+\frac{\partial^2}{\partial z^2}\right)+n^2.$$

Then the solution of Equation (4) can be written as:

$$\begin{aligned}
u_x^s(x+\Delta x,y,z)&=e^{ik\Delta x(\sqrt{Q}-1)}u_x^s(x,y,z)\\
u_y^s(x+\Delta x,y,z)&=e^{ik\Delta x(\sqrt{Q}-1)}u_y^s(x,y,z)\\
u_z^s(x+\Delta x,y,z)&=e^{ik\Delta x(\sqrt{Q}-1)}u_z^s(x,y,z)
\end{aligned} \tag{5}$$

As shown in Fig. 1, the unknowns in the $(x+\Delta x)th$ transverse plane can be calculated from those at $x\ th$ transverse plane. The calculation starts before the scattering target and ends beyond it. Moreover, the perfectly matched layer (PML) is applied to truncate the computational domain in each transverse plane. Finally, the radar cross section (RCS) results are calculated with the reduced scattered fields in the last transverse plane by near-far field conversion.

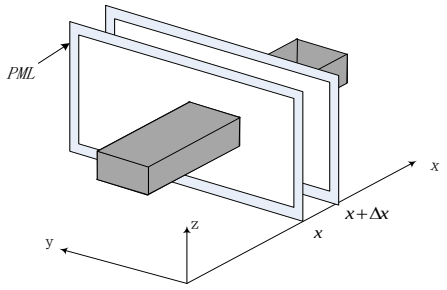

Fig. 1. The calculation process of the PE method.

B. Split-step Pade solution of parabolic equation

We substitute a rational approximation for the exponential operator:

$$e^{ik\Delta x(\sqrt{Q}-1)}=1+\sum_{l=1}^{N}\frac{a_l Q}{1+b_l Q}. \tag{6}$$

Suppose $N=2$ in Equation (6), we can rewrite the parabolic equation as:

$$\begin{aligned}
u_x^s(x+\Delta x,y,z)&=u_x^s(x,y,z)+\\
&\frac{a_1 Q}{1+b_1 Q}u_x^s(x,y,z)+\frac{a_2 Q}{1+b_2 Q}u_x^s(x,y,z)\\
u_y^s(x+\Delta x,y,z)&=u_y^s(x,y,z)+\\
&\frac{a_1 Q}{1+b_1 Q}u_y^s(x,y,z)+\frac{a_2 Q}{1+b_2 Q}u_y^s(x,y,z)\\
u_z^s(x+\Delta x,y,z)&=u_z^s(x,y,z)+\\
&\frac{a_1 Q}{1+b_1 Q}u_z^s(x,y,z)+\frac{a_2 Q}{1+b_2 Q}u_z^s(x,y,z)
\end{aligned}, \tag{7}$$

where the coefficients are [11-12]:

$$\begin{aligned}
a_1&=0.008664+0.1710i\\
b_1&=0.4929-0.1435i\\
a_2&=-0.008664+0.1431i\\
b_2&=-0.04016-0.1409i
\end{aligned}. \tag{8}$$

Define

$$\begin{aligned}
v_{l,x}^s(x+\Delta x,y,z)&=\frac{a_l Q}{1+b_l Q}u_x^s(x,y,z)\\
v_{l,y}^s(x+\Delta x,y,z)&=\frac{a_l Q}{1+b_l Q}u_y^s(x,y,z).\\
v_{l,z}^s(x+\Delta x,y,z)&=\frac{a_l Q}{1+b_l Q}u_z^s(x,y,z)\\
&\qquad l=1,2
\end{aligned} \tag{9}$$

It can be seen that the parabolic equation can be solved by solving $v_{1,\xi}^s(x+\Delta x,y,z)$ and $v_{2,\xi}^s(x+\Delta x,y,z)$

separately, where $\xi = x, y, z$. Then the split-step based parabolic equations can be written as follows:

$$\begin{aligned}
&\left[1+b_l\left(\frac{1}{k^2}\left(\frac{\partial^2}{\partial y^2}+\frac{\partial^2}{\partial z^2}\right)+1\right)\right]v^s_{l,x}(x+\Delta x,y,z)\\
&\qquad = a_l\left[\frac{1}{k^2}\left(\frac{\partial^2}{\partial y^2}+\frac{\partial^2}{\partial z^2}\right)+1\right]u^s_x(x,y,z)\\
&\left[1+b_l\left(\frac{1}{k^2}\left(\frac{\partial^2}{\partial y^2}+\frac{\partial^2}{\partial z^2}\right)+1\right)\right]v^s_{l,y}(x+\Delta x,y,z)\\
&\qquad = a_l\left[\frac{1}{k^2}\left(\frac{\partial^2}{\partial y^2}+\frac{\partial^2}{\partial z^2}\right)+1\right]u^s_y(x,y,z)\\
&\left[1+b_l\left(\frac{1}{k^2}\left(\frac{\partial^2}{\partial y^2}+\frac{\partial^2}{\partial z^2}\right)+1\right)\right]v^s_{l,z}(x+\Delta x,y,z)\\
&\qquad = a_l\left[\frac{1}{k^2}\left(\frac{\partial^2}{\partial y^2}+\frac{\partial^2}{\partial z^2}\right)+1\right]u^s_z(x,y,z).\\
&\qquad\qquad\qquad\qquad\qquad\qquad\qquad\qquad l=1,2
\end{aligned} \tag{10}$$

When the FD scheme is used Equation (10), the forward vector parabolic equations can be written as follows:

$$\begin{aligned}
&\frac{b_l}{k^2\Delta z^2}v^{s,m+1}_{l,\xi,p,q-1}+\frac{b_l}{k^2\Delta y^2}v^{s,m+1}_{l,\xi,p-1,q}\\
&+\left(1-\frac{2b_l}{k^2\Delta y^2}-\frac{2b_l}{k^2\Delta z^2}+b_l\right)v^{s,m+1}_{l,\xi,p,q}\\
&+\frac{b_l}{k^2\Delta y^2}v^{s,m+1}_{l,\xi,p+1,q}+\frac{b_l}{k^2\Delta z^2}v^{s,m+1}_{l,\xi,p,q+1}\\
&\qquad=\frac{a_l}{k^2\Delta z^2}u^{s,m}_{\xi,p,q-1}+\frac{a_l}{k^2\Delta y^2}u^{s,m}_{\xi,p-1,q}\\
&\qquad+\left(\frac{-2a_l}{k^2\Delta y^2}+\frac{-2a_l}{k^2\Delta z^2}+a_l\right)u^{s,m}_{\xi,p,q}\\
&\qquad+\frac{a_l}{k^2\Delta y^2}u^{s,m}_{\xi,p+1,q}+\frac{a_l}{k^2\Delta z^2}u^{s,m}_{\xi,p,q+1},\\
&\qquad\qquad\xi=x,y,z\quad l=1,2
\end{aligned} \tag{11}$$

where $u^m_{p,q}$ is the reduced scattered field at the point of $x_m = m\Delta x, y_p = p\Delta y, z_q = q\Delta z.$

The following coordinate transformation is introduced for PML domain [16]:

$$\begin{aligned}
\hat{y} &= y - i\int_0^y \sigma(\xi)d\xi\\
\hat{z} &= z - i\int_0^z \sigma(\xi)d\xi
\end{aligned}, \tag{12}$$

where $\sigma(\xi)=\frac{3}{2\delta}\times\frac{1}{\eta}\times\log(\frac{1}{10^{-3}})\times(\frac{\xi}{\delta})^2$, δ is the thickness of the PML and η is the wave impedance.

Similarly, the parabolic equation in the PML domain can be obtained:

$$\begin{aligned}
&(1+b_l)v^s_{l,\xi}(x+\Delta x,y,z)\\
&+\frac{b_l}{k^2}e_i\frac{\partial}{\partial y}\left(e_i\frac{\partial v^s_{l,\xi}(x+\Delta x,y,z)}{\partial y}\right)\\
&+\frac{b_l}{k^2}e_j\frac{\partial}{\partial z}\left(e_j\frac{\partial v^s_{l,\xi}(x+\Delta x,y,z)}{\partial z}\right)\\
&\qquad=\frac{a_l}{k^2}e_i\frac{\partial}{\partial y}\left(e_i\frac{\partial u^s_\xi(x,y,z)}{\partial y}\right)+\\
&\qquad\frac{a_l}{k^2}e_j\frac{\partial}{\partial z}\left(e_j\frac{\partial u^s_\xi(x,y,z)}{\partial z}\right)+a_l u^s_\xi(x,y,z),\\
&\qquad\qquad\xi=x,y,z\quad l=1,2
\end{aligned} \tag{13}$$

where

$$e_i=\frac{1}{1-i\sigma(y)},\quad e_j=\frac{1}{1-i\sigma(z)},\quad \sigma(y)=\sigma_0(y/\delta)^2,$$

$$\sigma(z)=\sigma_0(z/\delta)^2,\ \sigma_0=\frac{3}{2\delta}*\frac{1}{\eta}*\log\left(\frac{1}{R_0}\right),\ \eta=120\pi,$$

$R_0 = 10^{-2}, 10^{-3}, 10^{-4}.$

The Equation (13) can be rewritten as the following equation by using the FD scheme:

$$\begin{aligned}
&\left(\frac{b_l e_j^2}{k^2\Delta z^2}-\frac{b_l e_j e_j^{'}}{k^2\Delta z}\right)v^{s,m+1}_{l,\xi,p,q-1}+\left(\frac{b_l e_i^2}{k^2\Delta y^2}-\frac{b_l e_i e_i^{'}}{k^2\Delta y}\right)v^{s,m+1}_{l,\xi,p-1,q}\\
&+\frac{b_l e_i^2}{k^2\Delta y^2}v^{s,m+1}_{l,\xi,p+1,q}+\frac{b_l e_j^2}{k^2\Delta z^2}v^{s,m+1}_{l,\xi,p,q+1}\\
&+\left(1+b_l-\frac{2b_l e_i^2}{k^2\Delta y^2}+\frac{b_l e_i e_i^{'}}{k^2\Delta y}-\frac{2b_l e_j^2}{k^2\Delta z^2}+\frac{b_l e_j e_j^{'}}{k^2\Delta z}\right)v^{s,m+1}_{l,\xi,p,q}\\
&=\left(\frac{a_l e_j^{\,2}}{k^2\Delta z^2}-\frac{a_l e_j e_j^{'}}{k^2\Delta z}\right)u^{s,m}_{\xi,p,q-1}+\left(\frac{a_l e_i^{\,2}}{k^2\Delta y^2}-\frac{a_l e_i e_i^{'}}{k^2\Delta y}\right)u^{s,m}_{\xi,p-1,q}\\
&+\frac{a_l e_i^{\,2}}{k^2\Delta y^2}u^{s,m}_{\xi,p+1,q}+\frac{a_l e_j^{\,2}}{k^2\Delta z^2}u^{s,m}_{\xi,p,q+1}\\
&+\left(a_l-\frac{2a_l e_i^{\,2}}{k^2\Delta y^2}-\frac{2a_l e_j^{\,2}}{k^2\Delta z^2}+\frac{a_l e_i e_i^{'}}{k^2\Delta y}+\frac{a_l e_j e_j^{'}}{k^2\Delta z}\right)u^{s,m}_{\xi,p,q},\\
&\qquad\xi=x,y,z\qquad\qquad l=1,2
\end{aligned} \tag{14}$$

where $e_i^{'}$ and $e_j^{'}$ are the first order partial derivative of e_i and e_j, respectively.

C. Boundary conditions

The above scalar parabolic equations are coupled through inhomogeneous boundary conditions on the surface of the scattering target. For the PEC objects, the

tangential component of the total field equals zero on the surface:

$$\begin{cases} n_x u_y^s(p) - n_y u_x^s(p) = -e^{-ikx}\left(n_x E_y^i(p) - n_y E_x^i(p)\right) \\ n_x u_z^s(p) - n_z u_x^s(p) = -e^{-ikx}\left(n_x E_z^i(p) - n_z E_x^i(p)\right), \\ n_y u_z^s(p) - n_z u_y^s(p) = -e^{-ikx}\left(n_y E_z^i(p) - n_z E_y^i(p)\right) \end{cases} \quad (15)$$

where p is a point on the surface of the scatterer and (n_x, n_y, n_z) is the outer normal to the surface at p.

To ensure the unicity of the solution, the divergence-free condition is added [1]:

$$\frac{i}{2k}\left(\frac{\partial^2 u_x^s}{\partial y^2} + \frac{\partial^2 u_x^s}{\partial z^2}\right) + iku_x^s + \frac{\partial u_y^s}{\partial y} + \frac{\partial u_z^s}{\partial z} = 0 . \quad (16)$$

D. Rotating PE method

As shown in Fig. 2 (a), only a narrow-angle RCS result is obtained by a single PE run. Therefore, the rotating PE method [4] is introduced to obtain the full bistatic RCS at different frequencies for the proposed method. The scattering pattern of any angle can be calculated by decoupling the paraxial direction from the direction of the incidence. As shown in Fig. 2 (b), the paraxial direction is fixed at x-axis while both the incident wave and the scattering target are rotated by a specified angle.

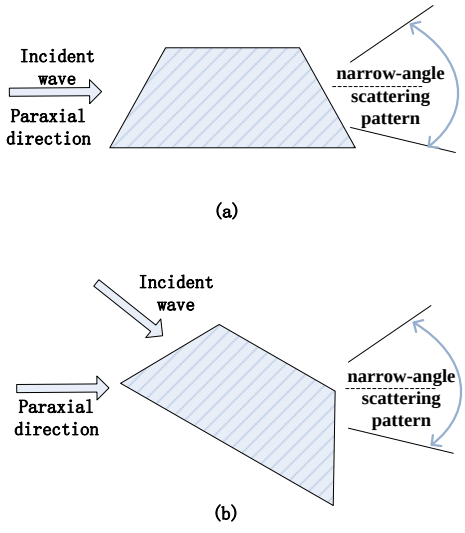

Fig. 2. Rotating TDPE method.

In our work, the scattering target is discretized with triangle grids. Then the cuboid grids which are needed by the FD scheme are obtained by taking advantage of the geometry information of the triangle ones. Only a narrow-angle RCS result is obtained by a single PE run. Therefore, the rotating PE method is introduced to obtain the full bistatic RCS result. After rotation, the triangle grids can be calculated directly by the coordinate transformation and then the cuboid grids should be regenerated.

III. NUMERICAL RESULTS

In this section, a series of examples are presented to demonstrate the accuracy and efficiency of the proposed method. All computations are carried out on Lenovo Intel Q9500 (2.83 GHz) with 8GB RAM.

A. The bi-static RCS for a PEC sphere

Firstly, the EM scattering from a PEC sphere is considered at the frequency of 300 MHz with the radius 4 m. The incident angle is fixed at $\theta_{inc} = 90°$ $\phi_{inc} = 0°$. The model of the PEC sphere is shown in Fig. 3. The transverse (y, z) plane of the air box is chosen to be $20m \times 20m$. There are totally 80 transverse planes to be calculated with 200×200 nodes in each transverse plane. In this simulation, all the range steps are chosen to be 0.1 m. As shown in Fig. 4, the bistatic RCS curves of the PEC sphere are compared between the traditional PE method, the proposed Split-Step Pade PE method and Mie Series. It can be seen that there is a good agreement between the Mie Series and the proposed Split-Step Pade PE method at wider angles than the standard PE method (SPE).

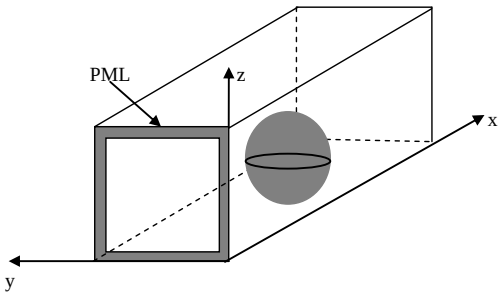

Fig. 3. Model of the PEC sphere.

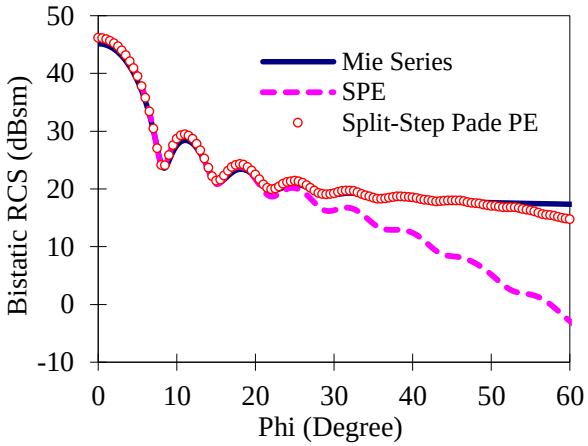

Fig. 4. Bistatic RCS result for the PEC sphere.

B. The monostatic RCS for a PEC cone

Secondly, the analysis of bisttatic RCS is taken for a PEC cone at the frequency of 300 MHz with upper radius 2 m, down radius 4 m and height 4 m. As shown in Fig. 5, the model of the cone is given. The incident angle is fixed at $\theta_{inc}=90°$ $\phi_{inc}=0°$. All the range steps are chosen to be 0.1 m and the transverse (y,z) plane of the air box is chosen to be $20m\times 20m$. As a result, there are 40 transverse planes to be calculated with 200×200 nodes in each transverse plane. As shown in Fig. 6, the bistatic RCS curves of the PEC sphere are compared between the traditional PE method, the proposed Split-Step Pade PE method and software FEKO. There is a good agreement between the FEKO and the proposed Split-Step Pade PE method at angles of 45° of the paraxial direction while 15° for the standard PE method (SPE).

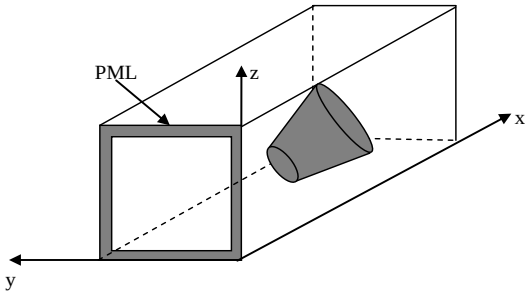

Fig. 5. Model of the PEC cone.

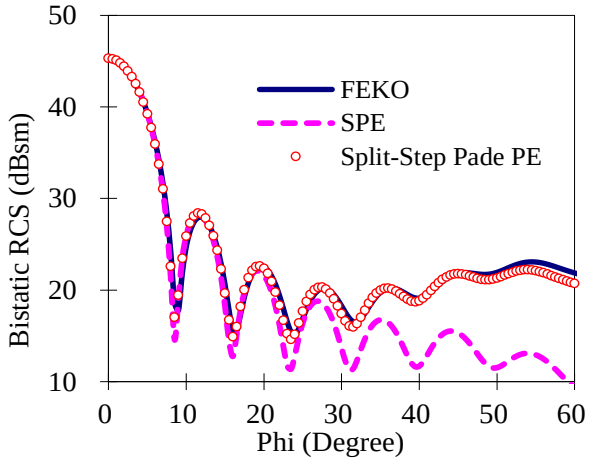

Fig. 6. Bistatic RCS result for the PEC cone.

C. Complete bistatic RCS for a PEC aircraft

At last, we consider the EM scattering from an aircraft at the frequency of 2.5 GHz and its maximum size in x, y and z directions are 10 m, 2.75 m and 8.5 m. The incident angle is fixed at $\theta_{inc}=90°$ $\phi_{inc}=0°$. In this simulation, the transverse (y,z) plane of the air box is chosen to be $12m\times 12m$. There are 167 transverse planes to be calculated with the range steps of 0.06 m and 200×200 nodes in each transverse plane. As shown in Fig. 7, the complete bistatic RCS results are compared between the proposed Split-Step Pade PE method and software FEKO. Moreover, as shown in Fig. 8, the detailed figure of the bistatic RCS result between 0° and 60° is given for better comparison. There is a good agreement between them. It should be noted that 4 rotating PE runs are used to obtain the complete bistatic RCS for the proposed method while 7 for the standard PE method. Therefore, the proposed Split-Step Pade PE method is more efficient than the standard PE method for analyzing the bistatic EM scattering problems.

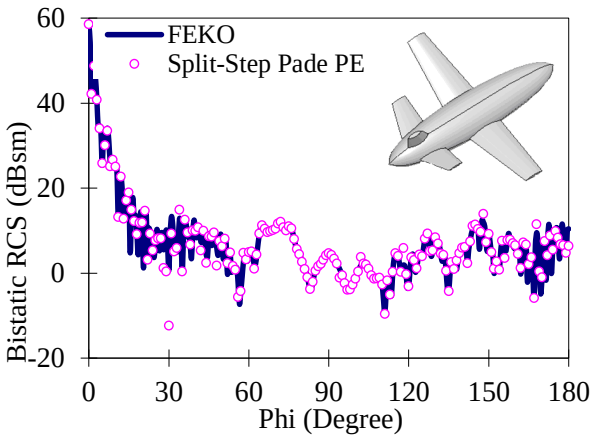

Fig. 7. Bistatic RCS result for the PEC aircraft.

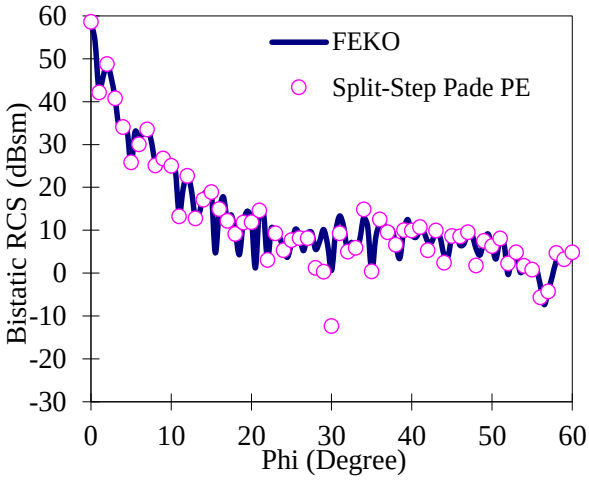

Fig. 8. Bistatic RCS result between 0° and 60° for the PEC aircraft.

IV. CONCLUSION

In this paper, the split-step Pade scheme is used to the parabolic equation for the analysis of EM scattering from electrically large PEC objects. By taking

advantage of the split-step Pade scheme, a high order Pade approximation can be divided into several one-order Pade approximations. Moreover, they can be calculated separately. In this way, high computational accuracy and efficiency can be achieved by the proposed method. The numerical results demonstrate that the proposed method can obtain accurate bistatic RCS results at angles even more than 45° of the paraxial direction.

ACKNOWLEDGMENT

This work was supported in part by Natural Science Foundation of 61431006, 61271076, 61171041, the Fundamental Research Funds for the central Universities of No. 30920140111003, No. 30920140121004, and in part by Jiangsu Natural Science Foundation of BK2012034.

REFERENCES

[1] A. A. Zaporozhets and M. F. Levy, "Bistatic RCS calculations with the vector parabolic equation method," *IEEE Trans. Antennas and Propagation*, vol. 47, no. 11, Nov. 1999.

[2] Z. He and R. S. Chen, "A vector meshless parabolic equation method for three-dimensional electromagnetic scatterings," *IEEE Transactions on Antennas and Propagation*, vol. 63, no. 6, pp. 2595-2603, 2015.

[3] Z. He, Z. H. Fan, D. Z. Ding, and R. S. Chen, "Efficient radar cross-section computation of electrically large targets with ADI-PE method," *Electronics Letters*, vol. 51, no. 4, pp. 360-362, 2015.

[4] M. F. Levy, *Parabolic Equation Methods for Electromagnetic Wave Propagation*. London: The Institution of Electrical Engineers, 2000.

[5] Z. He, Z. H. Fan, D. Z. Ding, and R. S. Chen, "A vector parabolic equation method combined with MLFMM for scattering from a cavity," *Applied Computational Electromagnetics Society Journal*, vol. 30, no. 5, pp. 496-502, 2015.

[6] Q. I. Dai, Y. H. Lo, W. C. Chew, and Y. G. Liu, "Generalized modal expansion and reduced modal representation of 3-D electromagnetic fields," *IEEE Transactions on Antennas and Propagation*, vol. 62, no. 2, pp. 783-793, 2013.

[7] M. A. Sharkawy and H. E. Ocla, "Electromagnetic scattering From 3-D targets in a random medium using finite difference frequency domain," *IEEE Transactions on Antennas and Propagation*, vol. 61, no. 11, pp. 5621-5626, 2013.

[8] J. M. Song, C. C. Lu, and W. C. Chew, "Multilevel fast multipole algorithm for electromagnetic scattering by large complex objects," *IEEE Transactions on Antennas and Propagation*, vol. 45, no. 10, pp. 1488-1493, 1997.

[9] W. L. Siegmann, G. A. Kriegsmann, and D. Lee, "A wide-angle three-dimensional parabolic wave equation," *J. Acoust. Soc. Am.*, vol. 78, iss. 2, pp. 659-664, 1985.

[10] Z. X. Huang, B. Wu, W. Sha, M. S. Chen, X. L. Wu, and H. Dai, "High-order parabolic equation method for electromagnetic computation," *APMC 2008, Asia-Pacific*, 2008.

[11] W. L. Siegmann, G. A. Kriegsmann, and D. Lee, "A wide-angle three-dimensional parabolic wave equation," *J. Acoust. Soc. Am.*, vol. 78, iss. 2, pp. 659-664, 1985.

[12] D. J. Thomson, "A wide-angle split-step algorithm for the parabolic equation," *J. Acoust. Soc. Am.*, vol. 74, iss. 6, pp. 1848-1854, 1983.

[13] M. D. Collins, "A split-step Pad solution for the parabolic equation method," *J. Acoust. Soc. Am.*, vol. 93, iss. 4, pp. 1736-1742, 1993.

[14] M. D. Collins, "Generalization of the split-step Pade solution," *J. Acoust. Soc. Am.*, vol. 96, iss. 1, pp. 382-385, 1994.

[15] M. D. Feit and J. A. Fleck, "Light propagation in graded-index fibers," *Appl. Opt.*, vol. 17, pp. 3990-3998, 1978.

[16] F. Collino, "Perfectly matched absorbing layers for the paraxial equations," *J. Comp. Phys.*, 94:1~29, 1991.

Zi He received the B.Sc. degree in Electronic Information Engineering from the School of Electrical Engineering and Optical Technique, Nanjing University of Science and Technology, Nanjing, China, in 2011.

She is currently working towards the Ph.D. degree in Electromagnetic Fields and Microwave Technology at the School of Electrical Engineering and Optical Technique, Nanjing University of Science and Technology. Her research interests include antenna, RF-integrated circuits, and computational electromagnetics.

Rushan Chen (M'01) was born in Jiangsu, China. He received the B.Sc. and M.Sc. degrees from the Department of Radio Engineering, Southeast University, China, in 1987 and 1990, respectively, and the Ph.D. degree from the Department of Electronic Engineering, City University of Hong Kong, in 2001.

He joined the Department of Electrical Engineering,

Nanjing University of Science and Technology (NJUST), China, where he became a Teaching Assistant in 1990 and a Lecturer in 1992. Since September 1996, he has been a Visiting Scholar with the Department of Electronic Engineering, City University of Hong Kong, first as Research Associate, then as a Senior Research Associate in July 1997, a Research Fellow in April 1998, and a Senior Research Fellow in 1999. From June to September 1999, he was also a Visiting Scholar at Montreal University, Canada. In September 1999, he was promoted to Full Professor and Associate Director of the Microwave and Communication Research Center in NJUST, and in 2007, he was appointed as the Head of the Department of Communication Engineering, NJUST. He was appointed as the Dean in the School of Communication and Information Engineering, Nanjing Post and Communications University in 2009. And in 2011 he was appointed as Vice Dean of the School of Electrical Engineering and Optical Technique, NJUST. Currently, he is a Principal Investigator of more than 10 national projects. His research interests mainly include computational electromagnetics, microwave integrated circuit and nonlinear theory, smart antenna in communications and radar engineering, microwave material and measurement, RF-integrated circuits, etc. He has authored or co-authored more than 260 papers, including over 180 papers in international journals.

Chen is an expert enjoying the special government allowance, Member of Electronic Science and Technology Group, Fellow of the Chinese Institute of Electronics (CIE), Vice-Presidents of Microwave Society of CIE and IEEE MTT/APS/EMC Nanjing Chapter and an Associate Editor for the International Journal of Electronics. He was also the recipient of the Foundation for China Distinguished Young Investigators presented by the China NSF, a Cheung Kong Scholar of the China Ministry of Education, New Century Billion Talents Award. Besides, he received several Best Paper Awards from the National and International Conferences and Organizations. He serves as the Reviewer for many technical journals, such as the IEEE Transactions on Antennas and Propagation, the IEEE Transactions on Microwave Theory and Techniques, Chinese Physics, etc.

A Miniaturized Polarization Independent Frequency Selective Surface with Stepped Profile for Shielding Applications

Muhammad Idrees [1], Saima Buzdar [1], Saifullah Khalid [2], and Muhammad Ali Khalid [3]

[1] Department of Telecommunication Engineering
University of Engineering and Technology, Taxila, 47050, Pakistan
1idrees23@gmail.com

[2] Department of Software Engineering
Military College of Signals (MCS) NUST, Islamabad, 44000, Pakistan
sukhalid@gmail.com

[3] Design and Devolvement Cell, R&D
National Radio and Telecommunication Corporation (NRTC), Haripur, 22060, Pakistan
10mseemkhalid@seecs.edu.pk

Abstract ─ In this paper, a miniaturized Frequency Selective Surface (FSS) with band-stop characteristics is presented for shielding applications. The FSS is designed to notch at 3.5 GHz frequency in the WiMAX band. The design is composed of a circular metallic patch with identical stepped profile printed on both sides of a low cost FR-4 laminate. The design provides an attenuation of 43 dB at desired resonant frequency. The FSS geometry makes it independent of polarization and it offers stable transmission response. Oblique angle variations don't affect the unit cell performance, for transverse electric and transverse magnetic modes of polarization. The FSS unit cell is compact with the dimensions of 25×25 mm^2. The simulated and measured results show good agreement for the proposed design.

Index Terms ─ Frequency Selective Surface (FSS), periodic structure, stepped profile, transverse electric, transverse magnetic, WiMAX band.

I. INTRODUCTION

The FSSs are periodically arranged metallic patches or slots in two or three dimensional fashion. They have comprehensive attraction for their microwave and optical applications including Radar Cross Section (RCS) reduction [1-3], antenna radomes, dichroic subreflectors, electromagnetic absorbers, wireless security, indoor wireless propagation, electromagnetic interference (EMI) reduction and many others [1, 4-9]. They are used as EBG structures and High Impedance Surfaces (HISs) to improve the antenna gain, directivity and bandwidth [10-13].

In recent reported literature, various researches on FSSs for band stop and electromagnetic shielding applications [14-19] are investigated. FSSs with band-stop characteristics for WLAN applications are reported in [5, 10]. Reconfigurable frequency selective surfaces for band-reject applications are studied in [20]. A tunable FSS for electromagnetic building architecture is stated in [21]. An FSS for gain enhancement of microstrip triangular slot antenna for X-band is presented in [12]. Polarization independent FSS used for RCS reduction is reported in [3].

In this research, a miniaturized FSS with shielding characteristics is proposed. The FSS suppresses interference at 3.5 GHz frequency in WiMAX band. The FSS unit cell consists of a circular patch of metal having symmetrical staircase profile realized on both sides of an FR-4 substrate. The FSS shows an attenuation of 43 dB at the desired frequency. Moreover, it shows stable and identical transmission frequency characteristics over oblique angle variations for Transverse Electric (TE) and Transverse Magnetic (TM) polarizations of the incident wave.

Rest of the paper is arranged as follows: in Section II the design description of proposed FSS is presented. The simulated results and discussions are presented in Section III. The measurement fixture and measurement results are discussed in Section IV. Finally, Section V summarizes and concludes the paper.

II. FSS UNIT CELL DESIGN

The FSS unit cell consists of a circular metallic patch with a staircase profile at the middle. The diameter of circular metallic patch is $L_1 + 2P$. FSS structure is designed and fabricated on both sides of a low cost FR-4 laminate having thickness of 1.6 mm, a relative permittivity of $\varepsilon_r = 4.4$ and dielectric loss tangent, tan δ,

Submitted On: October 29, 2015
Accepted On: March 19, 2016

of 0.02. Moreover, the FSS design has overall dimensions of L × W = 25 × 25 mm^2. The FSS unit cell is shown in Fig. 1.

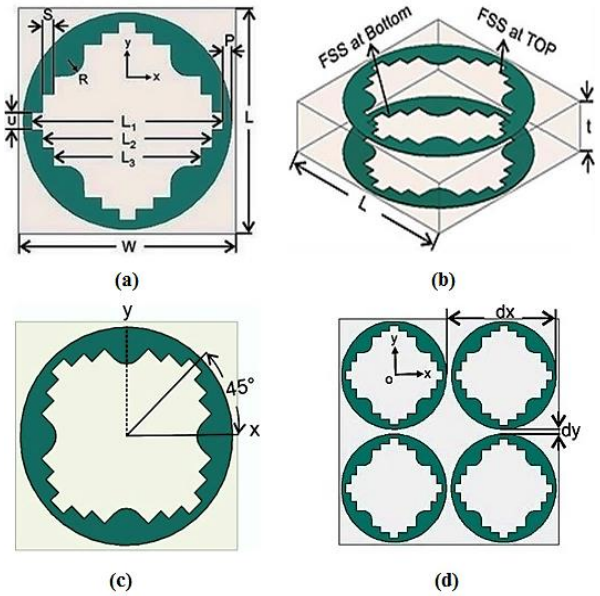

Fig. 1. FSS unit cell structure: (a) top view, (b) perspective view, (c) unit cell rotation at 45^o, and (d) A 2 × 2 unit cell array.

The stepped profile is designed by eliminating rectangular stubs from solid interior of circular patch. These stubs are variable in lengths but each has width of 2 mm. The step size of this staircase profile has length S = 1.25 mm and U = 2 mm height. The horizontal rectangular stub at center of the patch along x-axis has dimensions L_1 × U = 22 mm × 2 mm. Moreover, second and third stubs below the stub at center of patch have dimensions L_2 × U = 19.5 mm × 2 mm and L_3 × U = 17 mm × 2 mm respectively. The upper half of staircase profile along x-axis is a mirror replica of stubs below the central horizontal stub. In order to have symmetry in the unit cell along y-axis the same geometry is replicated.

It was realized from the simulations that the staircase profile works to obtain maximum attenuation at the frequency of interest. It provides angular stability in the frequency transmission response of the proposed FSS structure. Moreover, a bevelled notch with a radius of R = 2 mm as shown in Fig. 1 (a), gives an additional attenuation of 4 dB at the notching frequency. All other surface edges in unit cell structure have no effect on its performance. The design can bear up to 1.5 mm variation in the edges. A metallization of P = 1 mm on sides of the unit cell completes the circular patch. However, variation in the radius of the circular patch results in shift in the frequency transmission curve. Furthermore, the same FSS structure on the flip side of the substrate provides compactness and miniaturization in the unit cell size, along with the stability in the frequency response over incidence angle variations. The FSS unit cell is constructed and optimized in commercially available full-wave software HFSS®.

III. RESULTS AND DISCUSSIOS

In this section, the results of the proposed FSS are presented. Figure 2 shows the scattering characteristics of the FSS unit cell at normal incidence, for both TE and TM modes of polarization. The design provides good transmission loss at the frequency of interest, as shown in Fig. 2. It may be observed that the FSS offers stable and identical transmission response for both the TE and TM polarization modes at normal incidence (0^o), due to circular geometry of proposed FSS and symmetry in structure along x-axis and y-axis.

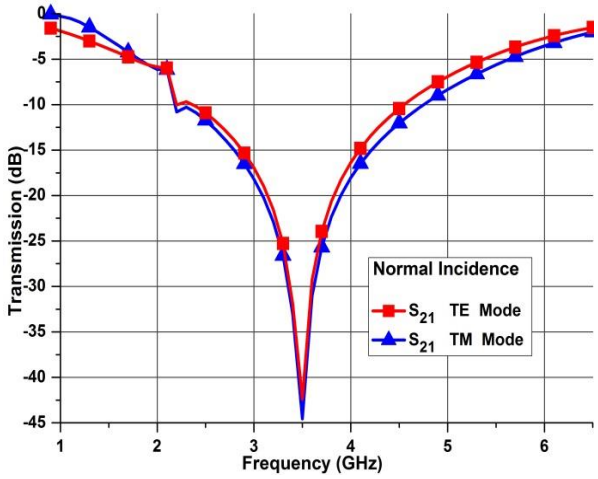

Fig. 2. Transmission behaviour of the FSS at normal incidence.

The magnitude of transmission coefficient (S_{21}) for TE mode at different incident angles is shown in Fig. 3. The angle of incidence of the incoming waves is changed from 0 to 60 degrees at regular intervals of 30 degrees. The FSS has stable frequency transmission characteristics irrespective of oblique angles variations.

Furthermore, the transmission characteristics of the FSS for TM mode at various incidences are plotted in Fig. 4. The results for TM mode are stable and identical to TE mode. It may be observed from the Figs. 3 and 4 that the FSS at -20 dB provides 1 GHz bandwidth of stopband, sufficient enough to suppress communication in the desired band. The rejection bandwidth increases as the oblique incident angle is varied. However, the bandwidth varies within the acceptable limits over angle variations, for both the TE and TM wave modes.

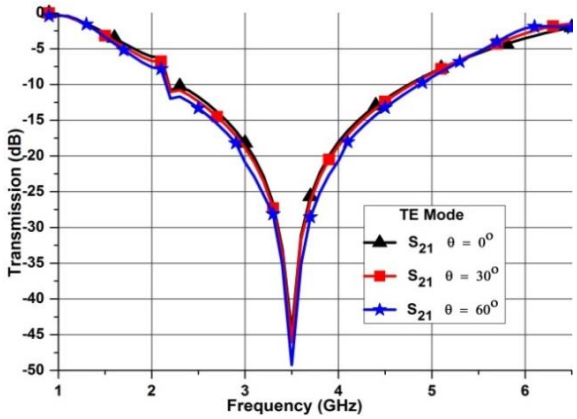

Fig. 3. Magnitude of transmission coefficient for TE mode of polarization at various incident angles.

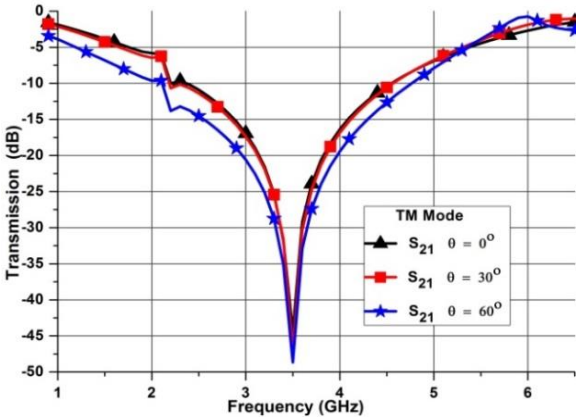

Fig. 4. S_{21} plot for TM mode over oblique angle variations.

A. Unit cell rotation at 45°

Furthermore, the FSS structure is rotated at an angle of 45°, to evaluate its performance as shown in Fig. 1 (c). The circular geometry of the FSS reduces the sensitivity to oblique incidences and makes it independent to polarization. The frequency transmission plots of the FSS when it is exposed to horizontal and vertical polarizations are shown in Figs. 5 and 6 respectively. It has been observed that the FSS shows stable response for both TE and TM modes. However, little deviations are observed in the resonant frequency with respect to the angle variations but these can be neglected at higher frequencies.

B. Dielectric thickness analysis

Thickness of the dielectric plays an important role in FSS characteristics. Variation in dielectric thickness results in shifting of the resonant frequency. The transmission characteristics as a function of dielectric thickness are plotted in Fig. 7. However, it is evident from the Fig. 7 that variations in the resonant frequency with respect to dielectric thickness are within the tolerable limits for the proposed design.

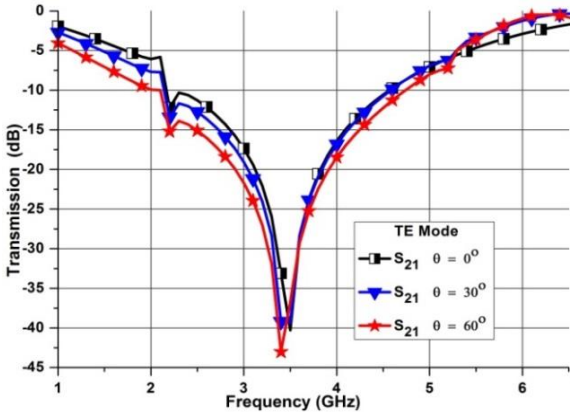

Fig. 5. Transmission response of FSS element rotated at 45° for TE mode.

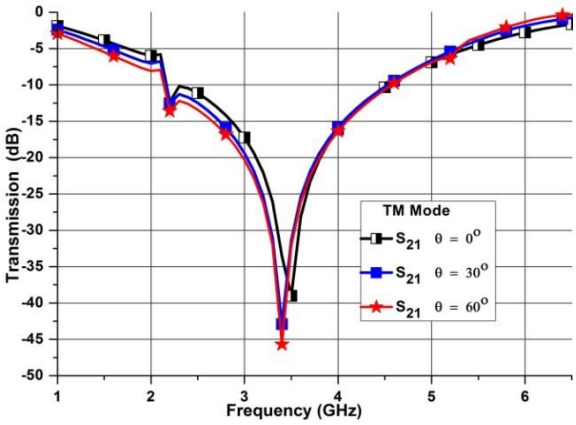

Fig. 6. Transmission characteristics of FSS rotated at 45° for TM mode over different oblique angles.

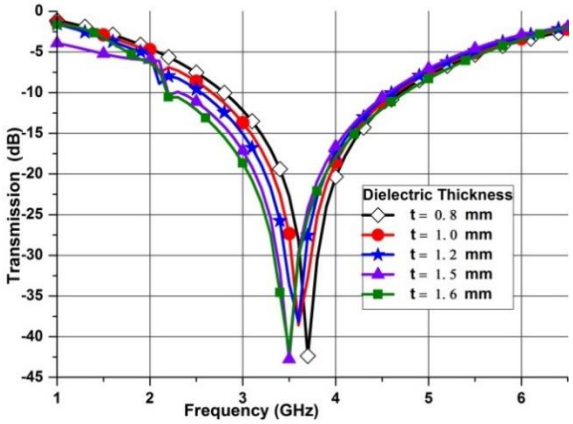

Fig. 7. Resonat frequency variations with respect to dielectric thickness.

IV. MEASUREMENT SETUP

To verify the designed FSS structure, a prototype is fabricated using the standard etching process. The FSS is realized on a lossy FR-4 substrate of 1.6 mm thickness. The fabricated FSS panel has dimensions of 256 × 256 mm^2. Moreover, it contains 10 × 10 FSS elements as depicted in Fig. 8. The measurements are carried out through standard free-space measurement method as shown in Fig. 9. The measurement setup consists of a pair of high gain horn antennas connected to Rohde & Schwarz FSH8 vector network analyzer (VNA) as shown in Fig. 10. The transmitting and receiving antennas are equally spaced from the FSS panel. The measured transmission responses of the fabricated prototype for both TE and TM modes are presented in Figs. 11 and 12 respectively. It is evident that the measured transmission response validates the simulations. However, some variations in the measured results are due to the lossy dielectric material used and measurement limitations.

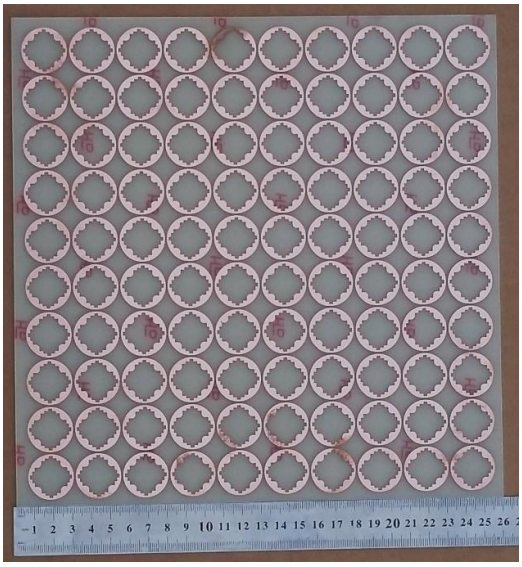

Fig. 8. Photograph of the fabricated FSS prototype.

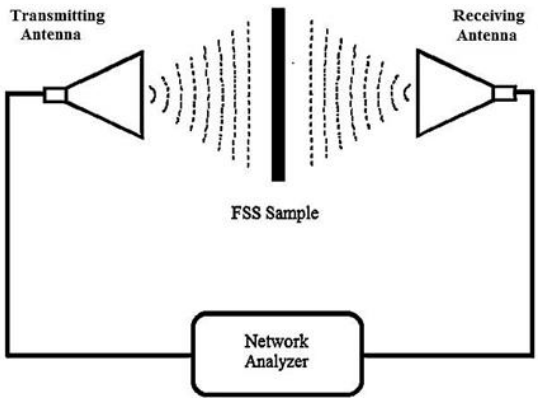

Fig. 9. FSS free-space measurement method.

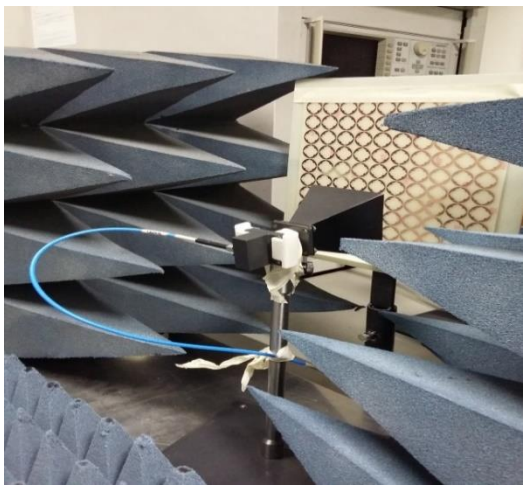

Fig. 10. Photo of measurement setup.

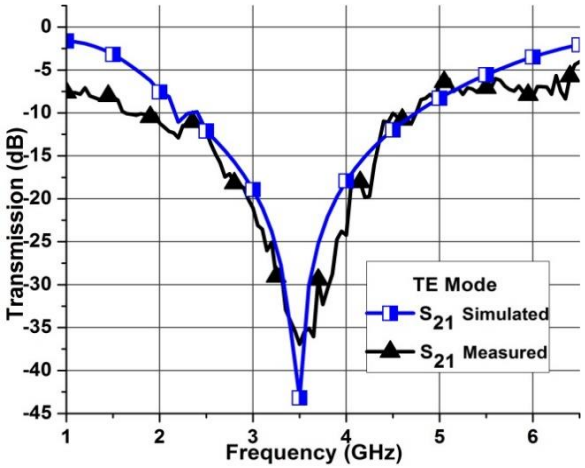

Fig. 11. Comparison of simulated and measured transmission coefficient for TE mode.

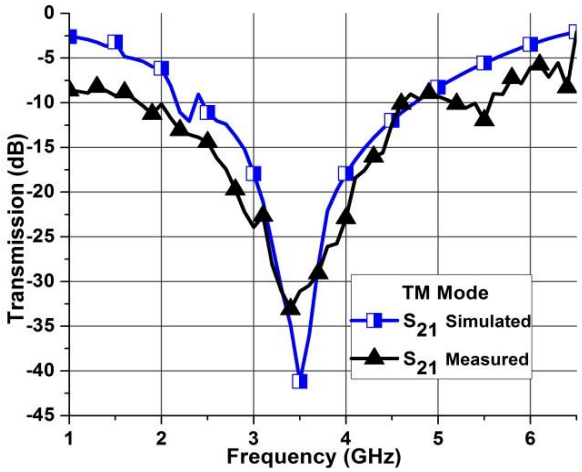

Fig. 12. Measured and simulated transmission for TM mode.

V. CONCLUSION

In this research work, a miniaturized polarization independent FSS with band-stop characteristics is proposed. The FSS is designed to notch at 3.5 GHz frequency and it offers shielding effectiveness of at least 43 dB. FSS design has a circular patch with staircase profile, realized on both sides of laminate. The staircase profile in the unit cell provides miniaturization and stability in response. Moreover, the FSS shows identical frequency transmission characteristics for TE and TM modes, making it suitable for angular as well as polarization independent operation. FSS unit cell has compact size and is scalable at other frequencies. More importantly the proposed FSS is a virtuous candidate to suppress communication in the WiMAX band.

ACKNOWLEDGMENT

The authors are thankful to National Radio and Telecommunication Corporation (NRTC) and National University of Sciences and Technology (NUST) for providing us the fabrication and testing facility.

REFERENCES

[1] B. A. Munk, *Frequency Selective Surfaces: Theory and Design*. John Wiley & Sons, 2005.

[2] H. Zhou, L. Yang, S. Qu, K. Wang, J. Wang, H. Ma, and Z. Xu, "Experimental demonstration of an absorptive/transmissive FSS with magnetic material," *IEEE Antennas and Wireless Propagation Letters*, vol. 13, pp. 114-117, 2014.

[3] A. Edalati and K. Sarabandi, "Wideband, wide angle, polarization independent RCS reduction using nonabsorptive miniaturized-element frequency selective surfaces," *IEEE Transactions on Antennas and Propagation*, vol. 62, pp. 747-754, 2014.

[4] X.-C. Zhu, W. Hong, K. Wu, H.-J. Tang, Z.-C. Hao, J.-X. Chen, H.-X. Zhou, and H. Zhou, "Design of a bandwidth-enhanced polarization rotating Frequency Selective Surface," *IEEE Transactions on Antennas and Propagation*, vol. 62, pp. 940-944, 2014.

[5] R. Natarajan, M. Kanagasabai, S. Baisakhiya, R. Sivasamy, S. Palaniswamy, and J. K. Pakkathillam, "A compact frequency selective surface with stable response for WLAN applications," *IEEE Antennas and Wireless Propagation Letters*, vol. 12, pp. 718-720, 2013.

[6] I. S. Syed, Y. Ranga, L. Matekovits, K. P. Esselle, and S. G. Hay, "A single-layer frequency-selective surface for ultrawideband electromagnetic shielding," *IEEE Transactions on Electromagnetic Compatibility*, vol. 56, pp. 1404-1411, 2014.

[7] S. Cimen, "Novel closely spaced planar dual-band frequency-selective surface," *IET Microwaves, Antennas & Propagation*, vol. 7, pp. 894-899, 2013.

[8] L. Meng and N. Behdad, "Frequency selective surfaces for pulsed high-power microwave applications," *IEEE Transactions on Antennas and Propagation*, vol. 61, pp. 677-687, 2013.

[9] A. K. Rashid, S. Zhongxiang, and S. Aditya, "Wideband microwave absorber based on a two-dimensional periodic array of microstrip lines," *IEEE Transactions on Antennas and Propagation*, vol. 58, pp. 3913-3922, 2010.

[10] I. G. Lee and I. P. Hong, "3D frequency selective surface for stable angle of incidence," *Electronic Letters*, vol. 50, pp. 423-424, 2014.

[11] Y. Mingbao, Q. Shaobo, W. Jiafu, Z. Jieqiu, Z. Hang, C. Hongya, and Z. Lin, "A miniaturized dual-band FSS with stable resonance frequencies of 2.4 GHz/5 GHz for WLAN applications," *IEEE Antennas and Wireless Propagation Letters*, vol. 13, pp. 895-898, 2014.

[12] E. Moharamzadeh and A. M. Javan, "Triple-band frequency selective surfaces to enhance gain of X-band triangle slot antenna," *IEEE Antennas and Wireless Propagation Letters*, vol. 12, pp. 1145-1148, 2013.

[13] C.-N. Chiu and W.-Y. Wang, "A dual-frequency miniaturized element FSS with closely located resonances," *IEEE Antennas and Wireless Propagation Letters*, vol. 12, pp. 163-165, 2013.

[14] C. J. Davenport and J. M. Rigelsford, "Design of comb reflection frequency selective surface for interference reduction in corridors of buildings," *Electronic Letters*, vol. 49, pp. 1478-1479, 2013.

[15] Y. Shi, W. Tang, W. Zhuang, and C. Wang, "Miniaturised frequency selective surface based on 2.5-dimensional closed loop," *Electronic Letters*, vol. 50, pp. 1656-1658, 2014.

[16] U. Rafique, S. A. Ali, M. T. Afzal, and M. Abdin, "Bandstop filter design for GSM shielding using frequency selective surfaces," *International Journal of Electrical and Computer Engineering (IJECE)*, vol. 2, pp. 846-850, 2012.

[17] A. K. Rashid and S. Zhongxiang, "A novel band-reject frequency selective surface with pseudo-elliptic response," *IEEE Transactions on Antennas and Propagation*, vol. 58, pp. 1220-1226, 2010.

[18] B. Sanz-Izquierdo and E. A. Parker, "Dual polarized reconfigurable frequency selective surfaces," *IEEE Transactions on Antennas and Propagation*, vol. 62, pp. 764-771, 2014.

[19] B. Li and Z. Shen, "Miniaturized bandstop frequency-selective structure using stepped-impedance resonators," *IEEE Antennas and Wireless Propagation Letters*, vol. 11, pp. 1112-1115, 2012.

[20] B. Sanz-Izquierdo and E. A. Parker, "Dual polarized reconfigurable frequency selective surfaces," *IEEE Transactions on Antennas and Propagation*, vol. 62, pp. 764-771, 2014.

[21] K. L. Ford, J. Roberts, S. Zhou, G. Fong, and J.

Rigelsford, "Reconfigurable frequency selective surface for use in secure electromagnetic buildings," *Electronic Letters*, vol. 49, pp. 861-863, 2013.

Muhammad Idrees received his B.S. Electrical Engineering from COMSATS Institute of Information Technology Wah, Pakistan, in 2013 and Masters in Telecommunication Engineering from University of Engineering and Technology (UET) Taxila, Pakistan, in 2015. He worked as Full-Time Researcher at University of Engineering and Technology Taxila from 2013-2015. His main research interests are in UWB Antennas, VHF/UHF High Power Antennas, UWB-MIMO systems, Metamaterials, Frequency Selective Surfaces, Antenna Radomes and RF and Microwave Engineering.

Saima Buzdar received her Bachelors Degree in Electrical (Telecommunication) Engineering from COMSATS Institute of Information and Technology, Islamabad, Pakistan in 2012. She received her M.Sc. degree in Telecommunication Engineering from University of Engineering and Technology, Taxila, Pakistan, in 2015. Her research interests involve UWB Antennas, Frequency Selective Surfaces, Electromagnetic analysis, RF & Microwaves, Waveguides and Optical Fiber Communication.

Saifullah Khalid received his B.S. and M.S. degrees from MCS, National University of Sciences and Technology (NUST) Islamabad in 1998 and 2013 respectively. He is currently working as Lecturer at NUST. His research interests include Antenna Design and Applications, RF and Microwave Engineering, Radio & wireless communications and Wireless Sensor Networks.

Muhammad Ali Khalid received his B.S. in Electrical (Electronics) Engineering from COMSATS Institute of Information Technology Abbottabad in 2009. He worked as Research Assistant at School of Electrical Engineering and Computer Science (SEECS), National University of Sciences and Technology (NUST), meanwhile he did his Masters in Electrical Engineering. His main areas of intrest are active electronics, Filter Design, Antenna on Chip, 5G Modulation Techniquies and Radio Communication.

Hybrid Analytical-Numerical Analysis of Plasmonic Photoconductive Antennas

Mohammadreza Khorshidi and Gholamreza Dadashzadeh

Department of Electrical and Electronic Engineering
Shahed University, Tehran, 3319118651, Iran
m.khorshidi@shahed.ac.ir, gdadashzadeh@shahed.ac.ir

Abstract ─ Photoconductive antennas (PCAs) have extensive technological applications as terahertz sources. Analysis of the performance of these antennas is typically challenging and time-consuming due to complicated interacting photonic and electromagnetic effects in the semiconductor material. The complexity even further increases in plasmonic PCAs because of the existence of periodic structures. In this paper, a numerical-analytical hybrid model is proposed for analysis plasmonic PCAs. Time-dependence and spatial-dependence of the electric field as well as carriers density generated in the semiconductor of plasmonic PCA, are calculated analytically and with finite element method, respectively. The presented model ultimately computes the current generated in the electrodes of plasmonic PCAs. Using this model, the performance of a typical plasmonic PCA as an example is investigated, and model results are validated by measurement results currently existing in the literature; though the model can also be used in the performance analysis of plasmonic PCAs with more complex periodic structures.

Index Terms─ Finite element method, optical wave, photo-generated current, plasmonic photoconductive antenna, terahertz source.

I. INTRODUCTION

Recently, terahertz (THz) waves have increased both researchers' interest and technological applications in security systems [1], spectroscopy [2] and medical imaging [3] to name a few. Various sources such as quantum cascade lasers (QCLs), frequency multipliers, and free-electron lasers (FELs) are utilized in THz technology, whereas each of them suffers from certain drawbacks [4]. Photoconductive antenna (PCA) is another type of THz sources which can be also used as a THz detector [5]. The PCA (also known as Auston switch [6]) converts incident optical waves into THz waves with the help of its pair of electrodes and the semiconductor material beneath them. Though working at room temperature, low cost of fabrication, and small size are the main favorable characteristics of PCAs, low radiation power and low efficiency are their important drawbacks [7]. In order to improve these deficiencies, plasmonic PCA has been proposed by Jarrahi and co-workers [8]. In the plasmonic PCA, periodic nano-scale rods are added to each of the pair of electrodes, for the purpose of increasing optical power transmitted into the semiconductor material. Laser illumination of periodic rods of plasmonic PCA generates carriers (both holes and electrons) in the region near the rods in the semiconductor material. Concentration of carriers in the vicinity of rods causes reduction in the distance and subsequently time required for carriers to reach the electrodes. Consequently, more number of carriers can arrive at the electrodes under the acceleration induced by bias electric field. When carriers arrive at the electrodes, current is generated in the electrodes and subsequently this current is transformed into THz wave by electrodes of the plasmonic PCA.

Analysis of the performance of PCA is challenging because of the complicated interacting electromagnetic field and photonic effects in the semiconductor material. For an accurate analysis, each step of the process of optical to THz-wave conversion including laser illumination of PCA, carriers generation, carriers acceleration due to the bias voltage applied on the electrodes, and THz wave radiated by electrodes of antenna should be rigorously taken into account. In plasmonic PCA, the complexity of analysis even further increases due to the existence of nano-scale periodic rods.

In this work, a hybrid model (combining analytical formulas with finite element method) is presented in the next section for analyzing plasmonic PCAs. In section III, by the use of the proposed model, a typical plasmonic PCA is studied as an example and results of the current model are compared with measurement results of reference [9].

II. THEORY

A plasmonic PCA as shown in Fig. 1 (a) consists of a pair of electrodes and a semiconductor material beneath them. Bias voltages are applied to the electrodes

Submitted On: February 13, 2016
Accepted On: May 3, 2016

and a laser as the source of optical wave is focused onto the semiconductor material beneath the periodic rods of anode electrode to maximize THz radiation [9]. The performance of the plasmonic PCA is mainly determined by its THz-radiated power that can be obtained by calculating the current induced on its electrodes. In plasmonic PCA, most of carriers are generated under the rods of anode electrode [9]. Moreover, here we assume that the laser illumination of rods is uniform along rods direction (z-axis of Fig. 1 (a)). Therefore, for calculating the generated current, the plasmonic PCA is assumed as a two-dimensional (2D) structure in the x-y plane perpendicular to rods direction. A unit cell of periodic rods in the x-y plane is shown in Fig. 1 (b); the left (x=0) and right (x=d_x) vertical lines are periodic boundaries and the width and height of rods are w_x and h_y, respectively. Based on plane-problem assumption, the amount of current density, $\boldsymbol{j}_c(x,y,t)$, generated at time t and point (x,y) within the unit cell, can be calculated by ([10]):

$$\boldsymbol{j}_c(x,y,t) = e\mu_e n(x,y,t)\boldsymbol{E}_{\text{bias}}(x,y), \qquad (1)$$

where e is the electron charge, μ_e is the electron mobility in semiconductor material, $n(x,y,t)$ is the carriers density in the semiconductor region of the unit cell as a function of position and time, and $\boldsymbol{E}_{\text{bias}}(x,y)$ is the bias electric field in the semiconductor region. It should be noted that, the value of μ_e is typically one order of magnitude larger than the value of hole mobility [11], therefore, the effect of holes in Eq. (1) is disregarded. According to Eq. (1), in order to calculate the current density, $\boldsymbol{j}_c(x,y,t)$, generated in the unit cell of plasmonic PCA, the carriers density, $n(x,y,t)$, and electric field, $\boldsymbol{E}_{\text{bias}}(x,y)$, should be first evaluated. The value of these quantities is calculated in the following sections separately.

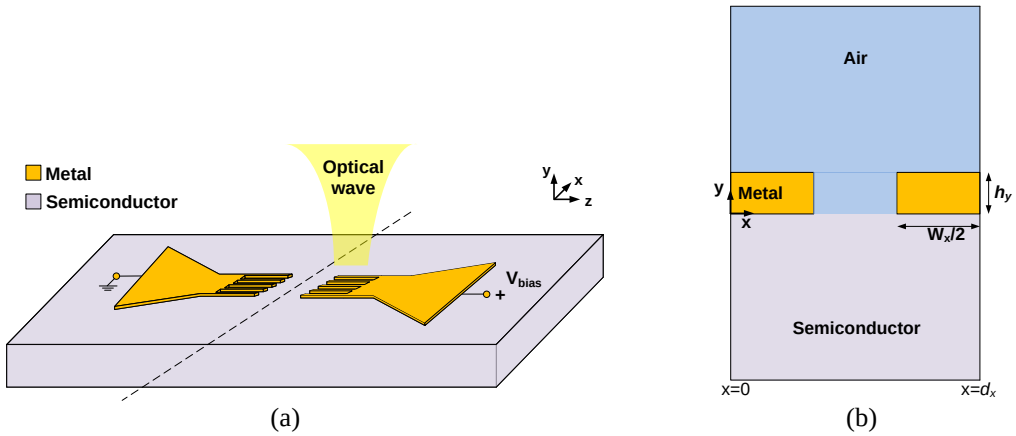

Fig. 1. (a) Schematic of a plasmonic PCA, and (b) x-y plane cross section of a period of plasmonic PCA electrode. The left (x=0) and right (x=d_x) vertical lines are periodic boundaries.

A. Calculation of *n(x,y,t)*

Carriers in the semiconductor region are generated due to illumination of optical wave to the rods of anode electrode. Pulses of laser power can be assumed to have a temporal Gaussian shape [10]:

$$P(t) = P_0(1-R)e^{-2\left(\frac{t}{\tau_l}\right)^2}, \qquad (2)$$

where the constant P_0 is the laser peak power and τ_l is the laser pulse duration. The dimensionless quantity R is the power reflection coefficient at the interface of air and rods of plasmonic PCA, and depends on the frequency of incident optical wave as well as permittivity constant of the semiconductor material. Since wavelength of incident optical wave is much smaller than the dimensions of each of the pair of electrodes, the value of R can be assumed independent of electrode dimensions, but depends on dimensions of rods of plasmonic PCA also. Therefore, for computing the value of R, a unit cell of 2D rods (shown in Fig. 1 (b)) are simulated by the finite element method within the COMSOL package.

Each photon of incident optical wave absorbed in the semiconductor region, generates a pair of hole and electron with capability of moving across the semiconductor material in their lifetime. In the conventional PCA with small gap between electrodes, the distribution of generated carriers (holes and electrons) can be assumed uniform in planes perpendicular to the propagation direction of incident optical power. Whereas, due to the existence of periodic rods in the electrodes of plasmonic PCA, the distribution of carriers generated in the plasmonic PCA is nonuniform, so that most of carriers are created in the vicinity of the periodic rods of the electrodes. Therefore, in order to accurately analyze the performance of plasmonic PCA, carriers density, $n(x,y,t)$, as a function of both time and position is required.

Temporal variation of carriers density, $n(x,y,t)$, depends on semiconductor material properties (which are constant values) and incident optical wave which varies with time only. On the other hand, spatial

distribution of $n(x,y,t)$ depends on rods dimensions only. Therefore $n(x,y,t)$ can be assumed separable in temporal- and spatial-dependencies:

$$n(x,y,t) = n_t(t)n_s(x,y), \quad (3)$$

where $n_t(t)$ is the total carriers density (number of carriers in the unit cell in unit length of z-direction) and $n_s(x,y)$ is the distribution of carriers density in the semiconductor region of the unit cell, normalized to unity. As will be discussed in the followings, we will obtain $n_t(t)$ from a theoretical model, whereas $n_s(x,y)$ is calculated by the finite element method within the COMSOL package. In practice we will calculate the electromagnetic power absorbed in semiconductor instead of $n_s(x,y)$, since we know that the absorbed electromagnetic power and $n_s(x,y)$ have the same distributions down to a constant multiplier (which indeed depends on time) [12]. It is important to note that a periodic pulse (such as the incident optical wave considered herein) typically has a wide frequency band, though its power mainly concentrates at its center frequency. Therefore, to calculate the absorbed electromagnetic power (while indeed depends on the pulse frequency band), considering only the central frequency of the pulse gives results within good enough accuracy.

Let us assume that each of the two electrodes of plasmonic PCA consists of N adjacent unit cells of Fig. 1 (b) plus a pair of half cells at the farthest ends of the electrode. In the following discussion we will ignore these two half cells, inspired by the fact that their effect becomes less important as N increases. All N cells experience the same electrostatic boundary conditions as they are all subjected to one bias voltage. On the other hand, if we further assume that the incident optical wave illuminates all N cells equally, then the number of carriers $n_t(t)$ generated in each of the N cells are the same. As the result, the total current density of plasmonic PCA, $\boldsymbol{j}(x,y,t)$, is related to the current density of each cell, $\boldsymbol{j}_c(x,y,t)$, according to:

$$j(x,y,t) = Nj_c(x,y,t). \quad (4)$$

For calculating $n_t(t)$, Drude model can be used (according to the reference [12]) to write the equation:

$$\frac{dn_t(t)}{dt} = -\frac{1}{\tau_c}n_t(t) + \frac{\alpha}{hf_{\text{opt}}}\frac{P(t)}{N}, \quad (5)$$

where h is the Planck constant, α is the optical absorption coefficient of semiconductor, τ_c is carrier lifetime of semiconductor, and f_{opt} is the optical wave central frequency. In Eq. (5), $\frac{P(t)}{N}$ is the optical power portion received by each cell. By substituting Eq. (2) into Eq. (5), and solving the resulting first-order ordinary differential equation, $n_t(t)$ as a function of time can be obtained as:

$$n_t(t) = \frac{P_0}{N}(1-R)\frac{\sqrt{2\pi}}{4}\frac{\alpha}{hf_{\text{opt}}}\tau_l \exp\left(-\frac{1}{8}\left(\frac{\tau_l}{\tau_c}\right)^2 - \frac{t}{\tau_c}\right)\left(\text{erf}\left(\sqrt{2}\frac{t}{\tau_l} - \frac{\sqrt{2}}{4}\frac{\tau_l}{\tau_c}\right) + 1\right). \quad (6)$$

After substituting Eqs. (1), (3) and (6) into Eq. (4), the expression for $\boldsymbol{j}(x,y,t)$ boils down to:

$$\boldsymbol{j}(x,y,t) = \text{e}\mu_e P_0(1-R)\frac{\sqrt{2\pi}}{4}\frac{\alpha}{hf_{opt}}\tau_l \, exp\left(-\frac{1}{8}\left(\frac{\tau_l}{\tau_c}\right)^2 - \frac{t}{\tau_c}\right)\left(erf\left(\sqrt{2}\frac{t}{\tau_l} - \frac{\sqrt{2}}{4}\frac{\tau_l}{\tau_c}\right) + 1\right) n_s(x,y)\boldsymbol{E}_{\text{bias}}(x,y). \quad (7)$$

It is important to note that N cancels out in Eq. (7), implying that our model does not depend on the considered number of unit cells N.

B. Calculation of $\boldsymbol{E}_{\text{bias}}(x,y)$

The bias voltage applied on the electrodes of plasmonic PCA, creates an electric field, $\boldsymbol{E}_{\text{bias}}(x,y,z)$, in the semiconductor region between electrodes. This field accelerates generated carriers and assists them to reach to the rods. Since most of the carriers are generated beneath the rods of anode electrode, they need to move in the plane (xy-plane of Fig. 1 (a)) perpendicular to the rods direction (z-direction of Fig. 1 (a)) to reach to the rods. Therefore, components of the electric field in this plane have the largest effect on the drift velocity of carriers in the semiconductor material. Hence, only x- and y-components of $\boldsymbol{E}_{\text{bias}}(x,y,z)$, in the semiconductor region need to be calculated. Moreover, due to the assumption that incident optical wave is focused onto the middle of rod (far from both ends) and consequently most of carriers are generated in the semiconductor region beneath the middle of rod, the effect of the both ends of rod on the bias electric field in the semiconductor region is neglected here; therefore $\boldsymbol{E}_{\text{bias}}(x,y,z)$ is assumed to be invariant of z coordinate, and we will drop the z argument hereafter. In order to obtain $\boldsymbol{E}_{\text{bias}}(x,y)$, the Laplace equation $\nabla^2 V_{\text{bias}} = 0$ (V_{bias} is the electric potential function due to the bias voltages) in companion with the Dirichlet boundary conditions of bias voltage values on the electrodes is solved in the semiconductor region of Fig. 1 (b) by COMSOL package, with $-\nabla V_{\text{bias}} = \boldsymbol{E}_{\text{bias}}$.

C. Field screening effect

Bias electric field, $\boldsymbol{E}_{\text{bias}}(x,y)$, in the semiconductor region causes generated electrons and holes to move in opposite directions. With spatial separation between electrons and holes, polarization, $\boldsymbol{p}(x,y,t)$, is induced in the semiconductor region. The time-dependence of polarization can be calculated by solving ([12]):

$$\frac{\partial \boldsymbol{p}(x,y,t)}{\partial t} = -\frac{1}{\tau_r}\boldsymbol{p}(x,y,t) + \boldsymbol{j}_{\mathbf{c}}(x,y,t), \quad (8)$$

where τ_r is the recombination time of carriers. According to the point-dipole model [11], electric field induced by polarization can be expressed as:

$$\boldsymbol{E}_{sc}(x,y,t) = \frac{1}{\eta\,\varepsilon}\boldsymbol{p}(x,y,t), \quad (9)$$

where ε is the permittivity constant of semiconductor material and η is a coefficient which depends on the antenna structure. The direction of induced electric field, $\boldsymbol{E}_{sc}(x,y,t)$, created due to the presence of polarization, is

in opposite to the direction of bias electric field. Therefore, bias electric field is opposingly "screened" by $\boldsymbol{E}_{sc}(x,y,t)$. By taking into account the field screening effect, the generated current density of Eq. (1), should be corrected as:

$$\boldsymbol{j}_{\mathbf{c}}(x,y,t) = \mathrm{e}\mu_{\mathrm{e}}\, n(x,y,t)(\boldsymbol{E}_{\mathrm{bias}}(x,y) - \boldsymbol{E}_{sc}(x,y,t)). \quad (10)$$

Eqs. (4), (9) and (10) give:

$$\boldsymbol{p}(x,y,t) = \eta\, \varepsilon\, \boldsymbol{E}_{\mathrm{bias}}(x,y) - \frac{\eta\, \varepsilon}{\mathrm{e}\mu_{\mathrm{e}}\, N} \frac{\boldsymbol{j}(x,y,t)}{n(x,y,t)}, \quad (11)$$

subsequently Eqs. (8) and (11) yield:

$$\frac{\partial \boldsymbol{j}(x,y,t)}{\partial t} = \frac{\mathrm{e}\mu_{\mathrm{e}}\, N}{\tau_r} \boldsymbol{E}_{\mathrm{bias}}(x,y) n(x,y,t) + \boldsymbol{j}(x,y,t)\left(\frac{1}{n(x,y,t)}\frac{\partial n(x,y,t)}{\partial t} - \frac{1}{\tau_r} - \frac{\mathrm{e}\,\mu_{\mathrm{e}}}{\eta\varepsilon}\, n(x,y,t)\right). \quad (12)$$

By numerically solving Eq. (12), current density, $\boldsymbol{j}(x,y,t)$, generated in plasmonic antenna with consideration of field screening effect can be calculated.

III. RESULTS AND DISCUSSIONS

In the previous section a hybrid model was presented for calculating current density of electrodes of plasmonic PCAs. In order to validate the accuracy of the proposed model, the current generated in electrodes of the plasmonic PCA proposed in the reference [9] is investigated herein. The plasmonic PCA of the reference [9], consists of two bow-tie electrodes placed on the low-temperature GaAs (LT-GaAs) substrate as shown in Fig. 1 (a). An optical wave from Ti:sapphire laser with a central frequency of 375 THz, repetition rate of 76 MHz, and pulse duration of 200 fs is focused onto the rods of anode electrode. Dimensions of the antenna and parameters of laser and LT-GaAs semiconductor utilized for analyzing the plasmonic PCA are given in Table 1; the values are tabulated along with their corresponding references.

Table 1: Antenna dimensions and parameters for laser and LT-GaAs semiconductor

Parameter	Value
Electron mobility for LT-GaAs [13]	$\mu_e = 0.02\ m^2V^{-1}s^{-1}$
Optical absorption coefficient [14]	$\alpha = 6000\ cm^{-1}$
Laser pulse duration [9]	$\tau_l = 200$ fs
Laser repetition rate [9]	$f_r = 76$ MHz
Carrier lifetime [15]	$\tau_c = 1$ ps
Carrier recombination time [12]	$\tau_r = 100$ ps
x-axis periodicity of rods [9]	$d_x = 200$ nm
Width of rods [9]	$w_x = 100$ nm
Height of rods [9]	$h_y = 50$ nm
Permittivity constant of LT-GaAs [14]	$\varepsilon = 12.86\ \varepsilon_0$
Coefficient related to the antenna structure	$\eta = 3*10^{-6}$
Power reflection coefficient at the interface of air and rods	$R = 0.3$

The power reflection coefficient at the interface of air and rods with rod dimensions given in Table 1 is 0.3 according to result of simulation of 2D structure (Fig. 1 (b)) within COMSOL package. For LT-GaAs semiconductor, with parameters given in Table 1, the total carriers density, $N*n_t(t)$, is calculated using Eq. (6) and is plotted in Fig. 2 for different values of incident optical power P_0. From both Fig. 2 as well as Eq. (6), it can be deduced that the rise time of $n_t(t)$ depends on the laser pulse duration, τ_l, whereas the decay time depends on the carrier lifetime, τ_c, of LT-GaAs.

As explained in the previous section another parameter needed for calculating generated current density, $\boldsymbol{j}(x,y,t)$, is the distribution of carriers density, $n_s(x,y)$. In order to compute $n_s(x,y)$, 2D rods (shown in Fig. 1 (b)) with parameters of Table 1 are simulated within the COMSOL package. Obtained values for the distribution of carriers density, $n_s(x,y)$, are shown in Fig. 3. As it can be seen in this figure, most of carriers are generated in the vicinity of rods especially near the corners; such that, the distance of most of generated carries to the nearest rod is less than 40 nm. Next the values obtained for $n_s(x,y)$ and $n_t(t)$ are used in Eq. (3) to result in the carriers density, $n(x,y,t)$.

As mentioned earlier also, electric field, $\boldsymbol{E}_{\mathrm{bias}}(x,y)$, in the semiconductor region, created by bias voltage, should be first determined for calculating generated current density $\boldsymbol{j}(x,y,t)$ in the electrodes of the plasmonic PCA. Therefore, within the COMSOL package, the Laplace equation is solved numerically in the LT-GaAs semiconductor region. Dirichlet boundary conditions for the Laplace equation are the bias voltage values at anode and cathode electrodes, set as 40 V and 0 V, respectively [9]. The absolute value of the bias electric field, $\boldsymbol{E}_{\mathrm{bias}}(x,y)$, in the semiconductor region beneath a period of rods determined from the simulation is shown in Fig. 4. It shows that the magnitude of $\boldsymbol{E}_{\mathrm{bias}}$ drastically decreases with the increase of the distance from the rods of electrodes along the y-axis.

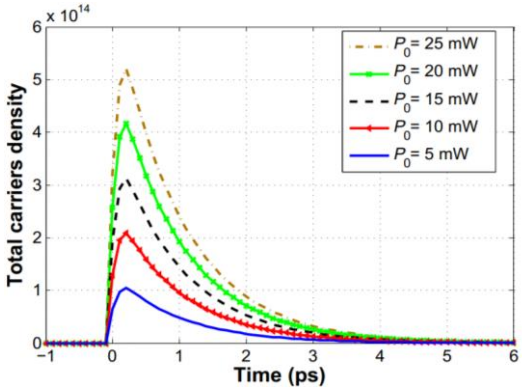

Fig. 2. Total carriers density, $N*n_t(t)$, in the LT-GaAs semiconductor of the plasmonic PCA versus time for different values of optical power, P_0.

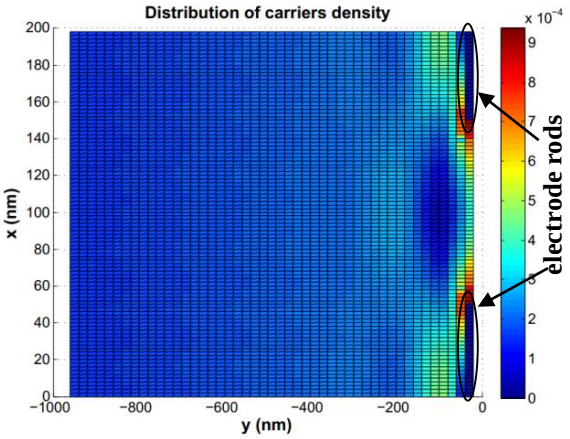

Fig. 3. The distribution of carriers density, $n_s(x,y)$, in LT-GaAs semiconductor beneath a period of rods of plasmonic PCA electrode.

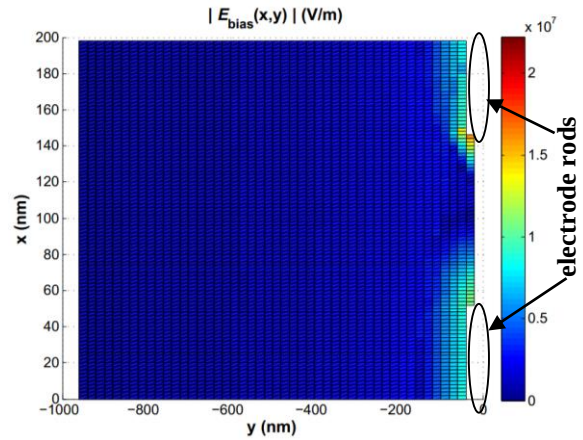

Fig. 4. The magnitude of bias electric field in the semiconductor region of a period of the plasmonic PCA electrode obtained from simulation.

Using the calculated carriers density, $n(x,y,t)$, and bias electric field, $\boldsymbol{E}_{\text{bias}}(x,y)$, the current density, $\boldsymbol{j}(x,y,t)$, generated in the plasmonic PCA is finally determined from both Eq. (12) with field screening effect and Eq. (4) without field screening effect. The generated currents (averaged over time) are calculated by the proposed model and are shown in Fig. 5 as a function of incident optical power. Along with them, measurement results of [9] are also plotted. It can be observed that in comparison with the measurement results, the theoretical results obtained by Eq. (12) with considering field screening effect (red solid curve of Fig. 5) are more accurate than the theoretical results obtained by Eq. (4) without considering field screening effect (green dashed curve of Fig. 5). To the best of the author's knowledge, this is the most accurate theoretical results for plasmonic PCA mimicking experimental observations, reported as far in the literature.

The difference between red solid curve and green dashed curve of Fig. 5 corresponds to the reduction of current generated in the plasmonic PCA due to the field screening effect. At low incident optical power, the field screening effect is negligible, however, this effect amplifies with the increase of optical power. As the number of generated carriers increases due to the increase of optical power, the polarization induced by spatial separation of them also increases; and consequently the field screening effect intensifies. On the other hand, according to Eq. (10) the increase of field screening effect leads to reduction in the rate of current generated in plasmonic PCA as can be also observed in Fig. 5; this is also consistent with the measurement results of reference [9].

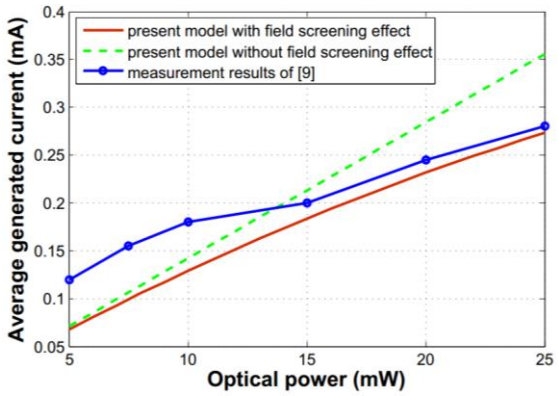

Fig. 5. Average current generated in the plasmonic PCA with the parameters given in Table 1.

IV. CONCLUSION

Plasmonic photoconductive antennas (plasmonic PCAs) have broad technological applications as terahertz (THz) sources. On the theoretical side, however, the analysis of these antennas (PCAs) is very challenging due to the existence of periodic structures. In this paper, a hybrid model consisting of both analytical and numerical methods was proposed which significantly reduces the complexity of plasmonic PCA analysis and subsequently the time required for its simulation. The model ultimately calculates the current generated in the electrodes of plasmonic PCA. For this purpose, the time-dependence and spatial-dependence of density of carriers generated in the semiconductor of plasmonic PCA were studied separately; the time-dependence was calculated analytically, whereas the spatial-dependence was computed using finite element method. For validation purpose, a typical plasmonic PCA as an example was analyzed by the model, and was found that model results match very well with experimental measurements published earlier in the literature. It was shown that field screening effect in the plasmonic PCA is negligible at

low incident optical power. However, this effect gets substantial as the optical power increases. The increase of field screening effect causes the rate of current generated in the plasmonic PCA to reduce. This fact can also be confirmed from the measurement results of plasmonic PCAs reported earlier.

REFERENCES

[1] N. Karpowicz, H. Zhong, C. Zhang, K. I. Lin, J. S. Hwang, J. Xu, and X. C. Zhang, "Compact continuous-wave subterahertz system for inspection applications," *Appl. Phys. Lett.*, 86, 054105, 2005.

[2] E. Pickwell and V. P. Wallace, "Biomedical applications of terahertz technology," *J. Phys. D: Appl. Phys.*, vol. 39, pp. R301-R310, 2006.

[3] H. Hoshina, A. Hayashi, N. Miyoshi, F. Miyamaru, and C. Otani, "Terahertz pulsed imaging of frozen biological tissues," *Appl. Phys. Lett.*, 94, 123901, 2009.

[4] X. Yin, B. Ng, and D. Abbott, *Terahertz Imaging for Biomedical Applications: Pattern Recognition and Tomographic Reconstruction*. © Springer Science Business Media LLC, 2012.

[5] N. Wang, M. R. Hashemi, and M. Jarrahi, "Plasmonic photoconductive detectors for enhanced terahertz detection sensitivity," *Optics Express*, vol. 21, no. 14, pp. 17221-17227, 2013.

[6] D. H. Auston, "Picosecond optoelectronic switching and gating in silicon," *Appl. Phys. Lett.*, vol. 26, pp. 101-103, 1975.

[7] D. S. Kim and D. S. Citrin, "Coulomb and radiation screening in photoconductive terahertz sources," *App. Phys. Lett.*, 88, 161117 365, 2006.

[8] C. Berry and M. Jarrahi, "High-performance photoconductive terahertz sources based on nanoscale contact electrode gratings," *IEEE Int. Microwave Symp. Digest (MTT)*, Montreal, Canada, 17-22 June 2012.

[9] C. W. Berry, M. R. Hashemi, M. Unlu, and M. Jarrahi, "Significant radiation enhancement in photoconductive terahertz emitters by incorporating plasmonic contact electrodes," *Nature Communications*, 4, Article number: 1622, doi: 10.1038/ncomms2638, 2013.

[10] N. Khiabani, Y. Huang, Y. Shen, and S. Boyes, "Theoretical modeling of a photoconductive antenna in a terahertz pulsed system," *IEEE Trans. on Antennas and Propagat.*, 61, no. 4, 1538, 2013.

[11] G. C. Loata, *Investigation of low-temperature-grown GaAs photoconductive antenna for continuous-wave and pulsed terahertz generation*, (Ph.D. dissertation), Goethe-University, Frankfurt, 2007.

[12] P. U. Jepsen, R. H. Jacobsen, and S. R. Keiding, "Generation and detection of terahertz pulses from biased semiconductor antennas," *J. Opt. Soc. Am. B*, vol. 13, no. 11, 1996.

[13] M. Tani, S. Matsuura, K. Sakai, and S. Nakashima, "Emission characteristics of photoconductive antennas based on low-temperature-grown GaAs and semi-insulating GaAs," *Appl. Opt.*, vol. 36, no. 30, pp. 7853-7859, 1997.

[14] J. Piprek, *Semiconductor Optoelectronic Devices Introduction to Physics and Simulation*, Academic Press an imprint of Elsevier Science, ISBN:0-12-557190-9, p. 230, 2003.

[15] M. C. Beard, G. M. Turner, and C. A. Schmuttenmaer, "Subpicosecond carrier dynamics in low-temperature grown GaAs as measured by timeresolved terahertz spectroscopy," *J. Appl. Phys.*, vol. 90, no. 12, pp.5915–5923, 2001.

Mohammadreza Khorshidi was born in Birjand, Iran in 1983. He received the Master of Science (M.Sc.) degree in 2009 from K.N. Toosi University of Technology, Iran. He is now Ph.D. candidate in Communication Engineering in Shahed University. His main research interest is terahertz technology, with focus on photoconductive antennas and plasmonic structures.

Gholamreza Dadashzadeh was born in Urmia, Iran, in 1964. He received Ph.D. degrees in Communication Engineering from Tarbiat Modarres University, Tehran, Iran. He is currently an Associate Professor with the Department of Electrical Engineering, Shahed University, Tehran. He has published more than 70 papers in referred journals and international conferences in the area of antenna design and smart antennas.

Wearable Graphene Based Curved Patch Antenna for Medical Telemetry Applications

Rajni Bala [1], Rajdeep Singh [1], Anupma Marwaha [1], and Sanjay Marwaha [2]

[1] Department of Electronics & Communication Engineering
[2] Department of Electrical and Instrumentation Engineering
SLIET Longowal, Punjab, 148106, India
rajnisliet@gmail.com, rajdeep.sliet91@gmail.com, marwaha_anupma@yahoo.co.in, marwaha_sanjay@yahoo.co.in

Abstract ─ In order to explore the expediency of graphene for biotelemetry in Wireless Body Area Network (WBAN), conformal square patch antenna design has been presented in this paper. The operational efficiency of the antenna is attributed to the incredible properties of graphene as patch conductor. The proposed antenna designed for operating in band from 1-4.88 GHz is fed with microstrip line and quarter wave transformer for impedance matching. The antenna however achieves best performance at 2.4 GHz in ISM band with good impedance matching, reasonable dB gain and high radiation efficiency for the wideband of frequencies in GHz range. The proposed wearable conformal graphene based antenna is optimally positioned at distance from body to make it suitable for Ultra Wide Band (UWB) health monitoring systems fulfilling the requirements of wideband operation, high gain and improved radiation efficiency at reduced SAR.

Index Terms ─ Biotelemetry, CST, curved patch antenna, graphene, WBAN.

I. INTRODUCTION

A WBAN consists of wireless nodes located on body which may communicate with each other and/or with an external base station using an efficient antenna. When body area network communicates with external base station, it is known as off-body communication. In biotelemetry applications more concentration is on off body communication. It is similar to mobile phone network, where mobile is in human proximity communicates with base station at distant place. The different antennas that have been used for body area networks include monopole Microstrip Patch Antenna (MPA) [1] and dipole microstrip patch antenna [2]. It is well documented that for telemetry applications the antenna should have small size high directivity, small Specific Absorption Ratio (SAR), circular polarization and should consume less power because it is not easy to carry a large battery with antenna [3-4]. Subhashini et al. observed that when inset feed MPA is placed 10 mm above the body phantom, the maximum SAR (10g) is 0.0190563 W/kg. Further the gain of antenna reduces when it is attached to the body phantom [5-6]. Kwon et al. showed that if the patch antenna is placed on body with given input power of 250 mW then maximum SAR value is 0.455 W/kg [4]. In order to flexibly place the antenna on any part of body including arm or wrist, it is desirable that the antenna should be curved along a cylindrical surface of desired radius. But as the radius changes, hence the curvature of body surface changes the performance parameters of antenna undergo variations. The radiation characteristics also depend upon radius of curvature [7]. It is desirable that the performance of the antenna should not be deteriorated on account of variations in radiation characteristics. The curved antenna designed here utilizes graphene as patch conductor to allow easy control of various parameters including resonant frequency, bandwidth on account of tunable surface conductivity on the basis of varying the chemical potential or the applied DC bias [8-9]. Moreover, the conductivity of graphene is highly frequency-dependent and the designed antenna can therefore possess completely different behavior. The constraints however for operating the planar graphene antenna in GHz range are the poor radiation efficiency and limited bandwidth [4]. The proposed square patch antenna is stretched to give curvature hence conforming to curved parts of body. The curved patch antenna also overcomes the drawback of limited radiation efficiency as the cylindrical structures offer better radiation efficiency performance than their planar counterparts [8]. The bandwidth can also be increased with increase in curvature [10]. Due the different curvatures of body parts for different persons the designed antenna with given dimensions may undergo up to 0.2% variation in resonant frequency [7]. In order to accommodate for these variations the proposed wearable antenna is designed to exhibit good resonant and radiation characteristics for operating band of 1-4.88 GHz. The microstrip line fed graphene based curved patch antenna designed on silicon substrate with dielectric constant

Submitted On: November 3, 2015
Accepted On: February 26, 2016

ε_r = 11.9 will prove to be useful to provide telemetry services for health monitoring systems in WBAN applications.

II. GRAPHENE MODELING

The radiation and absorption characteristics of graphene as patch conductor depend on the modeling of graphene conductivity coupled with Maxwell's equations. An infinitesimally thin layer of graphene sheet is modeled using the surface conductivity as derived from the Kubo's formula [11]. It has been noticed that in the low frequency range the inter band contributions of graphene conductivity can be ignored [12] and hence, the surface conductivity can be expressed by using only intraband contributions as:

$$\sigma = -j\frac{q_e^2 k_B T}{\pi \hbar^2(\omega - j2\Gamma)}\left[\frac{\mu_c}{k_B T} + 2\ln\left(e^{-\frac{\mu_c}{k_B T}} + 1\right)\right], \quad (1)$$

where ω is the angular frequency, k_B is the Boltzmann's constant, $\hbar$ is the reduced Planck constant, q_e is the electron charge, T is temperature, and μ_c is graphene chemical potential, Γ is electron scattering rate expressed in terms of relaxation time as $\tau = 1/2\Gamma$. In this work, the modeling of graphene material as patch is performed on CST (Computer Simulation Technology) 2014 commercial package with CST microwave studio [13] with help of macro program which permits the inclusion of graphene material characterized by appropriate physical, thermal and electrical properties. The present analysis is carried out at room temperature T = 300 ^{o}K, τ = 1 ps, and μ_c is kept below 1 eV in order to obtain sufficient radiation efficiency [14]. The various properties of graphene material considered for designing patch antenna are presented in Table 1.

Table 1: Electrical and non-electronic mechanical properties of graphene material

Parameter	Graphene Material Parameter Value
Dielectric loss tangent	0.077 [15]
Material density	2250 Kg/m^3
Heat capacity	2100 KJ/k/kg
Thermal conductivity	5000 W/mk [16]
Thermal diffusivity	1.0582×10^{-6} m^2/s
Breaking strength	40 N/m [17-18]
Young's modulus	1000 GPa [18]
Poisson's ratio	0.17 [18]
Thermal expression coefficient	17.7×10^{-6}/K

III. DESIGN OF GRAPHENE BASED CURVED PATCH ANTENNA

The graphene based curved patch antenna designed to resonate at 2.4 GHz is mounted on three layer cylindrical body phantom as shown in Fig. 1, keeping in view the installation of antenna flexibly on any curved parts of human body including arms and legs. The antenna can be oriented conforming to body in two ways either lengthwise or widthwise. When antenna is curved lengthwise along the width, there will be expansion in length due to stretching therefore affecting the fringing fields. The increased length is then required to be calculated as a function of angle of curvature [19]. Further, when the curved antenna is positioned along the length, the antenna gets curved widthwise; hence, increasing the width of patch due to stretching which will not effectively vary the resonant frequency. Conventionally, the width variations doesn't affect the resonant frequency however variations in frequency are still observed with curvature because due to stretching and compression in materials at different positions dielectric constant of material further changes and dielectric constant is inversely proportional to frequency.

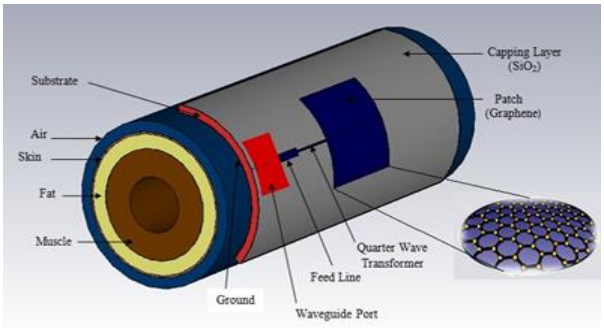

(a)

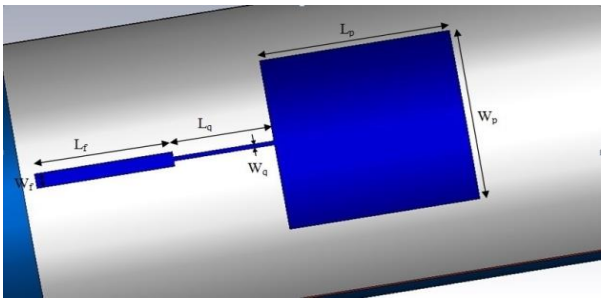

(b)

Fig. 1. (a) Graphene based curved patch antenna model, and (b) dimensional view.

For a flat rectangular microstrip patch antenna, the resonance frequency for any TM_{mn} mode is given by James and Hall [20] consisting of m and n are modes along length of patch (L_p) and width of patch (W_p) respectively. Bahl and Bhartia [21] defined the width W_p for efficient radiation as given below:

$$W_p = c/(2 * \frac{f*\sqrt{\varepsilon_r+1}}{\sqrt{2}}), \quad (2)$$

where c is velocity of light, f is resonant frequency and ε_r is the dielectric constant of the substrate. Due to the air-dielectric interface, effective dielectric constant (ε_{reff}) can be calculated as the combination of dielectric constant of substrate and dielectric constant of air above

it at the edges of the patch in order to account for the fringing fields around the periphery of the patch as given by [21]:

$$\varepsilon_{reff} = \frac{\varepsilon_r+1}{2} + \frac{\varepsilon_r-1}{2} / \sqrt{[1 + 12 * \frac{h}{W_p}]}, \quad (3)$$

where h is the height of substrate. Due to effect of fringing length of patch looks electrically wider than its physical length. Now actual length of patch can be calculated as the function of effective dielectric constant as:

$$L_p = \{\left[\frac{c}{2*f*\sqrt{\varepsilon_{reff}}}\right] - 2\left[0.412h * \frac{(\varepsilon_{reff}+0.3)*\left(\frac{W_p}{h}-0.264\right)}{(\varepsilon_{reff}-0.258)*\left(\frac{W_p}{h}-0.8\right)}\right]\}. \quad (4)$$

When the curved patch antenna is placed lengthwise, the length becomes stretched due to curvature and if the amount of curvature is θ, then actual length of patch required to resonate at same frequency will get reduced by a factor $\left[h * \frac{\theta}{2}\right]$ and the specific length of patch required will then be given by:

$$L_p = \left\{\left[\frac{c}{2*f*\sqrt{\varepsilon_{reff}}}\right] - \left[h * \frac{\theta}{2}\right] - 2\left[0.412 * h * \frac{(\varepsilon_{reff}+0.3)*\left(\frac{W_p}{h}-0.264\right)}{(\varepsilon_{reff}-0.258)*\left(\frac{W_p}{h}-0.8\right)}\right]\right\}. \quad (5)$$

The effect of curvature on resonant frequency has been presented by Krowne [3] as:

$$f_{mn} = \frac{1}{2\sqrt{\mu\varepsilon_r}} \sqrt{\left(\frac{m}{\theta r}\right)^2 + \left(\frac{n}{L_p}\right)^2}, \quad (6)$$

where r is radius of the curvature, θ is the angle bounded the width of the patch, ε_r is dielectric constant and μ is the magnetic permeability.

In the present case the curved antenna is placed widthwise so there will be no effect on length. Further, the proposed curved antenna uses graphene material as patch which supports Transverse Magnetic (TM) Surface Plasmon Polaritons (SPP) waves with an effective mode index given by [22-23]:

$$\eta_{eff}(\omega) = \sqrt{1 - \frac{4\mu_0}{\varepsilon_0 \sigma(\omega)^2}}. \quad (7)$$

The resonant behavior in graphene is therefore achieved due to the coupling of electromagnetic radiations with the SPP waves. The length of patch for the curved graphene patch antenna is thus based on the resonant conditions for graphene as given by:

$$m\frac{1}{2}\frac{\lambda}{\eta_{eff}} = L_P + 2\delta L, \quad (8)$$

where m is an integer determining the order of the resonance, λ is the wavelength of the incident radiation, L_p is the antenna length and δL is a measure of the field penetration outside the graphene-based patch antenna.

The graphene based curved patch antenna is designed as a four layer structure where at the bottom layer is ground plane of perfect electrical conductor (PEC), highly conducting material. The next layer is the high permittivity silicon (Si) substrate with dielectric constant, ε_r = 11.9 followed by a lower permittivity silicon dioxide (SiO_2) capping layer. The fourth layer situated on the top is the graphene patch radiator. The purpose of capping layer is to provide good optical contrast facilitating the visibility of even single graphene layer [24]. The antenna is edge fed by a microstrip line and quarter wave transformer for further impedance matching.

The dimensional parameters are selected to operate the designed antenna in the frequency range of 1-4.88 GHz as described in Table 2. The operating band includes the resonant frequency of 2.4 GHz that comes under the Industrial Scientific and Medical (ISM) band which is the approved frequency band for on body antennas according to Federal Communications Commission (FCC). The simulation analysis has been carried out with CST software based on finite integral technique. The software operates with automatic optimization tools utilizing transient solver for analyzing curved antenna structures with lossy and anisotropic material properties. CST software further supports coupled bio-electromagnetic problems and suitable for determining the absorption effects of radiations on human body.

Table 2: Dimensions of graphene curved patch antenna

Parameter	Value
Operating frequency band	1-4.88 GHz
Substrate length and width	(75.4×68) mm
Silicon (ε_r = 11.9) substrate height	2.5 mm
Length, width of curved patch ($L_p \times W_p$)	(35×35) mm
Patch thickness	10 nm
Height of capping layer SiO_2 (ε_r = 3.8)	1000 nm
Length, width of feed ($L_f \times W_f$)	(17.8×2.9) mm
Length, width of λ/4 transformer ($L_q \times W_q$)	(10.9×0.79) mm
Radius of curvature for antenna	30 mm

The entire graphene based curved patch antenna is placed on cylindrical body phantom of length 160 mm for analyzing the effect of radiation characteristics on the human body. The body phantom considered here consists of three cylindrical layers. The outer layer represents skin, middle layer being the fat layer and innermost layer is for muscle with the respective physical and dielectric properties as given in Table 3. The dimensions of body phantom layers can vary from person to person. Here the dimensions of different layers of body phantom for an average healthy person have been considered.

Table 3: Parameters of the body tissues at 2.4 GHz

Body Tissue of Length 160 mm	Skin (Dry)	Fat	Muscle
Thickness (mm)	0.65	5.25	10
Conductivity(s/m) [25]	1.464	0.10452	1.7388
Permittivity [20-21]	38.007	5.2801	52.729

IV. SIMULATION RESULTS

The curved shape antenna is designed with an objective to place the antenna conforming to curved body parts to facilitate health telemetry services at 2.4 GHz in ISM band for wireless communication networking. The careful examination of return loss, VSWR, gain, directivity, SAR and radiation characteristics is essential for performance evaluation of the antenna. The reference power is set at 1W for the operation at the resonant frequency. The wide operating band is obtained for the curved graphene antenna as is visible from the return loss plot given in Fig. 2. The return loss less than −10 dB show that the antennas are very well matched to the impedance transformer. It is evident from the plot that return loss S_{11} maintains less than −10 dB value in the operating band from 1-4.88 GHz. The value of S_{11} reaches a minimum value of -25.04 dB at resonating frequency of 2.4 GHz and -25.17 dB at resonating frequency of 3.94 GHz.

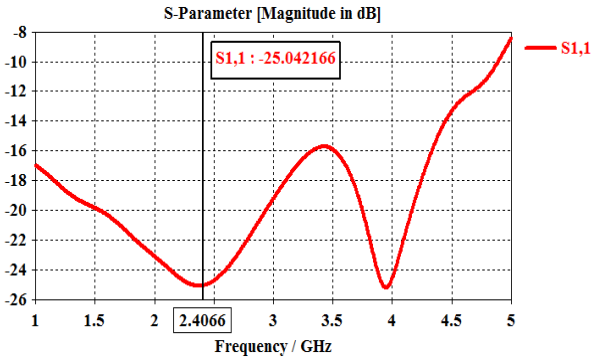

Fig. 2. Return loss versus frequency.

If the antenna impedance is matched to the transmission line at resonance, the mismatch off resonance is related to the voltage standing wave ratio. The value of VSWR which can be tolerated then defines the bandwidth of the antenna. The VSWR values of 1.118 and 1.12 are achieved at the respective resonating frequencies 2.4 GHz and 3.94 GHz as shown in Fig. 3.

In order to study the effect of curvature on the antenna performance, the radius of curvature is varied from 25 mm to 35 mm with an incremental step of 2 mm. As seen from Fig. 1, the curved graphene patch antenna is positioned widthwise along the length of body part so conventionally the variation in curvature will result in only minor variations in resonant frequency. However for graphene patch antennas it has been observed that increase in width of patch results in shifting of resonant frequency to higher side [22-23]. The variation in resonant frequency with curvature for the proposed graphene patch antenna is plotted in Fig. 4. The plot doesn't seem to follow any particular trend on account of increased width but the optimum resonant behavior is apparent for radius of curvature as 30 mm. For conformal antennas the analytical justification to determine the effect of curvature on resonant characteristics for graphene patch is yet to be explored.

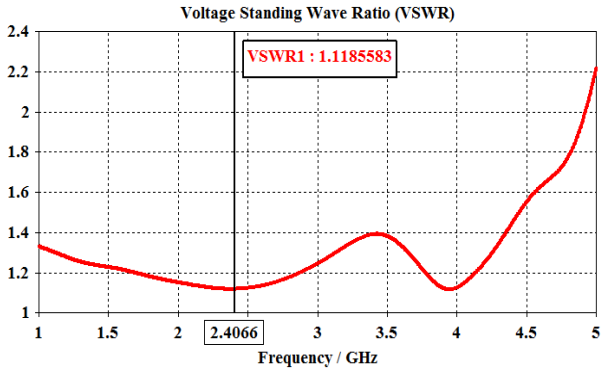

Fig. 3. VSWR versus frequency.

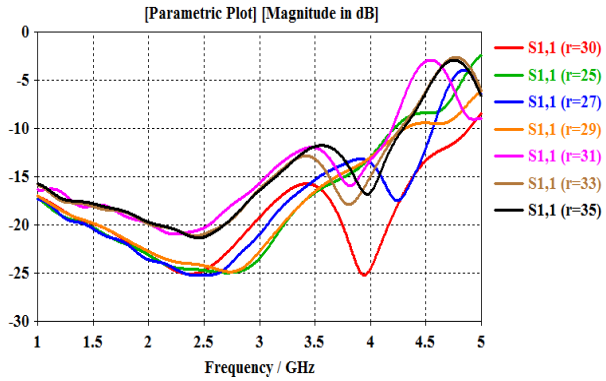

Fig. 4.Variation in resonant frequency with curvature.

The radiation efficiency of planar graphene patch antenna is deteriorated due to excessive absorption losses in GHz range. The radiation efficiency capabilities can however be compensated by using silicon substrate material with higher dielectric constant. The further improvement in radiation efficiency is obtained as compared to planar structure due to curvature. Figure 5 shows that the radiation efficiency achieved for the antenna is about 79.09% at resonating frequency of 2.4 GHz and drops down to 74.86% at resonating frequency of 3.94 GHz.

Figure 6 depicts that the peak gain attains value more than 5 dB for a very wide range of frequencies which is reasonably good for design of graphene curved

patch antenna for biotelemetry applications. The obtained gain is 10.19 dB at the desired frequency of 2.4 GHz and 2.8 dB at the second resonant frequency of 3.94 GHz.

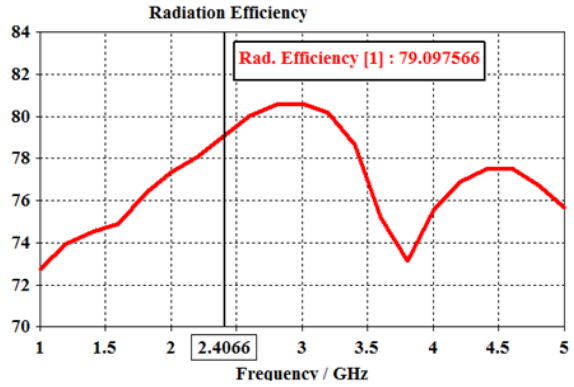

Fig. 5. Radiation efficiency (in %) versus frequency.

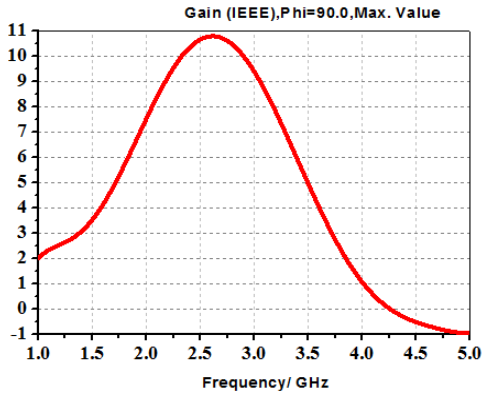

Fig. 6. 2D gain (in dB) as function of frequency.

The 3D radiation patterns for gain and directivity at 2.4 GHz are as plotted in Fig. 7. The simulated far field radiation patterns for dB gain in the azimuth plane for $\varphi = 0^0$ and 90^0 at 2.4 GHz for the graphene curved patch antenna are shown in Fig. 8, the symmetry and wide angular radiation patterns are observed. The proposed antenna offers the benefit of providing wide operating band hence facilitating its utility not only for short-range, high-data-rate communication ISM band but it also suits for UWB WBAN at 4-7 GHz in applications with human bodies. It can be made to resonate at multiple frequencies on account of inherent property of tunability of graphene material. The graphene based curved patch antenna built on silicon substrate ($\varepsilon_r = 11.9$) interestingly obtains multi resonant characteristics with simple design without resorting to complex methods of slot loading or texturing the patches by slits, stacked patches, extra microstrip resonators, additional parasitic patches as done by other researchers [4], [25-26].

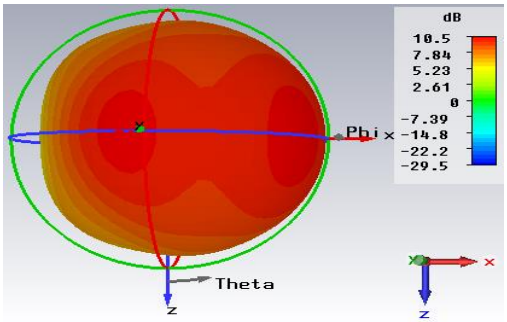

(a) Gain (in dB)

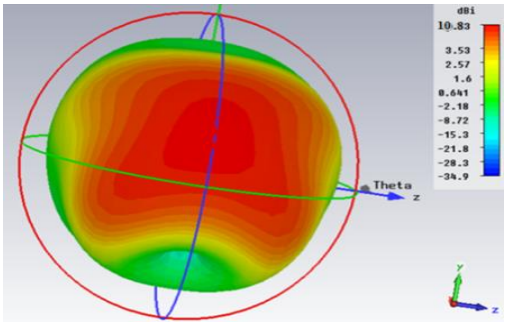

(b) Directivity (in dB)

Fig. 7. 3D polar plots.

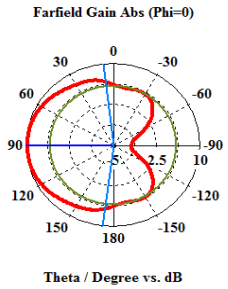

(a) Far field gain ($\varphi = 0^0$)

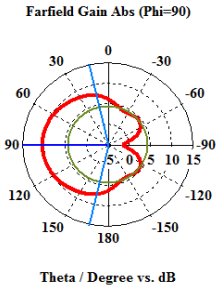

(b) Far field gain ($\varphi = 90^0$)

Fig. 8. Simulated radiation patterns of the graphene curved patch antenna.

Without air gap high permittivity of body tissues will absorb maximum amount of radiations which will have dangerous effect on body tissues. Further it also results in reducing the gain to a very low value. As the air gap increases antenna gain increases and SAR decreases. Figure 9 shows the measured SAR distributions of the graphene based curved patch antenna located on the human body phantom model. Since the wearable antennas are to be placed close to or even in contact with the human body, it is important that the level of electromagnetic radiation does not exceed the official recommendations. The present antenna design results in the maximum SAR value of 0.000148 W/Kg at 2.4 GHz calculated for an average mass of 10g of tissue which is

well below the specified limits [27].

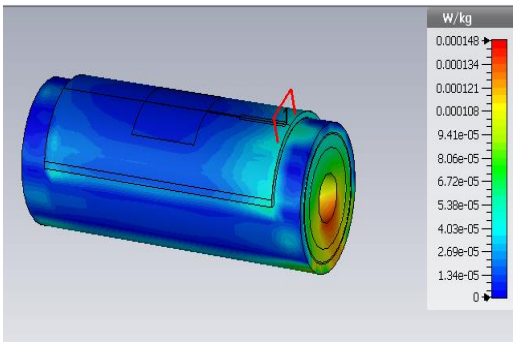

Fig. 9. SAR distribution at 2.4 GHz.

The SAR is an essential factor to be considered when the antenna is operated on or inside the body and to circumvent the absorption of the electromagnetic radiations emitted by the antenna by human body in WBAN, SAR value must be minimized. The SAR distribution is effected by the antenna parameters including its distance from body, radiation power and antenna type. The SAR value being influenced by the position of antenna from body, the antenna installation is done on the body keeping an air gap of 4 mm.

It has been observed that researchers are designing conformal antennas for wearable applications without analyzing the effect of radiated power from the antenna on human body.

Sankaralingam et al. have designed wearable textile antennas using different values of dielectric constant of fabric substrate materials and simulative analysis is performed using IE3D simulator based on Method of Moments (MoM) for GHz radiations [28]. All the results are presented for free space conditions ignoring the effects on body interaction. Moreover the gain and radiation efficiency achieved is more for the proposed graphene antenna. Much improvement in fractional bandwidth is also evident from Fig. 2. Huang et al. have designed printed graphene antenna on paper substrate and proved in their work that RF signal can be effectively radiated and received by the graphene antennas [29]. The experimental demonstration assures the potential use of graphene antenna in wireless wearable communications systems covering the bands for Wi-Fi, Bluetooth and WLAN by presenting a real life scenario. But the absorption effects of the antenna radiations on the human body have not been considered whereas the proposed antenna satisfies the permissible SAR limits. Overall the conformal graphene antenna performs well with enhanced gain of 10.19 dB at resonant frequency of 2.4 GHz and the maximum radiation efficiency constantly remains greater than 72% for the wideband of frequencies in 1-5 GHz range. The detailed comparative analysis performed is presented in Table 4.

Table 4: Comparison of proposed antenna with metallic patch antenna and other graphene antennas

Parameters		Proposed Design	Sankaralingam et al. [28]	Kwon et al. [4]	Huang et al. [29]
Material	Patch	Graphene	Copper	Copper	Graphene
	Substrate	Silicon with capping layer of SiO_2	Varieties of cotton and polyester	FR-4	Paper
Return Loss (S_{11}, dB)		-25.05 dB at 2.4 GHz -25.17 dB at 3.94 GHz	-28.5 at 2.44 GHz	-15 dB at 403.5 MHz -28.5 dB at 2.45 GHz	-18.7 dB at 1.97 GHz -19.2 dB at 3.26 GHz
Gain		10.5 dB at 2.4 GHz 2.8 dB at 3.94 GHz	7.730 dB	-31.98 dB at 403.5 MHz 0.24dB at 2.45 GHz	0.2 dB at 1.97 GHz -1dB at 3.26 GHz
Directivity		10.83 dB at 2.4 GHz	8.750 dB	Not evaluated	Not evaluated
VSWR value		1.118 at 2.4 GHz 1.12 at 3.94 GHz	Not evaluated	Not evaluated	Not evaluated
Radiation efficiency (%)		79.09 at 2.4 GHz 74.86 at 3.94 GHz	79.20 dB	Not evaluated	Not evaluated
Bandwidth		3.88 GHz	87.31 MHZ	15 MHz at 403.5 MHz 91 MHz at 2.45 GHz	1.29 GHz
SAR (W/Kg)		0.000148	Not evaluated	0.0087 at 403.5 MHz 0.0081 at 2.45 GHz	Not evaluated

V. CONCLUSION

In this paper the utility of graphene is investigated for designing curved patch antenna for flexible handy wireless body area network applications. An attempt has been made to examine the effect of radius of curvature on the resonant frequency which can be compensated by graphene tunability. The antenna however provides sufficient bandwidth to accommodate for the variations in resonant frequency.

The microstrip line edge fed graphene based curved

square patch antenna achieves acceptable radiation efficiency with minimum SAR in the operating range of 1-4.88 GHz. Quarter wave transformer is used for optimizing the resonant properties hence obtaining return loss of -25.05 dB at resonating frequency of 2.4 GHz and -25.17 dB at second resonating frequency of 3.94 GHz. FIT based CST microwave studio simulation software is used for graphene characterization and numerical modeling of the designed antenna. Owing to the tunability feature of graphene, the simple curved square patch antenna achieves wideband operation and is therefore suitable for UWB biotelemetry WBAN applications.

ACKNOWLEDGMENT

This work is supported by Department of Electronics and Communication Engineering of Sant Longowal Institute of Engineering and Technology, Longowal, Punjab, by providing software facilities such as HFSS, Matlab and other computational material.

REFERENCES

[1] S. Kumari and V. R. Gupta, "Measurement of specific absorption rate of monopole patch antenna on human arm," *International Journal Microwave Optical Technology*, vol. 10, pp. 190-194, 2015.

[2] N. A. Elias, N. A. Samsuri, M. K. A. Rahim, and N. Othman, "The effects of human body and bending on dipole textile antenna performance and SAR," *Microwave Conference Proceeding (APMC) Asia-Pacific Kaohsiung, Taiwan, 2012*, E-ISBN: 978-1-4577-1331-6, pp. 34-36, 2012.

[3] C. M. Krowne, "Cylindrical-rectangular microstrip antenna," *IEEE Transactions Antenna Propagation*, vol. 31, pp. 194-199, 1983.

[4] K. Kwon, J. Ha, S. Lee, and J. Choi, "Design of a dual-band on-body antenna for a wireless body area network repeater system," *International Journal Antenna Propagation*, pp. 1-5, 2012.

[5] A. Subhashini, "Design of microstrip patch antenna used in wireless body area network (WBAN)," *International Journal Scientific Research Development*, vol. 3, pp. 567-570, 2015.

[6] A. Elrashidi, K. Elleithy, and H. Bajwa, "The fringing field and resonance frequency of cylindrical microstrip printed antenna as a function of curvature," *Eurasip Journal Wireless Communication Networking*, vol. 3, pp. 1-12, 2012.

[7] T. Onishi and I. Fukai, "Analysis of microstrip antennas on a curved surface using the conformal grids FDTD method," *IEEE Transactions on Antenna Propagation*, vol. 42, pp. 423-427, 1993.

[8] G. Gottwald and W. Wiesbeck, "Radiation efficiency of conformal microstrip antennas on cylindrical surfaces," *Antenna Propagation Society International Symposium AP-S. Digest*, vol. 4, pp. 1780-1783, 1995.

[9] D. Correas-Serrano, J. S. Gomez-Diaz, J. Perruisseau-Carrier, and A. Alvarez-Melcon, "Graphene based plasmonic tunable low pass filters in the THz band," *Nano Technology, IEEE Transactions*, vol. 3, pp. 1145-1153, 2014.

[10] K. Luk, K. Lee, and J. S. Dahele, "Analysis of cylindrical-rectangular patch antenna," *IEEE Transactions on Antenna Propagation*, vol. 37, pp. 143-147, 1989.

[11] G. W. Hanson, "Dyadic green's functions and guided surface waves for a surface conductivity model of graphene," *Journal Applied Physics*, vol. 103, pp. 064302, 2008.

[12] M. E. Morote, J. Sebastian, J. S. Gomez-Diaz, and J. Perruisseau-Carrier, "Sinusoidally-modulated graphene leaky-wave antenna for electronic beamscanning at THz," *IEEE Transactions Terahertz Science Technology*, vol. 4, pp. 116-122, 2014.

[13] CST Microwave Studio Suite, User's Manual Computer Simulation Technology, Framingham, MA, USA, 2014.

[14] R. Bala and A. Marwaha, "Investigation of graphene based miniaturized terahertz antenna for novel substrate materials," *Elsevier Journal on Engineering Science and Technology, an International Journal*, ISSN: 2215-0986, pp. 1-7, 2015.

[15] M. Dragoman and D. Dragoman, "Graphene for microwaves," *IEEE Microwave Magazine*, vol. 11, pp. 81-86, 2010.

[16] S. Ghosh, I. Calizo, D. Teweldebrhan, et al., "Extremely high thermal conductivity of graphene: Prospects for thermal management applications in nanoelectronic circuits," *Applied Physics Letter*, vol. 92, iss. 15, pp. 151911, 2008.

[17] T. J. Balandin, P. Blake, R. R. Nair, et al., "Macroscopic graphene membranes and their extraordinary stiffness," *Nano Letter*, vol. 8, iss. 8, pp. 2442-2446, 2008.

[18] C. Lee, X. Wei, J. Kysar, and J. Hone, "Measurement of the elastic properties and intrinsic strength of monolayer graphene," *Science*, vol. 321, pp. 385-388, 2008.

[19] E. S. Ahmed, "Wearable conformal antennas for 2.4 GHz wireless body area networks," *Telkomnika*, vol. 11, pp. 175-180, 2013.

[20] J. R. James and P. S. Hall, *Handbook of Microstrip Antennas*, Peter Peregrinus, ISBN: 0-86341-150-9, London, 1989.

[21] J. Bahl and P. Bhartia, *Microstrip Antennas*, Artech House, Dedham, MA, 1980.

[22] I. Llatser, C. Kremers, D. Chigrin, J. Jornet, M. Lemme, A. Cabellos-Aparicio, et al., "Characterization of graphene-based nano-antennas in the terahertz band," *Antennas and Propagation (EUCAP), 6th European Conference*, pp. 194-198, 2012.

[23] R. Bala, A. Marwaha, and S. Marwaha, "Performance enhancement of patch antenna in terahertz region using graphene," *Current Nanoscience, Bentham Science*, ISSN: 1875-6786 (Online), ISSN: 1573-4137 (Print), vol. 11, pp. 1-7, 2015.
[24] S. Akcoltekin, M. El Kharrazi, B. Kohler, A. Lorke, and M. Schleberger, "Graphene on insulating crystalline substrates," *Nanotechnology*, vol. 20, pp. 155601, 2009.
[25] C. K. Wu and K. L. Wong, "Broadband microstrip antenna with directly coupled and gap coupled parasitic patches," *Microwave Optical Technology Letter*, vol. 22, pp. 348-349, 1999.
[26] A. A. Deshmukh and K. P. Ray, "Compact broadband slotted rectangular microstrip antenna," *IEEE Antenna Wireless Propagation Letter*, vol. 8, pp. 1410-1413, 2009.
[27] International Commission on Non-ionizing Radiation Protection, "Guidelines for limiting to time-varying electric, magnetic, and electromagnetic fields (up to 300 GHz)," Ed: Health Physics Society, 1998.
[28] S. Sankaralingam and B. Gupta, "Development of textile antennas for body wearable applications and investigations on their performance under bent conditions," *Progress In Electromagnetics Research B*, vol. 22, pp. 53-71, 2010.
[29] X. Huang, T. Leng, M. Zhu, et al., "Highly flexible and conductive printed graphene for wireless wearable communications applications," *Scientific Reports 5*, Article number: 18298, 2015.

Rajni Bala is presently working towards her Ph.D. at the Dept. of Electronics & Comm. Engg., SLIET Longowal, Deemed University. She obtained her M.Tech in (ECE) from SLIET Longowal, Deemed University in 2012 & B.Tech (Electronics and Communication Engg.) from MIMIT Malout, PTU Jalandhar in 2010. Her area of interest include Miniaturized Resonant THz antenna. She has published 24 research papers in refereed international and National journals and conferences.

Rajdeep Singh was born in Moga. He obtained his B.Tech in (ECE) from SLIET Longowal, Deemed University in 2014. He is presently working towards his M.Tech at the Dept. of Electronics & Comm. Engg., SLIET Longowal, Deemed University. His area of interest includes curved patch antenna for biomedical applications.

Anupma Marwaha is Professor in Electronics & Communication Engineering Department at SLIET Longowal, Distt. Sangrur, Punjab. Post Doctorate from GNDU, Amritsar in the year 2003 with specialization in the field of 'Design and Field Analysis of Electromagnetic Devices by FEM with applications to Communication Engg., Microwave and Antennas'. She has more than 75 publications to her credit in International and National Journals in the area of antenna design, bio-electromagnetics and in microscale and nanoscale structures.

Sanjay Marwaha is working as Professor in the faculty of EIE Dept. at SLIET, longowal, Punjab. He got his Ph.D. from Guru Nanak Dev University Amritsar in year 2000. He has more than 22 years of teaching experience and has more than 100 papers to his credit in various National & International Conferences and Journals. He is the author of Basic of Electrical Engineering and Basic of Electrical & Electronics Engineering; Satya Prakashan.

Active Metamaterial Transmission Line with Gain in SiGe BiCMOS Technology

C. X. Zhou [1], Yihu Li [2], Y. Z. Xiong [2], and W. Wu [1]

[1] Ministerial Key Laboratory of JGMT
Nanjing University of Science and Technology, Nanjing, 210094, China
zhouchx1010@gmail.com, wuwen@mail.njust.edu.cn

[2] Terahertz Research Center
CAEP, Chendu, 611731, China
yli2@e.ntu.edu.sg,eyzxiong@ieee.org

Abstract ─ We report the realization of an active composite right/left-handed (CRLH) metamaterial transmission line (TL) with gain. By employing the transistors in SiGe BiCMOS technology, an active CRLH TL has been realized exhibiting net gain, wide-band and flat S-parameter characteristics. Effective electromagnetic parameters of the active CRLH TL, including complex propagation constant γ, effective permittivity ε_{eff}, effective permeability μ_{eff} and index of refraction *n* are extracted, which reveal the left handed properties of the active CRLH TL. The electric plasma frequency f_{pe} and the magnetic plasma frequency f_{me} are observed in the proposed TL.

Index Terms─ Active, CRLH TL, metamaterial, SiGe BiCMOS.

I. INTRODUCTION

Metamaterials have special electromagnetic properties such as negative permittivity ε, negative permeability μ and negative index of refraction *n*, which are typically not observed in nature. Research on metamaterials has made great progress since experimental verification of negative index refraction [1] has been reported. Composite right/left-handed (CRLH) transmission line (TL) [2,3] and split ring resonators (SRRs) [4] are commonly two kinds of realization of metamaterials. However, the loss and narrow bandwidth inherently associated with the metamaterials are the main bottleneck that restrict their applications especially in high frequency. Active constituents, such as RF amplifer [5], gain medium rhodamine [6] and germanium tunnel diode [2] were adopted to alleviate the loss problem.

Silicon based SiGe CMOS technology is the most suitable platform for realization of the active CRLH TLs. Because it is available for producing various of active constituents such as transistors and diodes, and lumped elements such as inductance L and capacitance C. Also, it offers integration and small size which is a requirement as the unit length of the CRLH TL should be smaller than the wavelength. Thus, the operating frequency can be extended to microwave and millimeter-wave, even to terahertz (THz).

In this letter, an active CRLH TL with both gain and impedance matching in wideband is demonstrated. Effective electromagnetic parameters including transmission line complex propagation constant γ, effective permittivity ε_{eff}, effective permeability μ_{eff} and index of refraction *n* are extracted to analyze the characteristics of the active CRLH TL. The electric plasma frequency f_{pe} and the magnetic plasma frequency f_{me} are observed, which defined as the transition frequency between the negative and positive value of ε_{eff} and μ_{eff}, respectively.

II. DESIGN OF THE ACTIVE CRLH TL

The schematic of the active CRLH TL is shown in Fig. 1 (a), which contains two distributed unit cells and matching circuits. When the input signal is supplied to the base of the HBT transistor in one unit cell, the amplified output signal can be obtained in the collector. The output signals from each unit cell sum in phase as the delays of the input and output lines are made equal. Terminating matching loads are used to minimize destructive reflections. Its equivalent circuit model of one unit cell of the active CRLH TL is shown in Fig. 1 (b). The passive part of the active CRLH TL unit cell in Fig. 1 (b) is similar to the classic CRLH TL theory [7], including a series connection of inductance L_R and capacitance C_L and a shunt connection inductance L_L and capacitance C_R. They come from two parts: the lumped elements realized in Fig. 1 (a) and the parasitic effects of the HBT transistor. In this design, the designed values

Submitted On: January 30, 2016
Accepted On: May 3, 2016

of the passive part are: L_R =550.2 pH, L_L =249.0 pH, C_R= 220.1 fF, C_L=99.6 fF. Thus, the passive part is balanced at frequency:

$$f_0 = f_{se}(1/2\pi\sqrt{L_R C_L}) = f_{sh}(1/2\pi\sqrt{L_L C_R}) = 21.5 \text{ GHz}. \quad (1)$$

The active part of one unit cell in Fig. 1 (b) is an amplifier unit which provides a voltage-controlled current source to the traditional CRLH TL. It is used to not only compensate the loss from the lumped elements, but also providing gain to the CRLH TL.

Considering the parasitic effects of the transistors, the designed parameters in Fig. 1 (a) are L_{R1}=L_{R2}=500 pH, L_{L1}=L_{L2}=406 pH, C_{R1}=C_{R2}=148 fF, C_{L1}=C_{L2}=162.4 fF. The simulated and measured S parameters are shown in Fig. 2. The measured gain of the active CRLH TL is about 10.5 dB from 10.7 GHz to 31 GHz with ±1 dB ripple and good impedance matching can be observed in this band. Compared with other kinds of CRLH, the proposed CRLH TL in this paper has net gain, wide-band, and flat S-parameter characteristics. The left-handed properties of CRLH TL will be discussed by extraction of effective electromagnetic parameters in the following section.

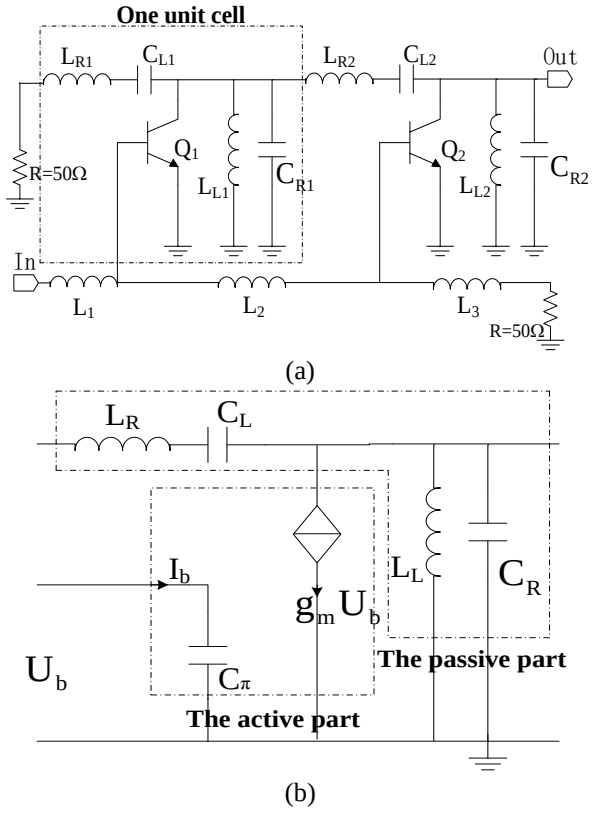

Fig. 1. (a) Schematic of the active CRLH TL. (b) The equivalent circuit model of one unit cell.

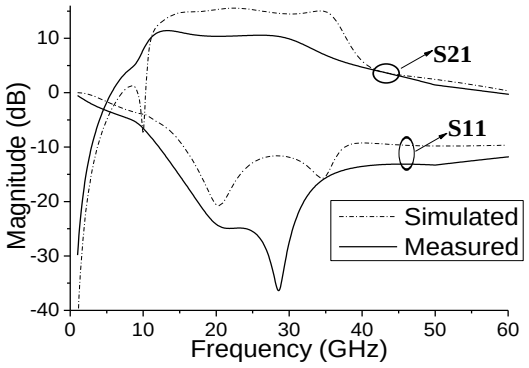

Fig. 2. Simulated (in dash line) and measured S-parameters (in solid line).

III. ANALYSIS OF THE ACTIVE CRLH TL

Effective electromagnetic parameters of passive metamaterials can be extracted from measured two-port S-parameters by Nicolson-Ross-Weir (NRW) approach [8-10]. In this method, the choice of sign of the transmission factor T and reflection factor Γ is determined by $|\Gamma| \le 1, |T| \le 1$. While for active metamaterials TL with gain in this design, the constraint is modified to $|\Gamma T| \le 1$. .With this method, the complex propagation constant γ=α+jβ (α is the propagation attenuation constant and β is the phase constant), effective permittivity ε_{eff}, effective permeability μ_{eff} and index of refraction *n* are shown in Fig. 3. From Fig. 3 (a), the negative β from 0 GHz to 19.5 GHz is observed. Thus, the TL exhibits left-handed property below 19.5 GHz and right-handed property above 19.5 GHz. This frequency is shifted downward compared with the designed frequency 21.5 GHz, which could be caused by the inaccuracy of the parameter extraction of the transistors and interconnects. Also, we can obtain negative α from 5 GHz to 57.5 GHz, which means that the magnitude of S21 is larger than 0 dB in this range. For further insight into the electromagnetic properties of the CRLH TL with gain, the effective permittivity ε_{eff} and permeability μ_{eff} are extracted and plotted in Fig. 3 (b). The inset shows the details of the original graph near zero-Y-axis. The real part of μ_{eff} is negative below 19.3 GHz and from 2.8 GHz to 19.5 GHz the real part of ε_{eff} is negative, which verify the left-handed properties below 19.5 GHz. Thus, the electric plasma frequency f_{pe} and the magnetic plasma frequency f_{me} is 19.3 GHz and 19.5 GHz, respectively. Below 3.4 GHz and above 7.2 GHz, the imaginary part of μ_{eff} is positive and from 3.4 GHz to 41.7 GHz, the imaginary part of ε_{eff} is positive, which account for the gain properties of the TL. The corresponding index of refraction *n* is calculated and plotted in Fig. 3 (c). The inset shows the details of the

original graph near zero-Y-axis. The real part of *n* is negative below 19.5 GHz, which indicates left-handed property of the CRLH TL in this band. From 5 GHz to 57.5 GHz, the imaginary part of *n* are negative, indicating the gain property of the CRLH TL.

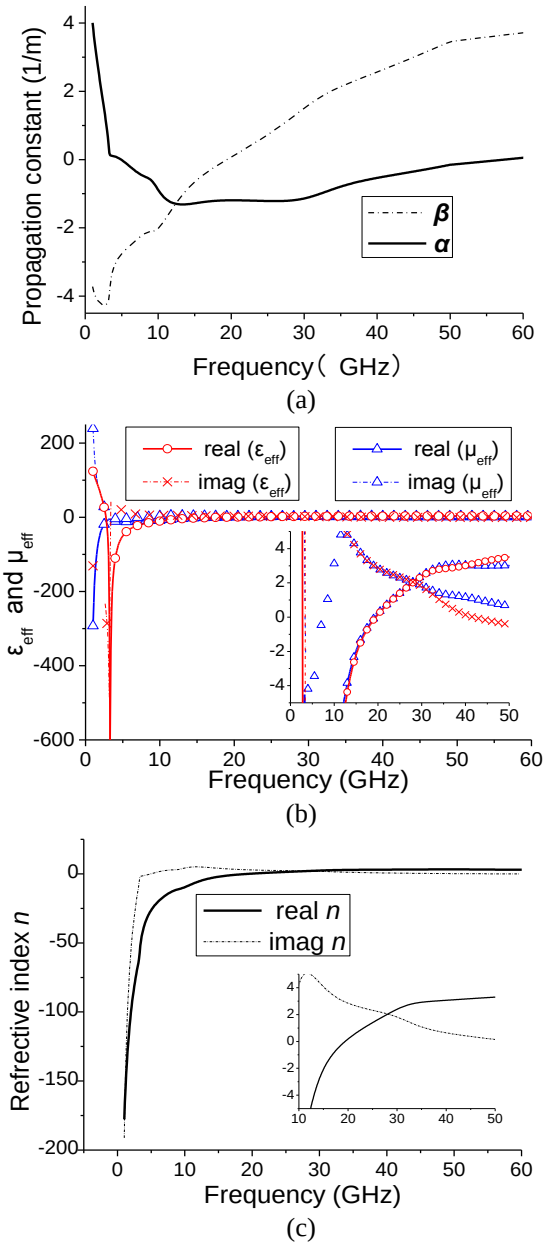

Fig. 3. (a) Extracted complex propagation constant γ(α+jβ) from measured two-port S-parameter. (b) Extracted effective permittivity ε_{eff} (red) and effective permeability μ_{eff} (blue) from measured two-port S-parameter. The inset shows the details near zero-Y-axis. (c) Extracted index of refraction *n* from measured two-port S-parameter. The inset shows the details near zero-Y-axis.

IV. CONCLUSION

In conclusion, we present an active CRLH TL based on BiCMOS technology. Improved performances were experimentally demonstrated in terms of high gain, wideband impedance matching and flat S-parameter characteristics. Effective electromagnetic parameters of the active CRLH TL are analyzed, which can be the basis to the design and application of active metamaterials. Potential applications of the proposed CRLH TL can be foreseen in filters, amplifiers, phase shifters etc.

ACKNOWLEDGMENT

This work is supported in part by NSFC under Grant No. 61401202.

REFERENCES

[1] R. A. Shelby, D. R. Smith, and S. Schulta, "Experimental verification of a negative index refraction," *Science*, vol. 292, pp. 77-79, Apr. 2001.

[2] T. Jiang, K. Chang, L. M. Si, L. Ran, and H. Xin, "Active microwave negative-index metamaterial transmission line with gain," *Phys. Rev. Lett.*, vol. 107, pp. 205503, Nov. 2011.

[3] A. A. Tavallaee, P. W. C. Hon, Q. S. Chen, T. Itoh, and B. S. Williams, "Active terahertz quantum-cascade composite right/left-handed metamaterial," *Appl. Phys. Lett.*, vol. 102, pp. 021103, Jan. 2013.

[4] A. L. Borja, J. Carbonell, V. E. Boria, and D. Lippens, "Highly selective left-handed transmission line loaded with split ring resonators and wires," *Appl. Phys. Lett.*, vol. 94, pp. 143503, Apr. 2009.

[5] Y. Yuan, B.-I. Popa, and S. A. Cummer, "Zero loss magnetic metamaterials using powered active unit cells," *Opt. Express*, vol. 17, pp. 16135-16143, Aug. 2009.

[6] S. Xiao, V. P. Drachev, and A. V. Kildishev, "Loss-free and active optical negative-index metamaterials," *Nature*, vol. 466, pp. 735-736, Aug. 2010.

[7] C. Caloz and T. Itoh, *Electromagnetic Metamaterials: Transmission Line Theory and Microwave Applications*. Wiley, New York, 2005.

[8] A. M. Nicolson and G. F. Ross, "Measurement of the intrinsic properties of materials by time-domain," *IEEE Trans. Instrum. Meas.*, vol. 19, no. 4, pp. 377-382, 1970.

[9] W. B. Weir, "Automatic measurement of complex dielectric constant and permeability at microwave frequencies," *Proc. IEEE*, vol. 62, pp. 33-36, Jan. 1974.

[10] J. Baker-Jarvis, E. J. Vanzura, and W. A. Kissick, "Improved techniques for determining complex permittivity with the transmission/reflection method," *IEEE. Trans. Microwave Theory Tech.*, vol. 38, pp. 1096-1103, Aug. 1990.

Chun-Xia Zhou (M'14) was born in Jiangsu Province, China, in 1985. She received the B.S. and Ph.D. degree in Electronic Engineering from Nankai University, Tianjin, China, in 2007 and 2012, respectively.

From September 2010 to February 2012, she was a joint Ph.D. student with the Department of Electrical and Computer Engineering, National University of Singapore (NUS), Singapore. From December 2012 to July 2012, she was a Research Fellow with Terahertz Science and Technology Research Center of China Academy of Engineering Physics, Chengdu, China. She is currently a Lecturer with the School of Electronic Engineering and Optoelectronic Technology, Nanjing University of Science and Technology, Nanjing, China. Her research interests include the design and optimization of microwave and millimeter-wave circuits, and microwave and millimeter-wave integrated circuits in CMOS technology.

Yihu Li received the B.S. degree in Electrical and Electronic Engineering from Nanyang Technological University, Singapore, in 2010, where he is currently working towards the Ph.D. degree in Electrical and Electronic Engineering.

He is currently attached to the Semiconductor Device Research Laboratory, China Academy of Engineering Physics.

Yong-Zhong Xiong (M'98–SM'02) received the B.S. and M.Eng. degrees in Communication and Electronic Systems from Nanjing University of Science and Technology, Nanjing, China, in 1986 and 1990, respectively, and the Ph.D. degree in Electrical and Electronic Engineering from Nanyang Technological University, Singapore.

From 1986 to 1994, he was with the Department of Electronic Engineering, Nanjing University of Science and Technology, Nanjing, China, where he was involved with microwave systems and circuit design. In 1994, he was a Research Scholar with Nanyang Technological University (NTU), Singapore. From 1995 to 1997, he was a Senior Engineer with the RF and Radios Department, Singapore Technologies. He was with the Microelectronics Center, NTU. Since September 2001, he was with the Institute of Micro-electronics, Agency for Science, Technology and Research, Singapore. He is currently a Professor and Director of the Semiconductor Device Research Laboratory, China Academy of Engineering Physics. He has authored or co-authored over 180 technical papers. His leading research areas include silicon-based monolithic integrated-circuit design and characterization for millimeter wave and terahertz applications and device RF and noise modeling and characterization.

Wen Wu(SM'10) received the Ph.D. degree in Electromagnetic Field and Microwave Technology from Southeast University, Nanjing, China, in 1997.

He is currently a Professor with the School of Electronic Engineering and Optoelectronic Technology and an Associate Director with the Ministerial Key Laboratory of JGMT, Nanjing University of Science and Technology, Nanjing, China.

He has authored and co-authored over 120 journal and conference papers. He has submitted five patent applications. His current research interests include microwave and millimeter-wave (mm-wave) theories and technologies, microwave and mm-wave detection, and multimode compound detection.

Wu was a six-time recipient of the Ministerial and Provincial-Level Science and Technology Award.

A Single-Layer Multi-Band Reflectarray Antenna in X/Ku/K-Bands

Zahra Hamzavi-Zarghani [1] and Zahra Atlasbaf [2]

[1] Faculty of Electrical and Computer Engineering
Tarbiat Modares University (TMU), Tehran, Iran
zahrahamzavi@yahoo.com

[2] Faculty of Electrical and Computer Engineering
Tarbiat Modares University (TMU), Tehran, Iran
atlasbaf@modares.ac.ir

Abstract ─ A new center-fed tri-band reflectarray antenna is presented in this paper. Elements of the reflectarray antenna are circular rings and patches loaded with slots. The proposed antenna operates in three bands (X, Ku and K). The introduced element, has been optimized to achieve large linear phase range at the three bands. Phase compensation is achieved by varying the size of elements. Height of the horn antenna has been optimized to get maximum gain and bandwidth at the three bands.

Index Terms ─ Microstrip, multi-band, reflectarray antenna, single layer.

I. INTRODUCTION

Reflectarray antennas combine the best features of reflector antennas and phased array antennas [1], so they have a lot of advantages such as: low profile, small mass and volume and low cost [2]. They are easy to manufacture and have potential for beam control and shaping. A reflectarray consists of many printed radiating elements, illuminated by a horn antenna. The elements provide required phase shift to produce a contoured beam [3].

A disadvantage of microstrip reflectarray antennas is their limited bandwidth because of the narrow bandwidth of microstrip patch elements and differential spatial phase delay as a result of different distance of the feed antenna to each element [4]. Phase compensation is achieved using patches with attached variable length stubs [5], or varying sized patches, dipoles and rings [6], or identical patches with different angular rotation [7]. Several techniques have been presented to overcome the limited bandwidth of the reflectarray antennas, such as using stacked two or more arrays [8], aperture-coupled patches [9], the elements with a large linear phase range [10], or multiresonant elements [11].

Multi-band operation of the reflectarray antenna can be achieved using two or more layers [12], or FSS-backed structures [13], with the drawback of more cost and complexity, while single-layer multi-band reflectarray antenna is easily manufactured and has a much less cost. In [14-16] single-layer, dual-band reflectarray antennas have been presented.

In this paper, a single- layer tri-band reflectarray antenna with linear polarization is introduced. By varying the size of the element, 600 degrees linear phase range within X-band (10.8 GHz~12.8 GHz), 680 degrees linear phase range within Ku-band (15.3 GHz~17.3 GHz) and 900 degrees linear phase range within K-band (24 GHz~26 GHz) have been achieved.

Variable sized patch elements have advantages of producing less dissipative loss and cross polarization, compared to the patches with attached variable length stubs [17].

II. DESIGN AND ANALYSIS OF THE PROPOSED REFLECTARRAY

A single-layer microstrip element, consisting of a circular ring and patch with slots on it, is introduced as the elements of tri-band reflectarray antenna in X-, Ku- and K-bands. The designed element structure is shown in Fig. 1. The unit cell is 10 mm. It operates in center frequencies of 11.8 GHz, 16.3 GHz and 25 GHz.

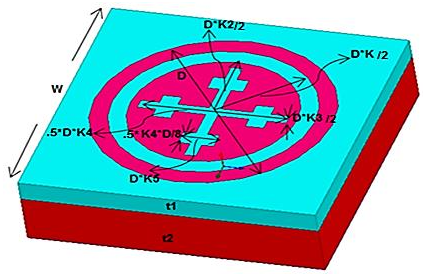

Fig. 1. Element structure.

Rogers 4003 with relative permittivity of 3.55 and the thickness (t1) of 0.813 mm is used as substrate. t2 is

Submitted On: September 15, 2015
Accepted On: February 25, 2016

an air distance between the ground plane and the substrate for obtaining a more linear phase range.

For analyzing the reflection phase characteristics of the element, an infinite periodic array model was performed, using the HFSS simulation [18]. The boundary conditions on the side walls are master-slave and the excitation is a floquet port as shown in Fig. 2 [2].

According to Fig. 1, there are six undefined parameters (k, k2, k3, k4, k5 and t2) whose values, should be optimized to obtain a large linear phase range at the three bands. Primary values of these parameters are chosen in a way that the element has three resonant frequencies.

Figures 3 to 8, show the phase responses of the element for different values of parameters at center frequencies in each band when one parameter changed and the other parameters keep unchanged, in order to study the influence of each parameter on the phase curves. It can be seen that k2 and k4 have the most effect on the phase response. Also we find that K3, K4 and K5 does not much effect on the phase curves at the first band and it shows that the slots are responsible for exciting two other bands. The curves indicate that the best values for these parameters are k=0.85, k2 = 0.7, k3 = 0.1, k4 = 1.25, k5 = 0.15, t2 = 2 mm, because with these values of parameters, the curves are more linear than other values.

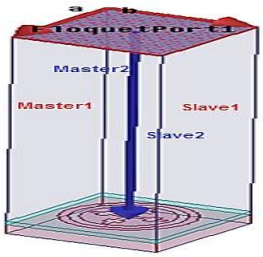

Fig. 2. HFSS model for obtaining the phase response.

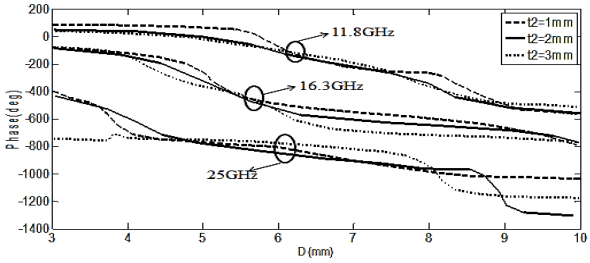

Fig. 3. The phase response of the element for different values of t2: (k=0.85, k2 = 0.7, k3 = 0.1, k4 = 1.25, k5 = 0.15).

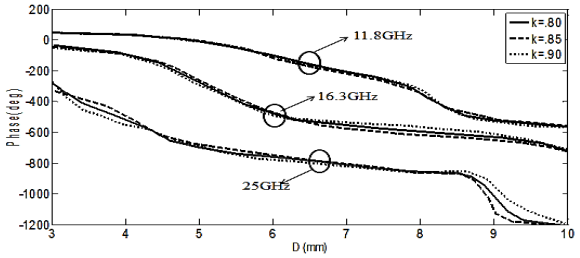

Fig. 4. Phase response of the element for different values of k: (t2=2 mm, k2 = 0.7, k3 = 0.1, k4 = 1.25, k5 = 0.15).

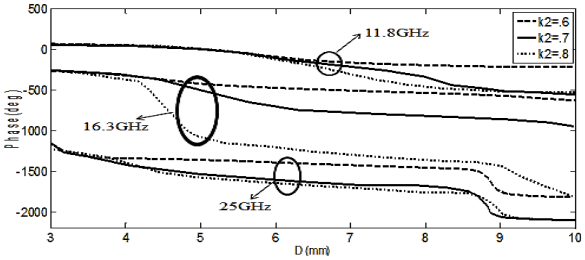

Fig. 5. The phase response of the element for different values of k2: (k=0.85, k3 = 0.1, k4 = 1.25, k5 = 0.15, t2=2 mm).

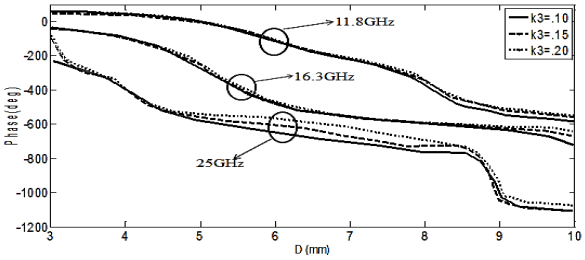

Fig. 6. The phase response of the element for different values of k3: (k=0.85, k2 = 0.7, k4 = 1.25, k5 = 0.15, t2=2 mm).

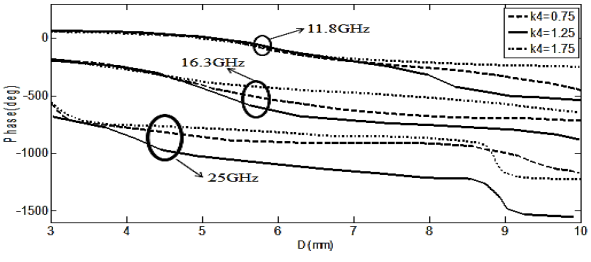

Fig. 7. The phase response of the element for different values of k4: (k=0.85, k2 = 0.7, k3 = 0.1, k5 = 0.15, t2=2 mm).

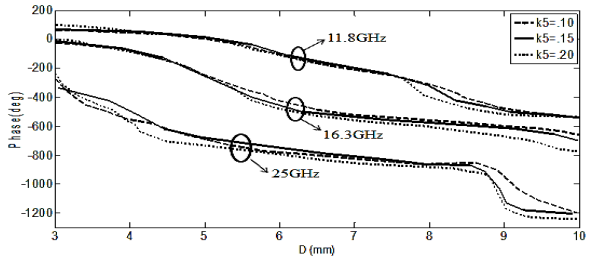

Fig. 8. The phase response of the element for different values of k5: (k=0.85, k2 = 0.7, k3 = 0.1, k4 = 1.25, t2=2 mm).

With these optimized parameters and by varying the ring size, 600 degrees linear phase range at 11.8 GHz and 680 degrees linear phase range at 16.3 GHz and 900 degrees linear phase range at 25 GHz have been achieved, as shown in Figs. 9 to 11. They also show that the phase curves, in all three bands are parallel in adjacent frequencies, resulting in a good bandwidth of the reflectarray antenna, designed with this element. Figure 12 shows the amplitude of the reflection coefficient for the proposed element. It can be seen that by increasing the frequency, dielectric loss increases.

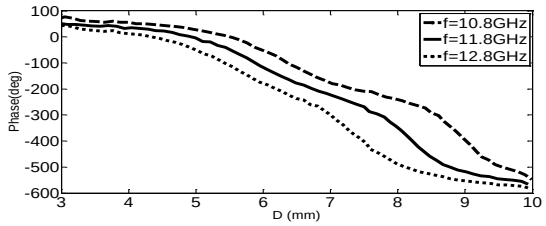

Fig. 9. Phase response to different frequencies at X-band.

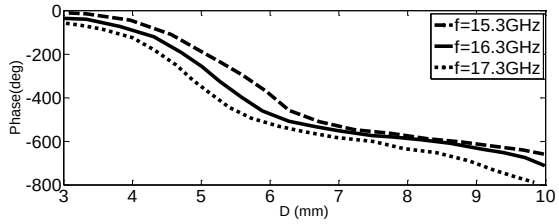

Fig. 10. Phase response to different frequencies at Ku-band.

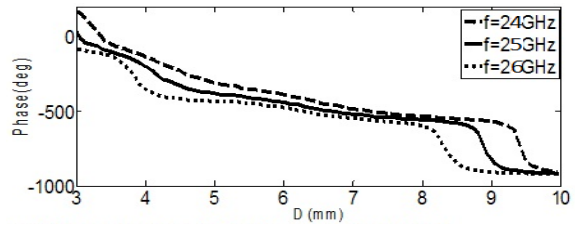

Fig. 11. Phase response to different frequencies at K-band.

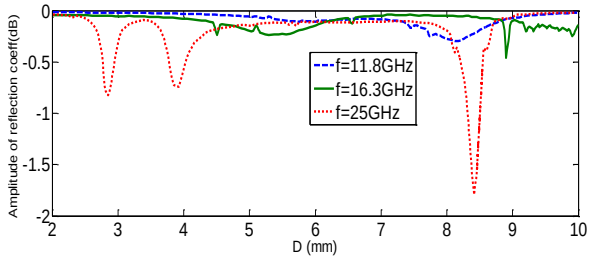

Fig. 12. Amplitude of the reflection coefficient for the element.

Figures 13 to 15 show the phase responses for different angles of incidence in the three bands. It is concluded that at 11.8 GHz the phase curves for theta=20 and 40 are the same as the phase curve for the normal incidence, but for oblique incidence more than 60 degrees, we cannot assume that it is the same as the normal incidence, because they are not similar enough according to Fig. 13. At 16.3 GHz and 25 GHz the phase curves for theta=20 and 30 are almost the same as normal incidence but for oblique incidence more than 40, it is not true. According to Equation (1) (where θ is angle of wave incidence, D is the biggest dimension of the reflectarray aperture and F is focal point of the reflectarray antenna), and maximum angles of incidence whose curves can be considered similar as the normal incidence (60 degrees for 11.8 GHz and 40 degrees for 16.3 GHz and 24 GHz), the ratio of F/D should be more than 0.29 at 11.8 GHz and 0.6 at 16.3 GHz and 25 GHz;

$$\theta = \tan^{-1}(D/2F). \quad (1)$$

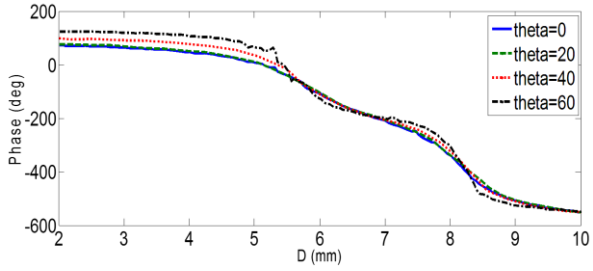

Fig. 13. Phase responses of the element at 11.8 GHz.

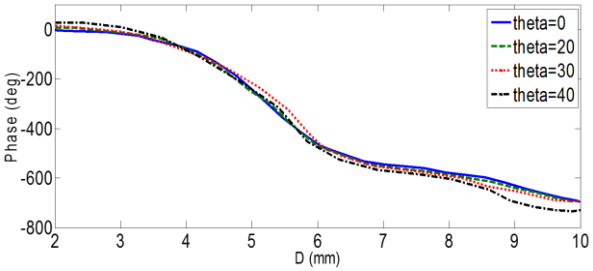

Fig. 14. Phase responses of the element at 16.3 GHz.

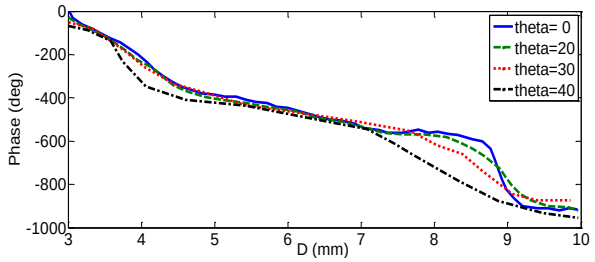

Fig. 15. Phase responses of the element at 25 GHz.

For feeding the reflectarray antenna, two horn antennas are used. The first horn is a pyramidal one with 4.8×3.3 cm^2 aperture size used for X- and Ku-bands and the second horn is a pyramidal one too, with 3.5×2.7 cm^2 aperture size used for feeding the reflectarray in K-band. Figure 16 shows the radiation patterns of the feeds at the center frequencies.

Next, the feed position is determined. It should be optimized, so that the required phase delay, calculated from the formula 1 [17] (where k0 is the propagation constant in a vacuum, di is the distance from the phase center of the feed to the element i, (xi, yi) is the coordinates of the element i, (xf, yf, zf) is the coordinates of the phase center of the feed and (θb, Ψb) is the direction of the main beam) is achieved at the three bands simultaneously, with the minimum phase error for each element.

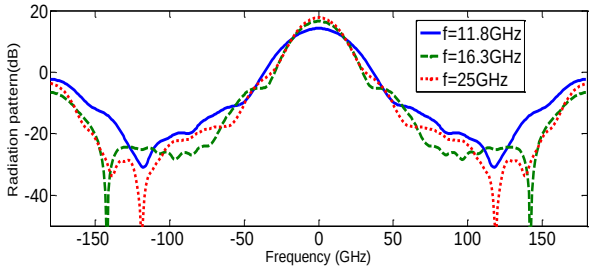

Fig. 16. Radiation patterns of the feeds in center frequencies at the three bands.

In other words, the feed position, should be considered in a way that, the size of each element, determined from the phase curves, is almost the same for the three bands, so that the single-layer reflectarray will operate properly at the three bands. The required phase shift was calculated with Matlab program[19] for each element at each band for several different feed positions and finally the optimum value for the distance, between the horn and the reflectarray antenna was chosen so that the phase curves in each three bands, could satisfy the Equation (2). If the height of the horn antenna is considered to be 22 cm for the first two bands and 28 cm for the third band, maximum required phase shift at 11.8 GHz will be 500 degrees, at 16.3 GHz will be 590 degrees and at 25 GHz will be 700 degrees. They are not the whole phase ranges which have been achieved of the element. By varying D from 3 mm to 8.5 mm required phase shift, can be satisfied at the three bands:

$$\Phi(R) = k_0(d_i - (x_i \cos(\Psi_b) + y_i \sin(\Psi_b)) \sin(\theta_b)), \quad (2)$$

$$d_i = ((x_i - x_f)^2 + (y_i - y_f)^2 + z_f^2)^{1/2}. \quad (3)$$

After finding the optimum feed position and calculating the size of each element, the elements are set in the reflectarray aperture in the proper positions, the horn antenna is put in the optimized location, and the boundary conditions are determined in CST Microwave Studio environment [20]. In order not to waste the simulation time and the computer memory, the symmetry planes are used.

III. RESULTS

A 21 cm×18.9 cm single-layer center-fed tri-band reflectarray antenna using 387 variable sized patch elements has been designed and fabricated on the 2 mm air and 0.813 mm Rogers 4003 substrate, as shown in Fig. 17. The feed position has been optimized to obtain minimum phase error and more efficiency at the three bands.

Figure 18 shows the measurement equipments and fabricated antenna with the 22 cm optimized distance of the horn antenna and reflectarray.

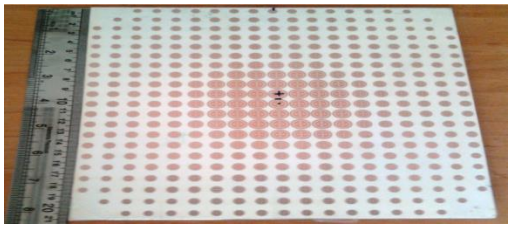

Fig. 17. Fabricated multi-band reflectarray antenna.

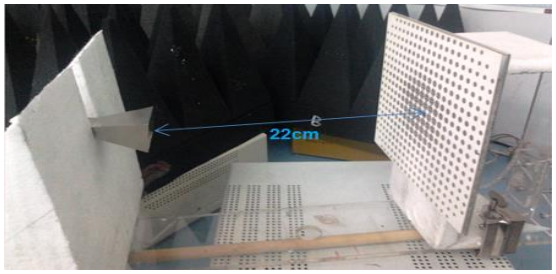

Fig. 18. Measurement equipment.

The simulated and measured radiation patterns for the E-plane and H-plane at the center frequencies of 11.8 GHz and 16.3 GHz are shown in Figs. 19 to 22. The side lobe level of this antenna is not good because the array is small and the feed aperture is big and it causes feed blockage. To overcome this problem, we should design bigger array and offset feed.

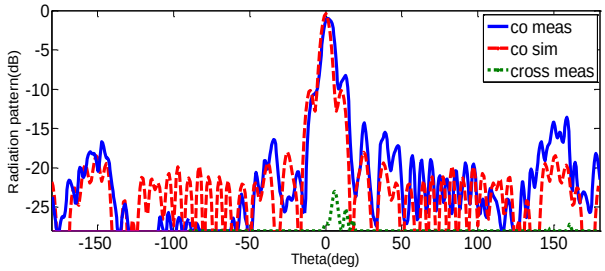

Fig. 19. Measured and simulated radiation pattern at 11.8 GHz for the E-plane.

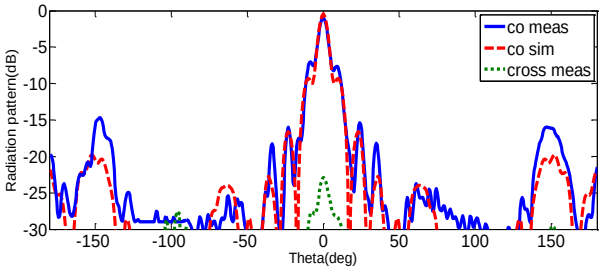

Fig. 20. Measured and simulated radiation pattern at 11.8 GHz for the H-plane.

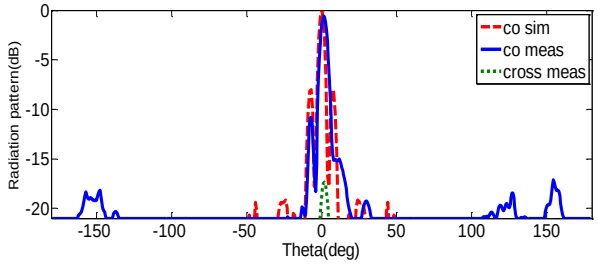

Fig. 21. Measured and simulated radiation pattern at 16.3 GHz for the E-plane.

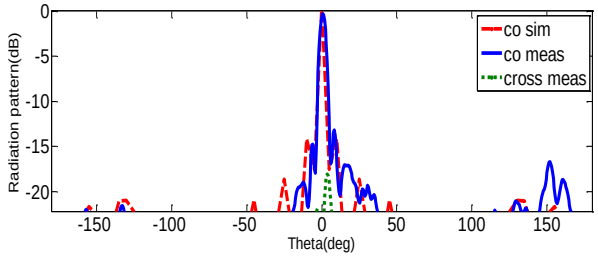

Fig. 22. Measured and simulated radiation pattern at 16.3 GHz for H-plane.

Because the measurement equipments don't have the potential to operate at very high frequencies, measurement of the antenna parameters in the third band, with the center frequency of 25 GHz was not possible for us, so the simulation has been done with two different methods of Transient Solver Parameters and Frequency Domain Solver Parameters. Figures 23 and 24 show radiation patterns at 25 GHz in the E-plane and H-plane, comparing these two methods.

Figure 25 shows the maximum gain of 22.9 dB at 11.8 GHz with 2980 MHz, 3 dB bandwidth; Fig. 26 shows the maximum gain of 27.5 dB with 2990 MHz, 3 dB bandwidth; Fig. 27 shows the maximum gain of 27.5 dB with 2500 MHz, 3 dB bandwidth.

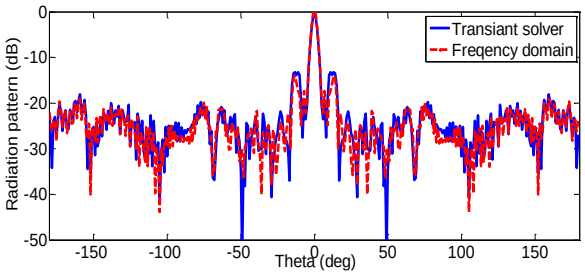

Fig. 23. Simulated radiation pattern at 25 GHz for E-plane with 2 different methods.

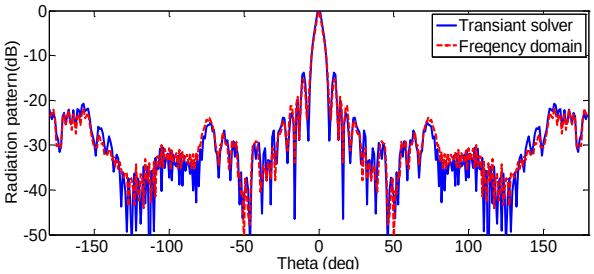

Fig. 24. Simulated radiation pattern at 25 GHz for H-plane with 2 different methods.

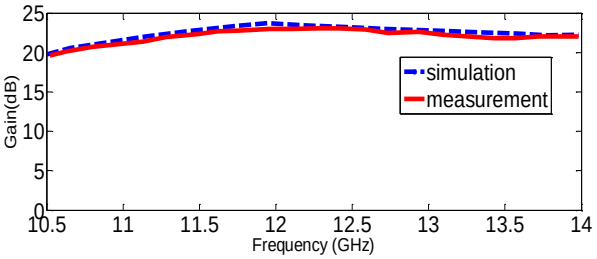

Fig. 25. Gain of the reflectarray antenna in X-band.

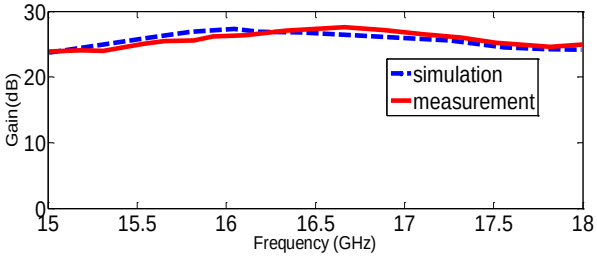

Fig. 26. Gain of the reflectarray antenna in Ku-band.

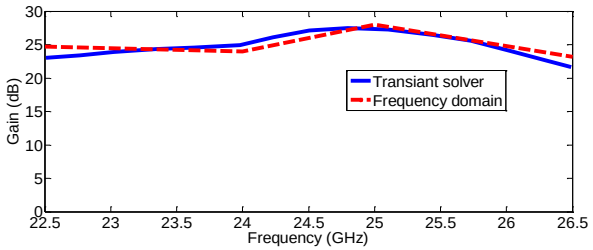

Fig. 27. Simulated gain of the reflectarray antenna in K-band.

The reflectarray antenna efficiency is 35.6% at 11.8 GHz, 33% at 16.3 GHz and 20% at 25 GHz. The most important reason that the efficiency is low, is the feed blockage due to the center-fed design. Feed-blockage shows its effect more at higher frequency because of reduction of the wavelength. Another reason is dielectric loss tangent. According to Fig. 12, this loss is much higher at 25 GHz. That's why the efficiency at 25 GHz is lower than the first two bands. By designing, offset-fed reflectarray and using substrate with lower dielectric loss tangent, much higher efficiency can be achieved.

IV. CONCLUSION

A tri-band single-layer patch and ring element was introduced to design a tri-band microstrip reflectarray antenna. Phase compensation was achieved by varying the size of the elements. By optimizing the element, 600 degrees linear phase range at 11.8 GHz, 680 degrees at 16.3 GHz and 900 degrees at 25 GHz was achieved. Feed position was optimized to get a minimum phase error and obtain better efficiency. The designed reflectarray antenna was simulated with CST Microwave Studio, fabricated and measured. Measurement results show good agreement with simulation results. The reflectarray antenna operates properly at the three bands with wide bandwidth.

REFERENCES

[1] Y. H. Cho, W. J. Byun, and M. S. Song, "High gain metal-only reflectarray antenna composed of multiple rectangular grooves," *IEEE Trans. Antennas Propag.*, vol. 59, no. 12, pp. 4559-4568, Dec. 2011.

[2] R. S. Malfajani and Z. Atlasbaf, "Design and implementation of a broadband single layer circularly polarized reflectarray antenna," *IEEE Antennas Wireless Propag. Lett.*, vol. 11, pp. 973-976, 2012.

[3] M. Arrebola, J. A. Encinar, and M. Barba, "Multifed printed reflectarray with three simultaneous shaped beams for LMDS central station antenna," *IEEE Trans. Antennas Propag.*, vol. 56, no. 6, pp. 1518-1527, June 2008.

[4] J. Huang, "Bandwidth study of microstrip reflectarray and a novel phased reflectarray concept," *in Proc. IEEE APS/URSI Symp.*, Newport Beach, CA, pp. 582-585, June 1995.

[5] H. Hasani, M. Kamyab, and A. Mirkamali, "Broadband reflectarray antenna incorporating disk elements with attached phase-delay lines," *IEEE Antennas Wireless Propag. Lett.*, vol. 9, pp. 156-158, 2010.

[6] J. A. Encinar, M. Arrebola, L. F. Fuente, and G. Toso, "A transmit-receive reflectarray antenna for direct broadcast satellite applications," *IEEE Trans. Antennas Propag.*, vol. 59, no. 9, pp. 3255-3264, Sep. 2011.

[7] J. Huang and R. J. Pogorzelski, "A Ka-band microstrip reflectarray with elements having variable rotation angles," *IEEE Trans. Antennas Propagat.*, vol. 46, pp. 650-656, May 1998.

[8] J. A. Encinar and J. A. Zornoza, "Broadband design of three-layer printed reflectarrays," *IEEE Trans. Antennas Propag.*, vol. 51, no. 7, pp. 1662-1664, July 2003.

[9] E. Carrasco, M. Barba, and J. A. Encinar, "Reflectarray element based on aperture - coupled patches with slots and lines of variable length," *IEEE Trans. Antennas Propagat.*, vol. 55, no. 3, pp. 820-825, Mar. 2007.

[10] R. S. Malfajani and Z. Atlasbaf, "Design and implementation of a broadband single-layer reflectarray antenna with large-range linear phase elements," *IEEE Antennas Wireless Propag. Lett.*, vol. 11, pp. 1442-1445, 2012.

[11] Q. Li, Y. Jiao, and G. Zhao, "A novel microstrip rectangular-patch/ring-combination reflectarray element and its application," *IEEE Antennas Wireless Propag. Lett.*, vol. 8, pp. 1119-1122, 2009.

[12] C. Han, C. Rodenbeck, J. Huang, and K. Chang, "A C/Ka dual-frequency dual-layer circularly polarized reflectarray antenna with microstrip ring elements," *IEEE Trans. Antennas Propagat.*, vol. 52, pp. 2871-2876, Nov. 2004.

[13] J.-F. Li, Q. Chen, S.-W. Qu, Q. Yuan, and K. Sawaya, "Dual-frequency reflectarray design using sandwiched FSS," *Asia-Pacific Microw. Conf. (APMC)*, pp. 877-880, 2010.

[14] T. Smith, U. Gothelf, O. S. Kim, and O. Breinbjerg, "Design, manufacturing, and testing of a 20/30-GHz dual-band circularly polarized reflectarray antenna," *IEEE Antennas Wireless Propag. Lett.*, vol. 12, pp. 1480-1483, 2013.

[15] R. S. Malfajani and Z. Atlasbaf, "Design and implementation of a dual-band single layer reflectarray in X and K bands," *IEEE Trans. Antennas Propagat.*, vol. 62, pp. 4425-4431, 2014.

[16] Z. Hamzavi-Zarghani and Z. Atlasbaf, "A new broadband single-layer dual-band reflectarray antenna in X- and Ku-bands," *IEEE Antennas*

Wireless Propag. Lett., vol. 14, pp. 602-605, 2015.
[17] J. Huang and J. Encinar, *Reflectarray Antennas*. Piscataway, NJ: IEEE Press, 2008.
[18] Ansoft HFSS User's Manual, Ansoft Corporation, 2010.
[19] Matlab package, ver. 2010.
[20] CST Microwave Studio, ver. 2008.

Design and Realization of a Wideband Microstrip Filter Using Signal-Interaction Techniques

Lixue Zhou [1,2], YingZeng Yin [1], Wei Hu [1], and Xi Yang [1]

[1] National Key Laboratory of Science and Technology on Antennas and Microwaves
Xidian University, Xi'an 710101, P. R. China

[2] Department of Microwave Engineering
Xi'an Electronic Engineering Research Institute, Xi'an 710100, P. R. China
Vesslan_zhou@163.com, yyzeng@mail.xidian.edu.cn, mwhuwei@163.com, yangxi@mail.xidian.edu.cn

Abstract ─ The signal-interaction techniques are adopted in this paper to design a novel wideband microstrip filter. The signal is transmitted from input port to the output one through two transmission paths in parallel which is composed of a wideband 180° inverter based on microstrip line and a 3λ/4 transmission line. Besides, two λ/4 shorted-ended lines is employed to improve the passband transmission performance of the BPF (Bandpass Filter). It is demonstrated from the simulation and measurement results of the novel BPF that three transmission zeros leading to the good harmonic suppression performance are achieved for the BPF operating from 0.99 to 2.51 GHz with 3-dB fractional bandwidth of 86.8%.

Index Terms ─ Passband, phase inverter, transmission path, transmission pole, transmission Zero.

I. INTRODUCTION

Recently, it is increasingly demanded for the filters with wide operating band in wireless communication area. In the engineering application, the interference signal is required to be suppressed for the wideband BPF. Various kinds of wideband filters employing parallel-coupled lines, ring resonators, short/open stubs, and composite microstrip coplanar-wave guide structure were designed and analyzed [1-9]. In [1-3], the parallel-coupled lines were observed to be good candidates for wideband systems design because of the advanced features such as simple design, compact size, and good linearity. However, smaller gap between the parallel-coupled lines is needed to achieve wider fractional bandwidth, which is not easy to fabricate. In [4-5], some wideband filters are implemented by cascading a low- and high-pass filter with good out-of-band rejection. However, there are some drawbacks for these structures, such as larger circuit size, and imperfect group delay over passband. In [6-9], filters was achieved by using etched patterns in the ground plane or via holes. Inevitably, the structures with etched patterns in the ground plane both have disadvantages as well, for instance, package problems, sensitivity, In [10-12], the disadvantages referred above is overcome by introducing two parallel transmission paths. Based on the concept of the signal interaction, several improved wideband filters are fabricated. However, for the adoption of another transmission path, the size of BPF is increased. So, in order to realize the miniaturization, 180° phase inverter is added to stand for a transmission line [13-14]. Even through, it is not convenient to adjust the 3-dB bandwidth of the filters.

In this paper, by adopting the signal interaction concept, a compact improved wideband bandpass filter using two shorted stubs and a 180° phase inverter based on microstrip line [15] is proposed. And it fails to be complicated to tune the 3-dB bandwidth of the filter through adjusting the characteristic impedances ratio of two transmission paths. Without other lowpass or bandstop networks, wide upper stopband can be implemented. In the following sections, detailed theoretical analysis, simulation and experimental result are given respectively.

II. THE ANALYSIS OF THE NOVEL WIDEBAND FILTER

The passband performance of the proposed filter is supposed to be improved through shunting one quarter wavelength short stub to the input and output 50 Ω feeding line [2]. Hence, The RF component is adopted here for the designed broadband bandpass filter, as demonstrated in Fig. 1.

In Fig. 1, two different transmission paths, one of which is θ in electrical length and another is 3 θ in electrical length (θ = 90° at the center frequency f_0,), are employed to transmit the signal from input port the output one. The characteristic impedance is denoted as

Submitted On: March 9, 2016
Accepted On: May 3, 2016

Z_1 and Z_2. To realize the miniaturization, an 180º inverter is added in path 1 to replace a transmission line. And two short-ended lines, θ in electrical length and Z_s characteristic impedance, are separately connected in parallel to the input and output transmission line with characteristic impedance of 50 Ω.

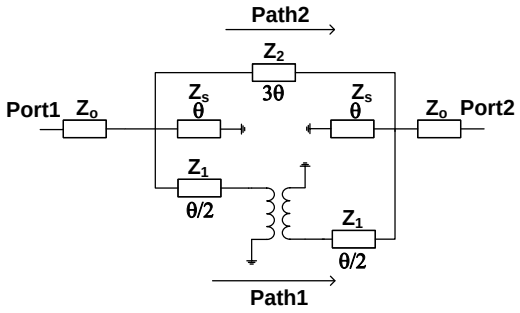

Fig. 1. Circuit of the novel wideband filter in this paper.

It is deduced from the signal-interaction concepts that the passband of the proposed filter can be achieved by the following equation [16]:

$$\theta_1(f_0) = \theta_2(f_0) \pm 2n\pi, \quad (n = 0,1,2...). \tag{1}$$

For the electrical length relationship between two different paths $\theta_1(f_0)=180°+\theta(f_0)=\theta_2(f_0)=3\theta(f_0)=270°$, a passband feature of the novel filter can be easily obtained at f_0 during the propagation of the signal from Port1 to Port2. In addition, at the second harmonic $2f_0$, $\theta_1(2f_0)=180°+\theta(2f_0)=360°=\theta_2(2f_0)-180°=2\theta(2f_0)-180°$, it is supposed to realize a stopband performance owing to the fact that signals from Path1 and Path2 are in the same magnitude but out-of-phase.

The ABCD matrix of the shorted lines, the 180° swap, and the two transmission paths are:

$$Ms = \begin{bmatrix} 1 & 0 \\ 1/\ jZs\tan\theta & 1 \end{bmatrix}, \tag{2}$$

$$M_{swap} = \begin{bmatrix} -1 & 0 \\ 0 & -1 \end{bmatrix}, \tag{3}$$

$$M_1 = \begin{bmatrix} \cos\theta/2 & jZ_1\sin\theta/2 \\ jY_1\sin\theta/2 & \cos\theta/2 \end{bmatrix}, \tag{4}$$

$$M_2 = \begin{bmatrix} \cos 3\theta & jZ_2\sin 3\theta \\ jY_2\sin 3\theta & \cos 3\theta \end{bmatrix}. \tag{5}$$

For Path1, the *ABCD* parameter matrix is $M_s\times M_1\times M_{swap}\times M_1\times M_s$; for Path2, the *ABCD* parameter matrix is $M_s\times M_2\times M_s$. After the *ABCD*-, *Y*-, and *S*-parameter conversions, two transmission zeros can be obtained when S_{21}= 0:

$$\theta_{tz1} = \arcsin\sqrt{(3Z_2 - Z_1)/4Z_2}, \tag{6}$$

$$\theta_{tz2} = \pi - \arcsin\sqrt{(3Z_2 - Z_1)/4Z_2}. \tag{7}$$

It is analyzed from above that one transmission zero appears when $\theta=\pi$. And, based on (6) and (7), another two transmission zeros which are determined by Z_1/Z_2 can be found symmetrically around θ=180°. How the transmission zeros and 3-dB fractional bandwidth is controlled by the ratio of Z_1 and Z_2 is indicated in Fig. 2. It is obvious that through changing Z_1/Z_2, the bandwidth for the filter is able to be adjusted conveniently. Besides, transmission zeros of the bandpass filter fails to be affected by the value of characteristic impedance Z_s, as shown in Fig. 3, where Z_1=Z_2=80 Ω. Moreover, when S_{11}= 0, we can get the following relationship:

$$A\tan^2\theta * \tan 2\theta + B\tan 2\theta - 2C\tan\theta = 0. \tag{8}$$

$$A = Z_1^2Z_2^2Z_S^2 - Z_0^2Z_1^2Z_S^2 - Z_0^2Z_2^2Z_S^2, B = Z_0^2Z_1^2 + Z_0^2Z_2^2 - 4Z_0^2Z_1Z_2,$$

$$C = Z_0^2Z_1Z_2Z_S + Z_0^2Z_1Z_2Z_S^2.$$

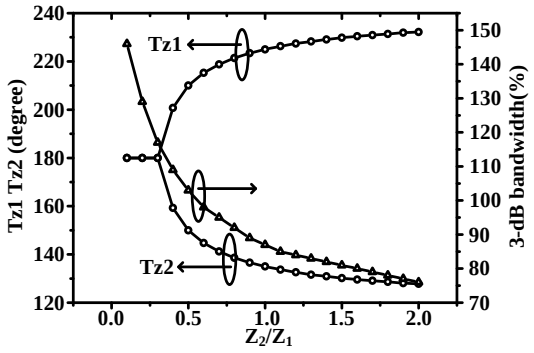

Fig. 2. Transmission zeros and the 3-dB bandwidth.

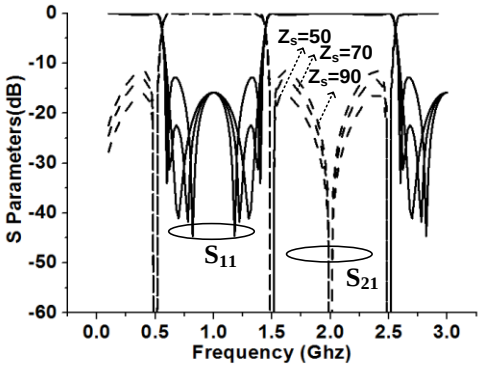

Fig. 3. S_{11} and S_{21} of circuit simulation.

The numbers of the transmission poles in the passband for the bandpass filter are mainly determined by the roots of the Equation (8), and the roots of the Equation (8) depend on the coefficients *A*, *B*, and *C*. Table 1 illustrates the numbers of the transmission poles for two cases in the Equation (8). In addition, the simulated results for the transmission poles are shown in Fig. 4 and Fig. 5, from which we can find that due to the introduction of the two shorted lines with characteristic

impedance Z_s, several transmission poles can be realized and thus improving the passband transmission characteristic for the filter.

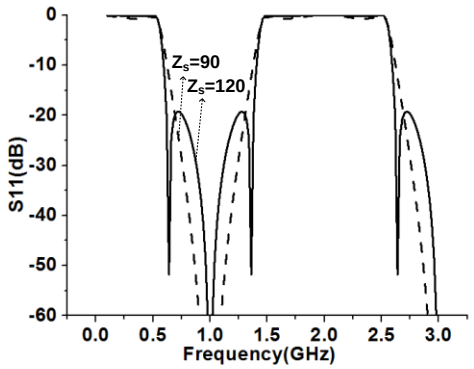

Fig. 4. Transmission pole (Z_1=Z_2=100 Ω).

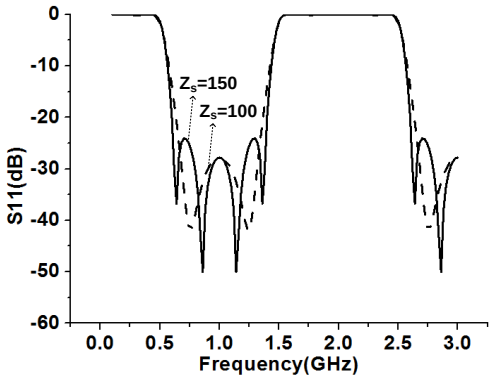

Fig. 5. Transmission pole (Z_1=120 Ω, Z_2=80 Ω).

Table 1: Numbers of transmission poles

Z_1 Z_2 Z_s		Transmission Poles
Z_1=100 Ω	Z_s>Z_1/2	$\theta_{tp1}<\theta_{tp2}=\pi/2<\theta_{tp3}$
Z_2=100 Ω	Z_s<Z_1/2	$\theta_{tp1}=\theta_{tp2}=\theta_{tp3}=\pi/2$
Z_1=120 Ω	Z_s>max(Z_1,Z_2)	$\theta_{tp1}=\theta_{tp2}<\pi/2<\theta_{tp3}=\theta_{tp4}$
Z_2=80 Ω	Z_s<max(Z_1,Z_2)	$\theta_{tp1}<\theta_{tp2}<\pi/2<\theta_{tp3}<\theta_{tp4}$

III. NOVEL WIDEBAND FILTER BASED ON 180o INVERTER

What's is analyzed above is focused on how to select the exact values of Z_1, Z_2 and Z_s, if one is given the design index. Besides, to design the novel wideband filter of excellent performance, one should construct a wideband 180° phase inverter. In this paper, the critical component [15] shown in Fig. 6 based on slot line and short-ended coupling line is employed to produce the 180° phase difference. And, the phase simulation result is given in Fig. 7.

Observing Fig. 7, one is able to conclude that the phase difference between the proposed phase inverter and a length of microstrip line nearly equals 180° from 1 GHz to 4 GHz. All the major parameters including gap width, coupling line width, coupling line length, via diameter, slot line width, slot line length, and slot line diameter are optimized in the software Ansoft HFSS to realize good impedance matching. When a signal is feed into phase inverter, the electrical line is supposed to reverse after it propagates through the slot line which can be seen clearly in Fig. 8.

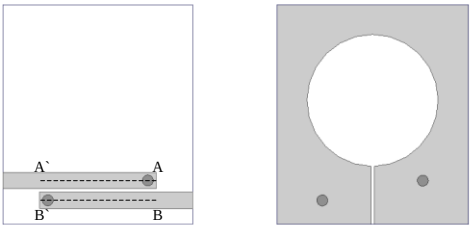

Fig. 6. The structure of the 180° phase inverter.

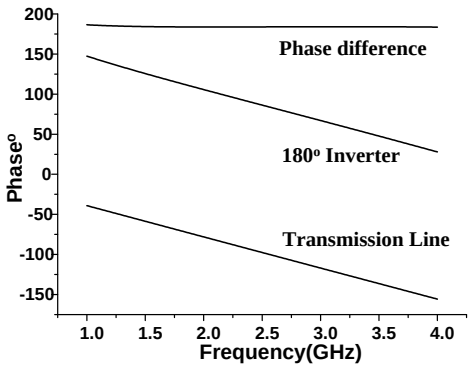

Fig. 7. Phase simulation of 180° inverter.

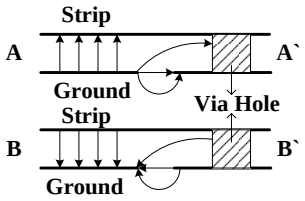

Fig. 8. The change of electrical line.

The initial physical length of each part of the proposed filter can be determined according to Fig. 1, if center frequency f_0 is given. Then, referred to Fig. 2 and Fig. 3, one can fix the ratio of Z_1 and Z_2 as long as the 3-dB bandwidth is given. Finally, Table 1, Fig. 4 and Fig. 5 tell how to find out the Z_1, Z_2 and Z_s.

Figure 9 illustrates the geometry of the wideband bandpass filter with a 180° swap, and the detailed circuit and structure parameters is shown below. The simulated results are shown in Fig. 11. Two transmission zeros are located at 0.9 GHz and 2.6 GHz, respectively; while four

transmission poles are realized in the passband (3-dB fractional bandwidth is approximate 86.8%). The insertion loss is less than 0.5 dB, while the return loss is over 19 dB (1.07-2.42 GHz). Furthermore, over 20 dB second harmony suppression is achieved.

One prototype of proposed bandpass filter with size of 22 mm×41 mm is fabricated on a substrate with ε_r = 2.55, h = 0.78 mm, and $tan\delta$ = 0.0006. Figure 10 illustrates the photograph of the filter. The measured S-parameters is illustrated in Fig. 11. Two transmission zeros are located at 0.83 GHz and 2.45 GHz; within the passband (0.91-2.34 GHz), the measured insertion loss for the filter is less than 1.0 dB while the return loss is over 11 dB. Furthermore, over 20 dB second harmony suppression is achieved. Good agreement can be observed between the simulation and the experiments. The slight frequency shift between measured and simulated results may be caused by measurement and fabrication errors.

To further demonstrate the performances of this filter, the comparisons of measured results for several transversal signal-interaction wideband filter structures [12-13] are shown in Table 2.

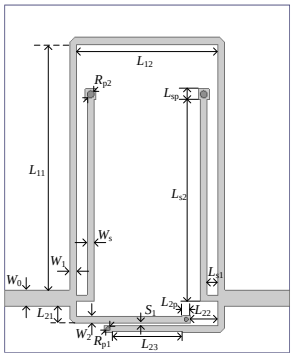

(a) Top view

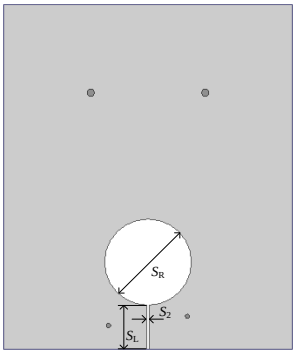

(b) Bottom view

Fig. 9. Geometry of the proposed filter.
(*W_0=2.2 mm; W_1=0.95 mm; W_2=0.95 mm; W_s=0.9 mm; S_1=0.3 mm; S_2=0.3 mm; S_R=12 mm; S_L=6.1 mm; L_{11}=34 mm; L_{12}=19.8 mm; L_{21}=2.35 mm; L_{22}=3.9 mm; L_{23}=9.8 mm; L_{2P}=1.1 mm; R_{P1}=0.6 mm; L_{s1}=1.55 mm; L_{s2}=27.9 mm; L_{sP}=1.5 mm; R_{P2}=1.0 mm.*)

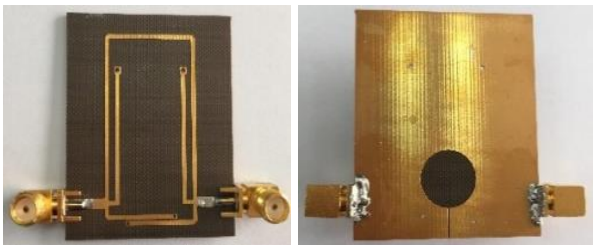

Fig. 10. Photograph of the proposed bandpass filter.

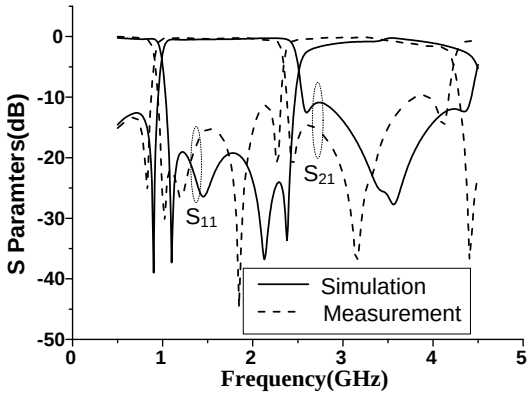

Fig. 11. Simulated and measured results.

Table 2: Comparisons with wideband filters in [12] and [13]

Different Structures	Filter in This Paper	Ref. [13]	Ref. [12]
f_0	1.63 GHz	6.8 GHz	6.8 GHz
Circuit size (λ_o)	0.17×0.32	0.63×0.49	0.62×0.47
Transmission zeros	3	1	1
Transmission poles	4	3	3
Second harmony suppression	20 dB	15 dB	15 dB

IV. CONCLUSION

In this paper, a novel compact wideband filter based on transversal signal-interaction concepts is proposed. Two transmission paths are used to realize the signal transmission from Port1 to Port2. The bandwidth for the bandpass filter can be easily adjusted by changing the impedances of the two transmission paths. Good frequency selectivity and harmonic suppression can be realized for the bandpass filter. Good agreements between simulated and measured responses of the filter are demonstrated, indicating the validity of the design strategies.

ACKNOWLEDGMENT

This work was supported by the National Natural Science Foundation of China (No. 61501340).

REFERENCES

[1] W. Menzel, L. Zhu, K. Wu, and F. Bogelsack, "On the design of novel compact broadband planar filters," *IEEE Trans. Microw. Theory Tech.*, vol. 51, no. 2, pp. 364-369, Feb. 2003.

[2] L. Zhu, S. Sun, and W. Menzel, "Ultra-wideband (UWB) bandpass filters using multiple-mode resonator," *IEEE Microw. Wireless Compon. Lett.*, vol. 15, no. 11, pp. 796-798, Nov. 2005.

[3] P. K. Singh, S. Basu, and Y.-H. Wang, "Planar ultra-wideband bandpass filter using edge coupled microstrip lines and stepped impedance open stub," *IEEE Microw. Wireless Compon. Lett.*, vol. 17, no. 9, pp. 649-652, Sep. 2008.

[4] J. Garcia-Garcia, J. Bonache, and F. Martin, "Application of electromagnetic bandgaps to the design of ultra-wide bandpass filters with good out-of-band performance," *IEEE Trans. Microw. Theory Tech.*, vol. 54, no. 12, pp. 4136-4140, Dec. 2006.

[5] C. W. Tang and M. G. Chen, "A microstrip ultra-wideband bandpass filter with cascaded broadband bandpass and bandstop filters," *IEEE Trans. Microwave Theory Tech.*, vol. 55, no. 11, pp. 2412-2418, Nov. 2007.

[6] A. Boutejdar, A. Batmanov, M. H. Awida, E. P. Burte, and A. Omar, "Design of a new bandpass fitler with sharp transmission band using multilayer-technique and U-defected ground structure," *IET Microwaves, Antennas and Propagation*, vol. 4, no. 9, pp. 1415-1420, Apr. 2010.

[7] A. Boutejdar, A. Elsherbini, A. Balalem, J. Machac, and A. Omar, "Design of new DGS hairpain microstrip bandpass filter using coupling matrix method," *Progress In Electromagnetics Research Symposium*, Prague, pp. 261-265, 2007.

[8] A. Boutejdar, "A new approach to design compact tunable BPF starting from simple LPF topology using a single T-DGS-resonator and ceramic capacitors," *Microw. Opt. Technol. Lett.*, vol. 58, no. 5, pp. 1142-1148, May 2016.

[9] A. Boutejdar, "Design of 5 GHz-compact reconfigurable DGS-bandpass filter using varactor-diode device and coupling matrix technique," *Microw. Opt. Technol. Lett.*, vol. 58, no. 2, pp. 304-309, Feb. 2016.

[10] R. Gómez-García and J. I. Alonso, "Design of sharp-rejection and low-loss wide-band planar filters using signal-interference techniques," *IEEE Microw. Wireless Compon. Lett.*, vol. 15, no. 8, pp. 530-532, Aug. 2005.

[11] R. Gómez-García, M. Sánchez-Renedo, B. Jarry, J. Lintignat, and B. Barelaud, "A class of microwave transversal signal-interference dual passband planar filters," *IEEE Microw. Wireless Compon. Lett.*, vol. 19, no. 3, pp. 158-160, Mar. 2009.

[12] M. A. Sánchez-Soriano, E. Bronchalo, and G. Torregrosa-Penalva, "Compact UWB bandpass filter based on signal interference techniques," *IEEE Microw. Wireless Compon. Lett.*, vol. 19, no. 11, pp. 692-694, Nov. 2009.

[13] W. Feng and W. Che, "Novel ultra-wideband bandpass filter using shorted coupled lines and transversal transmission line," *IEEE Microw. Wireless Compon. Lett.*, vol. 20, no. 10, pp. 548-551, Oct. 2010.

[14] K. W. Wong, L. Chiu, and Q. Xue, "Wideband parallel-strip bandpass filter using phase inverter," *IEEE Microw. Wireless Compon. Lett.*, vol. 18, no. 8, pp. 503-505, Aug. 2008.

[15] M. E. Bialkowski and Y. Wang, "Wideband microstrip 180° hybrid utilizing ground slots," *IEEE Microw. Wireless Compon. Lett.*, vol. 20, no. 9, pp. 495-497, Sept. 2010.

[16] M. K. Mandal and S. Sanyal, "Compact bandstop filter using signal interference technique," *IEEE Electron. Lett.*, vol. 43, no. 2, pp. 110-111, Jan. 2007.

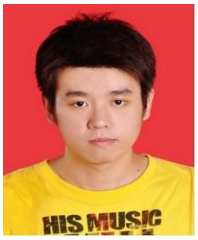

Lixue Zhou received the M.S. degree in Electromagnetic Fields and Microwave Technology from Nanjing University of Science and Technology, Nanjing, China, in 2010. He is now working toward the Ph.D. degree in Electrical Engineering Department of Xidian University, Xi'an, China. Since 2010, he has been an Electronic Engineer in Xi'an Electronic Engineering institute, where he developed the microwave and millimeter-wave circuit and RF component.

His research interests include microwave and millimeter-wave planar type circuit and multilayered circuit design and planner filter design in microwave and millimeter-wave frequency band.

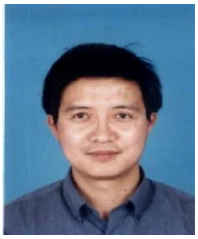

Yingzeng Yin Received the B.S. degree and the M.S. degree and Ph.D. degree in Electromagnetic Wave and Microwave Technology from Xidian University, Xi'an, P. R. China, in 1987, 1990 and 2002, respectively.

From March 1990 to June 1992, he was a Research Assistant and an Instructor at the Institute of Antennas and Electromagnetic Scattering, Xidian University. From July 1992 to June 1996, he was an Associate Professor in the Department of Electromagnetic Engineering, Xidian University. Since

June 2004, he has been a Professor at the University. His research interest includes the areas of design of antennas, feeds for parabolic reflectors, microstrip antennas, artificial magnetic conductors, phased array antennas, and computer aided design for antennas. He has published over 180 refereed journal articles.

Wei Hu received the B.S. and Ph.D. degrees in Electromagnetic Fields and Microwave Technology from Xidian University, Xi'an, China, in 2008 and 2013, respectively. He is Lecturer with the National Laboratory of Science and Technology on Antennas and Microwaves, Xidian University, Xi'an, China.

His research interests include multiband antennas, dual-polarized antennas, waveguide slot antenna arrays and feeding networks. He has published more than 20 research papers in refereed international journals and conferences, such as IEEE Transaction on Antennas and Propagation, IEEE Antennas and Wireless Propagation Letters, IET Electronics Letters and so on.

Xi Yang received the Ph.D. degrees in Electromagnetic Fields and Microwave Technology from Xidian University, Xi'an, China, 2011. He is now Lecturer with the National Laboratory of Science and Technology on Antennas and Microwaves, Xidian University, Xi'an, China.

His research interests include phased array antenna, compact antennas, reconfigurable antenna and MIMO technologies. He has published more than 20 research papers in refereed international journals and conferences, such as IEEE Transaction on Antennas and Propagation, IEEE Antennas and Wireless Propagation Letters, IET Electronics Letters.

Harmonic Suppression of Parallel Coupled-Line Bandpass Filters using Defected Microstrip Structure

Mohammad Naser-Moghadasi

Faculty of Eng., Science and Research Branch
Islamic Azad University, Tehran-Iran
mn.moghaddasi@srbiau.ac.ir

Abstract ─ This paper presents a novel miniaturized parallel coupled-line bandpass filter by etching some slot resonators on the strip for suppressing the first spurious response. These slots perform a serious *LC* resonance property in certain frequency and suppress the spurious signals. By properly tuning these slot dimensions, multiple closed notches can be generated in the vicinity of spurious harmonic and a wide stopband can be obtained. Slot on the strip that is called Defected Microstrip Structure (DMS). The DMS interconnection disturbs the current distribution only across the strip, thereby giving a modified microstrip line with certain stop band and slow-wave characteristics. The simulation and measurement of a 4.7 GHz prototype bandpass filter are presented. The measured results show a satisfactory rejection level more than 30 dB at first spurious passband without affecting the passband response. Good agreement between the experimental and full-wave simulated results has been achieved.

Index Terms ─ Defected Microstrip Structure (DMS), harmonic suppression, parallel coupled-line filter.

I. INTRODUCTION

High-performance microwave filters are essential circuits in many microwave systems where they serve to pass the wanted signals and suppress unwanted ones in the frequency domain. Microstrip parallel coupled-line bandpass filters are widely used in microwave circuits due to their low sensitivity to fabrication tolerances, wide realizable bandwidth, and simple synthesis procedure. However, despite the aforementioned advantages, an undesirable disadvantage is the existence of the first spurious passband at twice the passband frequency. This spurious response degrades the rejection properties of the system. The undesired spurious passband is related to the inhomogeneous dielectric medium surrounding the conductors, which causes the odd-mode wave to propagate faster than the even mode wave in the coupled microstrip lines [1-4]. The even and odd mode phase velocities are different for coupled microstrip lines due to their different field configuration in the vicinity of the air–dielectric interface. There are two basic methods in equalizing the modal transmission phase: providing different lengths for the even and odd mode waves, or equalizing the modal phase velocities. In [5], an over-coupled resonator was constituted to extend the odd-mode phase length, thus compensating the phase velocity difference between two modes. The structure in [6] uses capacitors to extend the travelling route of the odd-mode. The strip-width modulation technique tries to modify or perturb the widths of the conventional lines in various forms, such as wiggly [7], grooved [8], or even fractal [9] shapes. The above periodic structures can be used to create Bragg reflections so that the first spurious passband is rejected, while the desired passband response is maintained almost unchanged. Split Ring Resonator (SSR) structure was proposed to achieve a large imaginary component in effective permeability due to its unique resonance nature [10]. In recent years, Complementary Split Ring Resonator (CSRR) is presented and investigated on the basis of Defected Ground Structure (DGS) [11]. It has been demonstrated that CSRRs etched in the ground plane or in the conductor strip of planar transmission media (microstrip or CPW) provide a negative effective permittivity to the structure, and signal propagation is precluded (stopband behaviour) in the vicinity of their resonant frequency [12]. In DMS, there is no etching in ground plane. DMS is made by etching some uniform or non uniform slits or patterns over the transmission line. DMS was originally proposed in [13, 14]. In [15], the stopband characteristic of a DMS is studied and probes the relationships between the etched slot dimensions and the characteristics of the stopband.

For housing the DGS, it should be suspended for correctness of its performance. However, in DMS, the circuit needs not be elevated from the housing. The size of slot in DGS is much greater than to the size of slot in DMS for getting the same frequency response. So, this defect causes radiation problem. The radiation from the defects of interconnection is a harmful phenomenon for measurements or integration of components. Compared to DGS, if DMS is used as a filter, the harmful radiation

Submitted On: June 1, 2013
Accepted On: March 17, 2016

can be decreased with lower etched area of defect. Dissimilar DGS, the DMS has less radiated EMI ground noise. In addition, ground plane defect will significantly increase the crosstalk between parallel interconnections that cross over them [16].

In this paper, a new design of a parallel coupled bandpass filter using Defected Microstrip Structure (DMS) by etching Open Square Ring (OSR) is proposed to suppress the first spurious harmonic and its resonant properties are scrutinized. Low insertion loss in the passband, high rejection level and integrated structure should be mentioned as advantages for this resonator. By employing the DMS structure, the unwanted harmonics can be suppressed with appropriately selected slot length tuned to block some specific harmonic band and great rejection can be obtained. These resonators designed to resonate around $2f_0$ and will add a transmission zero at undesired frequency. Here, we merge DMS resonators in filter structure with no increase in used area while was excellent for the first harmonic suppression with rejection levels up to 30 dB. This enhanced performance of the proposed bandpass filter has been verified by full-wave analysis and experimental results; and a good agreement between these results is obtained. Analysis of the proposed DMS resonator is scrutinized in Section II. Section III presents the simulated and measured results of proposed filter.

II. DESIGN AND ANALYSIS OF THE RESONATOR

The basic topology of Complementary Open Square Ring-DMS (COSR-DMS) is depicted in Fig. 1, which is located in the center of the microstrip line. As shown in Fig. 1, the microstrip line width is chosen in a way to exhibit a 50 Ω transmission line. The substrate Rogers RO4350 with the thickness of 1.52 mm and dielectric constant of 3.66 is used in the simulation. The EM simulations are performed using Ansoft HFSS v.12 (an electromagnetic simulator). The amplitude simulation result is shown in Fig. 3, which illustrates the characteristic of a bandstop filter.

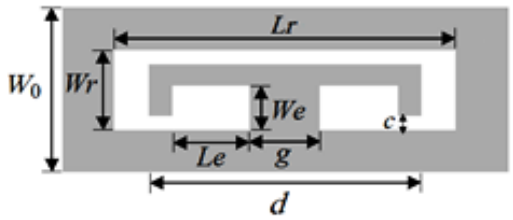

Fig. 1. Configuration of Complementary Open Square Ring-DMS (COSR-DMS).

As shown in Fig. 2, the frequency characteristics of the proposed DMS can be modeled by a single parallel *RLC* resonator circuit which blocks the signal as an open at the resonant frequency. The radiation effect and transmission loss are considered by including the resistor, *R*. A simple lumped element model is shown in Fig. 2. From the illustrated full-wave simulation results, the circuit model parameters can be extracted as follows:

$$R = 2Z_0\left(1/\left|S_{21}\right|-1\right)\Big|_{f=f_r}, \tag{1}$$

$$C = \frac{\sqrt{0.5\left(R+2Z_0\right)^2-4Z_0^2}}{2.83\pi Z_0 RB}, \tag{2}$$

$$L = \frac{1}{\left(2\pi f_r\right)^2 C}, \tag{3}$$

where Z_0 is the characteristic impedance of the transmission line, f_r is the resonant frequency, S_{21} is the transmission coefficient, and B is the 3dB bandwidth of S_{21} at f_r.

For the dimensions (Lr = 9 mm, Wr = 2 mm, We = 1.2 mm, Le = 1 mm, d = 7.1 mm, g = 1 mm, c = 0.2 mm, W_0 = 3.55 mm) the circuit model parameters are 1.33 kΩ, 0.3085 nH and 3.62pF.

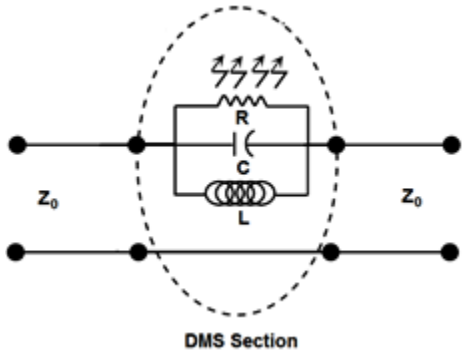

Fig. 2. The related equivalent circuit of unit cell DMS and its losses.

Figure 3 compares the S-parameters calculated by electromagnetic (EM) simulation for COSR-DMS in Fig. 1 and those calculated by using the equivalent circuit in Fig. 2. Circuit simulation is performed by employing Advanced Design System (ADS). For S_{21} simulation, the results are in good agreement over a wide frequency range.

The resonant frequency of COSR depends only on its total physical length for a constant value of space gap (g). The resonant frequency is independent of the physical width (c) of the COSR. The physical width determines bandwidth of frequency response.

Considering the frequency response of DMS resonator in Fig. 4 one transmission zero and two poles is observed. If we can move the poles closer together without any change at the location of zero (resonant frequency), afterwards resonator bandwidth decreases and according to the equation $Q=f_r/BW$, reduction of bandwidth will result in increase of Q.

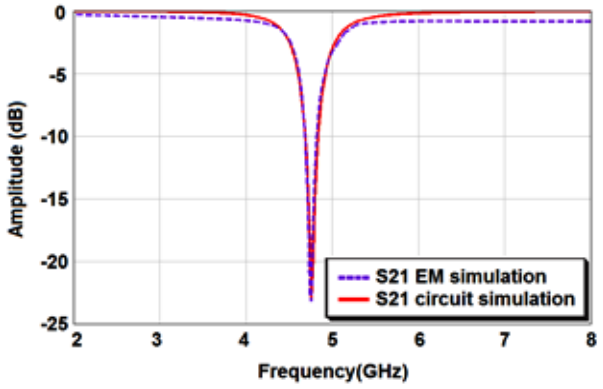

Fig. 3. Comparison between EM and circuit simulations for proposed COSR-DMS.

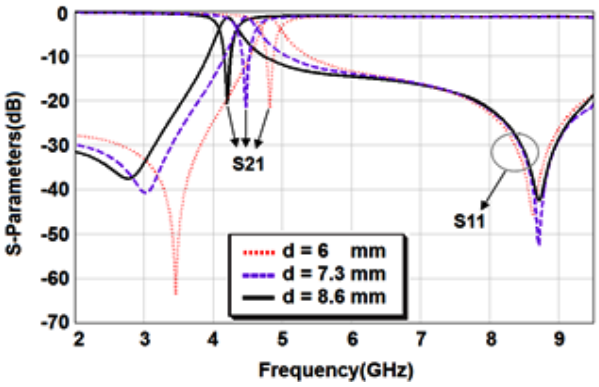

Fig. 4. Simulated scattering parameters for different length *d* (*Lr* = 12 mm, *We* = 1.3 mm, *Wr* = 2mm, *Le* = 1 mm, *g* = 0.2 mm, *c* = 0.3 mm).

To eliminate unwanted harmonics near the desired signal and also to improve oscillator phase noise, high quality factor resonator is required. By utilizing the introduced resonant structure and small physical changes we can adjust *Q*.

The first transmission pole occurs in frequencies lower than resonant frequency. Location of the pole is adjusted using *d*. Figure 4 shows resonant frequency of the resonator for different lengths *d* on the 50 Ω microstrip line. As can be seen second transmission pole remains constant.

In addition, appearance of second transmission pole which is observed in Fig. 4 is due to the length *Lr*. In other words, in frequencies where *Lr* = $\lambda/2$ one transmission pole appears in response. So we can control the second pole by changing the length *Lr*. As it was, before the designing high *Q* resonator, it is necessary that the poles be close to each other. By Increasing *Lr* not only the frequency of second pole decreases, but the first pole and the resonant frequency also will decrease. Decreasing *d* causes the first pole and resonant frequency increase while the second pole frequency does not change. Thus, with tuning *Lr* and *d* we can bring the two transmission poles closer to each other while the transmission zero remains constant. Figure 5 depicts *S*-parameters for different lengths *d* and *Lr* of this resonator etched on the 50 Ω microstrip line. Resonators which are merged in this filter structure must be having low *Q* or high bandwidth so difference between *Lr* and *d* should be equal to *c*.

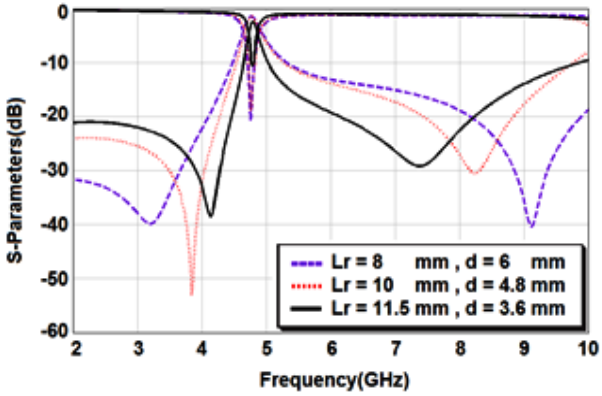

Fig. 5. Simulated scattering parameters for different length *Lr* and *d* (*We* = 1.3 mm, *Wr* = 2mm, *Le* = 1 mm, *g* = 0.2 mm, *c* = 0.3 mm).

III. FILTER IMPLEMENTATION

The DMS structure increases the electric length and the associated inductance of the microstrip. So, improvement in filter characteristics of the circuits can be achieved and size of the filter circuits can be reduced. DMS presents good cut off frequency characteristics due to the more effective inductance with respect to DGS.

In order to demonstrate the effectiveness of this DMS pattern to harmonic suppression, the novel filter is compared with a conventional parallel coupled-line filter with center frequency f_0 = 4.7 GHz with 600 MHz bandwidth on Rogers RO4350 substrate which has a relative permittivity ε_r = 3.66 and thickness *h* = 1.52 mm.

The conventional parallel coupled-line filter exhibiting a five-order filter response comprises of three open transmission line resonators which are designed to have a length of approximately half of the wavelength, $\lambda_g/2$, at the center frequency of The conventional parallel coupled-line filter exhibiting a five-order filter response comprises of three open transmission line resonators which are designed to have a length of approximately half of the wavelength, $\lambda_g/2$, at the center frequency of the conventional parallel coupled-line filter. Figure 6 shows the design parameters of the conventional parallel coupled-line filter. *Wi*, *Si*, and *Li* are width, separation between coupled sections, and length of the *i*th section, respectively.

Simulated S-parameters of the conventional parallel coupled-line filter are shown in Fig. 7. The response

curve shows that the spurious harmonic of the parallel coupled-line filter is around $2f_0$. This is major disadvantage of the conventional parallel coupled-line filter.

The configuration of the proposed parallel coupled-line filter with the four COSR-DMS sections is illustrated in Fig. 8.

Etched defects on the top metal conductor of microstrip line provide higher effective permittivity and characteristic impedance than those of the conventional microstrip line due to increase of the effective inductance of transmission lines.

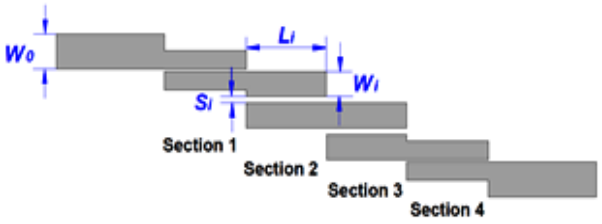

Fig. 6. Schematic of a five-order conventional parallel coupled-line filter ($W_1 = W_4 = 1.85$ mm, $W_2 = W_3 = 2.49$ mm, $S_1 = S_4 = 0.23$ mm, $S_2 = S_3 = 0.68$ mm, $L_1 = L_4 = 9.1$ mm, $L_2 = L_3 = 8.9$ mm).

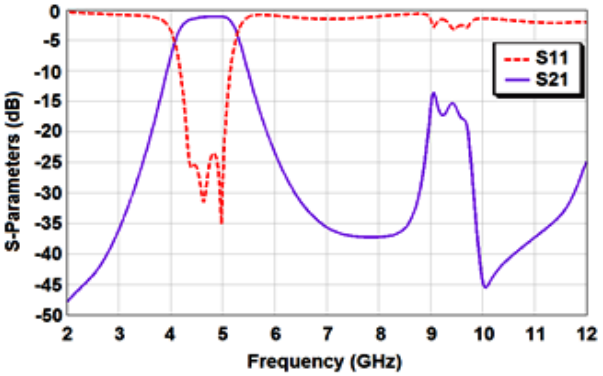

Fig. 7. Simulated S-parameters of the conventional parallel coupled-line filter.

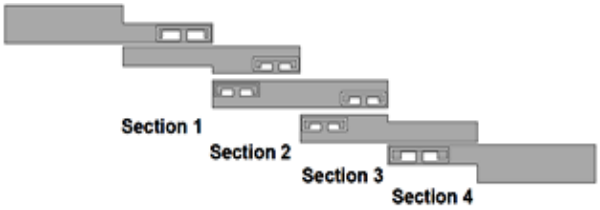

Fig. 8. Proposed parallel coupled-line filter.

The relevant design parameters of each resonator are optimized as follows: $Lr_1 = 5.5$ mm, $Lr_2 = Lr_3 = 4.53$ *mm*, $Lr_4 = 6$ mm, $Le_1 = 1.8$ mm, $Le_2 = Le_3 = 1.2$ mm, $Le_4 = 1.5$ mm, $We_1 = We_4 = 0.9$ mm, $We_2 = 0.65$ mm, $We_3 = 0.675$ mm, $Wr_1 = Wr_4 = 1.3$ mm, $Wr_2 = Wr_3 = 1.2$ mm. The input and output port strip width are $W_0 = 3.55$ mm, corresponding to 50 Ω. The etched physical width (c) and space gap (g) is chosen to be 0.2 mm and 0.7 mm for all DMSs. From this geometry, we have tuned COSRs dimensions in order to obtain multiple closed notches and hence achieve spurious passbands rejection.

DMS resonators perform a serious *LC* resonance property in certain frequency. The proposed structure uses the rejection properties of DMSs merged in filter structure to reject specific frequencies while having the least effect on the filter pass band response. Thus, it is more reasonable to use multiple DMSs to make a wide reject band without meaningful effect on main response. This technique eliminates the first harmonic response and makes better sharpness level of transition from passband to stopband region.

Comparison of transmission characteristics between conventional and proposed parallel coupled-line filter described in Fig. 8 is given in Fig. 9. As it is seen, the DMSs work as band-reject elements with almost no effect on filter performance and therefore could be designed independently. The simulation, exhibits that the proposed filter has successfully improved the spurious harmonics at $2f_0$. The center frequency and bandwidth of the fundamental passband is kept as in the original filter and no significant deviation is observed. Figure 10 displays the image of the fabricated proposed filter.

The first spurious passband is suppressed by more than 30 dB at twice the centre frequency and 50 dB suppression at 6.5 GHz. Figure 11 provides a comparison measured and full-wave simulated results. Good agreement between simulations and experimental data has been obtained.

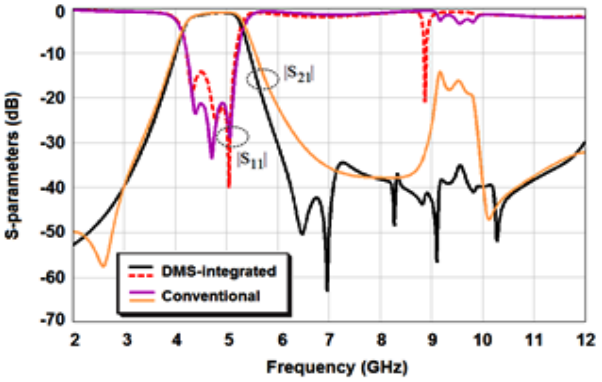

Fig. 9. Comparison between the simulated S_{21} of the proposed and conventional parallel coupled-line filter.

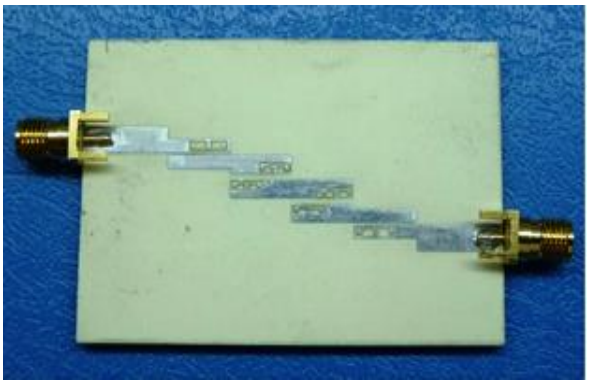

Fig. 10. Fabricated parallel coupled-line filter with COSR-DMS.

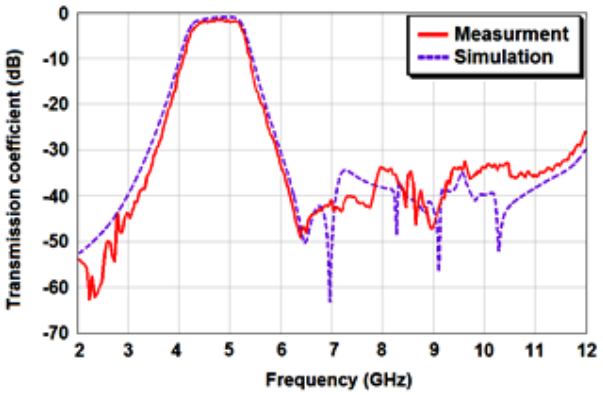

Fig. 11. Measured S_{21} of the fabricated proposed parallel coupled-line filter.

IV. CONCLUSION

In this paper, the compact parallel coupled-line filter having harmonic suppression has been presented. It has been demonstrated that the frequency response of proposed filter can be improved by merely etching COSR-DMS in parallel coupled sections. By properly tuning the dimensions of COSRs, it has been experimentally found that the first spurious band of the filter can be rejected, with no effect on the allowed band. By the simulation and experimental results of 4.7 GHz with a 600 MHz bandwidth a satisfactory rejection level more than 30 dB at first spurious harmonic in the stopband can be achieved, without affecting the original passband. We would like to highlight the fact that the topology of the proposed structure only differs from that of the conventional design on the presence of COSRs, and these are etched in the signal strip. The filter structure has great advantages as: achievable bandwidth, minimization of radiation from the defects and broad stopband. The proposed technique may have wide applications in miniaturization and harmonic rejection of various microwave circuits

REFERENCES

[1] M. D. Pozar, *Microwave Engineering*, New York, Wiley, ch. 8, pp. 477-485, 2004.

[2] D. Jiang, Y. Xu, R. Xu, and W. Lin, "A novel bandpass filters using complementary split ring resonator loaded half mode substrate integrated waveguide," *Applied Computational Electromagnetics Society (ACES) Journal*, vol. 28, no. 2, pp. 143-149, February 2013.

[3] L. Yang, Y. Hongchun, W. Yawei, and X. Shaoqiu, "Ultra-wideband bandpass filter based on parallel-coupled microstrip lines and defected ground structure," *Applied Computational Electromagnetics Society (ACES) Journal*, vol. 28, no. 1, pp. 21-26, January 2013.

[4] X. Li and J. Zeng, "A novel dual-band microstrip bandpass filter design and harmonic suppression," *Applied Computational Electromagnetics Society (ACES) Journal*, vol. 28, no. 4, pp. 348-352, April 2013.

[5] J.-T. Kuo, S.-P. Chen, and M. Jiang, "Parallel-coupled microstrip filters with over coupled end stages for suppression of spurious responses," *IEEE Microw. Wirel. Compon. Lett.*, vol. 13, no. 10, pp. 440-442, October 2003.

[6] I. J. Bahl, "Capacitively compensated high performance parallel coupled microstrip filters," *IEEE MTT-S Int. Microw. Symp. Dig.*, pp. 679-682, June 1989.

[7] T. Lopetegi, M. A. G. Laso, J. Hernandez, M. Bacaicoa, D. Benito, M. J. Garde, M. Sorolla, and M. Guglielmi, "New microstrip 'wiggly line' filters with spurious passband suppression," *IEEE Trans. Microw. Theory Tech.*, vol. 49, no. 9, pp. 1593-1598, September 2001.

[8] B. S. Kim, J. W. Lee, and M. S. Song, "An implementation of harmonic-suppression microstrip filters with periodic grooves," *IEEE Microw. Wirel. Compon. Lett.*, vol. 14, no. 9, pp. 413-415, September 2004.

[9] I. K. Kim, N. Kingsley, M. Morton, R. Bairavasubramanian, J. Papapolymerou, M. M. Tentzeris, and J. G. Yook, "Fractal-shaped microstrip coupled-line bandpass filters for suppression of second harmonic," *IEEE Trans. Microw. Theory Tech.*, vol. 53, no. 9, pp. 2943-2948, September 2005.

[10] J. B. Pendry, A. J. Holden, D. J. Robbins, and W. J. Stewart, "Magnetism from conductors and enhanced nonlinear phenomena," *IEEE Trans. Microw. Theory Tech.*, vol. 47, no. 1, pp. 2075-2084, November 1999.

[11] R. Azadegan and K. Sarabandi, "High-Q double-spiral slotline resonator filters," *IEEE Trans. Microw. Theory Tech.*, vol. 52, no. 1, pp. 1548-

1557, May 2004.

[12] J. Bonache, F. Martin, I. Gil, and J. Garcia-Garcia, "Novel microstrip filters based on complementary split rings resonators," *IEEE Trans. Microw. Theory Tech*., vol. 54, no. 1, pp. 265-271, January 2006.

[13] J. A. Tirado-Mendez and H. Jardon-Aguilar, "Comparison of defected ground structure (DGS) and defected microstrip structure (DMS) behavior at high frequencies," *Proc. 1st Conf. Electrical and Electronics Engineering*, Acapulco, Mexico, pp. 7-10, September 2004.

[14] J. A. Tirado-Merndez, H. Jardorn-Aguilar, F. Iturbide-Sarnchez, I. Garcia-Ruiz, V. Molina-Lopez, and R. Acevo-Herrera, "A proposed defected microstrip structure (DMS) behavior for reducing rectangular patch antenna size," *Microwave Opt. Technol. Lett*., vol. 43, pp. 481-484, October 2004.

[15] S. Zhang, J. K. Xiao, Z. H. Wang, and Y. Li, "Novel low pass filters using a defected microstrip structure," *Microwave J*., vol. 49, no. 9, pp. 118, September 2006.

[16] M. Kazerooni and A. Cheldavi, "Unit length parameters, transition sharpness and level of radiation in defected microstrip structure (DMS) and defected ground structure (DGS) inter-connections," *Prog. Electromagn. Res*., vol. 10, pp. 93-102, 2009.

Fast Simulation of Microwave Devices via a Data-Sparse and Explicit Finite-Element Time-Domain Method

T. Wan [1,2], L. Du [3], and J. Zhu [1]

[1] Department of Communication Engineering
Nanjing University of Posts and Telecommunications, Nanjing, 210003, China
want@njupt.edu.cn

[2] State Key Laboratory of Millimeter Waves
Southeast University, Nanjing, 210096, China

[3] Institute of Electrostatic and Electromagnetic Protection
Ordnance Engineering College, Shijiazhuang, 050003, China
billwanting@163.com

Abstract ─ An unconditionally stable and explicit finite-element time-domain (FETD) method is presented for the fast simulation of microwave devices. The Crank-Nicolson (CN) scheme is implemented leading to an unconditionally stable mixed FETD method. A data-sparse approximate inverse algorithm is introduced to provide a data-sparse way to approximate the inverse of FETD system matrix which is dense originally. This approximate inverse matrix can be constructed and stored with almost linear complexity, and then the FETD method can be computed explicitly at each time step without solving a sparse linear system. An efficient recompression technique is introduced to further accelerate the explicit solution at each time step. Some microwave devices are simulated to demonstrate the efficiency and accuracy of the proposed method.

Index Terms ─ Approximate inverse, electromagnetic simulation, finite-element time-domain (FETD), microwave devices.

I. INTRODUCTION

The finite-element time-domain (FETD) method has been widely used for electromagnetic analysis due to its ability to deal with complex geometries and broadband characterizations [1-9]. However, the FETD generally requires solving a sparse linear system at each time step. This greatly reduces the solution efficiency, and has been a major bottleneck for the development of the FETD. Hence, it is highly desirable to develop explicit schemes. Some research has been studied to obtain an explicit FETD method. One way is to construct diagonal or block diagonal mass matrix to avoid solving a sparse linear system, such as mass lumping [1], orthogonal vector basis function [2,3] and spectral-element time-domain (SETD) method [4]. Another way to achieve an explicit scheme is to directly invert the mass matrix. However, the computational costs can be very high and the inverse matrix is generally full. Recently, a thresholding method has been proposed to approximate the inverse mass matrix by a sparse matrix to obtain an explicit FETD [5,6]. Besides, a recursive sparsification method has been applied to approximate the inverse matrix in the alternating-direction implicit FETD method [7].

In this article, a data-sparse approximate inverse (DSAI) algorithm is developed to construct an explicit FETD method. The Crank-Nicolson (CN) scheme is employed to generate an unconditionally stable mixed FETD method [8,9]. The DSAI algorithm provides a data-sparse way to approximate the inverse of the CN-FETD system matrix which is dense originally. The inverse matrix is not sparse but data-sparse in the sense that its certain sub-blocks can be described by a product of two low-rank matrices [10,11]. Based on the hierarchical tree and the formatted hierarchical matrix arithmetic, the DSAI algorithm can reduce the computational complexity and storage requirement of matrix inversion to be almost linear [12,13]. The resulting data-sparse inverse matrix has been highly compressed but still contains redundant data [12,14]. A recompression technique is introduced to further compress the inverse matrix to accelerate the explicit update at each time step. Some numerical examples are presented and discussed.

II. DATA-SPARSE AND EXPLICIT FETD

A. Mixed E-B FETD method

According to the Maxwell's equations:

Submitted On: September 7, 2015
Accepted On: March 18, 2016

$$\frac{1}{\mu}\nabla\times\vec{B}=\varepsilon\frac{\partial\vec{E}}{\partial t}, \quad (1)$$

$$\nabla\times\vec{E}=-\frac{\partial\vec{B}}{\partial t}, \quad (2)$$

the examined 3-D domain is discretized by tetrahedral elements. The electric field $\vec{E}$ and the magnetic flux $\vec{B}$ are expanded in terms of Whitney 1-form vector basis function $W^{(1)}$, and Whitney 2-form vector basis function $W^{(2)}$, respectively, as follows:

$$\vec{E}=\sum\nolimits_i e_i W_i^{(1)}, \quad (3)$$

$$\vec{B}=\sum\nolimits_i b_i W_i^{(2)}. \quad (4)$$

Testing Equations (1) and (2) with corresponding basis function by Galerkin technique, one can obtain elemental matrix equations as follows:

$$[T^e]\frac{\partial e}{\partial t}=[C^e]^T[K^e]^T b, \quad (5)$$

$$\frac{\partial b}{\partial t}=-[C^e]e, \quad (6)$$

where $[C^e]$ is an incidence matrix [9] and,

$$[T^e]=\varepsilon\int_\Omega\left(W_i^{(1)}\bullet W_j^{(1)}\right)dv, \quad (7)$$

$$[K^e]=\frac{1}{\mu}\int_\Omega\left(W_i^{(2)}\bullet W_j^{(2)}\right)dv. \quad (8)$$

Using the Crank-Nicolson (CN) formulation for time discretization, and assembling all the elemental equations, one can get the global electric field and magnetic flux update equations [9]:

$$\left([T]+\frac{\Delta t^2}{4}[G]\right)e^{n+1}=\left([T]-\frac{\Delta t^2}{4}[G]\right)e^n+[L]\Delta t b^n, \quad (9)$$

$$b^{n+1}=b^n-\frac{\Delta t}{2}[C]\left(e^{n+1}+e^n\right), \quad (10)$$

where $[G^e]=[C^e]^T[K^e][C^e]$ and $[L^e]=[C^e]^T[K^e]$. It can be seen that the update of magnetic flux is explicit. However, the update of electric field needs to solve a linear system at each time step, which is a major obstacle to the FETD solution. Hence, it is very necessary to develop an explicit update for the electric field Equation (9). In view of (9), the most direct way to achieve an explicit update can be denoted as:

$$e^{n+1}=[A]^{-1}\left([T]-\frac{\Delta t^2}{4}[G]\right)e^n+[A]^{-1}[L]\Delta t b^n, \quad (11)$$

where $[A]$ denotes the system matrix $\left([T]+\Delta t^2[G]/4\right)$. Although $[A]$ is sparse, $[A]^{-1}$ is dense. Direct computation of $[A]^{-1}$ is very costly and even impractical for large problems. Here, an efficient DSAI algorithm is developed for the computation of $[A]^{-1}$ to produce a fully explicit FETD method.

B. Data-sparse approximate inverse algorithm

The DSAI algorithm can be performed by five steps as follows: 1. Construct the data-sparse representation $[A]_{\mathrm{DS}}$ of the system matrix $[A]$. 2. Compute the data-sparse inverse $[A]_{\mathrm{DS}}^{-1}$ in formatted hierarchical matrix arithmetic. 3. Complete the explicit update as (11) by the matrix-vector product of $[A]_{\mathrm{DS}}^{-1}$ at each time step. The details are given below.

First, a cluster tree should be constructed. A cluster is a finite index set of basis functions in the FETD. We define an original cluster $I = \{1,2,\ldots,N\}$ to denote all the basis functions W_i. A cluster tree T_I is generated by recursive subdivision of I, as shown in Fig. 1 (a). One index set is subdivided into two subsets recursively, until the number of basis functions in the subset (denoted as "#") is smaller than a threshold n_{leaf}. The resulting cluster tree T_I is a binary tree, as shown in Fig. 1 (b).

Then, a block cluster tree $T_{I\times I}$ can be constructed by the hierarchical partitioning of $I\times I$. A block cluster tree is nothing but the interaction of two cluster trees: T_I of original basis function set and T_I of testing basis function set. The block cluster tree terminates at blocks $t\times s\in T_{I\times I}$ ($t\in T_I$ and $s\in T_J$) satisfying:

1. $\#t\le n_{\mathrm{leaf}}$ or $\#s\le n_{\mathrm{leaf}}$.
2. Clusters t and s satisfy admissibility condition of:
$$\min\{diam(\Omega_t),diam(\Omega_s)\}\le\eta dist(\Omega_t,\Omega_s), \quad (12)$$

where *diam* and *dist* denote the Euclidean diameter and distance of the supports of the basis functions in s, t, and $\eta>0$ controls the trade-off between admissible blocks. Blocks $t\times s\in T_{I\times I}$ satisfying (12) are called admissible blocks, which can be approximated by low-rank matrices in the following representation:

$$G=XY^T\ (G\in\mathbb{R}^{m\times n},X\in\mathbb{R}^{m\times k},Y\in\mathbb{R}^{n\times k},k\ll m,n). \quad (13)$$

The process of building $T_{I\times I}$ is shown in Fig. 1 (c). There are only two types of blocks in $T_{I\times I}$, i.e., admissible blocks stored as low-rank matrices and inadmissible blocks stored as full matrices.

For constructing the data-sparse representation $[A]_{\mathrm{DS}}$, all the non-zero matrix entries in $[A]$ are filled in inadmissible leaves while admissible leaves keep empty because the partial differential operator is local. Hence, the representation of $[A]_{\mathrm{DS}}$ is exact without approximation.

The obtained $[A]_{\mathrm{DS}}$ has a structure of a quad tree, which be written as:

$$A=\begin{bmatrix}A_{11} & A_{12}\\ A_{21} & A_{22}\end{bmatrix}. \quad (14)$$

Then, $[A]_{\mathrm{DS}}^{-1}$ can be computed recursively from this 2×2 partitioned block matrix as follows:

$$A^{-1}=\begin{bmatrix} A_{11}^{-1}+A_{11}^{-1}A_{12}S^{-1}A_{21}A_{11}^{-1} & -A_{11}^{-1}A_{12}S^{-1} \\ -S^{-1}A_{21}A_{11}^{-1} & S^{-1} \end{bmatrix}, \quad (15)$$

where $S=A_{22}-A_{21}A_{11}^{-1}A_{12}$. The inverses A_{11}^{-1} and S^{-1} are computed using (15) recursively. Here, the exact addition and multiplication are replaced by the formatted hierarchical matrix counterparts ($\oplus$ and $\otimes$). $[A]_{\mathrm{DS}}^{-1}$ has the same block cluster tree structure as $[A]_{\mathrm{DS}}$, whereas the admissible blocks are not empty but filled with non-zero entries during the recursive inversion. The DSAI algorithm can reduce the computational complexity and storage requirement to be O($k^2N\log^2N$) and O($kN\log N$), respectively [12,13]. Here, k is the average rank of low-rank matrices. Once $[A]_{\mathrm{DS}}^{-1}$ is obtained, the MVP can be performed with O($kN\log N$) computational complexity to complete a explicit update at each time step.

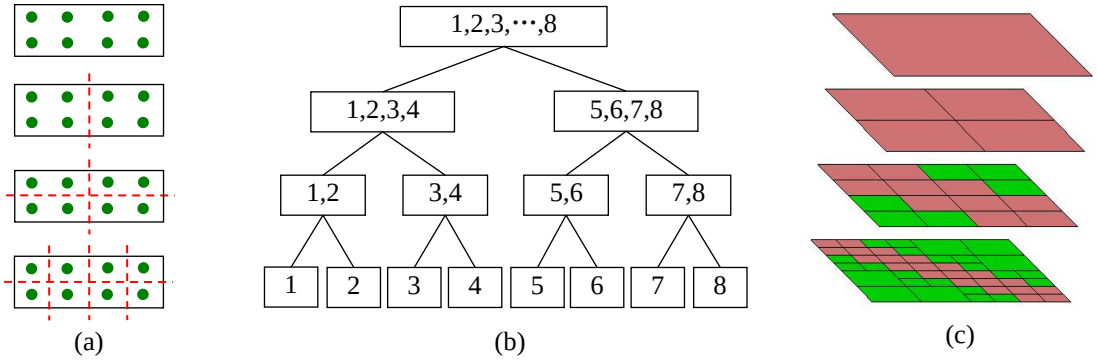

Fig. 1. (a) Recursive subdivision of the basis function set. (b) Cluster tree T_I. (c) Block cluster tree $T_{I\times I}$ based on T_I. Full matrices are red and low-rank matrices are green.

C. Recompression technique

As mentioned above, the DSAI algorithm compresses the originally dense inverse matrix to a data-sparse matrix, in which each admissible block $G_{m\times n}$ have a low-rank representation of $G_{m\times n}=X_{m\times k}Y_{n\times k}^T$ ($k\ll m,n$). However, these admissible blocks contain redundant information, and can be further compressed. In this section, a recompression technique is introduced to improve the efficiency of the explicit FETD solution.

In the recompressed inverse matrix $[A]_{\mathrm{RDS}}^{-1}$, any admissible block $G'_{m\times n}$ has a new low-rank representation of $G'_{m\times n}=U_{m\times k_1}S_{k_1\times k_2}V_{n\times k_2}^T$ ($k_1,k_2\ll m,n$), where U and V are called row cluster basis and column cluster basis, which satisfy $U^TU=I$ and $V^TV=I$, respectively. S is a coupling matrix.

Before introducing the recompression process, we define a far cluster set Far($\cdot$). For any cluster i on level l, Far(l_i) denotes the set of clusters satisfying the admissibility condition (12). If cluster $j\in$ Far(l_i), the interaction of i and j will lead to an admissible block $G_{m\times n}^{lij}=X_{m\times k}^{lij}(Y_{n\times k}^{lij})^T$, as shown in Fig. 2.

The recompression process can be divided into the following four steps:

1. For all $j\in$ Far(l_i), extract $X_{m\times k}^{lij}$ and put them together in sequence as $M^{li}=(\cdots,X_{m\times k}^{lij},\cdots)$.
2. Perform singular value decomposition (SVD) for the assembled matrix M^{li}, and truncate it with a pre-determined accuracy ε_t, we obtain $M^{li}=\tilde{U}^{li}\tilde{S}^{li}(\tilde{V}^{li})^T$, where $\tilde{U}^{li}$ and $\tilde{V}^{li}$ are orthogonal matrices, and $\tilde{S}^{li}$ is diagonal matrix. Matrix $\tilde{U}^{li}$ is the row cluster basis for cluster i on level l. U^{li} is also the column cluster basis for symmetric system matrix. The process of step 1 and 2 are described in Fig. 3.
3. For $j\in$ Far(l_i), $(\tilde{V}^{li})^T$ can be written as $(\cdots,\tilde{V}^{lij},\cdots)^T$. The coupling matrix S^{lij} of cluster i and j can be found by $S^{lij}=\tilde{S}^{li}(\tilde{V}^{lij})^T(Y^{lij})^T\tilde{U}^{lj}$.
4. For each level l ($2\le l\le L$, L is the depth of the cluster tree), repeat step 1 to 3 for all cluster to obtain all cluster basis matrices and coupling matrices.

In the resulting recompressed matrix $[A]_{\mathrm{RDS}}^{-1}$, each admissible block has a representation of $G_{m\times n}^{lij\prime}=G_{m\times n}^{lij\prime}=U_{m\times k_1}^{li}S_{k_1\times k_2}^{lij}(U_{n\times k_2}^{lj})^T$. Although $G'_{m\times n}$ has one more factor than $G_{m\times n}$, the compression degree of $[A]_{\mathrm{RDS}}^{-1}$ is higher than $[A]_{\mathrm{DS}}^{-1}$. The reason is that all the admissible blocks with the same row cluster share a row cluster basis U, and those with the same column cluster share a column cluster basis V. $[A]_{\mathrm{RDS}}^{-1}$ enters the explicit solution of FETD by the MVP at each time step.

The computational complexity of the MVP of $[A]_{\mathrm{RDS}}^{-1}$ is O($kN\log N$), which is the same as that of $[A]_{\mathrm{DS}}^{-1}$. However, the MVP of $[A]_{\mathrm{RDS}}^{-1}$ can be much faster because it reduces the constant in the complexity estimation. Hence, the recompression technique can further accelerate the efficiency of the FETD.

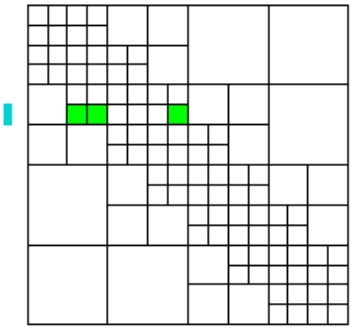

Fig. 2. The far cluster set Far($\cdot$).

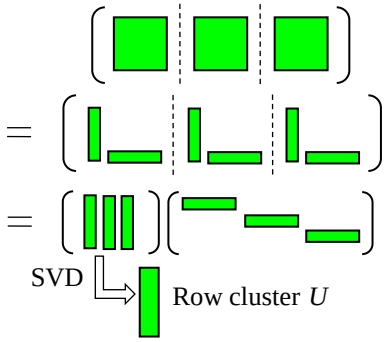

Fig. 3. Construction of the row cluster U.

III. NUMERICAL EXAMPLES

In this section, three numerical examples are presented to demonstrate the efficiency and accuracy of the proposed method for the fast simulation of microwave devices. For testing the accuracy of $[A]_{\mathrm{DS}}^{-1}$, the relative error is defined as $\delta = \left\| I - [A]_{\mathrm{DS}}^{-1}[A] \right\| / \|I\|$, where I is identity matrix and $\|\cdot\|$ denotes 2-Norm.

A. A dielectric-filled rectangular waveguide example

The first example analyzes a rectangular waveguide filled with a half-height dielectric block. The configuration and dimensions of this waveguide are presented in Fig. 4.

In order to obtain an input reflection coefficient, perfect match layers (PMLs) are placed at the input and out ports to simulate the matched loads. A modulated Gaussian pulse is applied with a center frequency of $f_0 = 10$ GHz and a bandwidth of 4 GHz. The time step size is $\Delta t = 1.67$ ps, which is ten times larger than conventional FETD method due to the unconditional stability of CN scheme. For the data-sparse approximate inversion, η in the admissibility condition (12) is set to be $\eta = 1.0$ and the minimal block size is chosen as $n_{\mathrm{leaf}} = 32$. The truncated rank k is set to be 10 and the accuracy of approximate inverse can reach the order of 10^{-5}, which is enough for an accurate solution. As shown in Fig. 5, the S parameters computed by the proposed method agree well with the results simulated by Ansoft HFSS software.

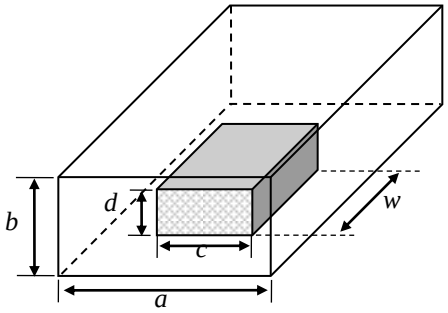

a=20.0, b=10.0, c=8.88, d=3.99, w=8.0 (Unit: mm)

Fig. 4. Dimensions of the dielectric-filled waveguide.

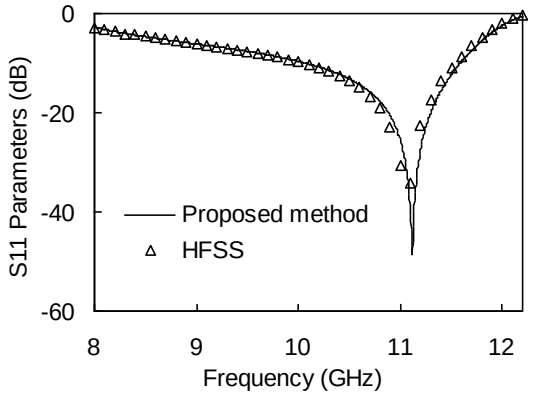

Fig. 5. S11 parameter of the dielectric-filled waveguide.

Then, the performance of data-sparse approximate inversion algorithm is tested for different mesh sizes and fixed accuracy. We increase the umber of unknowns N to test the time and memory costs of the DSAI algorithm, by increasing the mesh density and reducing Δt proportionally with the mesh density. As the theoretical analysis, the time and memory usages actually should be estimated as O($k^2N\log^2N$) and O($kN\log N$). For electrodynamic analysis, k will increase with N, but it is usually much smaller than N for the problems of moderate size. Hence, the time and memory usages can be observed to be very close to O($N\log^2N$) and O($N\log N$) for this example, as shown in Fig. 6 and Fig. 7.

In Table 1, the DSAI algorithm is compared with full matrix inversion algorithm for the explicit formulation. It can be seen that the DSAI can highly compress the original full inverse matrix with sufficient accuracy, and subsequently decrease the solution time.

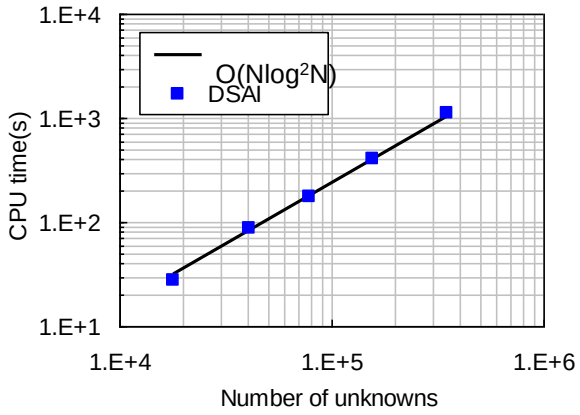

Fig. 6. Time usages for the DSAI algorithm.

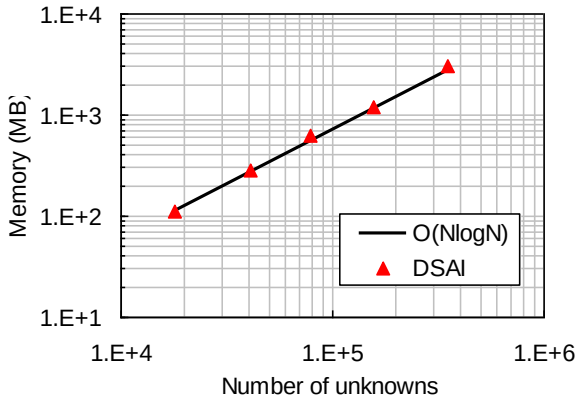

Fig. 7. Memory usages for the DSAI.

Table 1: Comparisons between the DSAI and full matrix inversion algorithm

Mesh Sizes	N_{unk}	M_{full} (GB)	M_{DSAI} (GB)	R_{comp}
Case 1	9,775	0.76	0.13	17.1 %
Case 2	18,068	2.49	0.26	10.4 %
Case 3	40,672	12.62	0.67	5.3 %

N_{unk}: number of unknowns.
M_{full}: memory required for the full inverse matrix.
M_{DSAI}: memory required for the DSAI matrix.
R_{comp}: compression ratio computed by M_{DSAI}/M_{full}.

B. An interdigital microstrip example

The second example deals with an interdigital capacitor microstrip filter. Its dimensions are shown in Fig. 8. The microstrip line is on a dielectric substrate with a height of h=0.508 mm and a relative inductivity of $\varepsilon_r = 2.2$.

A modulated Gaussian pulse is applied with a center frequency of $f_0 = 6.5$ GHz and a bandwidth of 5 GHz. The number of time steps is 2700. Mesh discretization generates 85,172 unknowns. The DSAI associated parameters are set to be $\eta = 2.0$ and $n_{leaf} = 16$. Figure 9 shows the S parameters computed by the proposed method in the case of truncated rank k=5, and compares the results with those simulated by Ansoft Designer software.

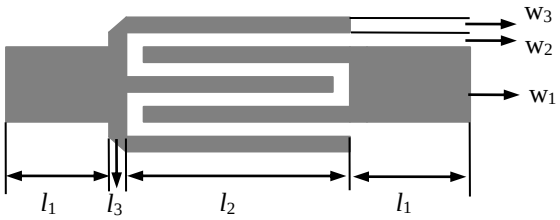

l_1=8.05, l_2=8.4, l_3=0.3, w_1=1.51, w_2=w_3=0.3 (Unit: mm)

Fig. 8. Dimensions of the interdigital microstrip.

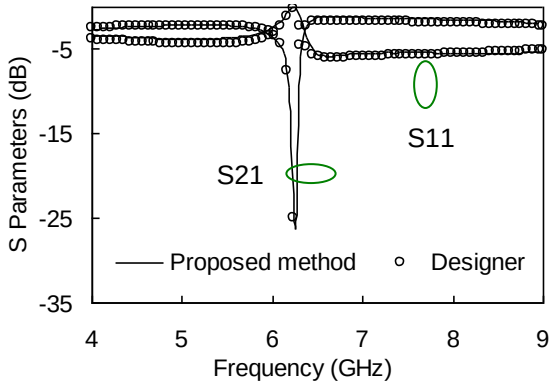

Fig. 9. S parameters of the interdigital microstrip.

Table 2 shows the performance of the DSAI algorithm. It can be seen that the inversion accuracy δ improves but the computational costs rise with the rank k increasing. The performance of the proposed recompression technique is tested for different mesh sizes and the results are reported in Table 3. For the three cases in the test, the accuracy of the solutions with and without recompression is controlled to be the same order of 10^{-5} by adjusting the rank k and the truncated SVD error ε_t. It is obvious that the total solution time can be significantly reduced by using the recompression technique. The main reason is that the recompression technique can further accelerate the DSAI-based MVP. Figure 10 demonstrates this conclusion more intuitively. As shown in Fig. 10, the recompressed MVP outperforms the unrecompressed MVP, although they both can be observed to scale nearly with O(Nlog$N$) computational costs.

Table 2: Performance of the DSAI algorithm

k	δ	T_{inv} (s)	M_{inv} (MB)	T_{MVP} (s)	T_{total} (s)
1	2.9e-3	289	364	0.64	1,758
5	1.0e-4	438	510	0.91	2,487
10	3.2e-5	763	691	1.23	3,391

T_{inv}: time used for DSAI algorithm.
M_{inv}: memory required for the data-sparse inverse matrix.
T_{MVP}: time used for the matrix-vector product of the data-sparse inverse matrix.
T_{total}: total solution time for all time steps.

Table 3: Performance of the recompression technique

Mesh Sizes	Without Recompression		With Recompression		
	T_{MVP}	T_{total}	T_{recomp}	T_{MVP}	T_{total}
Case 1	0.48	1,345	102.3	0.28	858
Case 2	1.37	3,780	323.3	0.79	2,541
Case 3	4.57	12,492	582.6	2.73	7,955

T_{MVP}: time used for the MVP of the inverse matrix.
T_{recomp}: time used for the recompression of the inverse matrix.
T_{total}: total solution time for all time steps.

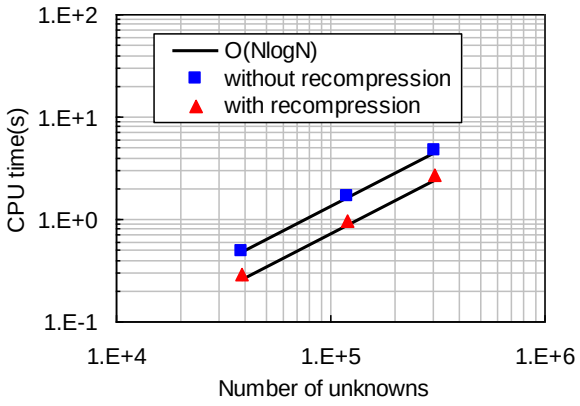

Fig. 10. Time usages for the data-sparse MVP.

C. A substrate integrated waveguide example

The last example considers a substrate integrated waveguide (SIW). SIW is a new type of microwave transmission line emerged in recent years, which holds the advantages of both conventional waveguide and microstrip line. The configuration and detailed dimensions of the SIW are presented in Fig. 11, respectively. The permittivity of the dielectric substrate is $\varepsilon_r = 2.2$ and the height of the substrate is h=0.787 mm. A modulated Gaussian pulse with a center frequency of $f_0 = 28$ GHz and a bandwidth of 8 GHz is adopted in our simulation.

In Fig. 12, S parameters computed by the proposed method are plotted together with the measurement results presented in [15], and good agreement can be observed. Then, the performance of the proposed recompression technique is tested. The numerical results are reported for three cases of different solution accuracy δ in Table 4. It can be found that the recompression technique can further reduce the total solution time of the FETD with the same order of solution accuracy.

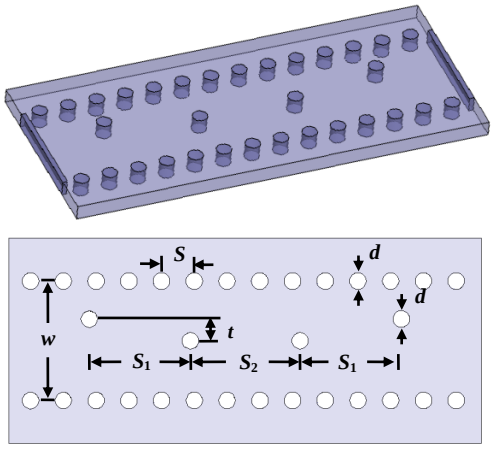

w=5.563, S=1.525, d=0.775, t=1.01, S_1=4.71, S_2=5.11 (mm)

Fig. 11. Configuration and dimensions of the SIW.

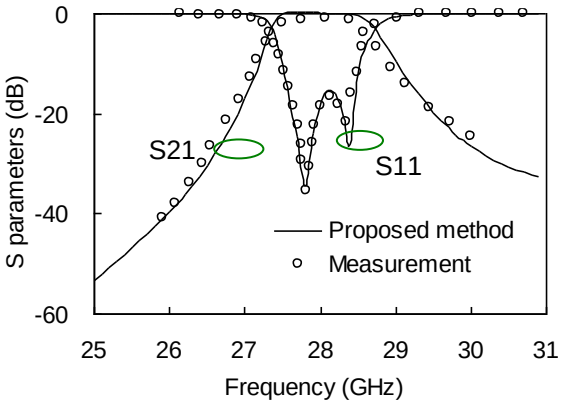

Fig. 12. S parameters of the SIW.

Table 4: Performance of the recompression technique

δ	Without Recompression		With Recompression		
	T_{MVP}	T_{total}	T_{recomp}	T_{MVP}	T_{total}
10^{-4}	1.42	3,620	281.5	0.72	2,153
10^{-6}	2.27	5,748	467.6	1.35	3,842
10^{-8}	3.91	10,109	834.1	2.23	6,558

IV. CONCLUSION

A data-sparse and fully explicit FETD method is developed for the fast electromagnetic simulation. By the data-sparse approximate inverse (DSAI) algorithm,

the inverse of the system matrix of CN-FETD electric field update equation can be computed and stored in a data-sparse way with almost linear costs, and then the solution at each time step is fully explicit. A recompression technique is proposed to further compress the data-sparse inverse matrix to improve the efficiency of explicit solution at each time step. Numerical results demonstrate the proposed method is robust for the simulation of microwave devices.

ACKNOWLEDGMENT

This work was supported by Open Research Program Foundation of State Key Laboratory of Millimeter Waves of K201411, Natural Science Foundation of Jiangsu Province of BK20140893, Natural Science Foundation of the Higher Education Institutions of Jiangsu Province of 14KJB510023, and NUPTSF of NY214040.

REFERENCES

[1] J. F. Lee, R. Lee, and A. Cangellaris, "Time-domain finite-element methods," *IEEE Trans. Antennas Propag.*, vol. 45, pp. 430-442, Mar. 1997.

[2] D. A. White, "Orthogonal vector basis functions for time domain finite element solution of the vector wave equation," *IEEE Trans. Magn.*, vol. 35, no. 3, pp. 1458-1461, May 1999.

[3] D. Jiao and J. M. Jin, "Three-dimensional orthogonal vector basis functions for time-domain finite element solution of vector wave equations," *IEEE Trans. Antennas Propag.*, vol. 51, no. 1, pp. 59-66, Jan. 2003.

[4] J. H. Lee, T. Xiao, and Q. H. Liu, "A 3-D spectral-element method using mixed-order curl conforming vector basis functions for electromagnetic fields," *IEEE Trans. Microw. Theory Tech.*, vol. 54, no. 1, pp. 437-444, Jan. 2006.

[5] B. He and F. L. Teixeira, "Sparse and explicit FETD via approximate inverse Hodge (mass) matrix," *IEEE Microw. Wireless Compon. Lett.*, vol. 16, no. 6, pp. 348-350, June 2006.

[6] J. Kim and F. L. Teixeira, "Parallel and explicit finite-element time-domain method for Maxwell's equations," *IEEE Trans. Antennas Propag.*, vol. 59, no. 6, pp. 2350-2356, June 2011.

[7] A. S. Moura, E. J. Silva, R. R. Saldanha, and W. G. Facco, "Performance of the alternating direction implicit scheme with recursive sparsification for the finite element time domain method," *IEEE Trans. Magn.*, vol. 51, no. 3, Mar. 2015.

[8] M. Movahhedi, A. A. H. Ceric, A. Sheikholeslami, and S. Selberherr, "Alternation-direction implicit formulation of the finite-element time-domain method," *IEEE Trans. Microw. Theory Tech.*, vol. 55, no. 6, pp. 1322-1331, 2007.

[9] R. S. Chen, L. Du, Z. B. Ye, and Y. Yang, "An efficient algorithm for implementing Crank-Nicolson scheme in the mixed finite-element time-domain method," *IEEE Trans. Antennas Propag.*, vol. 57, no. 10, pp. 3216-3222, Oct. 2009.

[10] M. Bebendorf and W. Hackbusch, "Existence of H-matrix approximants to the inverse FE matrix of elliptic operators with L∞-coefficients," *Numer. Math.*, 95, pp. 1-28, 2003.

[11] L. Grasedyck and W. Hackbusch, "Construction and arithmetics of H-matrices," *Computing*, vol. 70, no. 4, pp. 295-344, Aug. 2003.

[12] S. Börm, L. Grasedyck, and W. Hackbusch, "Introduction to hierarchical matrices with applications," *Engineering Analysis with Boundary Elements*, no. 27, pp. 405-422, 2003.

[13] H. Liu and D. Jiao, "Existence of H-matrix representations of the inverse finite-element matrix of electrodynamic problems and H-based fast direct finite-element solvers," *IEEE Trans. Microw. Theory Tech.*, vol. 58, no. 12, pp. 3697-3709, 2010.

[14] S. Borm, "Data-sparse approximation by adaptive H^2-matrices," *Computing*, vol. 69, no. 1, pp. 1-35, Sep. 2002.

[15] M. Bozzi, L. Perregrini, and K. Wu, "Modeling of conductor, dielectric, and radiation losses in substrate integrated waveguide by the boundary integral-resonant mode expansion method," *IEEE Trans. Microw. Theory Tech.*, vol. 56, no. 12, pp. 3153-3161, 2008.

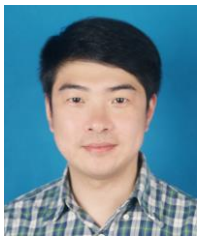

Ting Wan received the Ph.D. degree in Information and Communication Engineering from Nanjing University of Science and Technology.

He is currently a Lecturer of Nanjing University of Posts and Telecommunications. His research interests include computational electromagnetics, electromagnetic scattering and radiation, and electromagnetic modeling of microwave/ millimeter wave integrated circuits.

Lei Du received the Ph.D, degrees in Electromagnetic Fields and Microwave Technology from Nanjing University of Science and Technology, China, in 2010.

Her current research interest is computational electromagnetics.

Jian Zhu received the Ph.D. degrees in Electromagnetic Fields and Microwave Technology from Nanjing University of Science and Technology (NUST), China, in 2010.

She is currently a Lecturer of Nanjing University of Posts and Telecommunications. Her current research interests include CEM and antennas.

Design and Implementation of Claw Pole Alternator for Aircraft Application

Deepak Arumugam [1], Premalatha Logamani [2], and Santha Karuppiah [1]

[1] Dept. of Electrical & Electronics Engineering
Sri Venkateswara College of Engineering, Chennai, India
adeepakceg@gmail.com, santha@svce.ac.in

[2] School of Electrical Engineering
VIT University, Chennai, India
premaprak@yahoo.com

Abstract ─ Nowadays most of the countries develop special aircraft and utilize them for defense applications. This paper deals with the modeling, simulation, and implementation of the Claw pole synchronous generator. The design specifications of the designed generators are compatible for aircraft applications. The main objective of this work was to estimate and test the performance of the claw pole alternator under high speed operation. The electromagnetic design of the machine was carried out using Finite Element Analysis (FEA) software. The performance of the machine was tested under laboratory environment. The results of experimentation were compared with those of simulation and proved.

Index Terms ─ Claw pole alternator, electromagnetic analysis, finite element method, Light Combat Aircraft.

I. INTRODUCTION

The Indian Aircraft Project is now called the Light Combat Aircraft (LCA) in order to create an identity distinct from the Light Weight Fighter concept. In the early 1980s, India, knowing well that the Mig-21s, Mig-23s, and a variety of other aging Russian fighters composing a vast percentage of their air power would soon grow obsolete, decided to produce a new fighter to replace the MiG-21 "Fishbeds" legacy. The new aircraft would be of indigenous design, and its development would fall under the care of India's own Aeronautics Limited. The aircraft that would spawn from the program was designated the Light Combat Aircraft and it would be one of the world's lightest, yet most capable dedicated multi-role aircraft of all time [1]-[2]. In LCA, 30-60KVA generator provided electrical power supply for all electrical loads. When this power system fails, the backup power supply supports and is called integrated generator system (IGS) providing power supply for emergency loads such as cabin lighting, food preparation, gunshot and cockpit, etc. This IGS consists of 3 electrical generators, namely permanent magnet synchronous generator, brushless synchronous generator (also called main exciter) and synchronous generator (also called main generator) being mounted on single shaft which is driven by aircraft engine gear box. The basic structure of IGS is shown in Fig. 1 [3].The major problem in aircraft to fix in this IGS is the available space in aircraft, which is just 140 mm. Also, aircraft engine rotating speed lies between 7000 rpm and 24000 rpm. So, it does not provide any external cooling arrangements at this dimension for high speed operations. Due to these reasons, much heat is produced in the main generator.

In general, salient pole synchronous generators (SPSG) are used as a main generator in IGS. These SPSGs are normally suitable for low speed applications. For high speed operation SPSG produces much heat in a very short time. Also, it has large rotor diameter and short axial length. Due to their mechanical instability at higher speeds, they are used for generation at low and medium speeds only. On the other hand, the smooth cylindrical (round) rotors are characterized by smaller diameters and larger axial lengths. They are mechanically stable even at high speeds. They are used for generation at high speeds. Also in salient pole generator X_d is higher than X_q, hence more stable (electrically), maximum power transfer is possible at torque angle delta lesser than 90 degree in salient pole; thus electrical advantages are more, but mechanical stability is less at higher speed as said, hence not suitable for modern high speed generators.

These alternators reduce power output due to eddy current losses produced in the machine and these losses are converted into heat [4]. Flux distribution is relatively poor and generated emf is not good compared with non-salient pole type rotor. Salient pole rotors generally need damper windings to prevent rotor oscillations during operation. The finite element analysis based analysis of SPSG for aircraft application was discussed in [5]. This machine produced much heat within short duration when simulation model was developed as a prototype model.

Submitted On: January 7, 2016
Accepted On: March 18, 2016

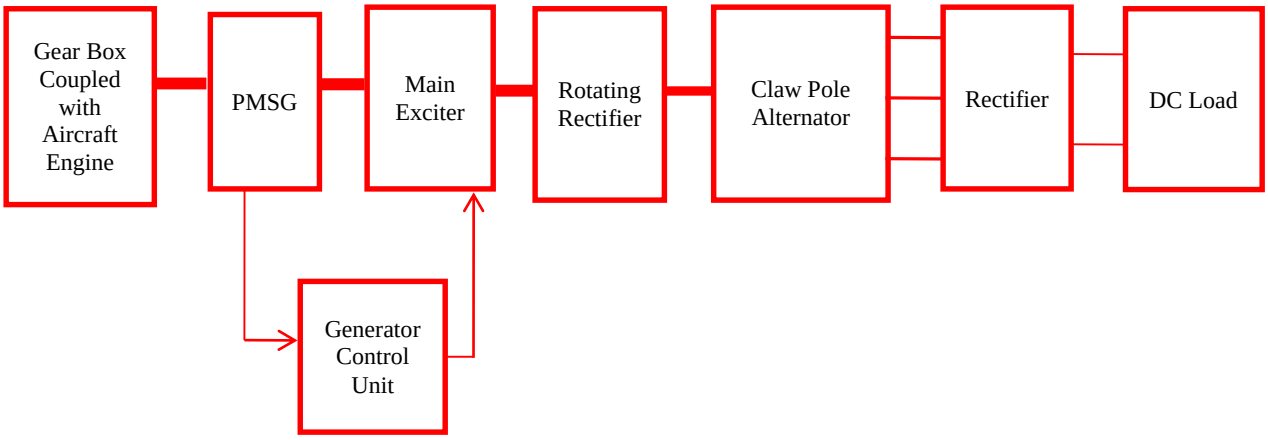

Fig. 1. Basic structure of IGS system.

On the other hand, claw pole alternator or Lundell alternators are able to produce large power density compared with the SPSG. It is a simple and highly reliable machine. The popularity of this type of electric machine is mainly due to its high pole pair number which increases the torque density and its robust structure allowing for high speed operation [6]. Generally claw pole alternators are applicable for automobile industry and aircraft [7]. Claw pole alternators have more air gap than the salient pole generators, so they allow more air to flow inside the machine and reduce heating effect when the machine is running at high speed. But it has the characteristics of high saturation, high magnetic leakage between claws, low efficiency and relatively large field time constant [8]-[10]. The 3D modeling and numerical analysis of the alternator with claw poles for electric car applications was discussed in [11]. The performance of the Lundell alternators for high power applications can be improved by reducing their number of turns & diode bridge rectifier replaced with PWM rectifier without modifying the dimensions of the generator [12]. The RMxprt motor design tool greatly simplifies this process and not only it provides the model parameters in seconds but also exports models for either FEA or system level simulation. It allows quick changes in physical design parameters and reduces time consumption for analytical design. The results obtained from RMxprt tools were directly applied to the 3D time stepping transient finite element analysis to directly study transient as well as steady-state performance of a machine [13]. The analytical modeling and testing of a 14V/6000 rpm claw pole alternator was presented in [14].

The above literature, however, does not deal with claw pole alternator pertaining to a specific dimension, speed and power rating. This work proposes the claw pole alternator for aircraft applications with required dimension and high speed operations. The simulation analysis & prototype model of 28V/180A/9000 rpm claw pole alternator are presented. The organization of the paper is as follows: Section II deals with the modeling & model description of the claw pole alternator. The simulation results of the proposed generator are given in Section III. The experimental results are presented in Section IV. The work is concluded in Section V.

II. DESIGN AND MODEL DESCRIPTION OF CLAW POLE ALTERNATOR

A. Basic equations of claw pole alternator and electromagnetic analysis

In claw pole alternator rotor construction differs from ordinary SPSG. It has cylindrical field windings surrounded by forged pole pieces or claw poles. The modeled machine has 4 poles and 24 slots with concentrated stator winding and cylindrical rotor winding. At the steady state the expression for stator current by dqo transformation is:

$$\begin{pmatrix} I_d \\ I_q \\ I_o \end{pmatrix} = \sqrt{\frac{2}{3}} \begin{pmatrix} \cos\varphi & \cos(\varphi - \frac{2\pi}{3}) & \cos(\varphi - \frac{4\pi}{3}) \\ -\sin\varphi & -\sin(\varphi - \frac{2\pi}{3}) & -\sin(\varphi - \frac{4\pi}{3}) \\ \frac{1}{2} & \frac{1}{2} & \frac{1}{2} \end{pmatrix} \begin{pmatrix} I_a \\ I_b \\ I_c \end{pmatrix}, \quad (1)$$

where

$$I_a = I_p \cos(\omega t + \varphi)$$
$$I_b = I_p \cos(\omega t + \varphi - \frac{2\pi}{3}) \quad (2)$$
$$I_c = I_p \cos(\omega t + \varphi - \frac{4\pi}{3}).$$

Here, I_p is the peak value of phase current. The stator voltages for d-q axis are:

$$V_d = I_d r_a + \frac{d\psi_d}{dt} - \omega\psi_q, \quad (3)$$

$$V_q = I_q r_a + \frac{d\psi_q}{dt} - \omega\psi_d. \quad (4)$$

The flux linkages for d-q axis are:

$$\psi_d = -I_d L_d + I_f L_{afd}, \quad (5)$$

$$\psi_q = -I_q L_q, \quad (6)$$

d-q axis reactances are:

$$X_d = \frac{\omega_b L_d}{Z_b}, \quad (7)$$

$$X_q = \frac{\psi_q}{I_q}, \quad (8)$$

where r_a is the armature winding resistance, L_q and L_d are d-q axis self inductances and L_{afd} is the mutual inductance between field winding and the direct axis and ω_b & Z_b are the base speed and base impedance.

The electromagnetic equations of the machine are given by:

$$\nabla \times E = \frac{\partial B}{\partial t}, \quad (9)$$

$$\nabla \times H = J + \frac{\partial D}{\partial t}, \quad (10)$$

$$\nabla . B = 0, \quad (11)$$

where E and H are electric and magnetic field intensities, D and B are electric and magnetic flux densities, J is current density and ρ is the amount of charge for unit volume.

The reluctance based magnetic equivalent circuit model of the claw pole alternator is presented in [15] which is shown in Fig. 2.

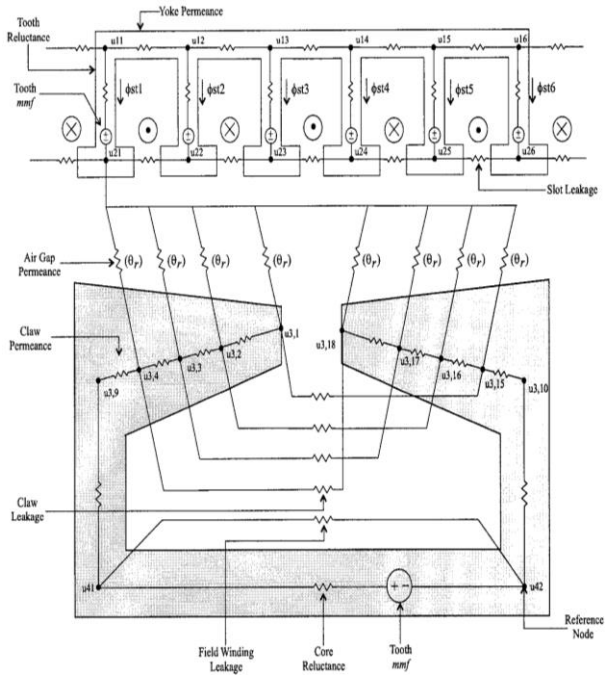

Fig. 2. Magnetic equivalent circuit of claw pole alternator.

The air gap permeance is:

$$P_{airgap} = \mu_0 \frac{A(\vartheta_r)}{g}, \text{ when claw aligned with stator teeth}$$
$$= 0 \quad \text{Otherwise}, \quad (12)$$

where $A(\vartheta_r)$ is the area of the overlap.

B. Analytical design of claw pole alternator

The initial dimensions include stator outer diameter and rotor inner diameter; power rating and speed range are given by Combat Vehicles Research & Development. Based on their input, stator design is carried out using design equations available in [16] and a few of them presented below. The design of claw pole rotor is carried out based on [17] and it is verified by using design software RMxprt.

The design can be optimized by using Matlab program with more iteration. The major factors considered for optimized design are efficiency, temperature rise at different load conditions (100%, 125% & 150% of full load) and losses. The optimization can be achieved only at 59th iteration and it is listed in the design table. The general design expressions are given below:

KVA rating of a 3 phase synchronous machine is:

$$\text{KVA} = 11\, K_{w1}\, B_{avg}\, q\, D^2\, L\, n_s * 10^{-3}, \quad (13)$$

where, K_{w1} is winding factor for stator winding, B_{avg} is specific magnetic loading, q is specific electric loading, D is diameter of stator bore and n_s is synchronous speed in rps.

Induced EMF per phase of a synchronous machine is:

$$E_{ph} = 4.44\, K_{w1}\, \Phi_m\, f\, T_{ph} \text{ in Volts}, \quad (14)$$

where, Φ_m is maximum flux passing through the core, f is frequency in Hz and T_{ph} is total number of turns per phase.

Stator Mean Diameter:

(MD) = (Slot Root Dia + Slot Tip Dia)/2. (15)

Pole Mean Diameter:

(PMD) = (Pole Tip Dia + Pole Root Dia)/2. (16)

Self-inductance:

$$L_g = \frac{\mu_0 \Pi L_{stk} r_1 T_p^2}{2 P_p^2 g'}, \quad (17)$$

where g' is the gap coefficient = C_g g and p = number of rotor poles,

$$\text{Peripheral speed} = \pi d n_s \frac{m}{s}, \quad (18)$$

where d = rotor diameter in mm.

The shape of the pole is determined by the pole pitch and it is denoted by τ,

$$\tau = \frac{\pi\, d\, m}{p}. \quad (19)$$

The dimension of claw pole rotor is shown in Fig. 3 which is obtained from simulation tool MagNet 7. In this figure w_b and w_t are the width of the pole at the bottom and the top respectively, r_r is the radius of the rotor and h is the height of the pole. t_t and t_b are the thicknesses of the pole at the top and the bottom respectively.

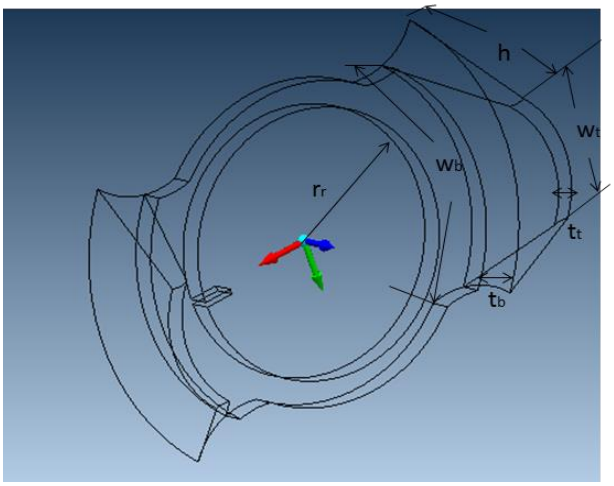

Fig. 3. Dimensions of claw pole.

The design specification of the machine according to the requirement is shown in Table 1.

Table 1: Design parameters

Parameter	Value
Stator diameter in mm	138.5
Core length in mm	23
Rated power in W	5000
Output voltage in V	28
Flux density in Wb/m^2	3.25
Phase current in A	133.3
Field excitation current in A	10
Power factor	0.88
Speed in RPM	9000
Number of slots	24
Number of poles	4
Length of the air gap in mm	0.37

III. FINITE ELEMENT ANALYSIS OF CLAW POLE ALTERNATOR

Finite element analysis is an effective simulation tool for analyzing complicated structure with non-linear elements. Normally electromagnetic analysis of the electrical machines is carried out using finite element software like SPEED, FLUX, MagNet, Motor Solve, etc. These tools act as intermediator between analytical calculation and prototype model for the purpose of reduced cost and improved performance. In this analysis simulation work was carried out using MagNet software which is used to see the visual effect of flux linkage, flux density, and voltage, current and ohmic losses. Generally claw pole alternator has magnetic field effect in the z direction also. So it is not possible to analyze this field in 2D software. Even though 3D analysis takes more time for solving the problems, it is necessary to analyze the electromagnetic effect of claw pole generator in all 3 directions.

Magnet software version 7 is used for performing magnetic analysis of the machine. Boundary used in this problem is closed boundary, so problem formulation is based on vector potential with magneto dynamic computations. Also number of nodes is 57317, number of edges is 178965, and number of faces is 121727. The FEM based 3D design of claw pole generator is shown in Fig. 4. In the preprocessor step the generator was designed based on analytical design values. After the design completion, machine stator and rotor core were filled with cold rolled steel and windings were filled with copper material. The stator-rotor structure is shown separately in Fig. 5. The mesh generated claw pole generator is shown in Fig. 6. In this problem the size of the meshes is 2 mm for entire generator includes stator and rotor. Also, the shape of mesh is triangular, because it will give accurate result when compared with other mesh shapes. If the size of mesh is reduced below 2 mm, overlap will occur between meshes and it will not be possible to get output properly. The calculation time of the generator can be increased by increasing the number of steps fixed in the software. The number of steps fixed to solve this problem is 10.

In the processing step, the machine goes through 10 steps and it takes 32 hours 12 minutes for solving the problem. In post processor, the flux linkage, magnetic flux density, voltage and current plots are obtained. In Fig. 7, the magnetic flux density plot and direction of magnetic flux density are shown. From the figure it is observed that the maximum value of flux density is 3.28 Wb/m^2.

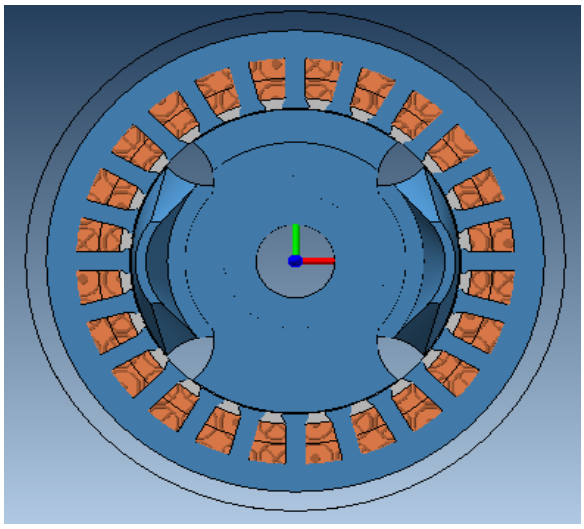

Fig. 4. 3D model of claw pole alternator.

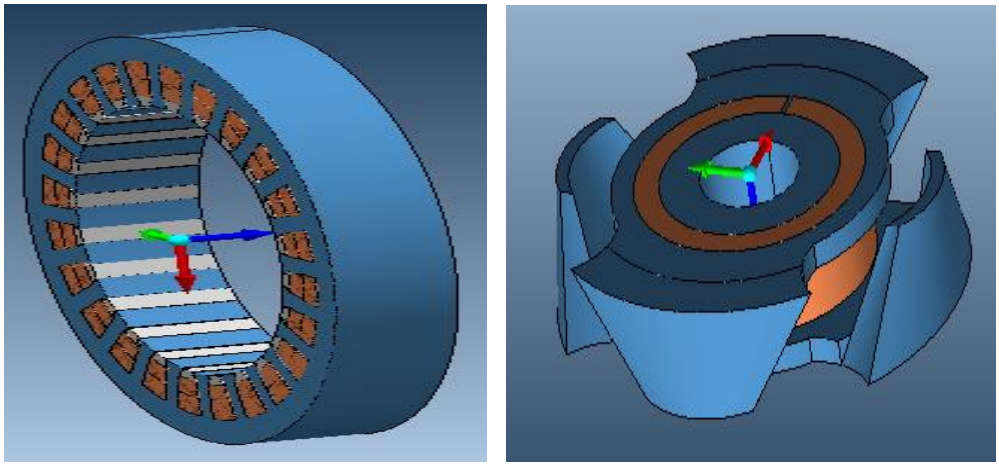

(a) Stator model (b) Rotor model

Fig. 5. Stator-rotor structure (3D view).

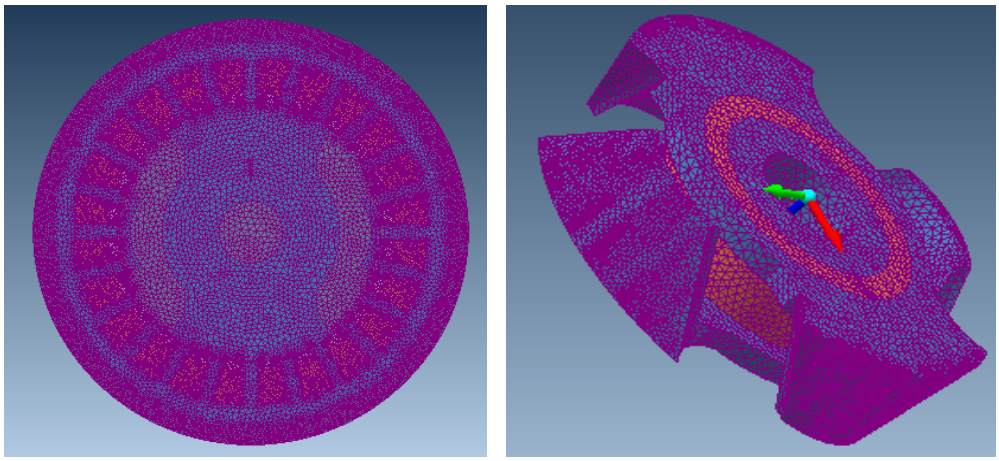

(a) Stator mesh (b) Rotor mesh

Fig. 6. Stator and rotor mesh generation.

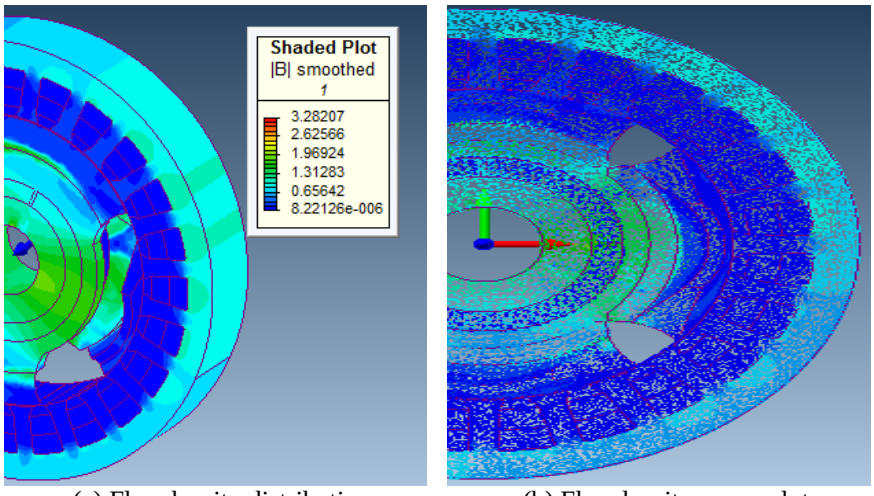

(a) Flux density distribution (b) Flux density arrow plot

Fig. 7. Flux density plot.

The required output from the claw pole generator is DC. So, the stator coils are connected to resistance load at a value of 0.155 Ω through a diode bridge rectifier circuit and this is shown in Fig. 8. The output AC voltage & current at armature windings, DC current & voltage at load are obtained from the machines which are shown in Fig. 9 and Fig. 10 respectively.

From Fig. 9 and Fig. 10 it is seen that both the voltage and the current waveforms are slightly oscillating on their peak values and approximately the value of the output voltage is 28V and the output current is 180A. From the simulation results it is seen that the values obtained from the simulation analysis are the same as the analytical values.

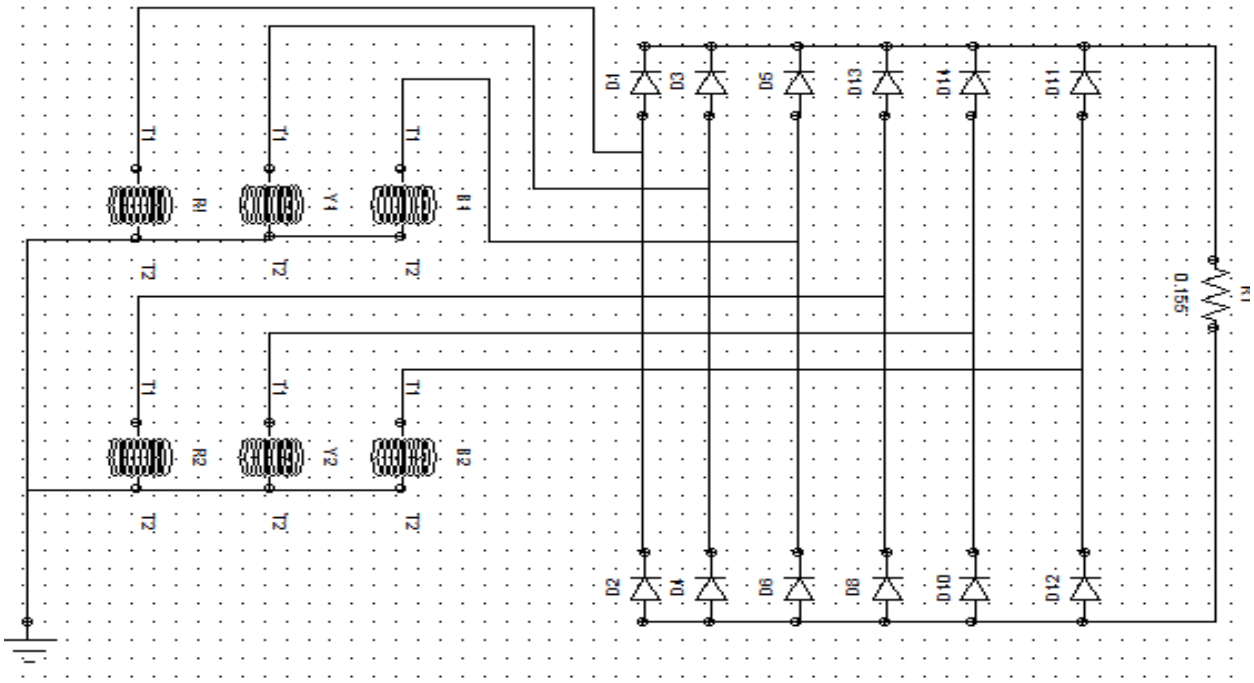

Fig. 8. Stator coil connected to external load.

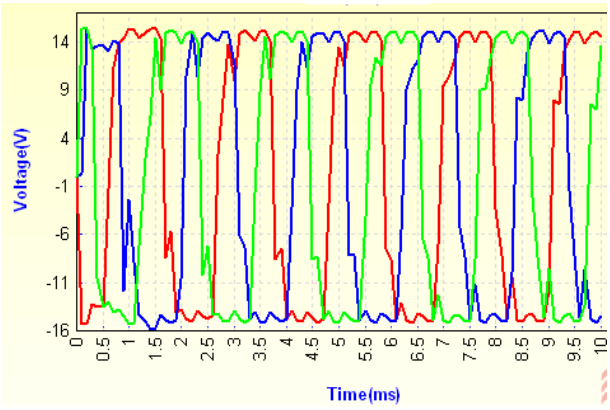

(a) Generated voltage at the armature

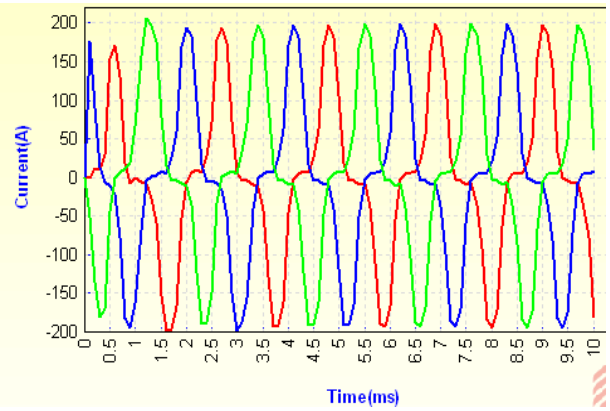

(b) Armature current

Fig. 9. Voltage and current at the armature.

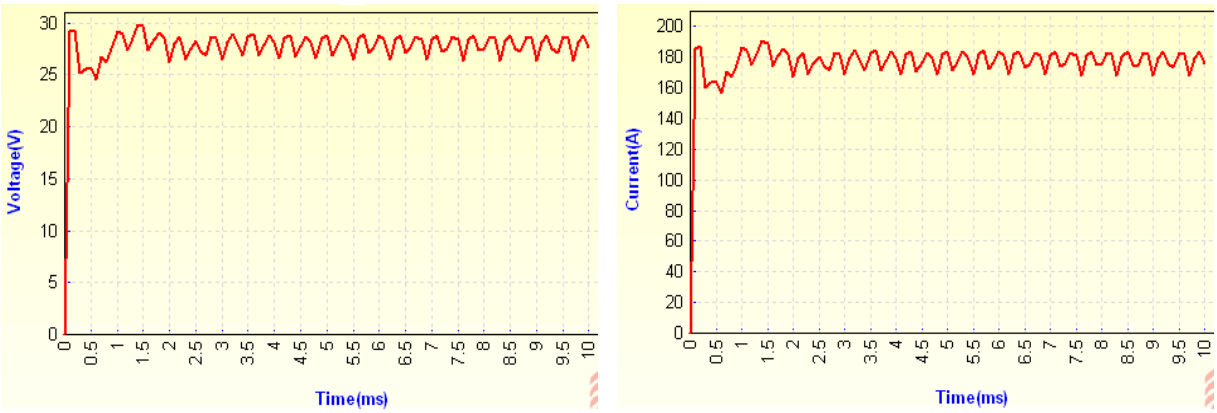

(a) Voltage across load (b) Current flowing through the load

Fig. 10. Voltage and current at load.

IV. HARDWARE IMPLEMENTATION

The structural block of the experimental set-up is shown in Fig. 11. In this figure generator control unit is the combination of rectifier and CUK converter to provide constant DC current to the field windings of the claw pole alternator. Diode bridge rectifier circuit is connected inside the claw pole alternator.

The prototype model of the 5KW claw pole alternator was fabricated and tested in the laboratory. The snapshot of the alternator is shown in Fig. 12. It consists of 5KW claw pole alternator coupled with induction motor acting as prime mover, gear box, generator control unit and load bank. The performance of the generator was tested under the speed of 2000 rpm to 10,000 rpm with 10A field excitation current. Under no-load condition generator terminal voltage varies linearly with respect to the speed, while the GCU is operated under manual control. On the other hand, terminal voltage varies inversely with respect to the load and current varies linearly with respect to the load and this is shown in Fig. 13. Similarly the terminal voltage of the generator under closed loop control of the GCU is shown in Fig. 14. It is observed that the peak values of terminal voltage & current are approximately 27.5V and 179.3A respectively. The analytical results were compared with those of simulation and experiment in Table 2.

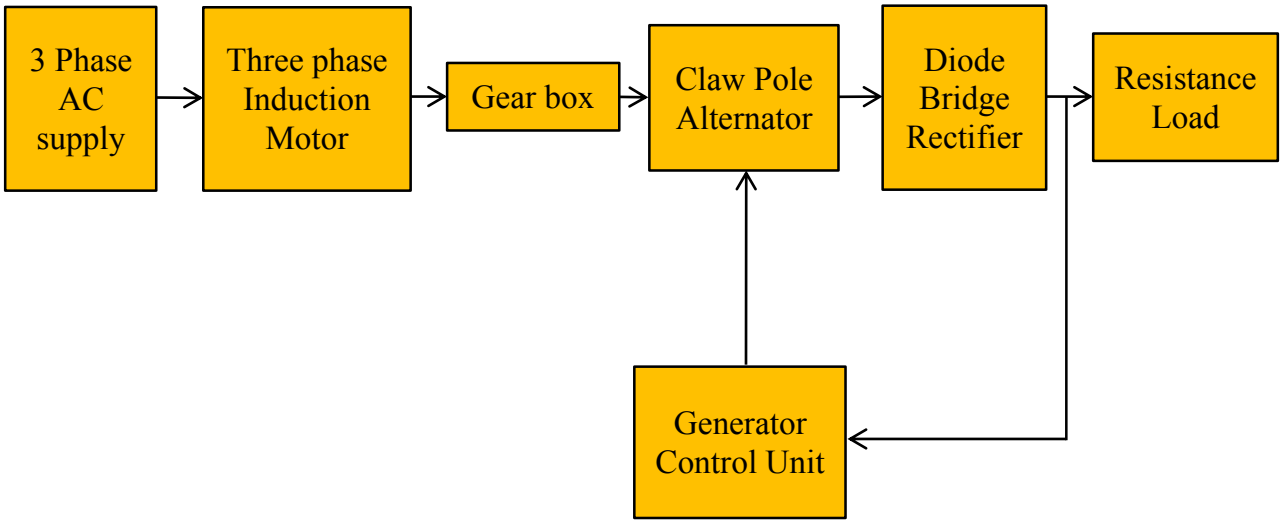

Fig. 11. Experimental set-up of the proposed alternator.

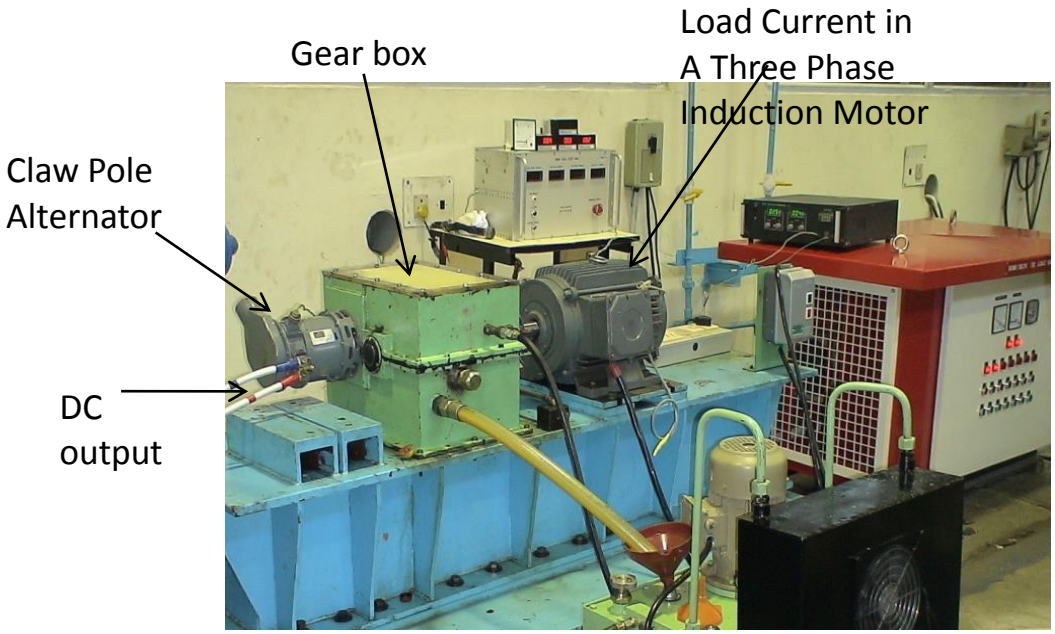

Fig. 12. Prototype model of the 5KW claw pole alternator.

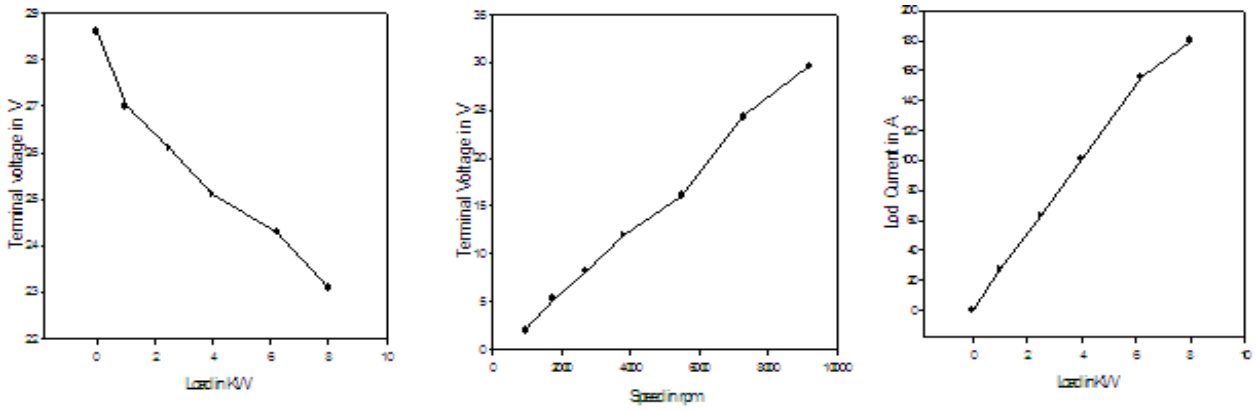

Fig. 13. Open loop characteristics with & without load condition.

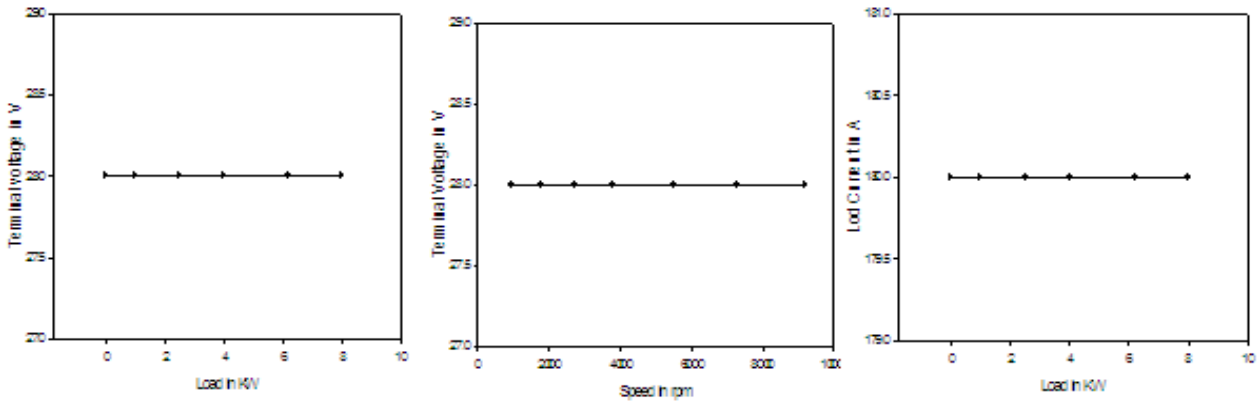

Fig. 14. Closed loop characteristics with & without load condition.

Table 2: Comparison of analytical, simulation, and hardware results

Parameter	Theoretical Design Value	Simulation Result	Hardware Result
DC output voltage	28V	27V	27.5V
DC output current	180A	178A	179.3A
Flux destiny	3.25 Wb/m^2	3.28 Wb/m^2	3.2 Wb/m^2

V. CONCLUSION

Integrated generator system provides continuous power supply to the aircraft during war and emergency conditions. Synchronous generator is the one main generator in this IGS. The performance of the non-salient pole alternator is better than that of the salient pole alternator for high speed applications due to large air-gap, less eddy current loss, and high efficiency. In this paper the electromagnetic analysis of the 5KW/28V claw pole alternator at a speed of 9000 rpm was presented using finite element analysis software. The prototype model of the 5KW claw pole alternator was tested in the laboratory and it was observed that the output voltage and the current obtained from the simulation tool were equal to the laboratory results. This generator has the advantages of more air gap space, less temperature rise, less eddy current loss, better ventilation compared with the salient pole generator. Significant results for the proposed system pertaining to the aircraft application were presented. The thermal analysis of the claw pole generator and the overall performance of the integrated generator system will be studied in future.

REFERENCES

[1] https://en.wikipedia.org/wiki/HAL_Tejas

[2] http://www.tejas.gov.in/

[3] D. Arumugam and P. Logamani, "Performance evaluation of brushless exciter for aircraft applications," *Australian Journal of Basic and Applied Sciences*, vol. 8, no. 18, pp. 151-158, 2015.

[4] H. B. Chen and M. T. York, "Alternator having claw-pole rotor," *US6989622 B1*, 24 Jan 2006.

[5] D. Arumugam and P. Logamani, "Coupled magnetic field and thermal analysis of synchronous generator," *Australian Journal of Basic and Applied Sciences*, vol. 8, no. 2, pp. 124-131, 2014.

[6] G.-H. Lee, G.-S. Choi, and W. Choi, "Design considerations for low voltage claw pole type integrated starter generator (IGS) systems," *Journal of Power Electronics*, vol. 11, no. 4, pp. 527-532, 2011.

[7] L. Tutelea, D. Ursu, I. Boldea, and S. Agarlita, "IPM claw-pole alternator system for more vehicle braking energy recuperation," *Journal of Electrical Engineering*, pp. 1-10, 2013.

[8] H. Bai, S. D. Pekarek, J. Tichenor, W. Eversman, D. J. Buening, G. R. Holbrook, M. L. Hull, R. J. Krefta, and S. J. Shields, "Analytical derivation of a coupled-circuit model of a claw-pole alternator with concentrated stator windings," *IEEE Transactions On Energy Conversion*, vol. 17, no. 1, pp. 32-38, 2002.

[9] A. G. Kladas, M. P. Papadopoulos, and J. A. Tegopoulos, "Design considerations for claw pole alternators for wind power applications," *The International Journal for Computation and Mathematics in Electrical and Electronic Engineering*, vol. 17, no. 1, pp. 151-154, 1998.

[10] S. Felicia, K. B. Agoston, M. C. Steluta, and T. Raluca, "Stator geometry influence on the machine magnetic field distribution for claw-pole generator," *International Conference on Clean Electrical Power (ICCEP)*, 2011.

[11] C. Barz, C. Oprea, and F. Dragan, "Numerical modeling of claw-poles alternator," *Carpathian Journal of Electronic and Computer Engineering*, vol. 5, pp. 9-12, 2012.

[12] R. Ivankovic, J. Cros, M. T. Kakhki, C. A. Martins, and P. Viarouge, *Power Electronic Solutions to Improve the Performance of Lundell Automotive Alternators, New Advances in Vehicular Technology and Automotive Engineering*, ch. 6, In Tech Press, Croatia, pp. 169-190, 2012.

[13] B. Knorr, D. Devarajan, D. Lin, P. Zhou, and S. Stanton, "Application of multi-level multi-domain modeling to a claw-pole slternator," *Society of Automotive Engineers*, pp. 1-7, 2004.

[14] S. C. Tang, T. A. Keim, and D. J. Perreault, "Thermal modeling of Lundell alternators," *IEEE Transactions On Energy Conversion*, vol. 20, no. 1, pp. 25-36, 2005.

[15] J. M. Williams, "Modeling and Analysis of Electrical Machines with Asymmetrical Rotor Poles using Reluctance based Magnetic Equivalent Circuit," *University of Missouri Rolla*, USA, 2004.

[16] A. K. Sawhney, *Course in Electrical Machine Design*, Dhanpat Rai & Sons Publications, Sixth edition, 2006.

[17] R. Arumugam and M. Azhagr Raj, "Performance Analysis of Claw-Pole Alternator by Three Dimensional Finite Element Analysis," *Anna University*, India, 2009.

CSC-SR Structure Loaded Electrically Small Planar Antenna

Rajni [1] and Anupma Marwaha [2]

[1] Department of Electronics and Communication Engineering
Shaheed Bhagat Singh State Technical Campus, Ferozepur, Punjab 152004, India
rajni_c123@yahoo.co.in

[2] Department of Electronics and Communication Engineering
Sant Longowal Institute of Engineering and Technology, Sangrur, Punjab 148106, India
marwaha_anupma@yahoo.co.in

Abstract ─ This paper aims at a new planar left hand metamaterial structure for loading planar microstrip antenna (MPA). A metallic planar dual turn spiral resonator (DTSR), useful for artificial magnetic media design, is merged with a capacitive loaded strip (CLS) on the same plane to design capacitive strip coupled spiral resonator (CSC-SR) unit cell structure. Apart from having small size, the new structure offers advantages of demonstrating wide left handed frequency band, and simplicity of fabrication being on same plane, hence indicating supremacy of its inclusion in engineering of left hand metamaterials. The size of proposed antenna is $0.177\lambda \times 0.243\lambda$. The electro-magnetic coupling of the proposed structure causes the MPA to resonate at lower frequency of 13.25 GHz due to loading effects. The proposed novel antenna is able to give better performance in terms of return loss, gain and fractional bandwidth and is suitable for satellite communication. The measured results are presented to validate simulated model of the proposed antenna.

Index Terms ─ High Frequency Structure Simulator, left hand metamaterials, spiral resonator.

I. INTRODUCTION

Today's need for multifunctional systems demands small handheld portable wireless equipment. In order to fulfill this demand, researcher community is always challenged to design new small sized and more multifunctional antennas. An ineffaceable mark in this direction has been created by outset of metamaterials by antenna researchers for improving the performance of conventional planar antennas such as patch antenna [1]. Metamaterials (MTMs) are structured composite materials with inimitable characteristics caused by interaction of electromagnetic waves with the finer scale repetition of natural materials [2]. These may be used to amend the effective electromagnetic parameters of planar antenna dielectrics and to design antennas with improved coupling to the feed, augmented impedance, matching bandwidths, scaled down size and narrower beam widths as compared to those which instead choose the conventional dielectric materials.

The notion of these materials come into sight with the revolutionary intangible idea of Veselago [3] but materialized with the work of Pendry to synthesize the materials artificially [4-6] with split ring resonators (SRRs) and thin wires. These are also termed as double negative materials or left hand materials (LHM). It is known that some metals like gold, silver show a negative permittivity at optical frequencies [5]. But no material with negative permeability exists in nature. Hence, several different approaches to design SRR have been developed and practiced for various microwave applications to investigate the physics behind them and effects of their geometry on the fundamental material parameters of LHM. The SRRs can be coupled in many different ways by coalescing them with microstrip, coplanar and stripline feed to add the planarity attribute. Depending on the type of coupling used and resonator, different characteristics of the circuit can be customized. Various shapes of SRRs including rectangular [7-8], symmetrical [9], triangular [10], hexagonal [11], spiral [12-14], circular [15-16], omega [17] and S-shaped [18] etc., and their configurations including edge-coupled and broadside-coupled [19] and complementary forms [20-21] etc. have been investigated in literature and are still in progress.

This paper focuses on electrically small rectangular microstrip patch antenna (MPA) loaded with new left hand metamaterial unit cell structure. This structure is formed by merging dual turn spiral resonator (DTSR) and capacitance loaded strip (CLS) on the same side of plane on which the antenna is fabricated. The main advantages of spiral resonator (SR) are its small electrical size at resonance, lack of magneto-electric coupling thus avoiding bi-anisotropic effects in the bulk medium made up of this inclusion and easy fabrication.

Submitted On: February 17, 2016
Accepted On: May 3, 2016

The paper is planned in four Sections. After introduction of the topic of interest in Section I, Section II describes the materials used and gives the method of design, modeling, simulation of CSC-SR structure and proposed antenna. Section III presents the results and analysis of simulated results of proposed structure and loaded antenna followed by measured results of fabricated proposed antenna. Section IV concludes the presented work.

II. MATERIALS AND METHODS

A. Modeling of proposed CSC-SR unit cell structure and CSC-SR loaded antenna

Mostly, SRR based LHMs exhibit a very narrow negative refraction band which can be widened by inclusion of thin wire structure due to inherently wide negative permittivity region [22]. The proposed CSC-SR LHM unit cell structure therefore consists of two turns spiral resonator and a capacitive loaded strip (CLS). The CLS is united with SR and combined structure is used to load the MPA in the same plane. The antenna of size $0.177\lambda \times 0.243\lambda$ with the parameters as mentioned in Table 1, is printed on Rogers RT/Duroid 5880 substrate of permittivity (ε_r) = 2.2, loss tangent = 0.0009 and thickness (h) = 2.361 mm. The patch antenna is displaced at a distance (d) of 0.5 mm from CSC-SR unit cell. Figures 1 (a) and 1 (b) show the cross sectional view and top view of proposed microstrip patch antenna respectively.

To simulate the CSC-SR loaded antenna, the coax base connector is used to feed the patch at an optimized position (-1.13, -2.5) mm with respect to origin for excellent impedance matching. The CSC-SR structure gets excited through the patch as it is placed near the patch.

The characteristic size of the basic unit cell should be much less than the operating wavelength to approximate it to the effective electric and magnetic properties of a medium according to effective medium theory. The dimensions of unit cell are calculated accordingly, with the fundamental equations used in [12]. Then, optimizing the parameters of CSC-SR structure and loaded antenna with 'Optimetrics' feature of High Frequency Structure Simulator (HFSS), final dimensions are determined.

As the unit cell structures can be approximated with appropriate lumped circuit elements with the quasi-static approach, the proposed structure may be equated to an LC circuit [13]. The SR ring is equivalent to an inductance coil and the split in the spiral produces a parallel plate capacitor. An electric current gets induced in the spiral when placed in a time varying magnetic field so that charge gets accumulated across the gap. The resonant response of the SR loop current to an external magnetic field produces a resonant magnetic moment. An extra capacitance is provided by CLS. The magnetic moment leads to negative values of material parameters for LHM.

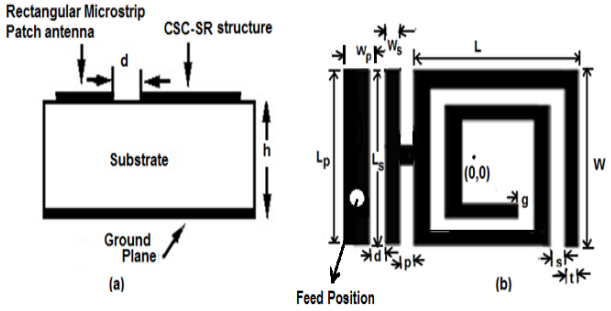

Fig. 1. (a) Cross sectional view of new planar CSC-SR structure loaded MPA, and (b) top view of new planar CSC-SR structure loaded MPA.

Table 1: Dimensional parameters of CSC-SR structure loaded MPA

S. No.	Parameters	Value (mm)
1.	Length of patch (L_p)	4
2.	Width of patch (W_p)	0.5
3.	Length of outermost turn of SR (L)	4.0
4.	Width of outermost turn of SR (W)	4.0
5.	Gap or split of turn (g)	0.2
6.	Spacing between inner turn and outer turn (s)	0.2
7.	Distance between patch antenna and LHM (d)	0.5
8.	Thickness of ring (t)	0.2
9.	Length of CLS (L_s)	4.0
10.	Width of CLS (W_s)	0.2
11.	Distance between CLS and SR (p)	0.3

B. Simulation of CSC-SR unit cell in waveguide

Initially, the proposed CSC-SR unit cell is simulated by putting it in a rectangular waveguide for investigating the metamaterial properties. The proposed CSC-SR unit cell used to load the antenna, is expected to demonstrate the left hand metamaterial properties. For this, the wire is excited by the electric fields, whereas the loop is excited by the magnetic fields. So, perfect electric conductor boundary conditions and perfect magnetic conductor boundary conditions are assigned on the y-direction and z-direction respectively. After applying boundaries, the metamaterial unit cell is applied excitations for field calculations. The CSC-SR unit cell depicted in Fig. 2 is simulated within a waveguide to observe its resonating frequency region and transmission frequency minimum. The proposed unit cell is numerically analyzed with HFSS software which

employs adaptive mesh refinement procedures iteratively in high error areas to enhance precision of solution. HFSS recalculates the error on each iteration until the convergence norms are fulfilled for ultimate solution. All the simulations are executed on Intel Core ™ i7, 2.67 GHz processor with 4 GB RAM system.

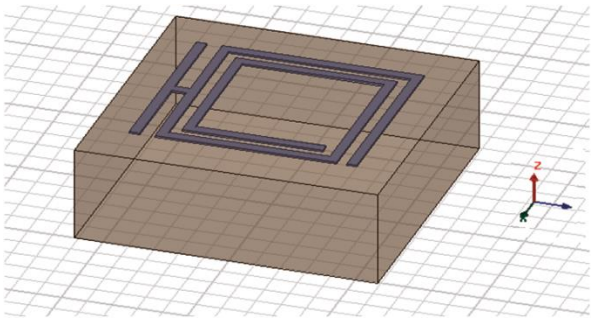

Fig. 2. Proposed CSC-SR unit cell on substrate.

The transmission spectrum of the CSC-SR is extracted from the S-parameter calculations. Further, effective permeability (μ_{eff}) and effective permittivity (ε_{eff}) of an equivalent metamaterial are determined from Nicolson-Ross-Weir (NRW) approach [6] for in-plane incidence to retrieve the effective electromagnetic parameters (μ_{eff} and ε_{eff}) from Scattering parameters, i.e., S_{11} and S_{21}. The reflection parameter (S_{11}) signifies the measure of EM wave reflected due to impedance mismatching in the transmission medium and transmission parameter (S_{21}) indicates the measure of EM wave passed through the conducting element;

$$V_1 = S_{21} + S_{11}, \quad (1)$$

$$V_2 = S_{21} - S_{11}. \quad (2)$$

The values, V_1 and V_2 indicate the summation and difference of S-parameters. The V_1 and V_2 are calculated from Equations (1) and (2):

$$\mu_{eff} = \frac{2}{jk_0h}\frac{1-V_2}{1+V_2}, \quad (3)$$

$$\varepsilon_{eff} = \frac{2}{jk_0h}\frac{1-V_1}{1+V_1}, \quad (4)$$

where k_0 is wave number in free space and is equated to ω/c, ω, is radian frequency and is = $2\pi f$ for frequency f, c is speed of light = 3×10^8 m/s, μ_{eff} is effective permeability of equivalent metamaterial, ε_{eff} is effective permittivity of equivalent metamaterial and h is thickness/height of substrate.

III. RESULTS

A. Simulated results of CSC-SR structure in waveguide

To evaluate the effective parameters of the structure, S-parameters, S_{11} and S_{21} are obtained by simulation of the CSC-SR structure. Figure 3 depicts S_{11} and S_{21} for the CSC-SR structure.

The S_{11} parameter for the proposed structure has a dip at frequency 2.45 GHz and transmission minimum of S_{21} is observed at frequency 2.85 GHz. The phase reversal of S_{11} and S_{21} at resonant frequency is depicted in Fig. 4. The phase reversal exhibited by the novel structure at the resonant frequency verifies its metamaterial behavior.

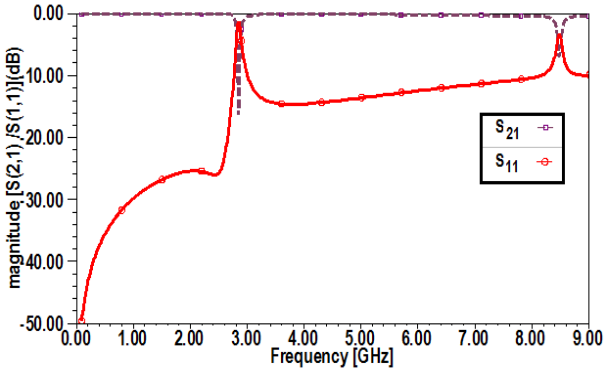

Fig. 3. S_{11} and S_{21} of CSC-SR structure.

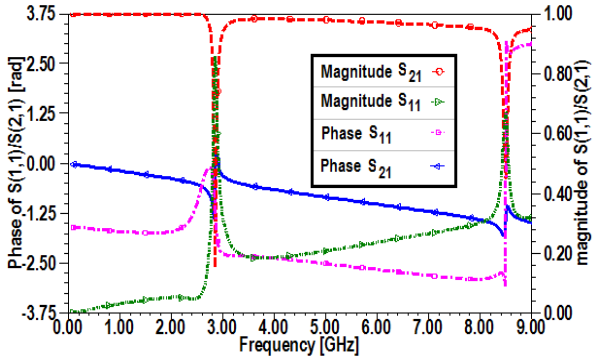

Fig. 4. Magnitude and phase of S_{21} and S_{11} of CSC-SR structure.

The effective parameters of CSC-SR structure are evaluated through S_{11} and S_{21} of new MTM structure. A MATLAB code is used to implement Equations (1) to (4) to demonstrate effective negative permeability and permittivity.

The values of effective electromagnetic parameters of CSC-SR such as effective permeability (μ_{eff}) and permittivity (ε_{eff}) are plotted in Fig. 5 (a) and refraction index (n) in Fig. 5 (b).

The regions of negative permeability and permittivity are clearly evident from the plots. It can be visualized in Fig. 5 (a) that the negative permeability is exhibited for the range 2.85 GHz - 6.15 GHz and the negative permittivity is achieved for the frequency range 2.00 GHz - 6.20 GHz. The negative refraction is thus observed from 2.00 GHz - 6.20 GHz and left hand region is from 2.85 GHz - 6.15 GHz as depicted in Fig. 5 (b). Hence the left hand (LH) bandwidth for the proposed structure is 3.3 GHz which is approximately same as

reported in [22]. In addition to the LH bandwidth, the proposed structure provides ease of fabrication as both conductors are on same side of substrate.

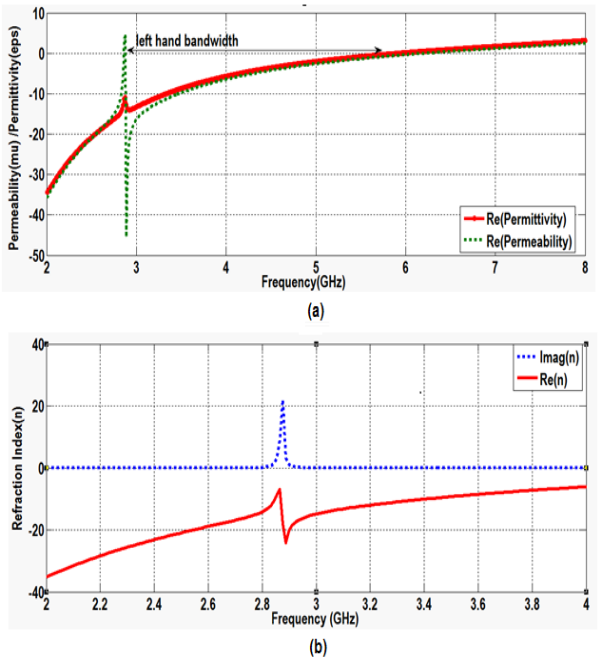

Fig. 5. (a). Effective permeability and permittivity of CSC-SR structure, and (b) refraction index of CSC-SR structure.

B. Simulated results of unloaded MPA and proposed MPA loaded with CSC-SR LHM unit cell

The MPA is placed near the CSC-SR MTM structure and excited by coaxial feed. The SR joined with wire gets excited due to mutual induction of MPA. Hence the complete proposed antenna consists of MPA with LHM unit cell. In the present work, the performance comparison for loaded MPA and unloaded MPA has been done and results are analyzed. The antenna model is initially executed without loading with the CSC-SR structure.

The unloaded antenna resonates at frequency of 27.12 GHz with return loss of 11.8 dB below 0 dB as depicted in Fig. 6. The value of voltage standing wave ratio (VSWR) is 1.69 which indicates high mismatch of impedance. The gain and directivity achieved for the unloaded antenna is 3.7 dB and 3.81 dB respectively. The comparative performance of unloaded MPA and the proposed CSC-SR loaded MPA is given in Table 2.

The novel antenna design is then obtained by loading CSC-SR LHM structure. The loading of SR is preferred for design of electrically small antenna (ESA) because conventional LC resonator uses unit cell area inadequately and so SR loading can be proposed to design ESA [14].

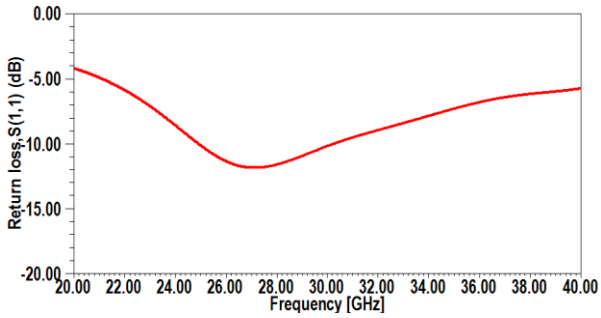

Fig. 6. Return loss of unloaded rectangular MPA.

Table 2: Comparison of proposed CSC-SR loaded MPA with unloaded MPA

S. No.	Parameters	Unloaded MPA	Proposed Antenna
1.	Return loss	-11.8 dB	-47 dB
2.	VSWR	1.69	1.0094
3.	Gain	3.7 dB	7.09 dB
4.	Directivity	3.87 dB	7.17 dB
5.	Antenna dimensions	4 mm × 0.5 mm	4 mm × 5.5 mm

The numerical simulations of the proposed antenna are performed with the intention to conceive the interaction between these conductors with the applied electromagnetic fields. The proposed antenna is also numerically analyzed with HFSS software. The resonant frequency of CSC-SR MTM loaded antenna shifts to low frequency side as compared to resonant frequency of unloaded antenna. This is because of change in capacitance due to geometrical parameters of structure. The loaded antenna resonates at 13.25 GHz with an impedance bandwidth of 1056 MHz as demonstrated in Fig. 7. Its value is 47 dB below 0 dB at resonant frequency, 13.25 GHz and corresponding VSWR value is 1.009 indicating good matching of impedance. The fractional bandwidth (FBW) achieved is 7.96%.

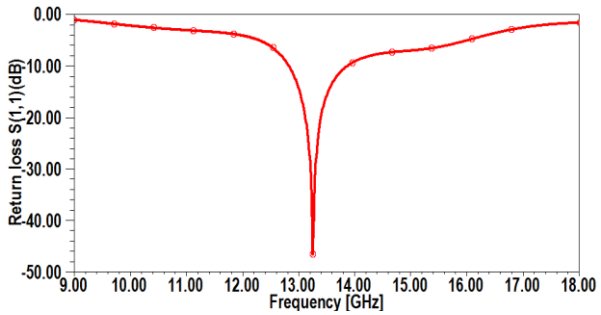

Fig. 7. Return loss of CSC-SR loaded MPA.

A 50 Ω impedance matching is achieved at the resonating frequency of 13.25 GHz as is depicted from

the input impedance variation over frequency sweep in Fig. 8.

Figure 9 displays 3D polar plot of gain with peak value 7.09 dB and 3D plot of directivity with maxima of 7.17 dB at resonant frequency. The elevation and azimuth gain radiation patterns are shown in Fig. 10 for proposed antenna.

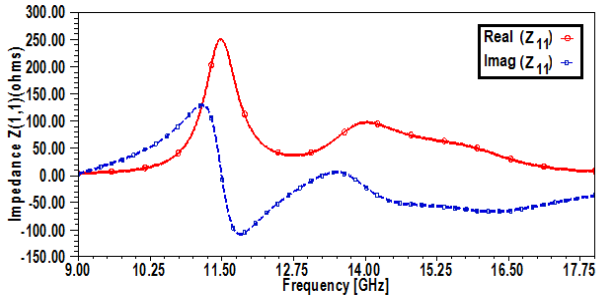

Fig. 8. Input impedance characteristics of CSC-SR structure loaded MPA.

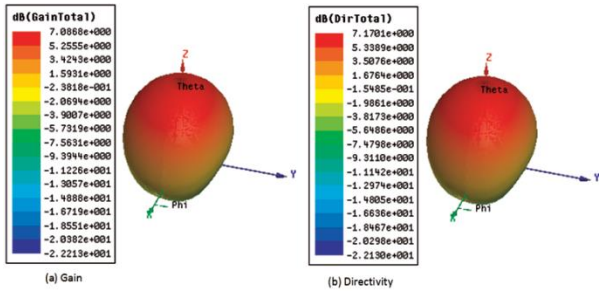

Fig. 9. 3D polar plot of gain and directivity of CSC-SR structure loaded MPA.

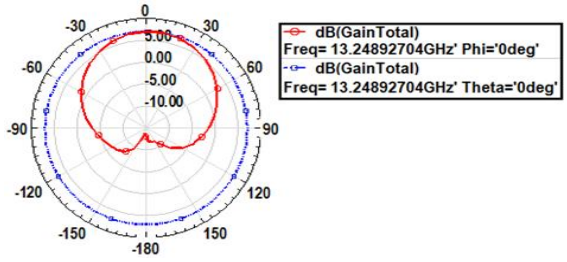

Fig. 10. Simulated radiation pattern of MPA loaded with CSC-SR.

The essential condition for being an electrically small antenna, the largest dimension of the proposed antenna must fit inside an imaginary sphere, termed as 'radian sphere' of radius 'a', and should satisfy the condition in Equation (5) [23,24]:

$$ka < 1, \tag{5}$$

where ka=(2π/λ)a and λ is operating wavelength. For the proposed antenna, ka=0.943 which is less than 1.

A relationship between minimum quality factor (Q_{chu}) and the radiation quality of an ESA was derived by Chu which is given by Equation (6) [25]:

$$Q_{chu} = \frac{1}{(ka)^3} + \frac{1}{ka}. \tag{6}$$

According to Chu limit, an antenna would experience poor efficiency at a size below Chu limit (Q_{chu}). The minimum calculated radiation factor (Q_{rad}) from equation (7) for the proposed antenna is 2.25. For an antenna to be ESA, its radiation factor, Q_{rad} should be > 10 [26]. The value of Q_{rad} can be calculated as:

$$Q_{rad} = \frac{1}{fractional\ BW}. \tag{7}$$

The value of Q_{rad} for proposed antenna is 12.7 and is >> Q_{chu}. Thus, the proposed ESA structure is practically realistic with stated parameters.

C. Experimentally measured results of proposed fabricated antenna

The proposed antenna is fabricated on Rogers Duroid substrate 5880 of dielectric constant 2.2 and height 2.361 mm. The photographs of two sides of fabricated antenna are shown in Fig. 11.

The return loss for the fabricated antenna is shown in Fig. 12 measured with Agilent N5222A PNA Microwave Network Analyzer. The measured value of return loss for the fabricated antenna is 24 dB below 0 dB and impedance bandwidth is 1085 MHz at resonant frequency 13.2 GHz as compared to simulated value of 47 dB below 0 dB with impedance bandwidth 1056 MHz. The observed difference of experimental results from simulated results is due to cable loss between the connector and antenna and soldering.

Figure 13 compares the simulated 2D gain for the CSC-SR loaded antenna with the measured values. The antenna shows good response in the frequency range from 10.25 GHz to 17.25 GHz with maximum gain at 13.25 GHz. It is also observed that measured results for return loss are close to numerically evaluated results.

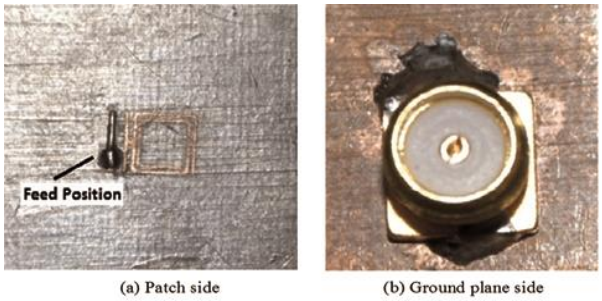

Fig. 11. Photographs of fabricated CSC-SR structure loaded MPA on Rogers Duroid substrate.

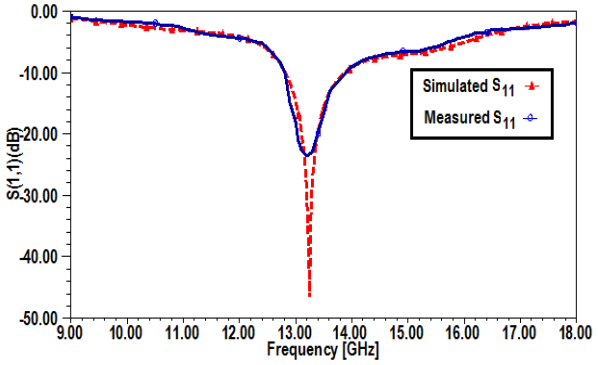

Fig. 12. Simulated and measured return loss of CSC-SR structure loaded MPA.

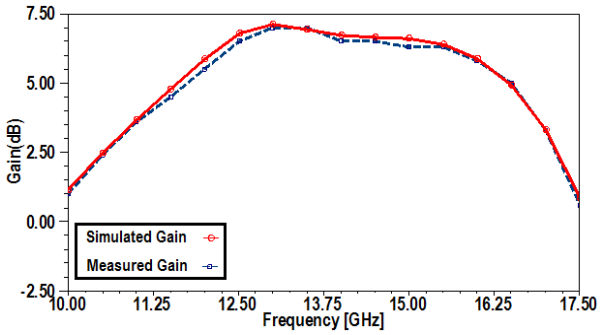

Fig. 13. Simulated and measured gain of CSC-SR structure loaded MPA as a function of frequency.

The proposed metamaterial antenna offers better performance characteristics along with miniaturization than the design reported in [7] as summarized in Table 3.

Table 3: Comparison of proposed antenna with ESA antenna reported in [7]

Antenna	Parameters	Joshi et al. [7]	Proposed Antenna
Simulated antenna	Return loss	-34 dB	-47 dB
	Gain	3.2 dBi	7.09 dB
	Directivity	7.8 dBi	7.17 dB
	Bandwidth	512 MHz	1056 MHz
	Electrically small antenna	ka=0.775 < 1	ka=0.943 < 1
	Electrical size	0.161λ × 0.192λ	0.177λ × 0.243λ
	Antenna dimensions	5 mm × 6 mm	4 mm × 5.5 mm
Fabricated antenna	Return loss	Not measured	-24 dB
	Gain	Not measured	7 dB
	Bandwidth	Not measured	1085 GHz

IV. CONCLUSION

In this work, a new planar CSC-SR metamaterial structure based planar antenna has been proposed. It is observed that proposed CSC-SR structure exhibits a very wide frequency band of 3.3 GHz with negative permittivity and negative permeability. Hence this metamaterial structure would have great prospects in designing broadband microwave devices. Further this new structure loaded MPA of size 0.177λ × 0.243λ is presented resonating at 13.25 GHz whereas the unloaded MPA was resonating at a frequency of 27.12 GHz. The resonant frequency of the antenna gets lowered with improved magnetic permeability of dielectric material by metamaterial loading. Thus it is concluded that the resonance of antenna can be controlled according to the desired application. Good impedance matching is demonstrated with S_{11} value reaching to -47 dB. The proposed antenna achieves high gain of 7.09 dB, an impedance bandwidth of 1056 MHz with fractional bandwidth of 7.96%. Measured results obtained are in good agreement with the simulated results. The proposed antenna satisfies the condition of ESA with good radiation factor and is practically feasible with stated parameters.

REFERENCES

[1] N. Engheta and W. Z. Richard, *Metamaterials Physics and Engineering Explorations*. Wiley & Sons, pp. 43-46, 2006.

[2] A. Semichaevsky and A. Akyurtlu, "Homogenization of metamaterial-loaded substrates and superstrates for antennas," *Progress in Electromagnetics Research*, vol. 71, pp. 129-147, 2007.

[3] V. G. Veselago, "The electrodynamics of substances with simultaneously negative values of 'ε, and μ'," *Sov. Phys.—Usp*, vol. 10, no. 4, pp. 509-514, 1968.

[4] J. B. Pendry, A. J. Holden, W. J. Stewart, and I. Youngs, "Extremely low frequency plasmons in metallic meso-structures," *Physical Review Letters*, vol. 76, pp. 4773-4776, 1996.

[5] J. B. Pendry, A. J. Holden, D. J. Robins, and W. J. Stewart, "Magnetism from conductors and enhanced non-linear phenomena," *IEEE Trans. Microwave Theory and Techniques*, vol. 47, no. 11, pp. 2075-2084, Nov. 1999.

[6] J. B. Pendry, A. J. Holden, D. J. Robbins, and W. J. Stewart, "Low frequency plasmons for thin wire structure," *J. Phys. Condens. Matter.*, vol. 10, pp. 4785-4809, Mar. 1998.

[7] J. G. Joshi, S. S. Pattnaik, S. Devi, and M. R. Lohokare, "Electrically small patch antenna loaded with metamaterial," *IETE Journal of Research*, vol. 56, no. 6, pp. 373-379, 2010.

[8] J. Y. Siddiqui, C. Saha, and Y. M. M. Antar, "Compact SRR loaded UWB circular monopole antenna with frequency notch characteristics,"

IEEE Transactions on Antenna and Propagation, vol. 62, no. 8, pp. 4015-4420, 2014.

[9] A. A. Sulaiman, A. S. Nasaruddin, and M. H. Jusoh, "Bandwidth enhancement in patch antenna by metamaterial substrate," *European Journal of Scientific Research*, vol. 44, no. 4, pp. 493-501, 2010.

[10] C. Sabah, "Tunable metamaterial design composed of triangular split ring resonator and wire strip for S- and C-microwave bands," *Progress in Electromagnetics Research B*, vol. 22, pp. 341-357, 2010.

[11] P. Natani, L. A. Shaik, C. Saha, and J. Y.Siddiqui, "Hexagonal SRR coupled UWB vivaldi antenna for frequency notched applications," in *2nd International conference on Emerging Trends in Electronics, Communication and Networking (ET2ECN)*, Surat (India), pp. 1-4, Dec. 2014.

[12] F. Bilotti, A. Toscano, and L. Vegni, "Design of spiral and multiple split-ring resonators for the realization of miniaturized metamaterial samples," *IEEE Transactions on Antennas and Propagation*, vol. 55, no. 8, pp. 2258-2267, 2007.

[13] Rajni and A. Marwaha, "Resonance characteristics and effective parameters of new left hand metamaterial," *Telkomnika Indonesian Journal of Electrical Engineering*, vol. 15, no. 3, pp. 497-503, Sept. 2015.

[14] K. Buell, H. Mosssoallaei, and K..Sarabandi, "A substrate for small patch antennas providing tunable miniaturization factors factors," *IEEE Transactions on Microwave Theory and Techniques*, vol. 54, pp. 135-146, Jan. 2006.

[15] Rajni, A. Marwaha, and G. Kaur, "Metamaterial inspired circular patch antenna using complementary split ring resonator and complementary spiral resonator," *International Journal of Applied Engineering Research*, vol. 10, no. 9, pp. 22717-22726, 2015.

[16] S. Jahani, J. R. Mohassel, and M. Shahabadi, "Miniaturization of circular patch antennas with MNG metamaterials," *IEEE Antenna and Wireless Letters*, vol. 9, pp. 1194-96, 2010.

[17] A. A. Sulaiman, A. Othman, M. H. Jusoh, N. H. Baba, R. A. Awang, and M. F. Ain, "A small patch antenna on omega structure metamaterial," *European Journal of Scientific Research*, vol. 43, pp. 527-537, 2010.

[18] J. Naqui, J. Corominan, K. H. Ali, C. Fumeaux, and F. Martín, "Angular displacement and velocity sensors based on coplanar waveguides loaded with S-Shaped split ring resonators," *Sensors*, vol. 15, no. 5, pp. 9628-9650, 2015.

[19] R. Marqués, F. Mesa, J. Martel, and F. Medina, "Comparative analysis of edge- and broadside-coupled split ring resonators for metamaterial design—theory and experiments," *IEEE Transaction on Antennas and Propagation*, vol. 51, no. 10, pp. 2572-2581, 2003.

[20] Rajni, A. Kaur, and A. Marwaha, "Detection of sub-millimeter crack on metal surface using complementary spiral resonator," *International Journal of Applied Engineering Research*, vol. 10, pp. 24025-24036, 2015.

[21] Rajni, A. Kaur, and A. Marwaha, "Complementary split ring resonator based sensor for crack detection," *International Journal of Electrical and Computer Engineering (IJECE)*, vol. 5, no. 5, pp. 1012-1017, 2015.

[22] X. Han, J. S. Hong, D. L. Jin, and Z. M. Zhang, "A novel structure for broadband left-handed metamaterial," *Chin. Phys. B*, vol. 21, pp. 094101, 2012.

[23] H. A. Wheeler, "Fundamental limitations of small antennas," *IRE Proceedings*, vol. 35, pp. 1479-84, 1947.

[24] L. J. Chu, "Physical limitations on omni-directional antennas," *Journal of Applied Physics*, vol. 19, pp. 1163-75, 1948.

[25] R. Singh, A. I. A .N. Ibraheem, M. Koch, and W. Zhang, "Asymmetric planar terahertz metamaterials," *Optics Express*, vol. 18, no. 12, pp. 13044-13050, 2010.

[26] J. McLean, "A re-examination of the fundamental limits on the radiation Q of electrically small antennas," *IEEE Transactions on Antennas and Propagation*, vol. 44, pp. 672-6, 1996.

Rajni is currently Associate Professor at SBS State Technical Campus, Ferozepur, India. She has done her M.E. from NITTTR, Chandigarh, India and B.Tech. from REC Kurukshetra (Now NIT, Kurukshetra). Presently, she is pursuing her Ph.D. in Metamaterial Antennas. She has approximately 18 years of academic experience. Her areas of interest include Wireless communication and Antenna design.

Anupma Marwaha is currently Professor at Sant Longowal Institute of Engg. and Tech, Longowal, Sangrur (Pb.) (India). She has done her Ph.D. from GNDU, Amritsar, M.Tech. from REC Kurukshetra (Now NIT, Kurukshetra), B.E. from Punjab University, Chandigarh. She has 22 years of academic experience. She has supervised

15 M.Tech. thesis, 04 Ph.D. thesis and 05 thesis are in progress. She has more than 75 publications to her credit in International and National Journals in the area of antenna design, bio-electromagnetics and in micro-scale and nano-scale structures.

A Switched Beam Antenna Array with Butler Matrix Network using Substrate Integrated Waveguide Technology for 60 GHz Radio

Nishesh Tiwari and Thipparaju R. Rao

Department of Telecommunication Engineering
SRM University, Chennai, Tamilnadu-603203, India
nitizaz@gmail.com, ramaraot@outlook.com

Abstract ─ A switched beam antenna array based on substrate integrated waveguide (SIW) technology is designed and simulated for 60 GHz communications. The antenna array is fed by 4x4 planar butler matrix network in order to achieve the switched beam characteristic. Each of the components is designed and verified through simulations in electromagnetic field simulation tools, CST MWS and HFSS. The components are integrated later to form the switched beam antenna array. The return losses and isolations are better than 10 dB from 57 GHz to 64 GHz for all of the input ports. The peak gain for the switched beam antenna array is 18 dBi at 60 GHz.

Index Terms ─ Beamforming, butler matrix, electromagnetic simulation, millimeter wave, slot antenna, substrate integrated waveguide, switched beam antenna.

I. INTRODUCTION

These days the availability of high bandwidth at 60 GHz band is a highly attractive option for high speed wireless communications allowing transfer of uncompressed data, voice and video at the speed of gigabit per second [1]. At millimeter wave frequency band the losses in the planar microstrip circuit is high. Therefore this requires more efficient technology like the substrate integrated waveguide (SIW) to be used, which provides advantages of the traditional rectangular waveguide such as low loss, high quality factor, complete shielding and capability of handling high power along with the combined advantage of planar circuit designs [2]. Analysis of SIW structures is presented and compared with HFSS simulation results in [3]. SIW structures have proved to be a good choice for the construction of millimeter wave beamforming networks and multi-beam antennas, which includes techniques like SIW based Butler matrix, Blass matrix, Rotman lens etc. As compared to Blass and Nolen matrix, the Butler matrix requires the least number of couplers [4]. Butler matrix has been widely used in radar, warfare and satellite applications. As the length of the crossover is small for 60 GHz it becomes difficult to design the phase shifter which fits that size using straight delay lines in the butler matrix. One option is to use a curved delay line. In this work, a new design approach is used in designing the switched beam antenna. Here, the SIW based 4x4 planar butler matrix consisting of curved phase shifters and constructed using circular vias is integrated with the SIW slot antenna array constructed using rectangular vias to form the switched beam antenna for 60 GHz communications. The switched beam antenna array structure is designed on a Rogers RT/Duroid 5880 substrate with a dielectric constant of 2.2, thickness of 0.254 mm and loss tangent of 0.0009 at 10 GHz. It is designed, simulated and verified utilizing the electromagnetic field simulation tools, CST MWS and HFSS.

II. DESIGN OF BUTLER MATRIX

Butler matrix is one of the most popular multiple beamforming network. The 4x4 butler matrix design has four input ports and four output ports. Exciting each input port provides a different output beam as the relative phases across the output ports change. The general block diagram of 4x4 butler matrix is shown in Fig. 1. The 4x4 butler matrix has four 3 dB 90° hybrid couplers, two crossovers and phase shifters.

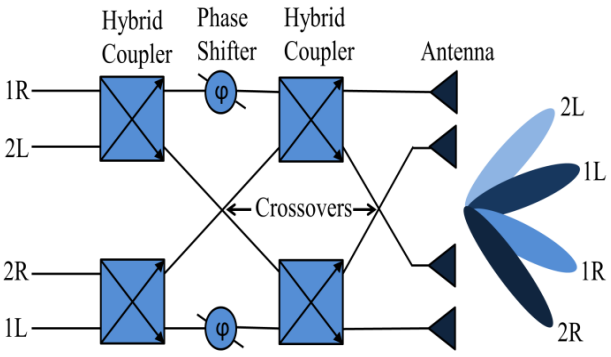

Fig. 1. Butler matrix block diagram with antenna array.

Submitted On: June 19, 2015
Accepted On: February 25, 2016

A. 3 dB 90° hybrid coupler and crossover

The diagram of the 3 dB hybrid coupler is shown in Fig. 2 where, Lc = 2.862 mm and Wc= 4.745 mm. The SIW designs are based on equations in [2] with diameter of vias as 0.2 mm and pitch as 0.35 mm. Figure 3 shows the magnitude and phase of the coupler. From Fig. 3 it is observed that the return loss and isolation are better than 10 dB from 57 GHz to 64 GHz. Also, S21 and S31 are almost equal in magnitude. Further, from Fig. 3 it is also observed that S21 and S31 have phase difference of almost 90° throughout the entire 60 GHz band. The simulation results from both HFSS and CST are observed to be similar. The schematic of crossover is also shown in Fig. 2 where, Lc = 6.012 mm and Wc = 4.745 mm. Figure 4 shows the magnitude and phase of the crossover. From Fig. 4 it is observed that S11, S21 and S41 are below -10 dB. Both HFSS and CST simulation results are observed to be similar.

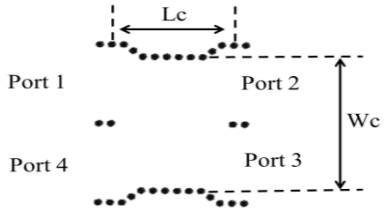

Fig. 2. Schematic of coupler and crossover.

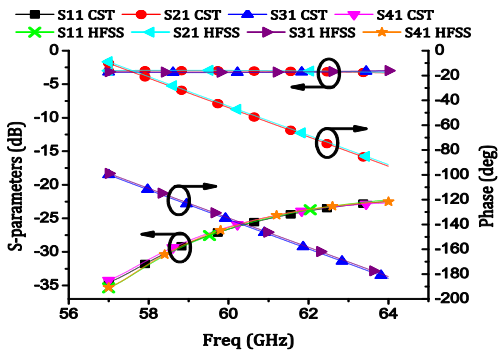

Fig. 3. S-parameters and phase of hybrid coupler.

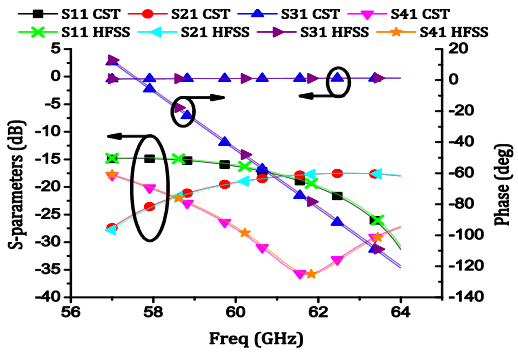

Fig. 4. S-parameters and phase of crossover.

B. Phase shifters

The phase shift is obtained in this design using curved transmission line as it is not possible to achieve the required phase shift of 0° and 45° using straight transmission line. Figure 5 (a) and Fig. 5 (b) show the 0° and 45° phase shifters respectively.

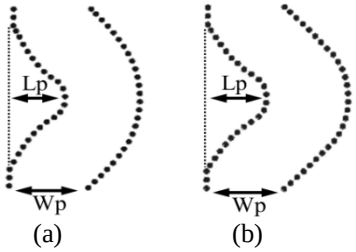

Fig. 5. Phase shifters: (a) 0° and (b) 45°.

In Fig. 5, Lp = 2.019 mm and Wp = 2.81 mm for 0° phase shifter. For 45° phase shifter Lp = 2.281 mm and Wp = 2.835 mm. The magnitude and phase of the 0° and 45° phase shifter is shown in Fig. 6. From Fig. 6 it is observed that the return loss for both phase shifters is better than 10 dB for the entire 60 GHz band. Also, from Fig. 6 it is observed that the phase difference between the phase shifters is 45° at 60 GHz. The simulation results from HFSS and CST agree well with each other.

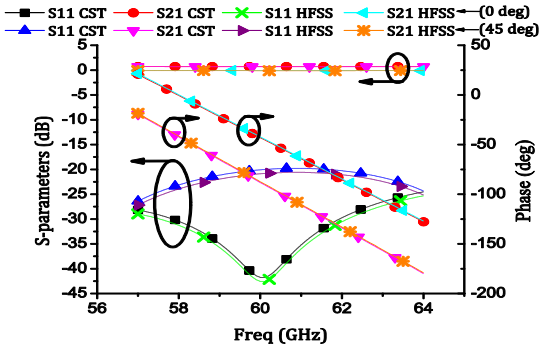

Fig. 6. Magnitude and phase of 0° and 45° phase shifters.

C. Butler matrix

The butler matrix is designed by integrating the components designed above. The performance of the butler matrix is verified through simulation in CST MWS and HFSS. Fig. 7 shows the designed butler matrix. Figure 8 shows the magnitude at the ports of the butler matrix when port 1 is excited, and Fig. 9 shows the relative phases at the output ports when port 1 is excited. Similarly, Fig. 10 shows the magnitude at the ports when port 2 is excited and Fig. 11 shows the relative phases at the output ports when port 2 is excited.

From Fig. 8 it is observed that when port 1 is excited, the return loss is better than 10 dB for the entire band from 57 GHz to 64 GHz. The magnitudes of output

at port 5, 6, 7 and 8 are also observed to be in acceptable range. Further, from Fig. 9 it is observed that the relative phase differences between the output ports are around -45°, -90° and -135° for ports 6, 7 and 8 with respect to port 5 when port 1 is excited.

From Fig. 10 it is observed that when port 2 is excited, the return loss is better than 13 dB for the entire band from 57 GHz to 64 GHz. Further, it is observed that the magnitudes of output at port 5, 6, 7 and 8 are also within the acceptable range. Similarly, from Fig. 11 it is observed that the phase differences between the output ports are around 135°, -90° and 45° for ports 6, 7 and 8 with respect to port 5. Also, the simulation results of CST MWS and HFSS are observed to be similar.

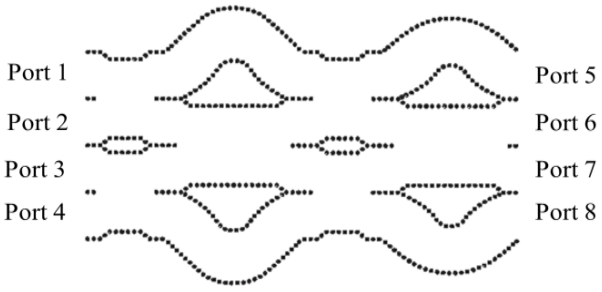

Fig. 7. SIW butler matrix structure.

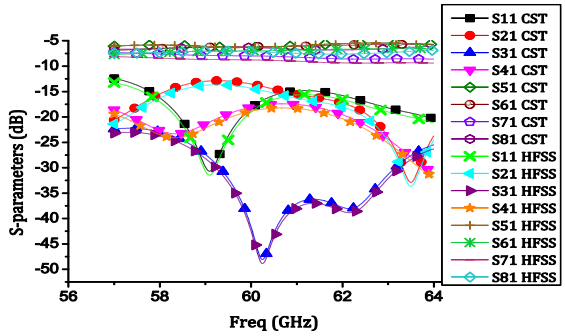

Fig. 8. S-parameters of butler-matrix when port 1 is excited.

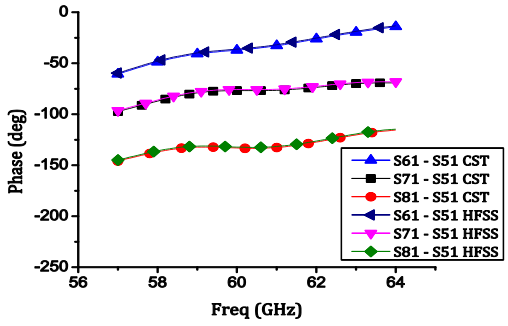

Fig. 9. Butler matrix output phase with port 1 excited.

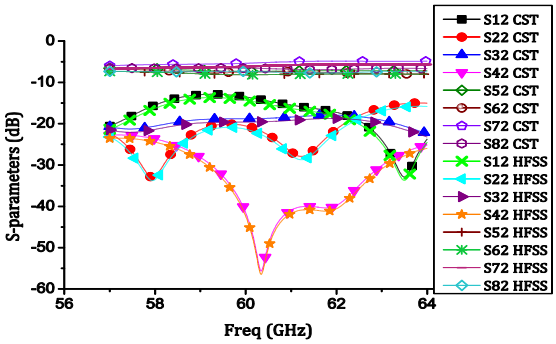

Fig. 10. Butler matrix S-parameters with port 2 excited.

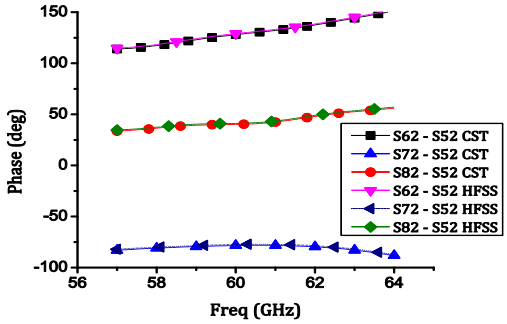

Fig. 11. Butler matrix output phase with port 2 excited.

III. SWITCHED BEAM SLOT ANTENNA

The waveguide longitude slot antennas are popular for beam steering applications. The diagram of slot antenna is shown in Fig. 12 (a) and Fig. 12 (b) shows the E-field in it. In Fig. 12 (a), S = 0.15 mm, W= 0.3 mm, Ws = 0.198 mm, Ls = 1.789 mm, Es = 2.1 mm and slots displacement from the center is 0.17 mm. The antenna is designed as per the design equations mentioned in [5] using SIW technology with rectangular shaped vias which act as the side wall of the waveguide.

The theoretical values are used in the design of the antenna slots and further the design is optimized through CST MWS and verified through HFSS simulations. Figure 13 shows the radiation pattern of the single antenna. The E-plane and H-plane radiation patterns are shown in the figure. It is observed that the gain is 13 dBi. Figure 14 shows the design of the complete switched beam slot antenna array.

The radiation pattern of the switched beam antenna array is shown in Fig. 15. The gain is observed to be 17 dBi when port 2 or port 3 is excited. However, the gain is observed to be 18 dBi when port 1 or port 4 is excited. Further, it is observed that the main beam is directed towards +15° and -15° when port 1 and port 4 is excited respectively. It shifts to -39° and +39° when port 2 and port 3 is excited respectively. It is observed that the simulation results from CST MWS and HFSS agree

well with each other.

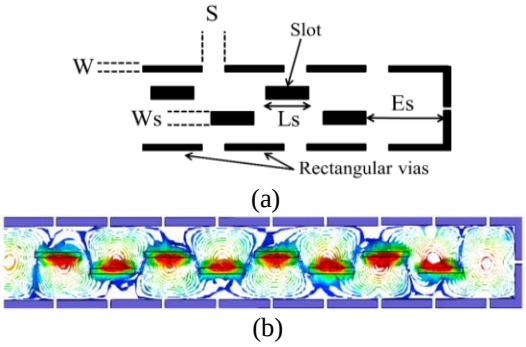

Fig. 12. Slot antenna: (a) schematic and (b) E-field distribution.

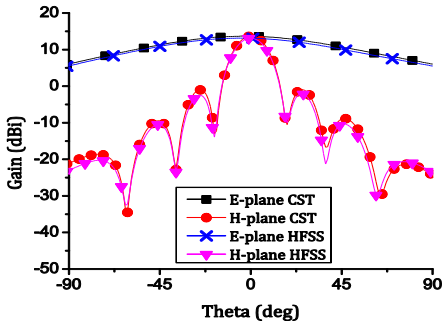

Fig. 13. Radiation pattern of slot antenna.

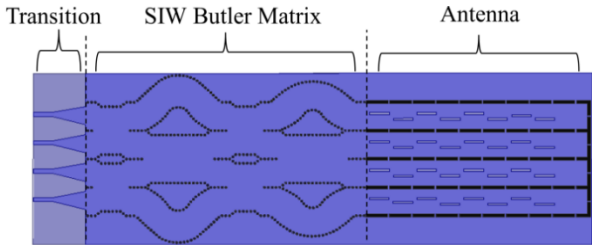

Fig. 14. Switched beam slot antenna array.

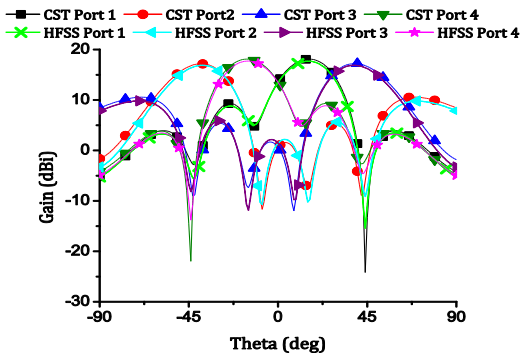

Fig. 15. Radiation patterns when different ports are excited.

IV. CONCLUSION

In this communication, a planar 60 GHz switched beam antenna array has been designed and simulated. The designed switched beam antenna demonstrates a good performance as a candidate for beam steering and for systems on substrate applications.

ACKNOWLEDGMENT

Authors are very much obliged to ISRO, Government of India, for the assistance provided for this work.

REFERENCES

[1] P. Smulders, "Exploiting the 60 GHz band for local wireless multimedia access: Prospects and future directions," *IEEE Commun. Mag*., vol. 40, no. 1, pp. 140-147, Jan. 2002.

[2] M. Bozzi, A. Georgiadis, and K. Wu, "Review of substrate-integrated waveguide circuits and antennas," *IET Microwaves, Antennas & Propagation*, vol. 5, no. 8, pp. 909-920, June 2011.

[3] R. Rezaiesarlak, M. Salehi, and E. Mehrshahi, "Hybrid of moment method and mode matching technique for full-wave analysis of SIW circuits," *ACES Journal*, vol. 26, no. 8, pp. 688-695, Aug. 2011.

[4] P. S. Hall and S. J. Vetterlein, "Review of radio frequency beamforming techniques for scanned and multiple beam antennas," *IEE Proceedings H - Microwaves, Antennas and Propagation*, vol. 137, no. 5, pp. 293-303, Oct. 1990.

[5] R. S. Elliott, "An improved design procedure for small arrays of shunt slots," *IEEE Trans. Antennas Propag*., vol. 31, no. 1, pp. 48-53, Jan. 1983.

Nishesh Tiwari is currently pursuing his Ph.D. from the Dept. of Telecommunication Engineering at SRM University, India. His current research interests are Antennas and Propagation and Wireless Communications.

Thipparaju R. Rao is currently working as Professor and Head Telecommunication Engineering Dept., SRM University, India. He received his Ph.D. degree from Sri Venkateswara University, India in 2000. His research interests are Antennas, Radio Channel Measurements & Modeling, Broadband Wireless Communications and Mobile Cellular Telecommunications.